Controlled Local Delivery of RNA: Regulating Tissue Morphogenesis

By

Steven Andrew Castleberry

B.S. Chemical Engineering, Biochemistry
Oklahoma State University – Stillwater, 2010

SUBMITTED TO THE HARVARD-MIT DIVISION OF HEALTH SCIENCES AND TECHNOLOGY IN PARTIAL FULFILLMENT OF THE REQUIREMENTS FOR THE DEGREE OF

DOCTOR OF PHILOSOPHY IN MEDICAL ENGINEERING AND MEDICAL PHYSICS

AT THE

MASSACHUSETTS INSTITUTE OF TECHNOLOGY

April 2015 [June 2015]

Signature of Author: Signature redacted

Harvard-MIT Division of Health Sciences and Technology
April 14, 2015

Certified by: Signature redacted

Paula T. Hammond, Ph.D.
Bayer Professor of Chemical Engineering
Thesis Supervisor

Accepted by: Signature redacted

Emery N. Brown, M.D., Ph.D.
Director, Harvard-MIT Program in Health Sciences and Technology
Professor of Computational Neuroscience and Health Sciences and Technology

Members of Thesis Committee

Thesis Supervisor

Paula T. Hammond, Ph. D.

Bayer Professor of Chemical Engineering

Massachusetts Institute of Technology

Committee Chair

Sangeeta N. Bhatia, M.D., Ph.D.

Professor of Electrical Engineering and Computer Science

Professor of Institute of Medical Engineering and Sciences

Massachusetts Institute of Technology

Thesis Committee Member

Daniel G. Anderson, Ph.D.

Associate Professor of Chemical Engineering

Associate Professor of Institute of Medical Engineering and Sciences

Massachusetts Institute of Technology

Thesis Committee Member

Robert F. Padera, M.D., Ph.D.

Assistant Professor of Pathology

Harvard Medical School

Controlled Local Delivery of RNA: Regulating Tissue Morphogenesis

By

Steven Andrew Castleberry

Submitted to the Division of Health Sciences and Technology on April 14, 2015 in Partial Fulfillment of the Requirements for the Degree of Doctor of Philosophy in Medical Engineering

Abstract

RNA interference (RNAi) is a powerful technology that provides a means to alter the expression of a specific protein based on a targeted RNA sequence. This is done by taking advantage of existing cellular machinery present within all eukaryotic cells which use short double-stranded RNA sequences as guides for RNA induced silencing. The potential for RNAi in medicine is enormous, providing a new approach to treat the complex biological dysregulation underlying many diseases. This promise of a new branch of therapeutics however has been mired with difficulties. RNA is quickly degraded by nucleases that are prevalent in the blood and throughout the body, it is highly immunogenic, and systemic delivery is complicated by high clearance rates. As such, developing formulations for the effective delivery of short RNAs presents significant hurdles.

Local delivery can limit numerous unwanted systemic side effects of therapies and it maintains the highest therapeutic index possible in a targeted area before clearance. As such, the local delivery of siRNA may hold just as much potential as systemic delivery with significantly reduced complications. Layer-by-layer (LbL) assembly is a robust method that has been successfully demonstrated for the localized and sustained delivery of many biologic therapeutics and biomolecules. Developing an LbL film capable of delivering siRNA locally would offer a powerful new approach to the treatment of local disorders. This approach could be combined with existing medical devices to improve patient outcomes by directly addressing pathologic

dysregulation in the area of interest. One field where the local treatment of dysregulation could be of particular interest is that of wound healing.

Wound healing is a complex and highly synchronized process of multiple biological pathways, consisting of an assortment of cytokines, growth factors, and varied cell types which evolves over time. The development of a drug delivery system that can locally modify cell behavior on the basic level of gene transcription would be a powerful tool to alter the dynamics of wound healing. There are many known complications of wound healing, ranging from chronic ulcerative wounds to hypertrophic contractile scars, which dramatically affect the lives of tens of millions of patients every year. Through RNA interference, one could specifically target the key mediators of these complications, providing a means to more effectively regulate the wound healing process *in vivo*. The capability to deliver siRNA locally to address these complications is a significant advance in the current state of wound treatment. As such, this work presents an opportunity to substantially improve the current standard of treatment for patients and their wound healing outcomes.

Herein, we present the design and preclinical evaluation of a number of strategies to develop ultra-thin polymer coatings for the controlled delivery of RNA both *in vitro* and *in vivo*. We used Layer-by-Layer assembly to create siRNA containing polymer-based films that can sustain the release of complexed siRNA over physiologically relevant timescales for local delivery into tissues. We describe the development of the first high-throughput approach for LbL assembly and screening and its use to identify lead candidate film architectures for RNA delivery. We then apply these findings to treat dysregulation in two distinct animal models; a chronic diabetic mouse wound model and a third-degree burn model in rats, targeting three different genes of interest independently. These coatings were demonstrated to effectively coat a number of medically relevant substrates including bandages, sutures, surgical staples, nanoparticles, microparticles, and microneedles. This body of work provides insight into how siRNA can be incorporated into thin film assemblies and the design criteria to achieve successful gene knockdown *in vitro* and *in vivo*.

Thesis Supervisor: Paula T. Hammond
Bayer Professor of Chemical Engineering

"We pass through this world but once. Few tragedies can be more extensive than the stunting of life, few injustices deeper than the denial of an opportunity to strive or even to hope, by a limit imposed from without, but falsely identified as lying within."

Stephen Jay Gould

The Mismeasure of Man, 1981

Acknowledgements

I want to my thesis advisor, Professor Paula Hammond, for being a great mentor to me. I appreciated your boundless enthusiasm and support as well as your guidance throughout my thesis. Your encouragement to keep looking for new designs and applications inspired me to develop new competencies and skills while broadening my scientific understanding.

I want to thank the members of my thesis committee, Professors Sangeeta Bhatia, Daniel Anderson, and Robert Padera, for there invaluable advice. I sincerely appreciated all of the discussions we have had and the time you spent to help shape the work presented in this thesis.

I want to thank all of my collaborators. Dr. Wei Li, it is hard to describe how much I valued our conversations. Your insight and wisdom were strong guiding forces in my research and career. I am proud to have you as a friend. I'm excited to see where your research takes you. Jason Kovacs, you have been a great friend. I appreciated our wandering rants and loud discussions. No matter where you end up you're going to make a positive impact in the world. Dr. Ben Almquist, thank you for all of your help in this work. Your personality and style were a great balancing influence for me. I am a more sound research scientist and confident investigator for knowing you. Tiago Reis, you possess an amazing sharp mind. Your drive to create new ideas and understand the world is inspiring. I know you will make a difference in the world.

I want to thank my undergraduate researchers. Mary Wang, you were a good person and your drive to learn and try new things was inspirational. John Chow, you're an incredibly strong and smart man. I am proud of how far you've come and I'm looking forward to seeing where you go. Sarah Mayner, your dedication to research was amazing. Malak abu Sharkh, your motivation and energy was a key factor in the finish of this thesis. I am amazed at how much you have learned and I am excited to see where your studies take you.

I want to thank my parents. You fed, clothed, and housed me for eighteen years. You put up with me when I was just that pestering bored kid who was always getting in trouble. Looking back now I understand a lot more of the struggles that you were going through and I truly appreciate your love and support.

I want to thank my brother Brian. Your dedication to your profession has been an inspiration to me. I want to thank my brother Aaron. You are stronger than you know, smarter than you think, and better than you care to realize. I love you and I know you will succeed in life.

I want to thank Kristina Hoeller. You are an amazingly strong person and you make a positive impact on my life. I love you.

This research was supported in part by funding and core facilities provided by the U.S. Army Research Office under contract W911NF-07-D-0004 at the MIT Institute of Soldier Nanotechnology and by funding from the Sanofi-Aventis and MIT Center for Biomedical Innovation. This work was also supported by use of core facilities at the Koch Institute for Integrative Cancer Research (supported by the NCI under grant 2P30CA014051-39). We thank the Koch Institute Swanson Biotechnology Center for technical support, specifically the microscopy, flow cytometry, and histology cores.

Biography

I grew up in small town in rural Oklahoma, the son of two public school teachers. I attended Oklahoma State University for five years, pursuing a degree in chemical engineering with a double major in biochemistry. During my sophomore year at OSU I worked in the nutritional sciences department studying the effects of antioxidant diets on the progression of osteoporosis in a murine model of menopause. In my junior and senior year at OSU I worked in the chemical engineering department investigating three-dimensional biodegradable constructs for tissue regeneration. These early experiences helped to mold my approach to research, seeking out collaborations with scientists of different backgrounds or perspectives.

I began my Ph.D. candidacy in the Harvard-MIT Health Sciences and Technology department, studying medical engineering and medical physics, in the fall of 2010. I joined the lab of Dr. Paula Hammond at the Institute for Soldier Nanotechnologies that following spring. In her lab I worked to investigate the use of ultra-thin polymer coatings for local RNAi therapy. This work was primarily focused on developing technology to improve wound healing, by accelerating wound closure and reducing scar formation. Throughout my research career I have collaborated with a diverse group of scientists, engineers, and medical professionals both in academia and industry to investigate new ideas and develop technology to improve patient care.

My personal interest in medical research began when I was a freshman at Oklahoma State. My father was hospitalized for over four months due to surgical complications. During this time I became dedicated to learn the science and engineering that goes into developing medical technology. This experience installed in me a deep desire to develop technologies to improve patient care, which has been the driving force behind my research career. I hope to work in the future along similar path, designing and developing technology to help people live longer and healthier lives.

Table of Contents

List of Figures and Tables

Chapter 1
Introduction

1.1 Introduction to Wound Healing

Wound healing is a complex, multi-stage process that involves several interdependent biological components[1-7]. It is classically thought of as occurring in four distinct phases: (1) hemostasis, (2) inflammation, (3) proliferation, and (4) tissue remodeling [5]. Each of these phases has its own balance of signaling molecules and cell types associated with it, creating a unique evolving microenvironment within the injured tissue in which wound healing interventions must operate[8-11]. Immediately post-injury the body responds by clotting within the site of injury. This clot acts both to stop blood loss as well as to seal the body's surface from bacteria that may try and infect the available tissue. The formed clot consists of a number of extracellular matrix (ECM) proteins as well as many cytokines and growth factors that are key in promoting wound healing. This clot forms the first scaffold within the wound site on which later granulation tissue will be built.

The process of hemostasis in healthy healing wounds only lasts a few minutes to hours[4,5]. Inflammation within the wound begins alongside hemostasis but can last for days or even longer in infected or chronic wounds. Inflammation plays an incredibly important role in determining the progression of the wound healing process. Recruitment of white blood cells into the healing tissue is driven by the cytokines of inflammation, brining neutrophils initially into the wound and later drawing monocytes and macrophages into the tissue[4]. Macrophages are especially important within the healing wound as they coordinate many of the later inflammatory processes.

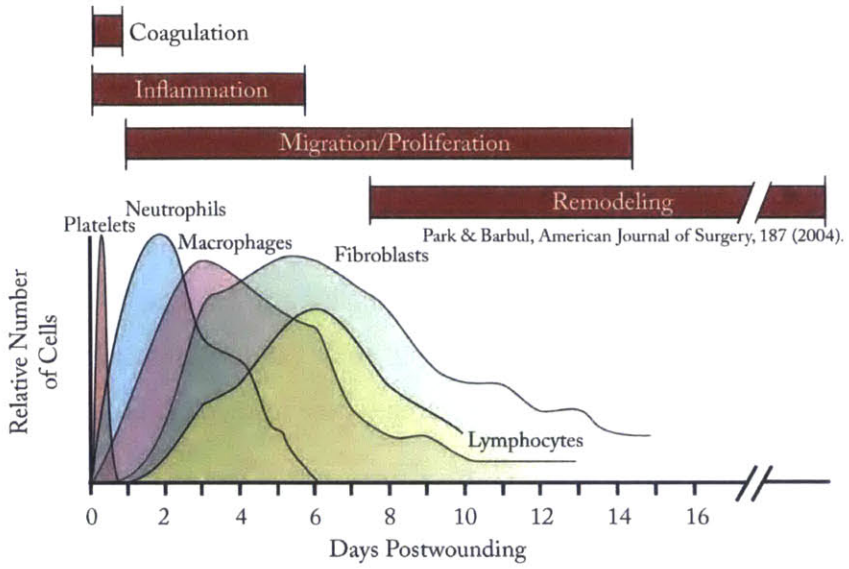

Figure 1-1 The phases and cellular make-up of the wound healing process

The wound healing process is a highly orchestrated process involving multiple overlapping phases each with its own unique make-up of cells and cytokines.[77]

The next stage of wound healing is proliferation, or new tissue formation, which begins during the later inflammatory phase[4]. This phase is responsible for creating the granulation tissue that closes the wound. During the proliferative phase fibroblasts and keratinocytes migrate into the healing tissue and divide to create a highly cellularized and disorganized tissue, called granulation tissue. This new tissue provides the scaffold for reorganization and regeneration of normal dermis, while also being home to many of the key regulators of the progressing wound healing process, such as macrophages, lymphocytes, and myofibroblasts. These cells produce an wide array of regulatory cytokines as well as proteases and ECM proteins that determine the progression of healing. The final phase of wound healing is tissue remodeling, which can last in some instances for up to 18 months after the original injury. This process is a slow and methodical reorganization of ECM proteins, formation of new and remodeled vasculature, and the regeneration of normal tissue structures, such as hair follicles and sweat glands.

Dysregulation in the highly orchestrated process of wound healing can lead to very significant complications for patients[10-12]. Disruption of the clotting cascade can lead to severe blood loss. Even when hemostasis is proceeding appropriately, large traumatic injuries often require interventional approaches to promote clotting to reduce blood loss. Chronic prolonged

inflammation within a wound often leads to fibrosis and scar tissue formation. In diabetic patients chronic inflammation often contributes to delayed wound healing, making it a major driver of ulcer formation[13,14]. Dysregulation in ECM deposition, low growth factor production, or poor growth factor signaling can slow angiogenesis, retard re-epithelialization, and impair subsequent wound healing[15-18]. Many of these processes are inter-connected and complications of wound healing often involve a number of them, making it difficult to determine potentially causative pathologic dysregulation. Developing tools and methods to better understand expression within poor healing wounds is a key area where research should focus to improve the treatment of these disorders.

To date little research has been done to investigate direct local intervention to address known dysregulated expression within wounds. This is due to a number of complicating factors, one of the most crucial of which is the lack of drug delivery systems that can effectively deliver targeted therapies into the wound environment. Developing new technologies to deliver therapeutics to wounds that can address known pathologic dysregulated expression, such as siRNAs, provides a necessary new approach to better understanding the pathology of wounds to create new treatments.

1.2 Prevalence of Soft Tissue Wounds

Soft tissue wounds are a broad and heterogeneous category of injuries varying in severity and prevalence[3-5]. They include things as seemingly simple as small cuts and bruises[19] to more major injuries such as chronic ulcers, major traumatic injuries, and burn wounds. Understanding that each of these pathologies affects soft tissues differently creates a major driving force to develop a versatile approach to their treatment. Treatment options for critical injuries vary based on the nature of the injury and the anticipated results of natural healing. In cases of delayed healing recombinant growth factors may be used or in some cases artificial tissue simulants or skin grafts may also be considered. These therapies require dramatically different approaches and are greatly limited in their flexibility as

Chronic ulcerative wounds are a major concern in many diseases, one of the most prominent of which is type two diabetes mellitus (T2DM). Patients with T2DM often have a complex pathology that creates a poorly vascularized and neuropathic environment in their

extremities. These conditions contribute significantly to the delay in wound healing. These patients often have significant lower extremity edema which along with nerve loss increases the likelihood of injury in that area. Chronic inflammation is also key in the pathology of these wounds once they are created, leading to increased inflammatory cytokine expression, increased proteolytic expression and activity, as well as decreased growth factor signaling. Diabetic foot ulcer (DFU) is one of the most serious complications of diabetes and it directly affects the quality of life for patients, with more than 750,000 DFUs and 70,000 lower extremity amputations annually in the USA. DFU contributes significantly to the morbidity and the financial burden of diabetes both for the patient and for healthcare providers[20,21].

Even when normal wound healing is allowed to progress and is not impeded by overlying chronic conditions it can become complicated due to the severity of the damage. Large soft tissue wounds can require significant medical intervention to heal completely and very often lead to scar tissue formation, which can be both disfiguring and debilitating[22, 23]. These injuries however are difficult to quantify due to the multitude of causes. Even in a seemingly controlled wound creating environment such as surgical operations, the risk of creating scars is nearly as prevalent[24,25]. It is estimated that over 60% of patients who undergo abdominal or pelvic surgery develop peritoneal adhesions as a result of complications during wound healing[25]. These adhesions are the result of inflammation and the natural healing response within the abdomen and contribute significantly to morbidity in these patients. Specifically abdominal adhesions are known to cause infertility in women, bowel obstructions, and chronic pain.

One class of difficult large traumatic injuries is burn wounds. Burns are graded based on the level of damage to the tissue affected from an approximation of the depth of tissue involved. These wounds are notorious for poor healing outcomes and contractile scarring. There are more that 6.6 million reported cases of burns in the United States each year[26]. The options for patients with burn wounds are often just simple hydration dressings and creams, which have been demonstrated to reduce contractions to a small degree, but no approach in clinic currently is able to address the pathology of scarring and gain meaningful changes in outcomes for these patients.

1.3 Inflammation during Wound Healing

Immediately following injury the physiological response of wound healing is well under way. The inflammatory response begins only a few hours after wounding, with the infiltration of neutrophils into the wound bed to phagocytize debris and bacteria[3,4]. Leukocyte infiltration and chemotaxis is mediated through a complex milieu of chemo-attractants and cytokines, a number of which are key targets of current therapeutics (e.g. TGFβ, TNFα, IL-1β). Within 24 to 48 hours, monocytes begin to move into the wound tissue, and differentiate into macrophages: together with other cells within the wound, they release many signaling molecules, including growth factors important for fibroblast proliferation and for re-epithelialization of the wound (e.g. FGF, VEGF, PDGF)[27-29]. Many of these same signaling molecules play key roles in the inflammatory response[30].

The hypoxic wound stimulates production of angiogenic growth factors that promote fibroblast and epithelial cell proliferation by inducing new capillary growth, while matrix metalloproteinases break down the extracellular matrix[4,17,31]. This process is controlled through a complex balance of growth factors and signaling molecules, where small imbalances can lead to improper or dysfunctional wound healing (e.g. diabetic ulcers, venous ulcers, etc). Myofibroblasts within the wound begin to contract this newly formed extracellular matrix, which can lead to scar tissue formation. Remodeling of the wound takes place over weeks and months. From initial wounding to the end of wound remodeling the healing process can take up to a year or more depending on complications[4,5].

1.4 Controlled Localized Drug Delivery

Controlled localized drug delivery refers to the concept of focusing therapeutic treatment to a discrete target site while being able to control the temporal distribution of the drug delivered[31, 32]. Controlled drug release systems have been used clinically for more than 35 years, and their sales now comprise a multi-billion dollar annual market[34]. By focusing delivery to a specific target area these systems provide increased control over the distribution of drug released and improved bioavailability of the drug where it is required[35]. For drugs that are delivered orally or intravenously the impact on the body is systemic and often inconsistent due to small variations in the patient's state of hydration or diet[33, 34]. This poses a significant difficulty for drug therapies; since the initial delivery of a therapeutic can often create a risk for toxicity and

re-administration the drug can be inefficient and dangerous as drug regimens are often hard to follow[33].

Controlling the release of a therapeutic in a target tissue can often be very difficult due to the complicating physiology of the target site. Often it is seen in tissues with medical implants that the body reacts to the foreign material by producing a fibrotic capsule to isolate the structure. This capsule presents a number of difficulties for drug delivery as diffusion through the fibrotic tissue is often greatly hampered compared to the normal behavior in that tissue. In the case of wound healing this behavior is less of an issue as the tissue is already trying to create tissue within the defect site. Redirecting this behavior through drug delivery presents a fascinating approach to modify the healing process while also extending the delivery capabilities of the device being used.

1.5 Benefits of Controlled Local Drug Delivery

There are many benefits to using controlled local drug delivery[34,35]. First, by focusing drug delivery only to the target tissues it reduces the amount of drug that is necessary to induce a therapeutic response[32-35]. Second, by delivering the therapeutic to the site where it is needed you can increase the bioavailability of the drug and subsequently increase its effectiveness[36,37]. One of the most promising benefits of controlled local drug delivery is the capability to deliver new therapeutics that cannot be safely or effectively administered systemically, such as recombinant growth factors[38], small interfering RNA[39], and many other powerful therapeutics that require targeted delivery to be safe and effective[40].

The effective release or delivery of a drug at a designed dose to a tissue is key in determining its effect on that tissue. Control over this characteristic is a primary target for pharmaceutical manufacturers and researchers. Achieving this control on a local level however is extremely difficult for technologies that rely on systemic delivery. By creating material that slowly elutes a compound or active complex locally one could imagine circumventing much of the constraints that currently complicate controlled delivery.

1.6 Existing Medical Devices

There are a number of existing medical therapies that take advantage of the concept of controlled local drug delivery[41,42]. One of the most common of these is localized drug delivery to augment the natural immune response to implanted devices. This can work both by reducing the likelihood of infections at the site of implantation, either by attenuating the local inflammatory response to decrease fibrosis or other negative tissue responses[24]. Examples of FDA approved medical devices that use local delivery of therapeutics include drug-eluting stents (e.g. TAXUS Express, Xience-V, Cypher), drug-impregnated central venous catheters (e.g. Cook Spectrum), as well as many other applications (e.g. Nuvaring, GLIADEL, etc.).

The success of drug-device combination products as described above demonstrates the potential of this approach and it highlights the promise that continued development of such technologies may hold for addressing complex conditions. These devices, though a step forward towards improving drug delivery technologies, rely on simple polymer-drug blends to incorporate sensitive drug materials making controlled release difficult and resulting in very low drug loading. Many of these formulations have as little as 0.5% of the drug within their coatings, with the majority of the volume being made of excipients, and often forming phase-exclusion structures supporting a burst-release profile of drug delivery that is often not desirable. This method of encapsulating drug product can also be quite harsh, resulting in significant inactivation of the drug product.

1.7 Layer-by-Layer (LbL) as a Platform for Controlled Localized Drug Delivery

The term "layer-by-layer" (LbL) is derived from the sequential "layering" of chemical species on an activated substrate. The process takes advantage of complementary features between different materials to bind them to a surface[43]. Electrostatic interactions, hydrogen bonding, and Van der Waals forces have all been demonstrated to create LbL films[43,44]. Each layer promotes the adsorption of the next, while layer saturation of one species repels excess aggregation. LbL assemblies can include many different types of materials from proteins[45], polymers[46], and small molecule drugs[47,48] to nanomaterials[49]. LbL films are an especially attractive technology for drug delivery as they can be coated onto very complex micro- or nano-scale features and do not require harsh handling techniques, making them well suited for delicate therapeutics[45].

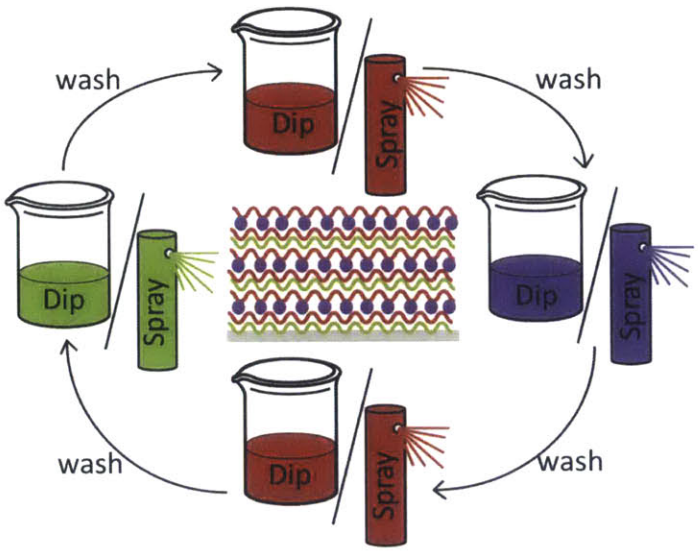

Figure 1-2 The process of Layer-by-Layer assembly

Materials are adsorbed to a surface sequentially either by dipping the substrate in a bath containing a high concentration of the material to be adsorbed or spraying that material solution over the surface. Materials are adsorbed through complementary interactions with the substrate surface and then washed thoroughly to remove non-specifically adsorbed materials. This process is repeated a pre-determined number of times to create robust ultrathin coatings.

1.8 Existing Layer-by-Layer Drug Delivery Assemblies

LbL assemblies have been used for the delivery of antibiotics[50-53], anti-inflammatory drugs[47], growth factors[48], and DNA[53-61]. Drug delivery from LbL films is dictated by two major factors: i) the rate of film erosion, and ii) the inter-layer diffusion of the therapeutic[51,52,62]. The inclusion of biodegradable synthetic polymers to regulate erosion within a film assembly is an especially promising concept, as it allows these film structures to be tailored to degrade at designed rates[53,62], thus permitting controlled drug release for therapeutics with limited inter-diffusion. However, many therapeutics that would benefit from localized delivery are small molecule drugs that readily diffuse within films[47,48]. This inter-diffusion results in a bulk release that can be useful, as in the case of antibiotics where a higher initial dose can help with immediate eradication of bacteria[51,52]. In many other cases, however, inter-diffusion is a significant drawback, as the body quickly clears the excess therapeutic without any realized

benefit. The use of barrier layers, macromolecule carriers, and covalent modifications have all been employed to address this issue to promising results[63].

Previous attempts to use LbL to create assemblies that could effectively load and deliver siRNA were seen to be poorly controlled and unable to achieve *in vitro* success[64]. These approaches viewed siRNA as behaving similarly to DNA. In some ways this is an obvious comparison, importantly both materials are made of nucleotide bases and the resulting biopolymer is densely negatively charged. These species however are incredibly different in their capability to interact with complexing materials based on the flexibility or lack of flexibility of siRNA. This rigidity of siRNA makes complex formation with a polycation species difficult, requiring both longer exposure to reach equilibrium on a surface and different materials for complex formation.

1.9 Localized Delivery of Nucleic Acids

Delivery of nucleic acids has been an active area of research for decades[65]. From this research a great deal of knowledge has been gained, especially in understanding the potential complications of systemic delivery of nucleic acids as it relates to clearance mechanisms and immunologic stimulation[66]. Recently, a great deal of focus has been on the development of nanomaterial platforms for the targeted systemic delivery of RNA[67-69]. RNA is far more easily degraded than DNA in body fluids, and elicits strong immunogenic activity if presented uncomplexed to cells through toll-like receptor binding[70]. Delivery of short interfering RNAs (siRNAs) has been an especially active area of research, as these short synthetically produced RNAs can potentially be used to target any gene expressed in the body for knockdown[71]. There have been significant difficulties in developing the technology to deliver siRNAs however, as we described earlier in this chapter.

Localized delivery of RNA provides a means to address one of the primary limiting factors for these approaches, creating the highest bioavailability of the delivery material directly at the sight of interest. Layer-by-layer has been used in this context for over a decade of research in the delivery of nucleic acids, primarily focused on the delivery of DNA[72,73]. The films that have been described for this purpose focus largely on pairing DNA with a poly(beta-aminoester) (PBAE). This same film architecture when tested with siRNA, however, demonstrated only limited efficacy in releasing siRNA and no ability to achieve siRNA-specific gene knockdown[64].

Other work in the field of localized delivery of siRNA has been focused on only a few different formulation strategies. In particular hydrogel and re-purposed nanoparticle systems have been two of the largest areas of focus[74-76]. There are however a number of substantial drawbacks to these types of approaches that are difficult to overcome. In the case of hydrogel-based formulations, they demand significant injection site volumes, where significant volume is occupied by either excipient material or water. Tuning delivery of siRNA from hydrogel formulations also presents a number of difficulties as it requires altering the injection volume significantly with dosing.

Nanoparticle formulations on the other hand are often quickly evacuated from the site of application through lymphatic drainage. These formulations become systemic and can contribute to many of the complications known from other systemic applications. Nanoparticle approaches also do not offer an obvious means for controlled delivery of siRNA, as the material that is taken up by cells is quickly active and that which is not goes systemic and often largely accumulates in the liver. Thus, chronic pathologies would require repeated dosing, which may be difficult for some application sites.

Here we describe the first successful application of LbL technology to incorporate and delivery siRNA in vitro and in vivo. We harnessed the films developed in this work to target a variety of disparate pathologies with great success in multiple animal models. The work described in this thesis is the first such demonstration of LbL for siRNA delivery *in vivo*.

1.10 Significance

Using LbL assemblies to locally deliver siRNA to soft tissue wounds is a novel approach to directly alter known pathologic dysregulation within wounds to improve wound healing outcomes. Layer-by-layer films are truly nano-scale, and as such are well suited for addition to existing structures without interfering with the beneficial physical properties of the coated device. As previously reported, LbL films have already been demonstrated to effectively functionalize orthopedic implants, catheters, and cardiovascular stents[51,52]. Applying this technology to one of the most commonly used medical devices, the bandage, is a new concept to incorporate drug delivery into existing technologies. This approach is especially promising for use in soft tissue wound healing, since delicate and powerful therapeutics can be incorporated

directly into wound dressings to treat the underlying causes of pathologies without requiring significant changes in wound care or additional medical devices to be used. This work has the potential to significantly advance the field of wound healing interventions as well as expanding opportunities in a myriad of other applications where control over local gene expression may be of interest.

Localized RNA interference has been previously described by a number of investigators. These approaches have taken a few different forms. Many of the published approaches to local RNA interference use nanoparticles either applied locally as a solution or entrapped within a larger material for application. These approaches have demonstrated limited success as the knockdown of a number of target genes has been achieved in vivo. These successes however have primarily focused on reported genes without limited pathology of the targeted tissues with minimal inflammation. Extrapolating these findings to suggest that they would perform similarly in treating pathologic disorders provides a great deal of motivation but this promise has yet to be realized.

1.11 Scope and Outline of Thesis

This thesis describes the development of layer-by-layer thin film coatings for the controlled local delivery of siRNA. The work presented here begins with early preliminary studies covering a multitude of LbL film architectures and potential material combinations. In the first chapter of this thesis we describe the background and rationale that drove the formation of the work presented here. Specifically, we focused on describing the current climate for localized delivery, current wound therapies, and the potential for RNA interference in medicine.

In Chapter 2 we detail our earliest preliminary results for the incorporation and delivery of siRNA from LbL films. This work covers material systems that incorporated nanoparticles as well as free siRNA into film assemblies. Within this chapter we also describe the potential for LbL assembly to achieve the controlled delivery of multiple siRNAs simultaneously as well as with temporal control. These findings suggest that LbL assembly could be a highly versatile tool in controlled siRNA delivery formulations in the future.

In Chapter 3 we described the first LbL film to successfully achieve significant siRNA-specific knockdown of a reporter gene *in vitro*. This film, $[PrS/CaP/PrS/Lap]_{25}$, was able to

sustain the delivery of siRNA out to ten days in vitro, while maintaining the bioactivity of the released siRNA. The film was demonstrated to uniformly coat a medically relevant substrate, a woven nylon bandage used in wound care. This film was demonstrated to sustain the knockdown of a reporter gene in multiple cell lines for out to one week in vitro without the need for external transfection agents and with minimal impact on cell viability.

In the fourth chapter of this thesis we describe the development of the capillary flow layer-by-layer (CF-LbL) system for the high-throughput assembly and screening of LbL films. The development of the device described within that chapter greatly accelerated our capability to investigate LbL films for the delivery of siRNA. The device as described is a modular microfluidic platform that allows for in situ testing of assembled LbL films for physic-chemical and biologic properties as well as in vitro assays. Additionally, the device can be operated as a stand-alone bench top tool or combined with liquid handling robotics for high-throughput screening, requiring less than 0.1% of material solutions per film constructed compared to traditional LbL methods.

In Chapter 5 we describe the first application of an LbL coated substrate *in vivo* for the targeted knockdown of a pathologically upregulated proteinase within a mouse model of chronic diabetic wound healing. Within this chapter we describe the extensive in vitro analysis of a tunable hierarchical LbL film structure. We demonstrated, similar to Chapter 3, that the film uniformly coated a nylon bandage substrate and could effectively knockdown a reported gene in vitro for up to one week with minimal impact on cell viability. Building beyond our previous investigations we applied these film coated bandages in vivo in a genetically diabetic mouse model of impaired wound healing, targeting a known upregulated protease that had been implicated in the pathology of diabetic ulcers, MMP-9. In vivo we observed a significant siRNA-specific reduction in MMMP-9 expression and activity. This knockdown correlated positively with increased granulation tissue formation within the healing wounds as well as accelerated wound closure. This work was the first such demonstration of effective siRNA delivery into a diabetic ulcer for the knockdown of MMP-9.

In Chapter 6 we turned our focus from Chapter 5 to another potential target within impaired diabetic wound healing, the pro-inflammatory cytokine TNFα. TNFα overexpression has also been well-reported as a potential cause for impaired wound healing in diabetic chronic

ulcers due to its pro-inflammatory nature within the healing wound. We applied the film first described within Chapter 3 *in vivo* within this chapter and demonstrated the effective sustained knockdown of TNFα in an siRNA-specific manner. The work presented in this chapter detailed the effect of TNFα knockdown on the expression of TNFα stimulated genes within the tissue, as well as its effect on wound healing. It was observe that the knockdown of TNFα within the wound significantly accelerated wound healing and improved granulation tissue formation within the wound bed. The work presented in this chapter reinforced our findings from the previous chapter that siRNA therapy within impaired wound healing may offer a powerful new approach to correct pathologic dysregulation within the healing tissue.

In Chapter 7 we decided to apply the same LbL film from Chapter 5 in a different animal model, a rat burn model, and on a new delivery substrate, a silk suture. In this chapter we targeted the well-reported connective tissue growth factor, an important mediator of TGFβ pro-fibrotic response in cutaneous wound healing. Previous research has demonstrated the efficacy of CTGF knockdown in vivo in reducing scar formation; however, we were interested in how our platform could improve on these studies by offering a means for controlled delivery within the healing tissue. Within this work we described thorough *in vitro* analysis of the LbL coated suture and its application in a third-degree burn model in rats. The knockdown of CTGF significantly altered the expression of related genes known to be upregulated by CTGF expression, and resulted in significantly reduced scar contraction out to one month in vivo. Histological analysis of the healing wound supported these gross findings, and suggested increased wound remodeling with reduced contraction.

In Chapter 8 we explored the delivery of siRNA from LbL coatings applied to a rapid release microneedle array for transdermal delivery of siRNA. This work was largely a proof-of-concept approach, where we aimed to demonstrate the flexibility of the LbL film on a new platform. We describe the in vitro study of the LbL film along with in vivo knockdown of a reporter gene in mice.

In Chapter 9 we cover a new area of work focused on the formulation of all-trans retinoic acid for sustained delivery. This work was built in a collaborative effort with Dr. Mohiuddin Quadir, a post-doctoral researcher in the Hammond lab. The concept we pursued in this work was the covalent conjugation of ATRA with an FDA approved excipient known to increase

residence within mucosa for dermal retention through an ester bond linkage. The work looked to establish the methods of producing an amphiphillic polymer-drug conjugate that could sustain the release of active ATRA out to 10 days. This conjugate, PATRA, was demonstrated to have improved in vivo tolerability along with substantial dermal residence, staying present within the skin of mice for up to six days.

The final chapter of this thesis covers an overview of each chapter, with the main findings and conclusions explained as well as a presentation of envisioned future work.

1.12 References

1. Kondo, T.; Ishida, Y. (2010), Molecular pathology of wound healing. Forensic Science International 203 (1-3), 93-98.
2. Rolfe, K. J (2010).; Grobbelaar, A. O., The growth receptors and their role in wound healing. Current Opinion in Investigational Drugs 11 (11), 1221-1228.
3. Dryden, M. S. (2010). "Complicated skin and soft tissue infection." J Antimicrob Chemother 65 Suppl 3: iii35-44.
4. Gurtner, G. C., S. Werner, et al. (2008). "Wound repair and regeneration." Nature 453(7193): 314-321.
5. Janis, J. E., R. K. Kwon, et al. (2010). "A practical guide to wound healing." Plast Reconstr Surg 125(6): 230e-244e.
6. Sen, C. K., G. M. Gordillo, et al. (2009). "Human skin wounds: a major and snowballing threat to public health and the economy." Wound Repair Regen 17(6): 763-771.
7. Abe, R., S. C. Donnelly, et al. (2001). "Peripheral blood fibrocytes: differentiation pathway and migration to wound sites." J Immunol 166(12): 7556-7562.
8. Pober, J. S. and W. C. Sessa (2007). "Evolving functions of endothelial cells in inflammation." Nat Rev Immunol 7(10): 803-815.
9. Wong, V. W., M. Sorkin, et al. (2011). "Surgical approaches to create murine models of human wound healing." J Biomed Biotechnol 2011: 969618.
10. Finnerty, C. C., M. G. Jeschke, et al. (2008). "Temporal cytokine profiles in severely burned patients: a comparison of adults and children." Mol Med 14(9-10): 553-560.
11. Mace, K. A., T. E. Restivo, et al. (2009). "HOXA3 modulates injury-induced mobilization and recruitment of bone marrow-derived cells." Stem Cells 27(7): 1654-1665.
12. Boucher, H., L. G. Miller, et al. (2010). "Serious infections caused by methicillin-resistant Staphylococcus aureus." Clin Infect Dis 51 Suppl 2: S183-197.
13. Ashcroft, G. S., X. Yang, et al. (1999). "Mice lacking Smad3 show accelerated wound healing and an impaired local inflammatory response." Nat Cell Biol 1(5): 260-266.
14. Massague, J. (1999). "Wounding Smad." Nat Cell Biol 1(5): E117-119.
15. Pastar, I., O. Stojadinovic, et al. (2010). "Attenuation of the transforming growth factor beta-signaling pathway in chronic venous ulcers." Mol Med 16(3-4): 92-101.
16. Jeffcoate, W. J. and K. G. Harding (2003). "Diabetic foot ulcers." Lancet 361(9368): 1545-1551.
17. Falanga, V. (2005). "Wound healing and its impairment in the diabetic foot." Lancet 366(9498): 1736-1743.

18. Thangarajah, H., D. Yao, et al. (2009). "The molecular basis for impaired hypoxia-induced VEGF expression in diabetic tissues." Proc Natl Acad Sci U S A 106(32): 13505-13510.

19. "A WHO Plan for Burn Prevention and Care." Geneva, Switzerland: World Health Organization, (2008).

20. Vital statistics. American Diabetes Association. (1996):31

21. Ramsey SD, Newton K, et al (1999). Incidence, outcomes, and cost of foot ulcers in patients with diabetes. Diabetes Care;22:382-387

22. Herzog, E. L. and R. Bucala (2010). "Fibrocytes in health and disease." Exp Hematol 38(7): 548-556.

23. Rahmani-Neishaboor, E., F. M. Yau, et al. (2010). "Improvement of hypertrophic scarring by using topical anti-fibrogenic/anti-inflammatory factors in a rabbit ear model." Wound Repair Regen 18(4): 401-408.

24. Bernard, L.; Hoffmeyer, P.; Assal, M.; Vaudaux, P.; Schrenzel, J.; Lew, D., (2004) "Trends in the Treatment of Orthopaedic Prosthetic Infections." Journal of Antimicrobial Chemotherapy, 53 (2): 127-129.

25. Chegini, N. (2008). "TGF-beta system: the principal profibrotic mediator of peritoneal adhesion formation." Semin Reprod Med 26(4): 298-312.

26. American Burn Association Fact Sheet. 2013. Available at: http://www.ameriburn.org/resources_factsheet.php. Accesses March 2015.

27. Mann, A., K. Breuhahn, et al. (2001). "Keratinocyte-derived granulocyte-macrophage colony stimulating factor accelerates wound healing: Stimulation of keratinocyte proliferation, granulation tissue formation, and vascularization." J Invest Dermatol 117(6): 1382-1390.

28. Flanders, K. C., C. D. Major, et al. (2003). "Interference with transforming growth factor-beta/ Smad3 signaling results in accelerated healing of wounds in previously irradiated skin." Am J Pathol 163(6): 2247-2257.

29. Fang, Y., J. Shen, et al. (2010). "Granulocyte-macrophage colony-stimulating factor enhances wound healing in diabetes via upregulation of proinflammatory cytokines." Br J Dermatol 162(3): 478-486.

30. Tan, S. L. et al. (2009). "Combined Use of Acid Fibroblast Growth Factor, Granulocyte Colony-stimulating Factor and Zinc Sulphate Accelerates Diabetic Ulcer Healing." Journal of Health Science 55(6): 910-922.

31. Bhatt, L. K. and V. Addepalli (2010). "Attenuation of diabetic retinopathy by enhanced inhibition of MMP-2 and MMP-9 using aspirin and minocycline in streptozotocin-diabetic rats." Am J Transl Res 2(2): 181-189.

32. Langer, R., (1998) "Drug delivery and targeting." Nature, 392 (6679): 5-10.

33. Uhrich, K. E.; Cannizzaro, S. M.; Langer, R.S.; Shakesheff, K.M., (1999) "Polymeric systems for controlled drug release." Chem. Rev., 99 (11): 3181-3198.

34. Wu, P.; Grainger, D. W., (2006) "Drug/device combinations for local drug therapies and infection prophylaxis." Biomaterials, 27 (11): 2450-2467.

35. Zilberman, M., A. Kraitzer, et al. (2010). "Drug-eluting medical implants." Handb Exp Pharmacol(197): 299-341.

36. Ndesendo, V. M., V. Pillay, et al. (2010). "In vivo evaluation of the release of zidovudine and polystyrene sulfonate from a dual intravaginal bioadhesive polymeric device in the pig model." J Pharm Sci.

37. Wong, S. Y., J. S. Moskowitz, et al. (2010). "Dual functional polyelectrolyte multilayer coatings for implants: permanent microbicidal base with controlled release of therapeutic agents." J Am Chem Soc 132(50): 17840-17848.

38. Macdonald, M. L., R. E. Samuel, et al. (2011). "Tissue integration of growth factor-eluting layer-by-layer polyelectrolyte multilayer coated implants." Biomaterials 32(5): 1446-1453.

39. Zhang, X. (2010). "SiRNA-loaded multi-shell nanoparticles incorporated into a multilayered film as a reservoir for gene silencing." Biomaterials 31: 6013 - 6018.

40. LaVan, D. A.; McGuire, T.; Langer, R., (2003) "Small-scale systems for in vivo drug delivery." Nature biotechnology, 21 (10): 1184-1191.

41. Pai, M. P.; Pendland, S. L.; Danziger, L. H., (2001) "Antimicrobial-coated/bonded and -impregnated intravascular catheters." Annals of Pharmacotherapy, 35 (10): 1255-1263.

42. Veenstra, D.L.; Saint, S.; Sullivan, S.D., (1999) "Cost-Effectiveness of Antiseptic-Impregnated Central Venous Catheters for the Prevention of Catheter-Related Bloodstream Infection." Jama-Journal of the American Medical Association, 282 (6): 554-560.

43. Decher, G.; Hong, J.D.; Schmitt, J., (1992) "Buildup of Ultrathin Multilayer Films by a Self-Assembly Process: III. Consecutively Alternating Adsorption of Anionic and Cationic Polyelectrolytes on Charged Surfaces." Thin Solid Films, 210(1-2): 831-835.

44. Kotov, N. A., (1999) "Layer-by-layer self-assembly: The contribution of hydrophobic interactions." Nanostructured Materials, 12 (5-8): 789-796.

45. Saurer, E. M., R. M. Flessner, et al. (2010). "Layer-by-Layer Assembly of DNA- and Protein-Containing Films on Microneedles for Drug Delivery to the Skin." Biomacromolecules.

46. Krogman, K. C., J. L. Lowery, et al. (2009). "Spraying asymmetry into functional membranes layer-by-layer." Nat Mater 8(6): 512-518.

47. Smith, R. C.; Riollano, M.; Leung, A.; Hammond, P. T., (2009) "Layer-by-Layer Platform Technology for Small-Molecule Delivery." Angewandte Chemie-International Edition, 48 (47): 8974-8977.

48. Schmidt, D. J., J. S. Moskowitz, et al. (2010). "Electrically Triggered Release of a Small Molecule Drug from a Polyelectrolyte Multilayer Coating." Chem Mater 22(23): 6416-6425.

49. Lee, S. W.; Kim, B. S.; Chen, S, et al (2009) "Layer-by-Layer Assembly of All Carbon Nanotube Ultrathin Films for Electrochemical Applications." Journal of the American Chemical Society, 131 (2): 671-679.

50. Chuang, H. F.; Smith, R. C.; Hammond, P.T., (2008) "Polyelectrolyte multilayers for tunable release of antibiotics." Biomacromolecules, 9 (6): 1660-1668.

51. Moskowitz, J. S., M. R. Blaisse, et al. (2010). "The effectiveness of the controlled release of gentamicin from polyelectrolyte multilayers in the treatment of Staphylococcus aureus infection in a rabbit bone model." Biomaterials 31(23): 6019-6030.

52. Shukla, A., S. N. Avadhany, et al. (2010). "Tunable vancomycin releasing surfaces for biomedical applications." Small 6(21): 2392-2404.

53. Lynn, D. M., Langer, R., (2000) "Degradable poly(beta-amino esters): synthesis, characterization, and self-assembly with plasmid DNA." Journal of the American Chemical Society, 122: 10761- 10768.

54. Jewell, C. M. and D. M. Lynn (2008). "Surface-Mediated Delivery of DNA: Cationic Polymers Take Charge." Curr Opin Colloid Interface Sci 13(6): 395-402.

55. Liu, X., J. Zhang, et al. (2008). "Ultrathin Multilayered Films that Promote the Release of Two DNA Constructs with Separate and Distinct Release Profiles." Adv Mater 20(21): 4148-4153.

56. Mehrotra, S., I. Lee, et al. (2009). "Multilayer mediated forward and patterned siRNA transfection using linear-PEI at extended N/P ratios." Acta Biomater 5(5): 1474-1488.

57. Flessner, R. M., Y. Yu, et al. (2011). "Rapid release of plasmid DNA from polyelectrolyte multilayers: a weak poly(acid) approach." Chem Commun (Camb) 47(1): 550-552.

58. Saurer, E. M., C. M. Jewell, et al. (2009). "Assembly of erodible, DNA-containing thin films on the surfaces of polymer microparticles: toward a layer-by-layer approach to the delivery of DNA to antigen-presenting cells." Acta Biomater 5(3): 913-924.

59. Sun, B. and D. M. Lynn (2010). "Release of DNA from polyelectrolyte multilayers fabricated using 'charge-shifting' cationic polymers: Tunable temporal control and sequential, multi-agent release." J Control Release.

60. Fredin, N. J., R. M. Flessner, et al. (2010). "Characterization of nanoscale transformations in polyelectrolyte multilayers fabricated from plasmid DNA using laser scanning confocal

microscopy in combination with atomic force microscopy." Microsc Res Tech 73(9): 834-844.

61. Saurer, E. M., D. Yamanouchi, et al. (2011). "Delivery of plasmid DNA to vascular tissue in vivo using catheter balloons coated with polyelectrolyte multilayers." Biomaterials 32(2): 610-618.

62. Wood, K.C.; Boedicker, J.Q.; Lynn, D.M.; Hammond, P.T., (2005). "Tunable drug release from hydrolytically degradable layer-by-layer thin films." Langmuir, 21 (4): 1603-1609.

63. Wood, K.C., Chuang, Helen F., et al. (2006). "Controlling interlayer diffusion to achieve sustained, multiagent delivery from layer-by-layer thin films." PNAS, 103 (27): 10207-10212.

64. Flessner RM, Jewell CM, Anderson DG, Lynn DM. Degradable polyelectrolyte multilayers that promote the release of sirna. *Langmuir*. 2011;27:7868-7876

65. Yin, H.; Kanasty, R. L.; Eltoukhy, A. A.; Vegas, A. J.; Dorkin, J. R.; Anderson, D. G., Non-viral vectors for gene-based therapy. Nat Rev Genet 2014, 15, 541-55.

66. Whitehead, K.A., Dahlman, J.E., Langer, R.S. & Anderson, D.G. Silencing or stimulation? siRNA delivery and the immune system. Annu Rev Chem Biomol Eng 2, 77-96 (2011).

67. Yin, H. et al. Non-viral vectors for gene-based therapy. Nat Rev Genet 15, 541-555 (2014).

68. Whitehead, K.A., Langer, R. & Anderson, D.G. Knocking down barriers: advances in siRNA delivery. Nature Reviews Drug Discovery 8, 129-138 (2009).

69. Love, K.T. et al. Lipid-like materials for low-dose, in vivo gene silencing. Proc Natl Acad Sci U S A 107, 1864-1869 (2010).

70. Gilmore, I.R., Fox, S.P., Hollins, A.J. & Akhtar, S. Delivery strategies for siRNA-mediated gene silencing. Curr Drug Deliv 3, 147-145 (2006).

71. Soutschek, J. et al. Therapeutic silencing of an endogenous gene by systemic administration of modified siRNAs. Nature 432, 173-178 (2004).

72. Jewell, C.M., Zhang, L.T., Fredin, N.J. & Lynn, D.M. Localized delivery of DNA from surfaces coated with multilayered polyelectrolyte films. Abstr Pap Am Chem S 230, U4167-U4167 (2005).

73. Jewell, C.M., Zhang, J.T., Fredin, N.J. & Lynn, D.M. Multilayered polyelectrolyte films promote the direct and localized delivery of DNA to cells. Journal of Controlled Release 106, 214-223 (2005).

74. Zheng, D. et al. Topical delivery of siRNA-based spherical nucleic acid nanoparticle conjugates for gene regulation. Proc Natl Acad Sci U S A 109, 11975-11980 (2012).

75. Nelson, C.E. et al. Tunable delivery of siRNA from a biodegradable scaffold to promote angiogenesis in vivo. Advanced Materials 26, 607-614, 506 (2014).

76. Nelson, C.E. et al. Sustained local delivery of siRNA from an injectable scaffold. Biomaterials 33, 1154-1161 (2012).

77. Park, J.E. & Barbul, A. Understanding the role of immune regulation in wound healing. *Am J Surg* **187**, 11S-16S (2004).

Chapter 2
Preliminary Studies of LbL for the Controlled Delivery of siRNA

2.1 Introduction

In Chapter 1 we described the complex process of wound healing, described two major pathologies related to complications in wound healing, and gave a brief overview of layer-by-layer technology in the arena of controlled delivery. In this chapter we introduce our earliest work in developing LbL films for incorporating and delivering siRNA. This work helped form the basis of our broadening investigations and gave us great insights into the capabilities of LbL technology for siRNA delivery.

Layer-by-layer (LbL) assembly of polyelectrolyte thin films has been used for a wide range of applications due to its simplicity and robustness[1-4]. These films have found a particularly interesting use in drug delivery as they have the capability to load significant quantities of a desired drug component with tunable release characteristics[2, 5]. This approach has demonstrated great success for the delivery of small molecule drugs[6-8], biologics[9-11], and DNA[12-14]. The use of LbL to incorporate and release siRNA however had not shown much promise[15]. A few reports have suggested that incorporation of into LbL films is possible, but releasing siRNA in a form that would transfect cells presents many more difficulties that must be addressed.

This difficulty can be understood by considering how siRNA is released from a complexed state on a surface. One common approach to achieve release of a material from LbL films includes the incorporation of a degradable polymer[9, 16, 17]. This polymer would either directly interact with the released component or make up some part of the film architecture so as to create controlled increasing instability within the film during degradation[18, 19]. Often the degradable polymer is hydrolytically degradable, which is a very suitable approach for drug delivery as all biological fluids are water-based. Other forms of degradable materials can also be

incorporated, such as enzymatically degradable[20, 21] or photo-cleavable polymers[18]. These approaches, either independently or in combination, can be used to develop ultra-thin films with controlled release properties that can be tuned by media conditions or external activation. The way in which a film degrades will influence how the incorporated material will be released, affecting both the rate of release as well as the form of the released material.

Short interfering RNAs have a high density of negative charge, allowing for effective complexation with positively charged polymers, called polycations[22, 23]. Numerous reports have demonstrated how the appropriate design and structure of the complex formed between polycations and siRNA influences important delivery properties such as biodistribution, cell uptake, and endosomal escape[24-26]. Similarly one would expect that the materials used to drive complex formation with the siRNA onto a surface, once released, would affect how the released material behaved. To begin to investigate this hypothesized role of the complexing polycation, we started by screening a number of commercially available polycations that had been reported in literature for their capability to complex with nucleic acids for *in vitro* delivery, in particular we focused on polymers reported for use in siRNA delivery **(Figure 2-1)**[27].

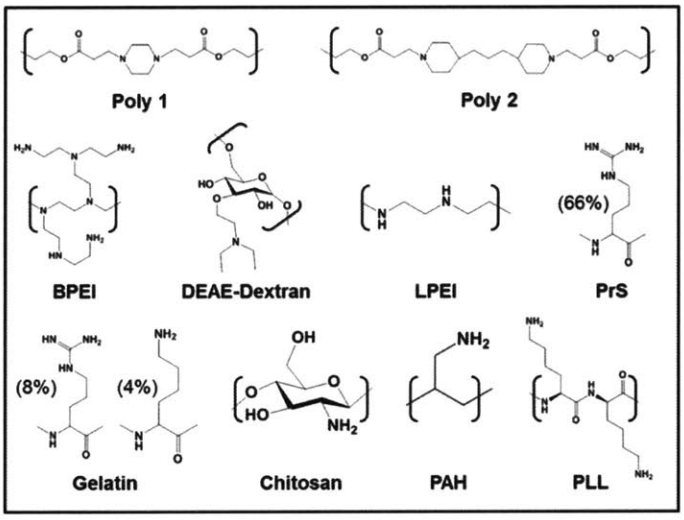

Figure 2-1 Chemical structures of polycation repeat units

Polycations commonly reported in the delivery of nucleic acids were investigated. Polymers ranged from synthetic to biologically derived and commercially available to in house produced.

These investigations were initially limited to the simple evaluation of siRNA incorporation and release in combination with analysis of film growth properties. The film architectures that were seen to effectively load siRNA and release that siRNA in a sustained fashion were evaluated in vitro for the knockdown of the reported gene green fluorescent protein (GFP) in NIH-3T3 cells. Cell cultures exposed to film coated substrates and were analyzed for film-specific and siRNA-specific changes in cell viability. The best performing architectures were identified and evaluated further *in vitro* to follow cell uptake and to assess the coating of meaningful medical devices such as bandages and medical staples.

2.2 Methods and Materials

2.2.1 Materials

SiRNA for GFP and siControl were received as a gift from Sanofi-Aventis. Alexafluor 488-labeled and Alexafluor 546-labeled siRNA were purchased from Qiagen (Valencia, CA). Linear poly(ethyleneimine) (LPEI, MW = 2.5 kDa, 25 kDa, and 250 kDa), Branched poly(ethyleneimine) (BPEI, MW = 5 kDa, 50-70 kDa, and 100 kDa) low molecular weight chitosan (LMW Chitosan, M_w of 15-30k), high molecular chitosan (HMW Chitosan, M_w of 300k), gelatin (pH=2.5), diethylaminoethyl-dextran (DEAE-Dextran), protamine sulfate (PrS), poly-L-lysine (PLL, M_w of 15-30k and 30-70k) and poly(allylamine hydrochloride) (PAH, M_w of 60k) were purchased from (St. Louis, MO); and the degradable poly(beta-aminoesters) (designated Poly 1, and Poly 2) were synthesized using the method that was previously published[16]. Dextran sulfate (DS, MW = 500 kDa), Alginate (ALG), and chondroitin sulfate (ChS) were purchased from Sigma Aldrich (St. Louis, MO). Phosphate buffered saline solution (PBS, 10x), Advanced-MEM, fetal bovine serum, antibiotic-antimycotic solution and 200mM L-glutamine solution were purchased from Invitrogen (Carlsbad, CA). NIH-3T3, MDA-MB-235, and M4A4 cells were purchased from ATCC (Manassas VA). Tegaderm® was purchased from Cardinal Health (Newark, NJ).

2.2.2 The Formation of siRNA Polyplexes

Polyplex nanoparticles containing siRNA were synthesized by rapid mixing of polycation and siRNA. N:P ratios were calculated based on monomer structure for each polymer and siRNA used. All complexes were tested at 100mM sodium acetate buffer at pH 5.0 unless

otherwise noted. All solutions prepared were nuclease free and sterile filtered prior to use with a 0.2μm syringe filter. The diameter and zeta potential of the formed nanoparticles were measured both prior to and after film assembly using a ZetaPALS dynamic light scattering and zeta potential analyzer. The siRNA nanoparticles were always prepared just prior to LbL film construction.

2.2.3 Fabrication of LbL Films

Film assembly was performed using an HMS series Carl-Zeiss programmable slide stainer. Substrates to be coated were first cleaned sequentially with methanol, ethanol, isopropanol and water and then dried under filtered nitrogen. These substrates were plasma cleaned for 5 minutes on the high RF setting and then immediately placed in a 2 mg/mL solution of LPEI and allowed to adsorb the material for at least 30 minutes prior to use. After this initial coating, substrates were then placed into specially designed holders for the programmable slide stainer to move between dipping baths. A generic bilayer LbL assembly protocol consists of first dipping the substrate into a polycation solution for some specified time, then moving that substrate through two wash steps where excess polymer is allowed to desorb from the surface. The washed substrate is then placed in a polyanion solution and allowed to adsorb polymer. After adsorption of the polyanion the substrate is then washed two more times to remove any excess polymer. This process can then be repeated for multiple depositions of the bilayer architecture.

All films were assembled on top of 10 baselayers of (LPEI/DS) to ensure a conformal charged coating of the substrate for siRNA film deposition. Assembly of baselayers was carried out in 100 mM sodium acetate solution at pH 5.0. All solutions were filtered using a 0.2 μm membrane syringe filter prior to use. Polymer solutions used were prepared at a 2 mg/mL concentration and all siRNA solutions contained a 20 μg/mL concentration of siRNA. Polymer deposition steps were done for 10 minutes and polyplex nanoparticle or siRNA deposition steps were done for 30 minutes. All deposition steps were followed with two 1 minute washes in pH adjusted nuclease free water.

2.2.4 Film Thickness and Surface Characterization

The thickness of the LbL films were assessed for films assembled on silicon and glass substrates using both spectroscopic ellipsometry (XLS-100 Spectroscopic Ellipsometer J.A. Woollam Co., Inc) and profilometry (Dektak 150 Profilometer). Ellipsometric measurements were performed on LbL films assembled on silicon substrates. Films were dried under filtered nitrogen prior to measurement. Measurements were performed at room temperature with a 70° incidence angle. The acquired spectra were then fit with a Cauchy dispersion model to obtain an estimated thickness for the film. For measurement of film thickness by profilometry, films were built on either silicon or glass and scored by a razor then tracked over. Step height from the untouched film to the bottom of the score was measured in six different locations on each sample to obtain an average thickness.

Atomic force microscopy (AFM) was performed using a Dimension 3100 AFM with Nanoscope 5 controller (Veeco Metrology) in tapping mode. Film areas of 25 μm by 25 μm were examined for each film after 5, 15 and 25 architecture depositions. Nanoscope analysis v1.10 software was used to calculate the root mean squared roughness for films.

2.2.5 Quantification of siRNA Loading into LbL Assembly

Incorporation of siRNA within the LbL film assemblies were quantified after 5, 10, 15 and 25 architecture repeats. To quantify the amount of siRNA within the film a one square centimeter sample of a film coated substrate was placed into 500μL of 1 M NaCl solution prepared from nuclease free water. The sample was then subjected to vigorous agitation for 30 minutes to completely remove the film from the surface. The substrate was then removed from the salt solution, washed with deionized water and dried under filtered nitrogen. These substrates were evaluated by SEM to check that the entire film had been removed from the surface. Quantification of siRNA was performed using Oligreen dsDNA reagent (Invitrogen) as per the manufacturer's instructions or by quantification of fluorescently labeled siRNA.

For quantification using Oligreen the degradation solution containing the released film was diluted 1:20 into nuclease free water to reduce salt concentration to within the tolerance range of the assay. 25 μL of degradation sample was then added to 100μL of prepared Oligreen reagent (diluted 1:200 in TE buffer of reagent in kit) in a fluoroblock (BD) 96-well plate. Samples were then read with a fluorescent plate reader with 490/520 Ex/Em wavelengths.

SiRNA standards were prepared using similar salt concentrations to that in the diluted degradation samples.

2.2.6 Degradation Studies and Release Characterization

Experiments for the quantification of film degradation were carried out in either PBS or cell conditioned media at 37°C. To assist in the visualization of the degradation of the film, AlexaFluor 488-labeled siRNA was used. Cell conditioned media was prepared from NIH-3T3 cells grown to confluence. NIH-3T3s were seeded into a 24-well plates (50,000 cells/well) and cultured in Advanced-MEM (Invitrogen) media containing 5% FBS, 1% antibiotic-antimycotic solution, and 2mM L-glutamine. Cells grew to confluence within approximately 1 day after seeding. Media was removed from wells after 72 hours in contact with the cells. This media was filtered using a 0.2 μm syringe filter to remove cellular debris. This filtered media was then placed directly onto of the films to be degraded. Degradations were carried out at 37°C with the entire degradation media exchanged daily. Unlabeled siRNA served as a blank non-fluorescent control. A standard curve of the fluorescently labeled siRNA was used to interpret the concentration of siRNA within the release media. SEM analysis of all samples was done in JEOL 6700F scanning electron microscope. Confocal imaging of degrading samples was performed on a Zeiss LSM 510 Confocal Laser Scanning Microscope.

2.2.7 Characterization of in Vitro Knockdown

GFP knockdown was characterized by flow cytometry measurements of mean cell fluorescence in NIH-3T3, MDA-MB-435, and M4A4 cells that constitutively expressed GFP. 5,000 cells per well were seeded in a 48 well plate in 600μL of cell growth media and allowed to incubate for 24 hours. Films coated substrates were cut into 0.5x0.5 cm (0.25cm^2 total area) squares and placed into the wells with the cells. After 3, 5, or 7 days of exposure to the film coated substrates cells were trypsinized and mean cell fluorescence was determined by flow cytometry, using a BD FACSCalibur flow cytometer.

2.2.8 In vitro Transfection with Fluorescently Labeled siRNA

Transfection of NIH-3T3s was monitored using fluorescently labeled siRNA. Similar to knockdown experiments films containing the labeled siRNA were built on Tegaderm samples and placed in culture with NIH-3T3 cells grown on coverslips in cell growth media. Cells were exposed to films for up to 1 week in vitro with media being changed every two days. At day 3,

5, and 7 samples were taken for microscope analysis of transfection. Cells were fixed in formalin diluted in PBS and counterstained with DAPI nuclear stain.

2.3 Results

Initial testing was conducted to determine if any single or combination of film architectures could effectively incorporate and release siRNA. These films were then evaluated *in vitro* for their efficacy in knocking down a reporter gene green fluorescent protein (GFP). Incorporation and release of siRNA was quantified by a number of approaches. Early trials were evaluated using Picogreen or Oligreen assays for nucleic acid quantification. These dyes are highly sensitive to nucleic acids, Oligreen assay is especially well suited for quantifying dsRNA, however they rely on direct interaction with the RNA which may be difficult in a complexed state. One way to prove such a behavior is to force complex dissolution by the addition of heparin to solutions containing complexed siRNA. Heparin is a highly negatively charged natural polymer that can out-compete siRNA for interactions with complexing polycations[28]. In this process the heparin makes siRNA available for binding to the dyes used, theoretically allowing for the differential quantification of loose siRNA and complexed siRNA. This approach however is difficult to reproduce and results in wide variability between samples. A more straightforward approach is to use fluorescently labeled siRNAs. This process is somewhat more expensive than the previous approach but the results were found to be more consistent for our purposes. In this work the labeled siRNA can be used as all of the siRNA incorporated or as a fraction of the siRNA, so as to dope the film with the labeled siRNA.

2.3.1 Polyplex Nanoparticles for the Incorporation of siRNA into LbL Films

The first films investigated in this work focused on the incorporation of nanoparticles containing siRNA and a complexing polycation. This structure, regardless of the siRNA complexing polymer, will be referred to as a polyplex. The first such film that was evaluated was a polyplex of linear polyethylene amine (LPEI). The formation of these polyplexes is known to be determined by the ratio of charge species in the polycation to charge species in the RNA[29-31]. This ratio is referred to as the N:P ratio[32]. Investigating the role that the N:P ratio played in the size and stability of the complexed siRNA was performed for up to 24 hours at room temperature. Size of particles was determined by dynamic light scattering (DLS). All

polyplex particles were seen to increase in size during the study period. Particles at lower N:P ratios were significantly larger than those at high N:P ratios and were seen to aggregate up to multiple microns in size.

To incorporate these polyplexes into the LbL film architecture, they were assembled with material that could form stable complementary interactions with them. The polyplexes being made at an N:P ratio greater than one were on average strongly positively charged providing a means to incorporate them into the film structure with negatively charged polymers, called polyanions. Films were built and evaluated for growth rate and siRNA release in PBS at each N:P ratio shown in **Figure 2-2**. Growth rate was seen to vary significantly between the films. Increased film thickness was observed to correlate with increased siRNA incorporation in all films tested.

The first approach tested was a simple bilayer structure using three different polyanions: (1) dextran sulfate (DS), (2) hyaluronic acid (HA), and (3) alginate (AL), with a selection of different N:P ratio polyplexes. None of these films were observed to release any siRNA, though incorporation of siRNA was observed in all films assembled to varying degrees. The highest siRNA incorporating of these films was the 10 N:P ratio film with dextran sulfate which loaded approximately 5.8 ± 0.9 μg of siRNA per cm^2 of coated surface after 15 layers.

The issue of promoting the release of siRNA was apparent after these tests. One possible cause for this issue was identified shortly after reconsidering our approach, as none of the material used in the film assemblies significantly changed during the attempted release, there was little driving force to facilitate the desired release. To improve the release of siRNA from the films we decided to incorporate a hydrolytically degradable polymer commonly used in LbL delivery assemblies called a poly(beta-aminoester) (PBAE)[16]. Specifically we turned to two such PBAEs called Poly 1 and Poly 2 in this work **(Figure 2-1)**. This was done by including the PBAE as part of a tetralayer architecture. An example of one such architecture is $[PBAE/DS/NP/DS]_n$ where n is the number of architecture repeats.

Total siRNA incorporation into the tetralayer polyplex nanoparticle films was relatively low, with the highest incorporation being seen in the 10 N:P film of [Poly2/DS/NP/DS], which

achieved approximately 7.2 ± 0.6 μg of siRNA per cm^2 of coated surface after 15 layers. Release of siRNA from all tetralayer films was near completion after six days in PBS at 37°C.

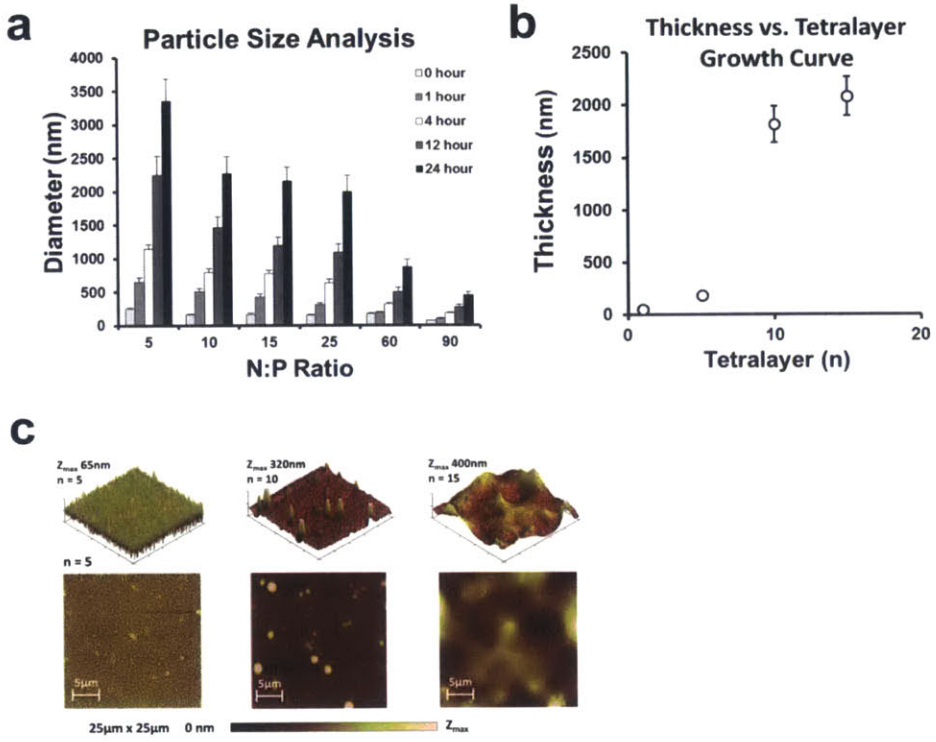

Figure 2-2 Early investigations into LPEI polyplex LbL film assemblies

(a) Time-study comparison of hydrodynamic diameter for different N:P ratio LPEI/siRNA polyplexes at room temperature. (b) Growth curve for [Poly 2/DS/NP/DS] where N:P = 10. (c) AFM of assembled films after 5, 10, and 15 layers assembled on silicon substrate.

Film growth for the 10 N:P LPEI polyplex containing tetralayer film was observed to not follow a linear growth pattern. Instead the film was observed to grow slowly at first and then rapidly increase in size followed by a slower period of film deposition. These findings may be indicative of the increasing particle diameter during the dipping process, expedited by the removal of loose LPEI from the solution. We investigated the dipping baths during this process and found that the particle diameter was on average increased after dipping compared to those left alone in solution. Assessment of the growing surfaces by AFM shows a fascinating change from relatively small sub-micron particulate to larger multiple micron size materials

incorporating on the surface. After 15 tetralayers these features however are largely ablated and a more flat surface with fine peaks is observable.

Both 10 N:P and 90 N:P films were applied to cells to observe their impact on cell viability over a five day period. These films were observed to significantly reduce cell viability compared to uncoated control. The 10 N:P film had a significantly more negative impact on cell viability, this was believed to be due to the increased amount of film material released from the surface compared to the 90 N:P film. Neither film was observed to successfully knockdown the reporter gene GFP *in vitro*. Together these results suggested that the material was released, however the contained siRNA was unable to effectively transfect cells. Combining this material with Lipofectamine 2000, as per the manufacturer's protocol, did achieve significant reduction in GFP expression in NIH-3T3 cells. This reduction was greatest in cells treated with the pooled release material from the 10 N:P ratio film, achieving an approximate 37% reduction in mean cell fluorescence.

Table 2-1 Summary of polyplex containing LbL film architectures

Architecture	Degradable Polycation	siRNA Loaded (μg/cm²)	siRNA Released (μg/cm²)	Film Thickness (μm)	GFP Knockdown	Described Release Profile
LPEI Tetralayer $(N:P\ 10)_{15}$	Yes	7.2 ± 0.6	6.2 ± 1.0	2.3 ± 0.7	0.99 ± 0.03	Small bolus release initially with large destabilization at around 1 day.
LPEI Tetralayer $(N:P\ 15)_{15}$	Yes	4.3 ± 1.1	4.1 ± 0.3	2.5 ± 0.8	1.01 ± 0.02	Small bolus release, with film destabilization around 1 day. siRNA in complex with LPEI.
LPEI Tetralayer $(N:P\ 25)_{15}$	Yes	2.0 ± 0.3	1.9 ± 0.5	2.4 ± 0.7	1.00 ± 0.04	Similar to N:P 15 film with less siRNA release, and not able to visualize siRNA complex with LPEI.
LPEI Tetralayer $(N:P\ 60)_{15}$	Yes	1.2 ± 0.2	0.8 ± 0.1	1.8 ± 0.9	1.02 ± 0.04	Full release in 3 days, no bolus.
LPEI Tetralayer $(N:P\ 90)_{15}$	Yes	1.1 ± 0.2	0.6 ± 0.1	1.9 ± 0.5	0.96 ± 0.07	Sustained release over first three days of degradation.
BPEI Tetralayer $(N:P\ 5)_{15}$	Yes	9.4 ± 1.2	0.6 ± 0.3	1.1 ± 0.3	0.98 ± 0.08	Small bolus release within first 6 hours.
BPEI Tetralayer $(N:P\ 90)_{15}$	Yes	0.6 ± 0.4	0.1 ± 0.04	0.6 ± 0.1	1.01 ± 0.10	Small bolus release within first 12 hours.
PrS Tetralayer $(N:P\ 90)_{25}$	Yes	1.6 ± 0.8	1.5 ± 0.5	0.9 ± 0.2	0.99 ± 0.07	Near complete release seen after 24 hours.
Multi-Bilayer LPEI (N:P 10) $[(Poly2/DS)_3(NP/DS)_5]_3$	Yes	3.8 ± 0.9	0.9 ± 0.2	1.6 ± 0.6	1.02 ± 0.06	80% bolus siRNA release in first 30min, full degradation in 3 days.
Multi-Bilayer LPEI (N:P 10) $[(Poly2/DS)_5(NP/DS)_3]_3$	Yes	4.6 ± 1.1	0.4 ± 0.2	1.4 ± 0.6	0.96 ± 0.09	Low sustained release over first two days, no release beyond that.

Polyplex containing LbL films were attempted using Poly-l-lysine at two different molecular weights. At N:P ratios from 5 to 90 no polyplexes were observed by DLS at any condition evaluated. Similarly, no nanoparticles were seen for mixtures of chitosan, at two different molecular weights, with siRNA. In contrast, 10 kDa BPEI was seen to form very stable complexes with the siRNA at N:P ratios of 5 and above. These nanoparticles were built into tetralayer films. The highest siRNA incorporating film of BPEI polyplex tetralayer architecture was reached for the 5 N:P particles, with a total loading a total of 9.4 ± 1.2 μg of siRNA per cm^2 after 15 layers. These films were observed to release only 0.6 ± 1.2 μg of siRNA over a 14 day release period in PBS at 37°C. It has been shown by numerous previous investigations that LbL films undergo inter-penetrating processes during construction. We believe that the lack of release in these BPEI containing films compared to the LPEI films was due to the increased inter-layer diffusion and subsequently increased film stabilization.

No polyplexes were observed for mixtures of Poly 1 or Poly 2 and siRNA at any N:P ratio tested, ranging from 5 to 90. We also investigated a number of commercially available polycations including protamine sulfate (PrS) and poly(allylamine) hydrochloride (PAH). PrS did form nanoparticles with the siRNA at N:P ratios about 10 but loading of complexed siRNA into LbL films was very low, approximately only 1.6 ± 0.8 μg of siRNA per cm^2 after 25 layers. Nearly all of this siRNA was observed to be released from the film after 1 day of degradation in PBS at 37°C. This material was unable to achieve significant reduction in GFP expression *in vitro*, but when combined with lipofectamine 2000, as per the manufacturer's protocol, was able to reduce mean cell fluorescence significantly. These data and more investigations are summarized in **Table 2-1**.

Beyond only using tetralayer architectures to incorporate polyplex nanoparticle we also investigated the use of hierarchical film architectures. We termed this approach multi-bilayer films as they aimed to separate the two roles that the LbL film was attempting to simultaneously play: (1) incorporate siRNA and (2) release siRNA in a controlled fashion. By separating these roles in the nanoparticle film we hoped to reduce the interaction between the siRNA incorporating materials and the other film components. This approach however was not observed to appreciably increase siRNA incorporation or improve controlled release of the siRNA. In fact, what was seen was a significant increase in film thickness and a reduction in

both the amount of siRNA incorporated and the fraction of siRNA released. These findings pushed us away from this approach for polyplex film architectures; however, later in our further investigations into other film architectures we revisited this concept.

2.3.2 Direct Incorporation of siRNA into LbL Films

Incorporating siRNA first into nanoparticles and then into LbL assemblies was a largely unsuccessful endeavor, with no polyplex nanoparticle containing films capable of effectively delivering siRNA *in vitro*. This failure to achieve gene knockdown pushed us to investigate other formulations. One such approach, which has been investigated for the delivery of DNA, was to directly incorporate the material as a polyanion species into the LbL assemblies. This route, which we will term direct incorporation, was used to investigate a number film architectures comprised of a myriad of polycation species.

Table 2-2 Summary of siRNA bilayer LbL film architectures

Architecture	Degradable Polycation	siRNA Loaded (μg/cm²)	siRNA Released (μg/cm²)	Film Thickness (nm)	GFP Knockdown	Described Release Profile
$(LPEI_{2.5K}/siRNA)_{25}$	No	4.9 ± 1.1	2.1 ± 0.4	52 ± 8	1.02 ± 0.08	All siRNA release occurs within first 12 hours
$(LPEI_{25K}/siRNA)_{25}$	No	6.1 ± 0.9	2.8 ±0.8	48 ± 6	0.99 ± 0.07	Large burst release of over 80% total release in first 30 minutes.
$(LPEI_{250K}/siRNA)_{25}$	No	6.4 ±0.6	2.2 ± 0.7	46 ± 9	0.97 ± 0.10	Nearly 50% of siRNA release occurs in first 30 minutes.
$(DEAE\text{-}Dextran/siRNA)_{25}$	No	7.1 ± 1.7	1.3 ± 0.4	87 ± 11	1.04 ± 0.08	No burst release observed, sustained release for three days.
$(PLL_{15K}/siRNA)_{25}$	Yes	3.6 ± 0.8	1.8 ± 0.6	63 ± 8	0.92 ± 0.05	Sustained siRNA release for five days with no further observed.
$(PLL_{50K}/siRNA)_{25}$	Yes	4.1 ± 1.2	1.2 ± 0.5	59 ± 12	0.99 ± 0.09	Sustained siRNA release for two days with no further observed.
$(BPEI_{1.2K}/siRNA)_{25}$	No	3.3 ± 0.9	0.4 ± 0.3	55 ± 11	1.06 ± 0.11	All observed siRNA release occurs in first 24 hours.
$(BPEI_{10K}/siRNA)_{25}$	No	6.9 ± 1.2	0.4 ± 0.2	51 ± 9	1.01 ± 0.08	All observed siRNA release occurs in first 12 hours.
$(BPEI_{50K}/siRNA)_{25}$	No	3.9 ± 0.5	0.6 ± 0.1	33 ± 4	0.98 ± 0.06	All observed siRNA release occurs in first 30 minutes.
$(Poly\ 2/siRNA)_{25}$	Yes	3.9 ± 0.5	0.6 ± 0.1	33 ± 4	0.98 ± 0.06	All observed siRNA release occurs in first 30 minutes.
$(Poly\ 1/siRNA)_{25}$	Yes	3.9 ± 0.5	0.6 ± 0.1	33 ± 4	0.98 ± 0.06	All observed siRNA release occurs in first 30 minutes.

Our first attempts at direct incorporation of siRNA into LbL assemblies looked at relatively simple bilayer structures of siRNA with a complexing polycation **(Table 2-2)**. The first architecture investigated was the bilayer [Poly2/siRNA]. This film was able to load fairly

high amounts of siRNA per area, reaching 11.6 ± 2.1 μg of siRNA per cm^2 after 25 layers. It was noted for this film that significantly more siRNA was incorporated when a lower concentration buffer solution was used, from 100mM to 10mM. This film demonstrated sustained release of siRNA for up to eight days in PBS at 37oC. This released material was pooled and then dosed onto GFP expressing NIH-3T3 cells. At no tested concentration was any significant siRNA-specific gene knockdown observed. Films containing Poly 1 behaved similarly *in vitro*, though loading significantly less siRNA (3.2 ± 1.1 μg) per cm^2 after 25 layers, and releasing siRNA for only approximately five days.

Films comprised of LPEI were built using three different molecular weights ranging from 2.5 kDa to 250 kDa. These films loaded relatively high amounts of siRNA, reaching approximately 6.4 ± 0.6 μg of siRNA per cm^2 of coated surface after 25 layers. Release of siRNA from these films however was observed to only occur within the first hour to six hours of release. Approximately 30-40% of the loaded siRNA in each of these formulations was observed to be released in this time period. This released siRNA was unable to effect siRNA-specific knockdown when dosed onto GFP expressing NIH-3T3 cells. This style of release, which is common in many drug formulations, is referred to as a burst release. It is often due to a rapid change in the media surrounding a drug releasing device, which alters the interactions that facilitate the inclusion of the drug to be delivered. This burst profile of release is not desirable in controlled delivery formulations as it takes away the designed ability to slowly deliver a drug and maintain a therapeutic level. In this specific formulation the destabilization of the siRNA complexed within the film not only takes away control of release but also changes the form of the released material. The siRNA released in this burst profile is uncomplexed, demonstrated both by DLS measurement and gel electrophoresis of the released material, and thus open for rapid degradation and unable to effectively transfect cells.

Burst release of material from the coatings was a common issue observed in nearly all direct incorporation formulations tested. A number of approaches were investigated to minimize this effect. One such approach we looked into was to incorporate materials that would not go under changes in charge density between assembly and release or biological conditions. Particularly we looked to include PrS, poly-l-arginine (PLA), and poly-l-lysine (PLL) as these are biologically degradable polycations that have been reported in literature for use in siRNA

delivery formulations. Of these PrS reduced siRNA burst release the most while maintaining the highest loading of siRNA (5.6 ± 0.8 μg/cm^2 after 25 layers) when incorporated in a tetralayer structure with Poly 2. PLA and PLL were observed to load far less siRNA than PrS (1.6 ± 0.6 and 0.9 ± 0.4 μg/cm^2 respectively after 25 layers), and have only minimal effects on the burst release of siRNA from the films. Release of siRNA from the PrS tetralayer film was sustained for nearly 10 days in vitro in PBS at 37oC. When applied to cells in culture none of these films were observed to significantly impact cell viability after 72 hours, however none were also observed to effectively reduce GFP expression in an siRNA-specific manner. These *in vitro* studies were followed out to one week with no positive results observed **(Table 2-3)**.

Interpreting these results we considered the impact that the positively charged polymer might have on endosomal escape. One mechanism by which materials have been hypothesized to escape the endosomal compartment is by the proton sponge effect[33], wherein the some component of the material taken up by a cell buffers the endosome during its maturation[34-36]. This buffering effectively forces the cell to increase the amount of counter ions introduced into the endosome subsequently increasing osmotic pressure and creating instability in the compartments structure. By using polycations that do not buffer in this physiological range we hampered this capacity of our films released material. This consideration inspired a change in focus to use a strongly negatively charged material that could also create a physical barrier to inter-layer diffusion. To do this we looked at nanomaterials used in other reported drug delivery formulations and decided upon using laponite clay (Lap), a silicate clay platelet that is strongly negatively charged and which has been reported in the creation of LbL films[37-39].

Table 2-3 Summary of more complex siRNA LbL film architectures

Architecture	Degradable Polycation	siRNA Loaded (μg/cm²)	siRNA Released (μg/cm²)	Film Thickness (nm)	GFP Knockdown	Described Release Profile
$(LPEI_{25K}/siRNA/DS)_{25}$	No	10.6 ± 1.8	4.7 ± 1.2	526 ± 72	0.91 ± 0.05	35% of siRNA release in first 30 minutes with sustained release over one week.
$(LPEI_{25K}/siRNA/ALG)_{25}$	No	2.2 ± 0.4	0.9 ± 0.5	691 ± 110	1.06 ± 0.11	Over 90% of siRNA release occurs within first day.
$(DEAE\text{-}Dextran/siRNA/DS)_{25}$	No	5.1 ± 1.2	1.6 ± 0.6	741 ± 86	0.94 ± 0.08	Over 30% of siRNA released in first 30 minutes with sustained release out to four days.
$(Poly2/siRNA/DS)_{25}$	Yes	4.6 ± 1.2	3.9 ± 0.8	620 ± 80	0.90 ± 0.05	40% initial bolus in first 30 minutes, sustained release out to five days.
$(LPEI_{25K}/siRNA/LPEI_{25K}/DS)_{25}$	No	6.3 ± 2.2	0.6 ± 0.3	905 ± 68	0.98 ± 0.10	Over 85% of release within first day.
$(LPEI_{25K}/siRNA/LPEI_{25K}/ALG)_{25}$	No	5.5 ± 1.9	1.0 ±0.4	1608 ± 197	1.02 ± 0.06	Over 90% of siRNA release observed in first 12 hours.
$(LPEI_{25K}/siRNA/Poly2/DS)_{25}$	Yes	9.7 ± 2.4	1.9 ± 0.7	1210 ± 131	0.96 ± 0.09	Nearly 70% of siRNA release occurs in the first day followed by sustained release for five days.
$(LPEI_{25K}/siRNA/Poly2/ALG)_{25}$	Yes	7.1 ± 2.6	2.3 ± 0.9	2211 ± 315	0.89 ± 0.08	Over 50% of siRNA release observed in first day with sustained release out to three days.
$(LPEI_{25K}/siRNA/LPEI_{25K}/DS/Poly2/DS)_{25}$	Yes	11.1 ± 2.1	9.6 ± 1.8	5240 ± 406	1.02 ± 0.04	All siRNA release observed in first hour.

As laponite clay is a negatively charged species its incorporation into LbL assemblies with siRNA required the use of tetralayer and more complicated film architectures. Our first attempt to use Lap focused on the film architecture of [Poly 2/siRNA/LPEI/Lap]. This film loaded approximately 9.8 ± 1.2 μg/cm^2 after 25 layers and released this siRNA with only approximately 10% burst release and sustained release out to seven days. When placed in culture however this film did not significantly reduce gene expression in a siRNA-specific manner. When the released material was pooled and mixed with lipofectamine 2000 however the siRNA was able to achieve significant knockdown of nearly 40% at 100nM concentrations. This observation demonstrated that the siRNA was still intact and capable of knocking down a targeted gene, but the released material was unable to effectively gain access to the cytoplasm of the cells. We then began to screen other material combinations using Lap in tetralayer architectures.

Of these films one demonstrated early *in vitro* success, [Chi/siRNA/Poly 2/Lap], where low molecular weight chitosan (Chi) was used as the polycation for incorporating siRNA into the film **(Figure 2-3)**. Chitosan has been well reported in literature for use in a number of siRNA delivery formulations[40-43]. To this point the use of chitosan in bilayer and tetralayer structures

with Poly 2 had not demonstrated any efficacy in releasing significant quantities of siRNA. Particularly the simple bilayer structure of [Chi/siRNA] did load nearly 14 $\mu g/cm^2$ siRNA after 25 layers, but nearly 80% of the release of the siRNA occurred in the first few hours with no observable in vitro efficacy. Combining this bilayer structure into a tetralayer architecture containing Poly 2 and Lap however resulted in a significant improvement in the *in vitro* delivery of siRNA.

The [Chi/siRNA/Poly 2/Lap] tetralayer film was observed to grow in a near-linear fashion on flat silicon substrates over the range investigated. SiRNA loading was observed to increase per tetralayer similarly, achieving nearly 12.3 ± 1.9 $\mu g/cm^2$ after 25 layers. It took approximately 15 hours to fully assemble the 25 tetralayer film for testing. This film when placed in culture with NIH-3T3 cells constitutively expressing GFP was able to achieve significant and sustained knockdown in an siRNA-specific manner of up to 45% for five days with no significant loss in cell viability.

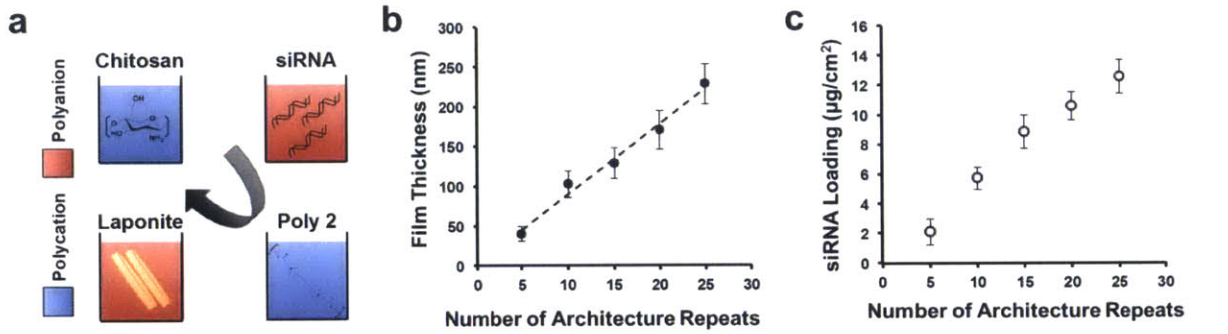

Figure 2-3 Assembly of Tetralayer Lap Containing LbL Film Architecture
(a) Schematic representation of assembly process for tetralayer structure. (b) Growth curve for [Poly 2/Lap/Chi/siRNA]. (c) Quantification siRNA incorporation during film assembly.

This finding was a very interesting observation as the introduction of the Lap and Poly 2 material into the film architecture facilitated the sustained release of siRNA in a form that could effectively transfect cells. When this structure was combined with the previously tested $[LPEI/siRNA]_{25}$ film we also saw a positive *in vitro* response, resulting in an approximate 22% reduction in mean cell fluorescence after three days in an siRNA-specific manner. It was noted

however that this film also negatively impacted cell viability, reducing it by approximately 30% compared to uncoated controls.

After a number of attempts to combine the previously investigated bilayer films with [Lap/Poly 2] we determined that the [Chi/siRNA/Poly 2/Lap] film architecture was the best performing one. This film both sustained delivery of siRNA over a physiologically relevant timescale and that the siRNA that was released after five days was still able to transfect cells to achieve significant siRNA-specific gene knockdown. In evaluating this system we were also very interested to see if siRNA sequence would make any significant difference in the loading or release of siRNA. To do this we used two different siRNA sequences, one for GFP targeting and one for GADPH which do to their different sequences had different molecular weights. In both cases we saw statistically similar incorporation and no significant changes in release profiles.

2.3.3 Tuning siRNA Incorporation

It has been widely reported that siRNA incorporation in most formulations does not significantly change based on the siRNA used[44, 45]. This is understandable considering the physic-chemical similarities that all siRNA share that are used for assembly of these formulations. We were then interested to see if we could tune the loading of one siRNA in respect to another within this film structure. This was visualized by using two different labeled siRNA, one labeled with an alexafluor-488 (AF-488) label and one with an alexafluor-546 label (AF-546). We found that indeed we could design the differential loading of one siRNA over another by controlling their relative concentrations in the assembly material **(Figure 2-4)**. These films were followed *in vitro* and demonstrated no preference for uptake of one siRNA over another, suggesting that we could theoretically target multiple genes using this approach in a very specifically controlled fashion.

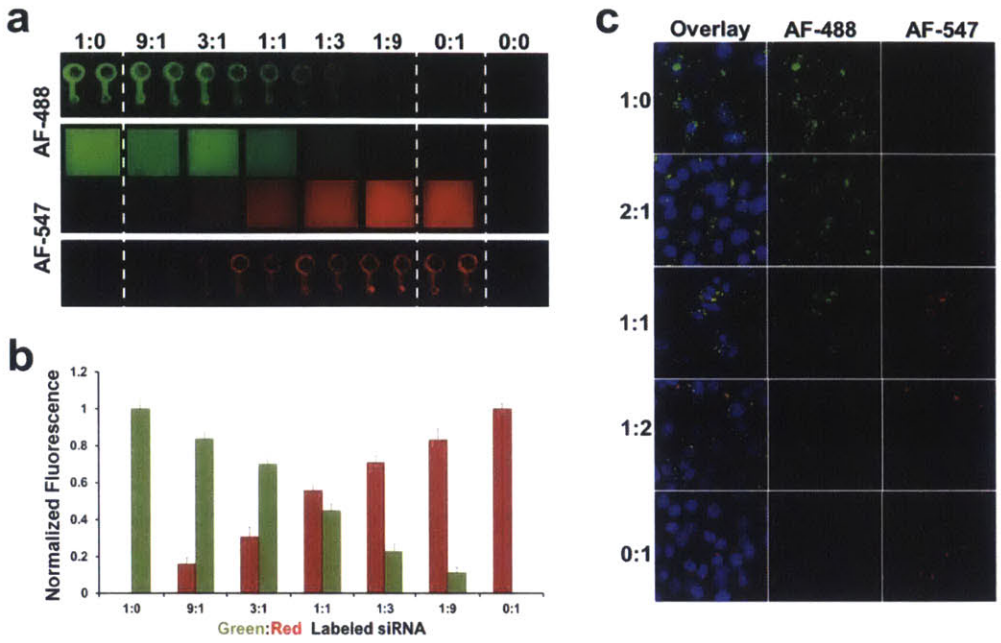

Figure 2-4 Controlled Incorporation and Delivery of Multiple siRNAs within a Tetralayer LbL Film Architecture

(a) Fluorescent imaging of LbL assemblies constructed within a microchannel device demonstrating the controlled tunable incorporation of one siRNA relative to another. (b) Quantification of relative channel fluorescence normalized to films only containing one labeled siRNA. (c) Fluorescent imaging of HeLa cells treated with film coated substrates constructed of different ratios of labeled siRNA, demonstrating no preferential uptake of one siRNA over the other.

Attempts to target multiple reporter genes *in vitro* however were significantly complicated by a number of issues including contamination and poor cell viability. Preliminary results seemed to indicate that we were able to effectively achieve siRNA-specific reductions in both reporter genes targeted, but reproducing these results was made difficult by lost timepoints and the eventual loss of the dual reporter expressing cell within our lab. Following the controlled delivery of multiple differentially labeled siRNAs *in vitro* support the assertion that we should be able to knockdown multiple genes however.

We were also interested in targeting multiple genes simultaneously with control over the sequential delivery of siRNA. This sort of temporal control over release would be important in the effort to create coatings that could address the evolving nature of a wound environment[46, 47]. Timing knockdown of individual factors so as to better control biological processes and from this develop better outcomes. The ability to sequentially deliver factors from LbL films has been described by a number of previous researchers for other drug delivery formulations[48-51]. Here we took a similar approach, but were able to leverage the benefits of already including a high-aspect ratio nanomaterial as a means to reduce layer interdiffusion and thus improve control. Our approach is detailed in **Figure 2-5a**.

Loading of siRNA was seen to behave similarly to what we had found in our precious study of this films architecture. Unlike our previous investigations however we assembled up to 50 total layers of film onto the surface. The incorporation of the two differently labeled siRNAs is shown in **Figure 2-5b**. It was observed that there was some level of replacement during the film construction as the total amount of siRNA labeled with AF488 reduced slightly from the increasing layers of AF546 labeled siRNA. To evaluate the release of the labeled siRNAs from the film we coated samples of Tegaderm® and degraded the film in PBS at 37°C for up to 14 days. At predetermined time points we drew samples from the degradation media and imaged the degrading samples. Release of the top most layer of siRNA containing LbL film was seen to start in these films immediately after being placed in the PBS for degradation. It was noted that release of the lower LbL film began similarly to the upper most layer, with a more delayed and sustained profile. This style of release suggests that even though the top layer may physically block the lower layer that both may be releasing simultaneously from the coated surface.

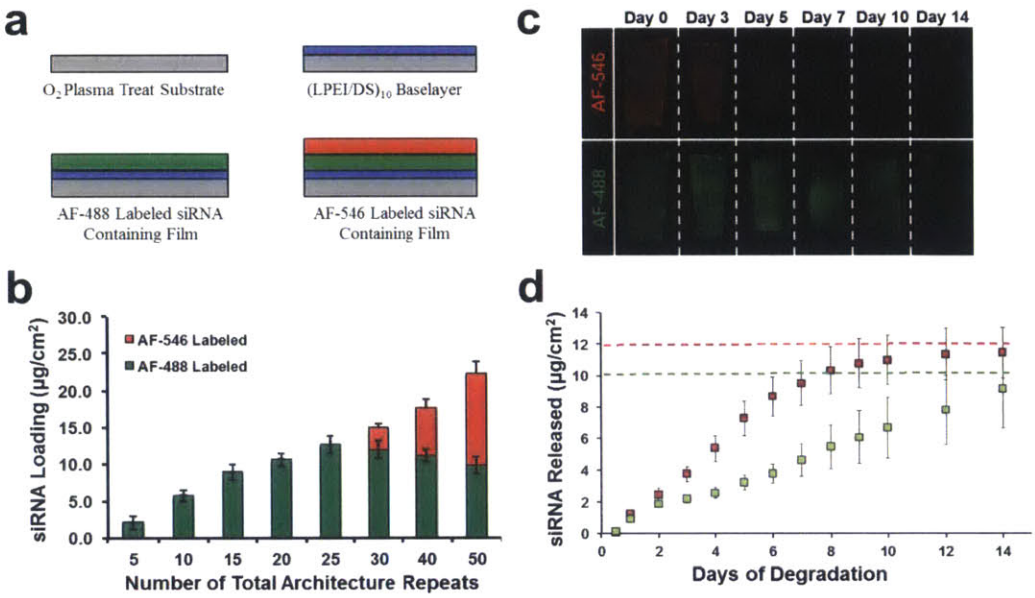

Figure 2-5 Control over Sequential Delivery of siRNA Based on Hierarchical LbL Film Architecture

(a) Schematic detailing the assembly of LbL film architecture. (b) Quantification of incorporated fluorescently labeled siRNA. (c) Fluorescent imaging of Tegaderm® coated with LbL film demonstrating sequential controlled release of siRNA. (d) Quantification of siRNA release from coated substrate in PBS at 37°C followed over a two week period.

After 14 days of degradation it was observed that the majority of the film had been released from the coated surface. The uppermost layer of the film had finished releasing after approximately 10 days while the lower film released out until the end of our study. These findings endorse two very important concepts, (1) that we should be able to control the release of a single siRNA based on total film constructed and (2) that the potential exists to design a tuned sequential delivery of siRNAs from a single LbL coating for more complex therapies.

2.4 Discussion

Within this chapter we have covered the early and very broad approaches that we took to investigate LbL films to incorporate and deliver siRNA. This work ranged from using polyplex nanoparticles encapsulating siRNA to directly incorporating siRNA as a film component as well as a multitude of variations in film architectures. A number of interesting phenomena were

described by their impact on film assembly. We believe most important of which were many of the negative results we observed, demonstrating the need for such a thorough screen of potential film combinations. From this early screen of film architectures we arrived at an LbL film which could incorporate and deliver siRNA *in vitro*.

As a proof of concept we demonstrated many of the interesting potential opportunities that LbL-based siRNA delivery could present with this selected film architecture. Using LbL assembly we were able to effectively coat surfaces with nanometer thin polymer coatings that could load micrograms of intact siRNA and active siRNA. This work was expanded to detail much of the potential that these films could have in the design of controlled release formulations of siRNA. We also demonstrate some early findings of how LbL assembly could be used to create hierarchical film structures for sequential release of siRNA.

While not easily described through text, numerous early stumbling blocks were discovered during this work, refining our conceptions and overall plan for the work. An example of such a shift in thought can be readily seen in our first attempts at building siRNA LbL films focusing on architectures used for the delivery of DNA. We thought that due to their similar composition, incorporating siRNA should be practically the same as DNA. However, this was not at all what we found. Many, if not most, reported LbL approaches for the delivery of DNA had focused on the use of a simple bilayer film architecture using Poly 2 as the complexing polycation. When we used this film for siRNA delivery we found that very little of it loaded into the film structure and that which we could release was unable to transfect cells effectively. This early work for us was essential to make apparent the important role that the released complex must play in that siRNA delivery.

2.5 References

1. Matsusaki, M., Ajiro, H., Kida, T., Serizawa, T. & Akashi, M. Layer-by-layer assembly through weak interactions and their biomedical applications. Advanced Materials 24, 454-474 (2012).

2. Hammond, P.T. Building biomedical materials layer-by-layer. Materials Today 15, 196-206 (2012).

3. Becker, A.L., Zelikin, A.N., Johnston, A.P.R. & Caruso, F. Tuning the Formation and Degradation of Layer-by-Layer Assembled Polymer Hydrogel Microcapsules. Langmuir 25, 14079-14085 (2009).

4. Becker, A.L., Johnston, A.P.R. & Caruso, F. Layer-By-Layer-Assembled Capsules and Films for Therapeutic Delivery. Small 6, 1836-1852 (2010).

5. Shukla, A., Avadhany, S.N., Fang, J.C. & Hammond, P.T. Tunable Vancomycin Releasing Surfaces for Biomedical Applications. Small 6, 2392-2404 (2010).

6. Shukla, A., Fang, J.C., Puranam, S. & Hammond, P.T. Release of vancomycin from multilayer coated absorbent gelatin sponges. J Control Release 157, 64-71 (2012).

7. Schmidt, D.J., Moskowitz, J.S. & Hammond, P.T. Electrically Triggered Release of a Small Molecule Drug from a Polyelectrolyte Multilayer Coating. Chemistry of materials : a publication of the American Chemical Society 22, 6416-6425 (2010).

8. Wong, S.Y. et al. Dual functional polyelectrolyte multilayer coatings for implants: permanent microbicidal base with controlled release of therapeutic agents. J Am Chem Soc 132, 17840-17848 (2010).

9. Shah, N.J., Hong, J., Hyder, M.N. & Hammond, P.T. Osteophilic Multilayer Coatings for Accelerated Bone Tissue Growth. Advanced Materials 24, 1445-1450 (2012).

10. Facca, S. et al. Active multilayered capsules for in vivo bone formation. Proc Natl Acad Sci U S A 107, 3406-3411 (2010).

11. Shukla, A., Fang, J.C., Puranam, S., Jensen, F.R. & Hammond, P.T. Hemostatic Multilayer Coatings. Advanced Materials 24, 492-+ (2012).

12. Jewell, C.M. et al. Release of plasmid DNA from intravascular stents coated with ultrathin multilayered polyelectrolyte films. BioMacromolecules 7, 2483-2491 (2006).

13. DeMuth, P.C., Su, X., Samuel, R.E., Hammond, P.T. & Irvine, D.J. Nano-layered microneedles for transcutaneous delivery of polymer nanoparticles and plasmid DNA. Advanced Materials 22, 4851-4856 (2010).

14. DeMuth, P.C. et al. Polymer multilayer tattooing for enhanced DNA vaccination. Nat Mater 12, 367-376 (2013).

15. Flessner, R.M., Jewell, C.M., Anderson, D.G. & Lynn, D.M. Degradable Polyelectrolyte Multilayers that Promote the Release of siRNA. Langmuir 27, 7868-7876 (2011).

16. Lynn, D.M. & Langer, R. Degradable poly(beta-amino esters): Synthesis, characterization, and self-assembly with plasmid DNA. J Am Chem Soc 122, 10761-10768 (2000).

17. Green, J.J., Langer, R. & Anderson, D.G. A combinatorial polymer library approach yields insight into nonviral gene delivery. Acc Chem Res 41, 749-759 (2008).

18. DeMuth, P.C. et al. Vaccine delivery with microneedle skin patches in nonhuman primates. Nat Biotechnol 31, 1082-1085 (2013).

19. Demuth, P.C., Min, Y., Irvine, D.J. & Hammond, P.T. Implantable Silk Composite Microneedles for Programmable Vaccine Release Kinetics and Enhanced Immunogenicity in Transcutaneous Immunization. Adv Healthc Mater (2013).

20. Craig, M., Holmberg, K., Le Ru, E. & Etchegoin, P. Polypeptide multilayer self-assembly studied by ellipsometry. J Drug Deliv 2014, 424697 (2014).

21. Vergaro, V. et al. TGF-Beta Inihibitor-loaded Polyelectrolyte Multilayers Capsules for Sustained Targeting of Hepatocarcinoma Cells. Curr Pharm Des 18, 4155-4164 (2012).

22. Sun, X. & Zhang, N. Cationic polymer optimization for efficient gene delivery. Mini Rev Med Chem 10, 108-125 (2010).

23. Yin, H. et al. Non-viral vectors for gene-based therapy. Nat Rev Genet 15, 541-555 (2014).

24. Tiera, M.J., Winnik, F.O. & Fernandes, J.C. Synthetic and natural polycations for gene therapy: state of the art and new perspectives. Curr Gene Ther 6, 59-71 (2006).

25. DeLong, R.K. et al. Characterization and performance of nucleic acid nanoparticles combined with protamine and gold. Biomaterials 30, 6451-6459 (2009).

26. Averick, S. Preparation of Cationic Nanogels for Nucleic Acid Delivery. BioMacromolecules (2012).

27. Eliyahu, H., Barenholz, Y. & Domb, A.J. Polymers for DNA delivery. Molecules 10, 34-64 (2005).

28. Danielsen, S., Strand, S., de Lange Davies, C. & Stokke, B.T. Glycosaminoglycan destabilization of DNA-chitosan polyplexes for gene delivery depends on chitosan chain length and GAG properties. Biochim Biophys Acta 1721, 44-54 (2005).

29. Shrestha, R., Elsabahy, M., Florez-Malaver, S., Samarajeewa, S. & Wooley, K.L. Endosomal escape and siRNA delivery with cationic shell crosslinked knedel-like nanoparticles with tunable buffering capacities. Biomaterials 33, 8557-8568 (2012).

30. Jere, D. et al. Bioreducible polymers for efficient gene and siRNA delivery. Biomed Mater 4, 025020 (2009).

31. Jere, D. et al. Degradable polyethylenimines as DNA and small interfering RNA carriers. Expert Opin Drug Deliv 6, 827-834 (2009).

32. Glebova, K.V., Marakhonov, A.V., Baranova, A.V. & Skoblov, M.Y. Therapeutic siRNAs and nonviral systems for their delivery. Molecular Biology 46, 335-348 (2012).

33. Behr, J.P. The proton sponge: A trick to enter cells the viruses did not exploit. Chimia 51, 34-36 (1997).

34. Sawant, R.R. et al. Polyethyleneimine-lipid conjugate-based pH-sensitive micellar carrier for gene delivery. Biomaterials 33, 3942-3951 (2012).

35. Forrest, M.L. & Pack, D.W. On the kinetics of polyplex endocytic trafficking: implications for gene delivery vector design. Mol Ther 6, 57-66 (2002).

36. Zhang, Y., Satterlee, A. & Huang, L. In vivo gene delivery by nonviral vectors: overcoming hurdles? Mol Ther 20, 1298-1304 (2012).

37. Min, J., Braatz, R.D. & Hammond, P.T. Tunable staged release of therapeutics from layer-by-layer coatings with clay interlayer barrier. Biomaterials 35, 2507-2517 (2014).

38. Elzbieciak, M., Wodka, D., Zapotoczny, S., Nowak, P. & Warszynski, P. Characteristics of model polyelectrolyte multilayer films containing laponite clay nanoparticles. Langmuir : the ACS journal of surfaces and colloids 26, 277-283 (2010).

39. Kehlbeck, J.D. et al. Directed self-assembly in laponite/CdSe/polyaniline nanocomposites. Langmuir : the ACS journal of surfaces and colloids 24, 9727-9738 (2008).

40. He, C., Yin, L., Song, Y., Tang, C. & Yin, C. Optimization of multifunctional chitosan-siRNA nanoparticles for oral delivery applications, targeting TNF-alpha silencing in rats. Acta Biomaterialia (2015).

41. Han, L., Tang, C. & Yin, C. Enhanced antitumor efficacies of multifunctional nanocomplexes through knocking down the barriers for siRNA delivery. Biomaterials 44, 111-121 (2015).

42. Yang, C. et al. Chitosan/siRNA nanoparticles targeting cyclooxygenase type 2 attenuate unilateral ureteral obstruction-induced kidney injury in mice. Theranostics 5, 110-123 (2015).

43. Yhee, J.Y. et al. Cancer-targeted MDR-1 siRNA delivery using self-cross-linked glycol chitosan nanoparticles to overcome drug resistance. J Control Release 198, 1-9 (2015).

44. Dahlman, J.E. et al. In vivo endothelial siRNA delivery using polymeric nanoparticles with low molecular weight. Nat Nanotechnol 9, 648-655 (2014).

45. Dong, Y. et al. Lipid-like nanomaterials for simultaneous gene expression and silencing in vivo. Adv Healthc Mater 3, 1392-1397 (2014).

46. Park, J.E. & Barbul, A. Understanding the role of immune regulation in wound healing. Am J Surg 187, 11S-16S (2004).

47. Gurtner, G.C., Werner, S., Barrandon, Y. & Longaker, M.T. Wound repair and regeneration. Nature 453, 314-321 (2008).

48. Shah, N.J. et al. Tunable dual growth factor delivery from polyelectrolyte multilayer films. Biomaterials 32, 6183-6193 (2011).

49. Macdonald, M.L., Rodriguez, N.M., Shah, N.J. & Hammond, P.T. Characterization of tunable FGF-2 releasing polyelectrolyte multilayers. BioMacromolecules 11, 2053-2059 (2010).

50. Chuang, H.F., Smith, R.C. & Hammond, P.T. Polyelectrolyte multilayers for tunable release of antibiotics. BioMacromolecules 9, 1660-1668 (2008).

51. Wood, K.C., Boedicker, J.Q., Lynn, D.M. & Hammond, P.T. Tunable drug release from hydrolytically degradable layer-by-layer thin films. Langmuir : the ACS journal of surfaces and colloids 21, 1603-1609 (2005).

Chapter 3
Nanolayered siRNA Dressings for Sustained Localized Knockdown

Reproduced in part with permission from "Nanolayered siRNA Dressing for Sustained Localized Knockdown" by Castleberry, S., Wang, M. & Hammond, P.T. *ACS Nano* **7**, 5251-5261 (2013).

3.1 Introduction

In Chapter 2 we discussed our preliminary investigational studies that helped us refine our techniques and focus for developing LbL films for local delivery of siRNA. This work looked at polyplex nanoparticle and direct incorporation approaches to determine film structures that could achieve siRNA delivery in vitro. Further investigation into other possible film structures, however, led us in a new direction from that described in Chapter 2, primarily focusing on calcium phosphate nanoparticles for siRNA incorporation. In Chapter 3 we present our *in vitro* investigations into LbL film architectures using calcium phosphate nanoparticles.

RNA interference (RNAi) is the process in which small segments of double stranded RNA are used to identify and facilitate the destruction of target mRNA sequences. RNAi holds enormous potential both as a tool in molecular biology as well as a powerful therapeutic agent[1-6]. Currently however there remain significant questions as to the viability of RNAi in medicine due to the difficulty in delivering the molecule effectively to areas of interest while maintaining its activity and avoiding toxicity[7-10]. Whether advances in the systemic delivery of siRNA[11-17] can effectively address these concerns is yet to be seen; technologies for the local administration of RNAi may offer more easily realized opportunities[18-23]. Local delivery can limit numerous unwanted systemic side effects of therapies and maintains the highest load possible in the targeted area before clearance[24, 25]. The direct release of siRNA to certain regions of the body could be of significant interest in many applications: modifying cellular interactions with medical implants such as orthopedic implants and vascular stents, altering how cells respond to tissue engineering constructs, or serving as a localized reservoir for sustained therapeutic benefit.

To the best of our knowledge there have been relatively few attempts to develop material systems for localized and sustained delivery of siRNA to tissues[22, 26-28].

Layer-by-layer (LbL) assembly is a robust method that has been successfully demonstrated for the localized and sustained delivery of many biologic therapeutics and biomolecules[29-32]. LbL is the sequential adsorption of materials onto a surface using electrostatic, hydrogen bonding, or other complementary interactions[33, 34]. Materials of interest can be uniformly coated on a surface with alternating interactions to generate nanometer-scale thin films that can deliver small molecule drugs35, growth factors[36], and DNA[37]. LbL films have been used to coat many different surfaces ranging from stainless steel[38] and titanium[39] to synthetic and naturally derived polymer constructs and even coating living organisms[40]. In addition, the delivery of siRNA from an LbL film could provide a platform for future applications where sequential and coordinated release[41,42] siRNAs along with other biologically relevant components[26] may be possible.

The potential for localized RNAi in regenerative medicine is of particular interest, as the opportunities for a therapeutic that could selectively tune expression locally so as to modulate the natural healing response are immense. As described in the introductory chapter of this thesis, we are primarily focused on using localized siRNA delivery to treat complications in wound healing. The known complications of healing are numerous and varied, however RNAi has the potential diversity to target all of them. This unique characteristic of RNA interference is the driving force behind a lot of this work. By systematically investigating the knockdown of one target after another, and potentially in combination, we can gain better insight into the biology of these pathologies as well as develop materials to improve outcomes for patients.

Herein we describe the development of an LbL assembled nano-layer coating for the delivery of siRNA that is capable of sustaining significant knockdown in multiple cell lines for over one week *in vitro*. This film as described required no externally delivered transfection vectors or mechanical transfection techniques (e.g. electroporation) to achieve these results. This coating was applied to a commercially available woven nylon bandage for testing and showed only minimal impact on the viability of cells exposed to it. A schematic of the application of such an LbL film is presented in **Figure 3-1** where the coating is shown applied to a generic

woven substrate. **Figure 3-1b** illustrates a range of potential applications for such a coating in multiple different localized delivery applications.

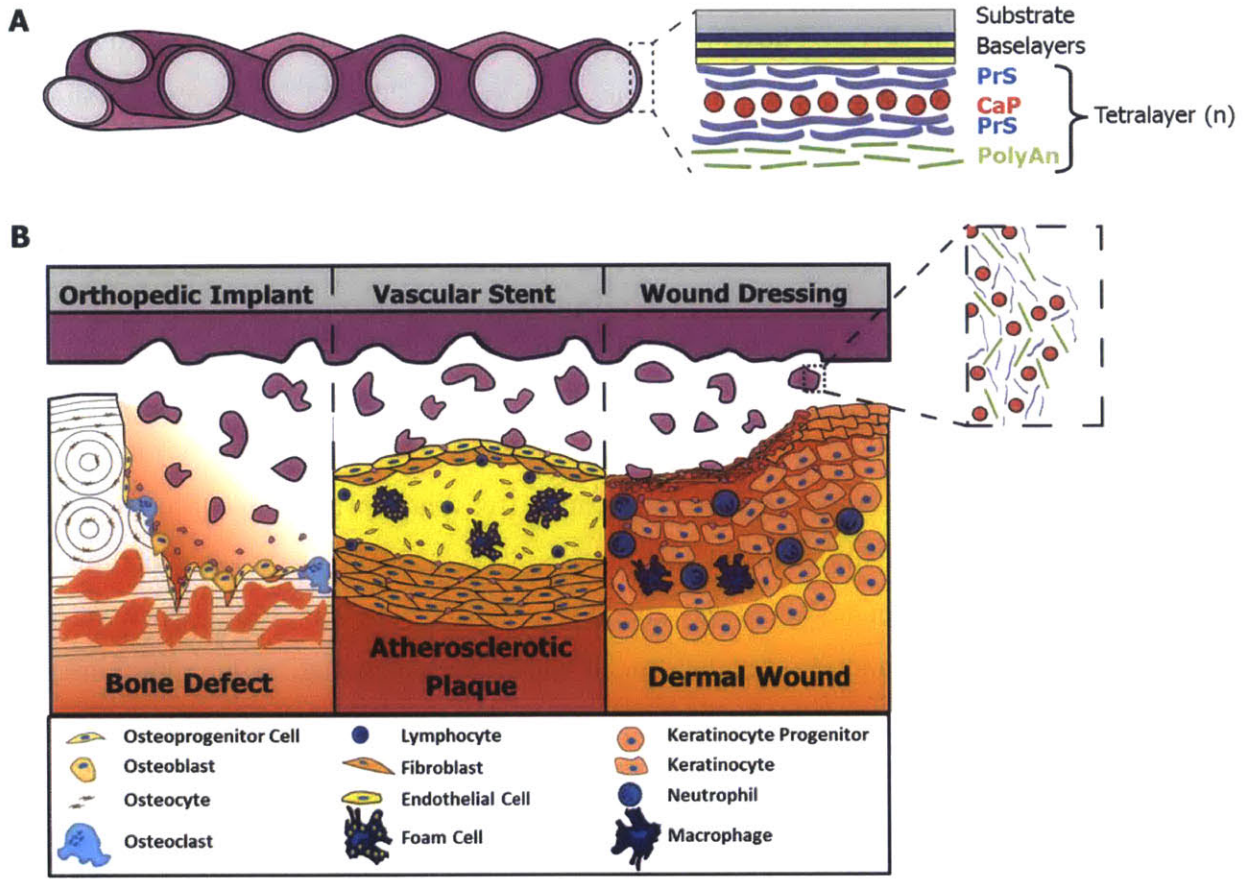

Figure 3-1 Layer-by-layer coating Tegaderm® and potential applications for localized delivery of siRNA

(A) Schematic representation of LbL Film coated Tegaderm. Shown in the zoomed in portion is a depiction of the Laponite® containing LbL film architecture. (B) Potential application of LbL films releasing siRNA containing fragments of film into various environments where modulation of cellular responses may provide some therapeutic benefit. Inset illustrates an idealized film mixture released from the coating.

3.2 Methods and Materials

3.2.1 Materials

SiRNA for GFP and siControl were received as a gift from Sanofi-Aventis. Alexafluor 488-labeled siRNA was purchased from Qiagen (Valencia, CA). Linear poly(ethyleneimine) (LPEI, MW = 25 kDa) and dextran sulfate (DS, MW = 500 kDa or 9kDa) were purchased from Polysciences (Warrington, PA). Phosphate buffered saline solution (PBS, 10x), Advanced-MEM, fetal bovine serum, antibiotic-antimycotic solution and 200mM L-glutamine solution were purchased from Invitrogen (Carlsbad, CA). NIH-3T3, MDA-MB-435, and M4A4 cells were purchased from ATCC (Manassas VA). Tegaderm® was purchased from Cardinal Health (Newark, NJ).

3.2.2 The Formation of siRNA loaded Calcium Phosphate Nanoparticles

Calcium phosphate nanoparticles containing siRNA were synthesized by rapid precipitation of $CaCl_2$ and NH_3PO_4 in the presence of siRNA. NH_3PO_4. (3.74mM) and $CaCl_2$ (6.25mM) working solutions were prepared in nuclease free water pH 8.5 and filtered using a 0.2μm syringe filter. To prepare 3 mL of CaP nanoparticles, a dipping solution containing 20 μg/mL siRNA and 200 μL of NH_3PO_4 was added to 60μg of siRNA in 100μL nuclease free water. 200 μL of the $CaCl_2$ solution was then added with vigorous mixing. After approximately 30 seconds 2.5 mL of pH 8.5 nuclease free water was then added to dilute the particles to the dipping concentration. The diameter and zeta potential of the formed nanoparticle were measured both prior to and after film assembly using a ZetaPALS dynamic light scattering and zeta potential analyzer. The CaP siRNA particles were always prepared just prior to LbL film construction.

3.2.3 Fabrication of LbL Films

Film assembly was performed using an HMS series Carl-Zeiss programmable slide stainer. Substrates to be coated were first cleaned sequentially with methanol, ethanol, isopropanol and water and then dried under filtered nitrogen. These substrates were plasma cleaned for 5 minutes on the high RF setting and then immediately placed in a 2 mg/mL solution of LPEI and allowed to adsorb the material for at least 30 minutes prior to use. After this initial coating, substrates were then placed into specially designed holders for the programmable slide stainer to move between dipping baths. A generic bilayer LbL assembly protocol consists of first dipping the substrate into a polycation solution for some specified time, then moving that substrate through two wash steps where excess polymer is allowed to desorb from the surface.

The washed substrate is then placed in a polyanion solution and allowed to adsorb polymer. After adsorption of the polyanion the substrate is then washed two more times to remove any excess polymer. This process can then be repeated for multiple depositions of the bilayer architecture.

All films were assembled on top of 10 baselayers of (LPEI/DS) to ensure a conformal charged coating of the substrate for siRNA film deposition. Assembly of baselayers was carried out in 100 mM sodium acetate solution at pH 5.0. All solutions were filtered using a 0.2 μm membrane syringe filter prior to use. Polymer solutions used were prepared at a 2 mg/mL concentration and all CaP nanoparticle solutions contained approximately 20 μg/mL concentration of siRNA. Polymer deposition steps were done for 10 minutes and CaP nanoparticle deposition steps were done for 45 minutes. All deposition steps were followed with two 1 minute washes in pH adjusted nuclease free water. All solutions for siRNA containing films were prepared in pH 9.0 nuclease free water.

3.2.4 Film Thickness and Surface Characterization

The thickness of the LbL films were assessed for films assembled on silicon and glass substrates using both spectroscopic ellipsometry (XLS-100 Spectroscopic Ellipsometer J.A. Woollam Co., Inc) and profilometry (Dektak 150 Profilometer). Ellipsometric measurements were performed on LbL films assembled on silicon substrates. Films were dried under filtered nitrogen prior to measurement. Measurements were performed at room temperature with a 70° incidence angle. The acquired spectra were then fit with a Cauchy dispersion model to obtain an estimated thickness for the film. For measurement of film thickness by profilometry, films were built on either silicon or glass and scored by a razor then tracked over. Step height from the untouched film to the bottom of the score was measured in six different locations on each sample to obtain an average thickness.

Atomic force microscopy (AFM) was performed using a Dimension 3100 AFM with Nanoscope 5 controller (Veeco Metrology) in tapping mode. Film areas of 25 μm by 25 μm were examined for each film after 5, 15 and 25 architecture depositions. Nanoscope analysis v1.10 software was used to calculate the root mean squared roughness for films.

3.2.5 Quantification of siRNA Loading into LbL Assembly

Incorporation of siRNA within the LbL film assemblies were quantified after 5, 10, 15 and 25 architecture repeats. To quantify the amount of siRNA within the film a one square centimeter sample of a film coated substrate was placed into 500μL of 1 M NaCl solution prepared from nuclease free water. The sample was then subjected to vigorous agitation for 30 minutes to completely remove the film from the surface. The substrate was then removed from the salt solution, washed with deionized water and dried under filtered nitrogen. These substrates were evaluated by SEM to check that the entire film had been removed from the surface. Quantification of siRNA was performed using Oligreen dsDNA reagent (Invitrogen) as per the manufacturer's instructions. The degradation solution containing the released film was diluted 1:20 into nuclease free water to reduce salt concentration to within the tolerance range of the assay. 25 μL of degradation sample was then added to 100μL of prepared Oligreen reagent (diluted 1:200 in TE buffer of reagent in kit) in a fluoroblock (BD) 96-well plate. Samples were then read with a fluorescent plate reader with 490/520 Ex/Em wavelengths. siRNA standards were prepared using similar salt concentrations to that in the diluted degradation samples.

3.2.6 Degradation Studies and Release Characterization

Experiments for the quantification of film degradation were carried out in cell conditioned media. To assist in the visualization of the degradation of the film, AlexaFluor 488-labeled siRNA was used. Cell conditioned media was prepared from NIH-3T3 cells grown to confluence. NIH-3T3s were seeded into a 24-well plates (50,000 cells/well) and cultured in Advanced-MEM (Invitrogen) media containing 5% FBS, 1% antibiotic-antimycotic solution, and 2mM L-glutamine. Cells grew to confluence within approximately 1 day after seeding. Media was removed from wells after 72 hours in contact with the cells. This media was filtered using a 0.2 μm syringe filter to remove cellular debris. This filtered media was then placed directly onto of the films to be degraded. Degradations were carried out at 37°C with the entire degradation media exchanged daily. Unlabeled siRNA served as a blank non-fluorescent control. A standard curve of the fluorescently labeled siRNA was used to interpret the concentration of siRNA within the release media. SEM analysis of all samples was done in JEOL 6700F scanning electron microscope. Confocal imaging of degrading samples was performed on a Zeiss LSM 510 Confocal Laser Scanning Microscope.

3.2.7 Characterization of *In Vitro* Knockdown

GFP knockdown was characterized by flow cytometry measurements of mean cell fluorescence in NIH-3T3, MDA-MB-435, and M4A4 cells that constitutively expressed GFP. 5,000 cells per well were seeded in a 48 well plate in 600μL of cell growth media and allowed to incubate for 24 hours. Films coated substrates were cut into 0.5x0.5 cm (0.25cm2 total area) squares and placed into the wells with the cells. After 3, 5, or 7 days of exposure to the film coated substrates cells were trypsinized and mean cell fluorescence was determined by flow cytometry, using a BD FACSCalibur flow cytometer.

3.2.8 Preservation of siRNA Knockdown During Release

Films were created using GFP specific siRNA. GFP expressing NIH-3T3s were seeded as previously described. Films were pre-degraded in cell conditioned media for 24, 72 or 120 hours and then placed in culture with cells. Cells were exposed to films for 72 hours. Mean cell fluorescence was measured using flow cytometry. Films containing negative control siRNA were used for quantification of relative cell fluorescence.

3.2.9 *In Vitro* Transfection with Fluorescently Labeled siRNA

Transfection of NIH-3T3s was monitored using fluorescently labeled siRNA. Similar to knockdown experiments films containing the labeled siRNA were built on Tegaderm samples and placed in culture with NIH-3T3 cells grown on coverslips in cell growth media. Cells were exposed to films for up to 1 week in vitro with media being changed every two days. At day 3, 5, and 7 samples were taken for microscope analysis of transfection. Cells were fixed in formalin diluted in PBS and counterstained with DAPI nuclear stain.

3.3 Results

3.3.1 Thin Film Assembly

Here we report the investigation of four LbL film architectures containing siRNA loaded calcium phosphate (CaP) nanoparticles for the sustained localized delivery of siRNA. We chose to use CaP nanoparticles based on a number of advantageous characteristics, most important of which was the fact that they have been previously demonstrated to remain intact after incorporation into LbL assemblies[43]. CaP nanoparticles are known to dissociate with the maturation of the endosome. This happens when the pH of the endosome falls below approximately 6.6-6.8. Within the endosomal compartment, the dissociation of the CaP

nanoparticles creates increased osmotic pressure and this increased pressure can for endosomal rupture and subsequent release of the packaged siRNA into the cytosol[44, 45].

The films to be tested were constructed of different film architectures consisting of bilayer or tetralayer combinations of polyelectrolyte materials and CaP nanoparticles. Protamine sulfate (PrS), a naturally derived protein isolated from salmon sperm, was chosen for the polycation for all of the films investigated in this paper. PrS was chosen based on its relatively high isoelectric point of around pH 12[46] and its capability to readily complex with nucleic acids in an effective manner[47-49]. PrS consists largely of arginine and has been shown to bind DNA and siRNA and protect them from nuclease degradation for multiple days when exposed to serum nucleases[49, 50]. We investigated three polyanions to use in combination with the CaP nanoparticles and PrS in LbL assemblies: (1) low molecular weight (9kDa) dextran sulfate (DSL), (2) high molecular weight (500 kDa) dextran sulfate (DSH), and (3) Laponite® silicate clay (Lap)[51]. All of these components are either readily degraded by enzymes in the body, or are naturally occurring biomolecules that can be readily resorbed or cleared from the body.

The four films tested in this investigation were: (1) [PrS/CaP nanoparticle] bilayer, (2) [PrS/CaP nanoparticle/PrS/DSL] tetralayer, (3) [PrS/CaP nanoparticle/PrS/DSH] tetralayer, and (4) [PrS/CaP nanoparticle/PrS/Lap] tetralayer. These four different films gave very different results in their respective rates of film growth, siRNA incorporation, and the level of knockdown observed.

CaP nanoparticles were analyzed using a ZetaPALS dynamic light scattering and zeta potential analyzer before and after film construction to evaluate any change in particle characteristics during the film building process. Prior to film construction the average nanoparticle diameter was approximately 217 nm and had a negative zeta potential of nearly -30 mV. After the generation of the LbL multilayer film (25 bi- or tetralayers), the particle size of the remaining CaP particles in solution was 199nm and the particles exhibited a similar zeta potential to nanoparticles prior to dipping (-28 mV).

Film growth was measured for each film using both profilometry and ellipsometry on films built on silicon substrates[31, 52]. The growth curve for each architecture is plotted in **Figure**

3-2A. The thinnest film, [PrS/CaP], grew linearly (as plotted R^2=0.97) with an average growth rate of approximately 4 nm per layer, reaching 103 nm ± 18.5 nm after 25 layers. Even after 25 layers this film did not approach a thickness equal to the average diameter of the particles being incorporated, suggesting that less than a complete monolayer of coverage was obtained during assembly. Interestingly, AFM imaging of the surface of the film at different stages of assembly showed many small nanoparticle-sized features that were observed to increase in density with increasing number of bilayers. The roughness of this film was also seen to increase during film assembly from approximately 9.6 nm at 5 bilayers to 16.6 nm at 25 bilayers. The linear nature of the film growth suggests that siRNA may have been incorporating directly into the film, with only a fraction of the incorporated siRNA loaded being encapsulated within CaP nanoparticles.

The [PrS/CaP/PrS/DSL] film growth was not truly linear over the 25 layers investigated (as suggested by the plotted R2= 0.91 for a linear fit). For the first 15 layers the film grew at approximately 6.8 nm per layer which increased significantly in to nearly 25 nm per layer from layers 15 to 25. Although it is unclear from the growth rate data alone, this kind of increase in film thickness is a characteristic of inter-diffusion taking place during film construction[35, 53]. After 25 tetralayers, the [PrS/CaP/PrS/DSL] was the second thickest film tested at 380 nm ± 30.2 nm and had a surface roughness of approximately 35 nm.

Both the Lap and DSH containing films were observed to exhibit near linear growth patterns over the 25 architecture repeats tested (as plotted R^2= 0.98, and 0.95, respectively). The [PrS/CaP/PrS/DSH] film grew by approximately 10.5 nm per tetralayer and reached a total thickness of 257 nm ± 24.5 at 25 tetralayers. The [PrS/CaP/PrS/Lap] film in contrast grew by nearly three times that rate at approximately 31 nm per layer reaching 633 nm ± 72 nm at 25 layers. The roughness of these two films however was similar with the DSH containing film being around 18.3 nm and the Lap being 21.6 nm after 25 layers.

The amount of siRNA incorporated into each coated square centimeter of the different film architectures varied significantly with the choice of polyanion (**Figure 3-2B**). After 25 layers the [PrS/CaP/PrS/DSL] film had incorporated the least amount of siRNA, only 2.1 ± 0.6 $\mu g/cm^2$, while the [PrS/CaP/PrS/Lap] film contained nearly 10 times that amount (18.9 ± 1.4 $\mu g/cm^2$). It is interesting to note that increased film thickness did not correlate with increased siRNA loading, as the DSL containing film was nearly 1.5 times thicker than the DSH film at 25

tetralayers and yet held less than one-sixth the amount of siRNA (12.9 ± 2.6 μg/cm^2). The [PrS/CaP] film incorporated 6.3 ± 0.7 μg/cm^2 after 25 layers, approximately one-third as much as the Lap containing tetralayer film, however it was one-sixth as thick. Together these data suggest that siRNA incorporation is dependent not only on the polycation used to complex the siRNA onto the surface, but also on the other materials used in the film architecture. In addition to this it is also apparent when comparing the DSH and Lap tetralayer films to the bilayer architecture that increasing overall film thickness in combination with appropriate materials may also be important in achieving high siRNA incorporation.

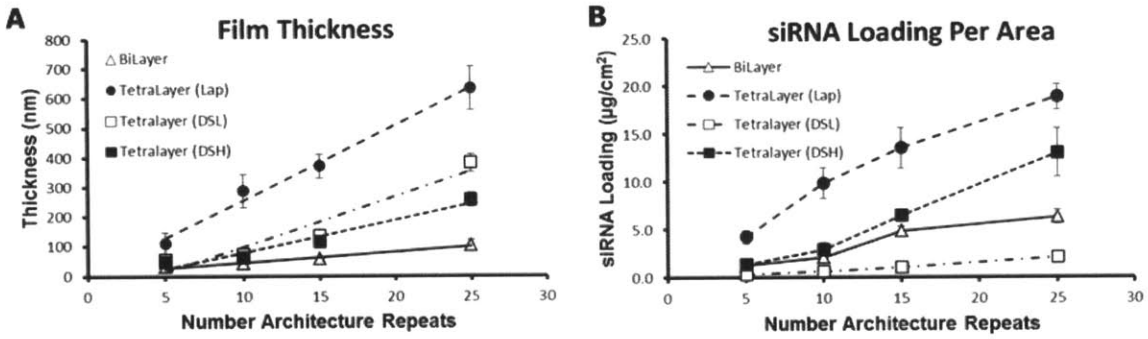

Figure 3-2. LbL film growth and siRNA incorporation

(a) Plot of film thickness versus the number of film architecture repeats for all four film architectures deposited on flat silicon substrates. The data points represent average measurements taken by both profilometry and ellipsometry, error bars represent 95% confidence interval. (b) Plot of total siRNA loading per film area of all four tested films measured using Oligreen dsDNA assay of fully degraded samples.

To test the *in vitro* efficacy of films, each of the four films needed to be assembled on a non-degradable inert substrate that could be placed in close contact with cells. In this way the assembled film and substrate would function as a sort of reservoir from which the films would degrade and release siRNA. We chose to use a woven nylon bandage (Tegaderm®) for this substrate. Tegaderm® is commonly used in medical practice as a contact layer on top of wounds to reduce tissue infiltration into absorbent wound dressings, thereby greatly reducing the level of

unwanted tissue adhesion to the dressings. The structure of the material is highly uniform, consisting of woven fibers of approximately 50μm in diameter which form pores within the weave of nearly $0.01mm^2$ **(Figure 3-3B)**. Coating the substrate with LbL film did not disturb these features, as can be seen by SEM in **Figure 3-3A**.

Films were created using both siRNA specific for GFP and a control sequence of siRNA that is known to not target any mRNA sequence (siControl). Knockdown of GFP was followed for one week *in vitro*. Film coated substrates were placed into culture with GFP expressing NIH-3T3 cells in 48-well plates. Relative mean cell fluorescence of the cell populations treated with each of the different film architectures on days 3, 5, and 7 can be seen in **Figure 3-3C**. GFP expression was most reduced in cells exposed to the [PrS/CaP/PrS/Lap] film coated bandages. On day 3, cells exposed to this film had a 55% reduction in mean cell fluorescence which increased to 58% by day 5 and finally to a 64% reduction by day 7 compared to cells treated with the siControl containing film.

Building on our earlier findings of the importance for material choice in assembling LbL films for siRNA incorporation, it was observed that even in the case of the same material, changing the molecular weight can make a significant impact on siRNA delivery. This is seen in the strikingly different levels of GFP knockdown for the two dextran sulfate containing films. The [PrS/CaP/PrS/DSL] film reached a maximum reduction in mean cell fluorescence of approximately 18% on day 5, which decreased slightly by day 7 to only 14%. The [PrS/CaP/PrS/DSH] film on the other hand achieved nearly a 48% reduction in mean cell fluorescence on day 3 which had increased to a 53% reduction by day 7.

The [PrS/CaP] bilayer film showed no measurable reduction in GFP expression over the 1 week period *in vitro*. Further investigation into this film architecture demonstrated that this lack of efficacy most likely was due to the lack of siRNA release from the coated substrate. Measurement of the siRNA remaining in the film after degradation showed more than 80% of the loaded siRNA remained within the film after one week. This unreleased siRNA when combined with Lipofectamine 2000 was demonstrated to be able to transfect cells and achieve significant gene knockdown.

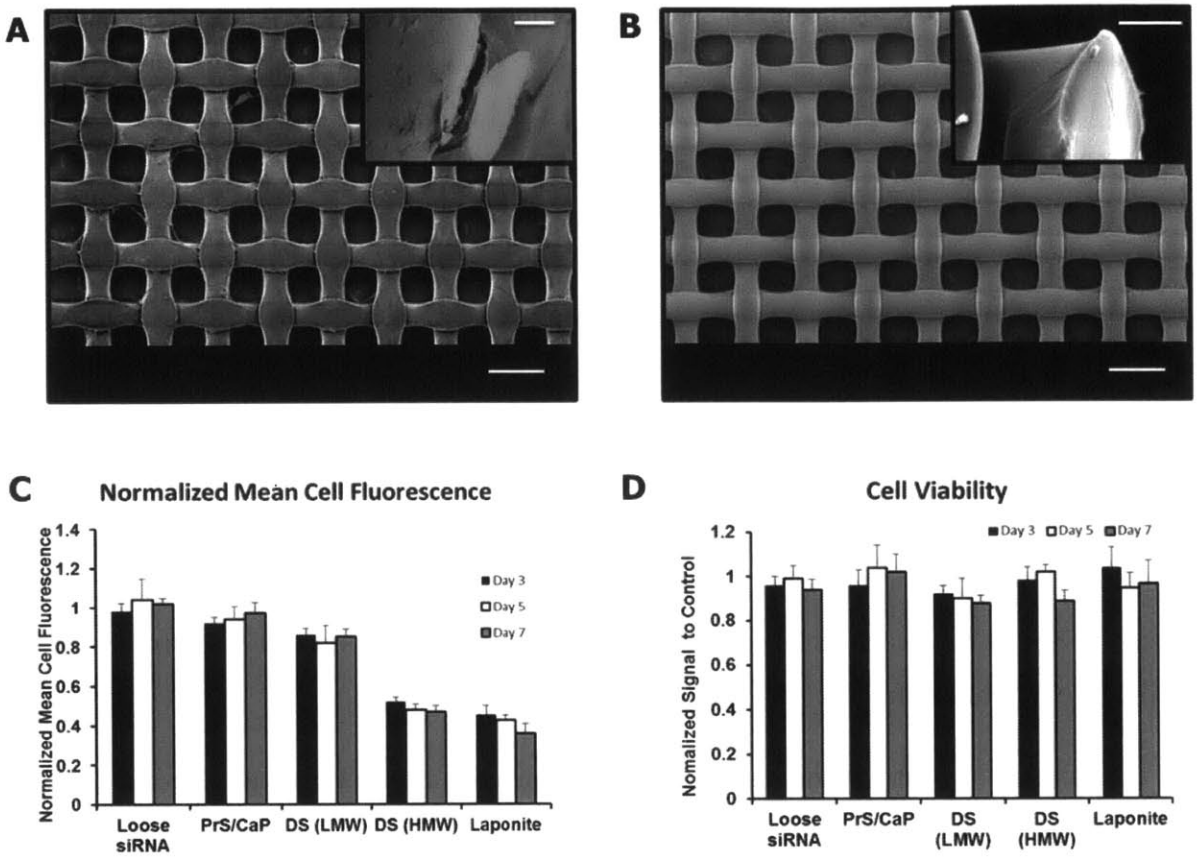

Figure 3-3. ***In vitro*** **characterization of LbL films**

(a) SEM image showing the regular woven pattern of Laponite® containing film coated on Tegaderm® used for in vitro testing. Scale bar =100 μm, inset scale bar = 10 μm. (b) SEM of uncoated Tegaderm® substrate. Similar scales as in A. (c) Plot of flow cytometry data for NIH-3T3 cells stably expressing GFP exposed to LbL film coated Tegaderm for 3, 5, and 7 days. Data is shown as relative mean cell fluorescence normalized to cells treated with siControl containing films of the same architecture. (d) Cell viability of NIH-3T3 cells exposed to LbL film coated Tegaderm as compared to cells exposed to uncoated Tegaderm®, measured using AlamarBlue® metabolic assay.

The impact on cell viability for each film was quantified using AlamarBlue assay. The viability of cells exposed to film coated substrates was normalized to cells exposed to uncoated substrates. This was done to control for the effects of the bandage making contact with the cell

surfaces. This control was not seen to be statistically different from cells left untreated, suggesting that the bandage within the well was inert. These results can be seen in **Figure 3-3D**. Cells proliferated rapidly under all testing conditions, growing to near confluence by day 5. Exposure of cells to 100 pmol of free siRNA did not impact cell viability significantly.

Of the films tested only the [PrS/CaP/PrS/Lap] film exhibited no statistically significant cytotoxicity at any time over the one week test period. The other film coated substrates were observed to reduce cell viability from 10-30%. An important comparison to make is in the case for the DSH and DSL films. The DSL film was seen to cause significant reductions in cell viability while the DSH film did so to a much lesser degree. We believe this is due to the increase in overall film material released from the DSL coated surface compared to the DSH surface.

3.3.2 siRNA Film Characterization

Of the four films tested the [PrS/CaP/PrS/Lap] film showed the greatest reduction in GFP expression, had the least impact on cell viability, and incorporated the most siRNA per area. For these reasons this film was determined to be the best performing film and was chosen to be the focus of further investigation. Specifically we were interested to investigate the full siRNA release profile and characterize the siRNA-specific gene knockdown in multiple cell lines.

SEM imaging of the film coated substrate showed near uniform coating with some bridges of film appearing to connect the woven fibers **(Figure 3-4A)** confirming our gross examination of the LbL coated bandages. Incorporation of siRNA was similarly uniform over the coated substrate; as observed by confocal imaging of the coated bandages using a fluorescently labeled siRNA in **Figure3- 4B**. The sections used to render the projection highlight the uniform and continuous nature of the coating on the fibers **(Figure 3-4C)**. The sections shown are at 8 μm steps, starting near the apex of a fiber, moving through the fiber until reaching the center.

Fluorescent imaging of the coated bandages made apparent a punctate presentation of fluorescent localizations within the film coating **(Figure 3-4B)**. This feature was observed uniformly over the coated surface and had an almost regular appearance to it, suggesting that it was not an artifact of assembly or drying. In contrast we have seen for a number of films

assembled on flat silicon substrates that there are "edge effects" on the coated surface where aggregation of material is observed due to drying of the film between depositions. This appearance however does not look like it is caused by such an effect.

To investigate these formations, the same film was built on silicon substrates and characterized by atomic force microscopy (AFM). **Figure 3-4 D-F** show the surface topography as measured by AFM at 5, 15, and 25 architecture repeats on the surface. Large (approx. 3-5μm in diameter) features began to appear on the surface of the film at 15 tetralayers. These features are in close agreement with the size of the punctate fluorescent localizations seen by confocal imaging. As we are incorporating nanoparticles into our LbL film we were understandably concerned that our film assembly process was leading to particle aggregation and that these aggregates were what we were observing. Dynamic light scattering measurements of the solutions used to construct the films however showed no particulate in excess of 300 nm in diameter. These findings suggest that the aggregations we are observing are most likely formed on the surface during film growth and do not represent the incorporation of particle aggregates from solution. This is a fascinating observation as LbL assembly is based on a uniform creation of films on surfaces. It is intuitive however that incorporation of nanomaterials on the same scale as the final thickness of the LbL film may lead to less-than uniform growth pattern.

AFM imaging showed a gradual change in surface profile during film construction. Initially small sub-micron particulate can be observed in a near uniform layer covering the surface. After 5 layers these particulate range in size from 100nm to 500nm with the majority lying around 250nm in width. At 15 layers of film deposited larger 1-2 micron aggregates begin to appear on the surface. These clusters are rough and have multi-globular features, suggestive of aggregations of smaller particulate. When 35 layers have been assembled these clusters now form large 5+ micron clumps on the surface. It is these foci that we believe correlate with the increased fluorescent intensities.

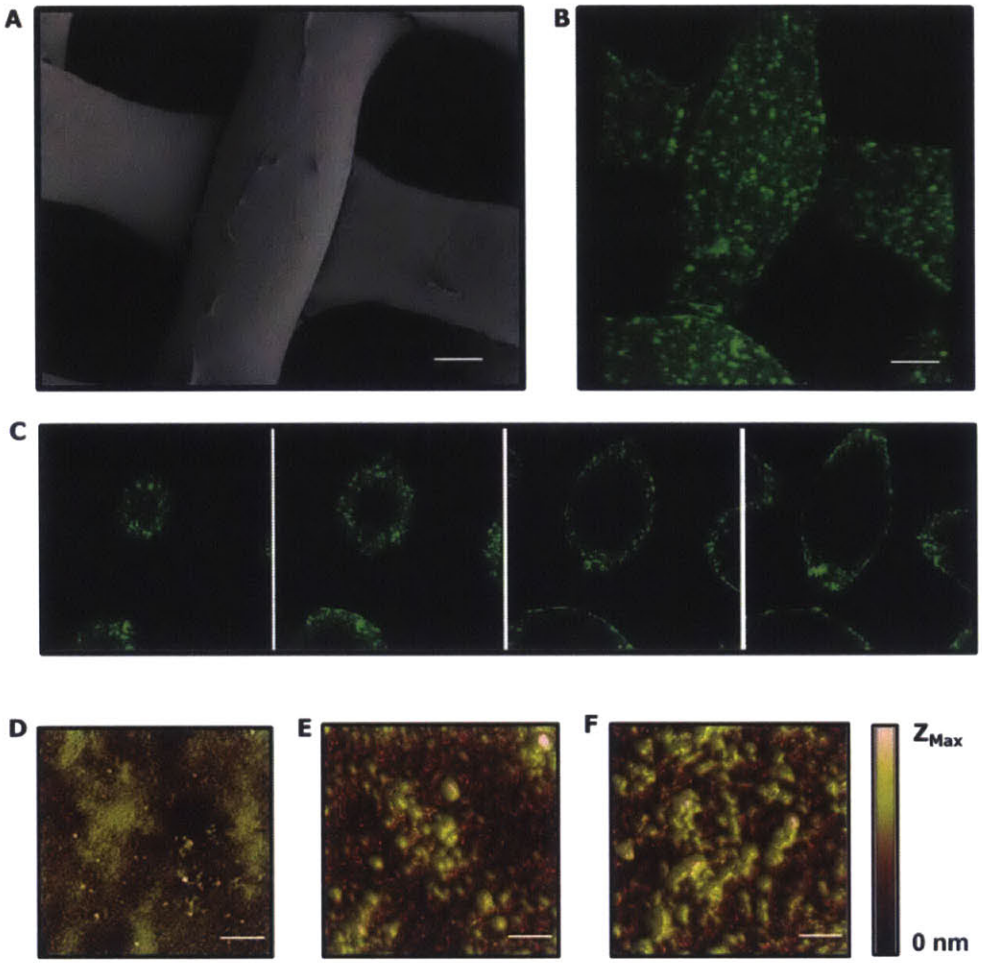

Figure 3-4. Characterization of Laponite® containing LbL film coating on Tegaderm® substrate.

(a) SEM imaging of film coated substrate, scale bar = 25 μm. (b) Three dimensional projection of fluorescent confocal imaging of film coated substrate using AlexaFluor 488-labeled siRNA. Scale bar = 25 μm. (c) Selected confocal images used to generate projected image. Images were selected at 8 μm steps to show the conformal nature of the film coating. (d-f) Atomic force micrographs at 5, 15, and 25 architecture repeats respectively, Zmax = 57nm (d), 138nm (e), and 182nm (f), scale bar = 5 μm.

3.3.3 Degradation and Sustained Release Profiles of LbL siRNA

Release of siRNA from the [PrS/CaP/PrS/Lap] film was followed in cell conditioned media at 37°C for 10 days using fluorescently labeled siRNA. The release profile can be seen in **Figure 3-5A-B**. Over the first six days of degradation, the film released siRNA at an average

rate of 1.8μg/cm^2 per day. This rate dropped to approximately 0.5μg/cm^2 per day after day 6 until the end of the study period. The cumulative release of siRNA for the 10 days was 12.7μg/cm^2. The total amount of siRNA incorporated within this film was shown to be nearly 19μg/cm^2, meaning that approximately two-thirds of the siRNA incorporated was released over the 10 day test period. No further release of siRNA from the film was observed after 10 days.

When this study was carried out in PBS at 37°C only 0.7μg/cm^2 of siRNA was observed to be released. This siRNA was released in a burst within the first 6 hours of study and no other quantifiable siRNA release was observed. This style of release suggests that materials within the cell conditioned media were required to facilitate its degradation and the subsequent siRNA release. The concept of environmentally stimulated release of a therapeutic is a long-standing goal in drug delivery, and using biologically degradable materials is one means that has been well studied. Here the use of the enzymatically degradable protamine sulfate allows for such control, however we do not know at this time what sort of tenability we would desire to better treat wounds with our released siRNA material. This idea however suffices to provide more conceptual framework for our later focused approaches.

The degradation and release of the film from the substrate was monitored optically by SEM and by confocal fluorescent imaging. A sample taken prior to degradation is shown in **Figure 3-5C**. The non-degraded film coats the substrate with few surface defects and fluorescent imaging shows uniform covering of the substrate with only a few areas of increased fluorescent signal. Samples of degraded film were taken on day three and day seven to inspect the film that remained attached to the substrate. Images of the film at three days of degradation show that it has swelled noticeably and that the distribution of fluorescence along the bandage surface has become less uniform. Large defects in the coating are apparent and flaps of film that are falling off of the coated surface are visible where the fibers of the bandage cross. SEM images show large surface defects in the coating with significant portions of the film loosely bound to the substrate **(Figure 3-5D)**.

After seven days of degradation most of the film was observed to be largely released from the substrate surface with only a few notable pieces of film remaining attached. The fluorescent images of the film at this point also show that most of labeled siRNA contained within the film has been released **(Figure 3-5E)**. SEM imaging of the bandage shows only small patches of film

loosely associate with the surface. These patches ranged from a few microns in diameter to tens of microns and could be easily removed from the substrate by vigorous agitation in deionized water.

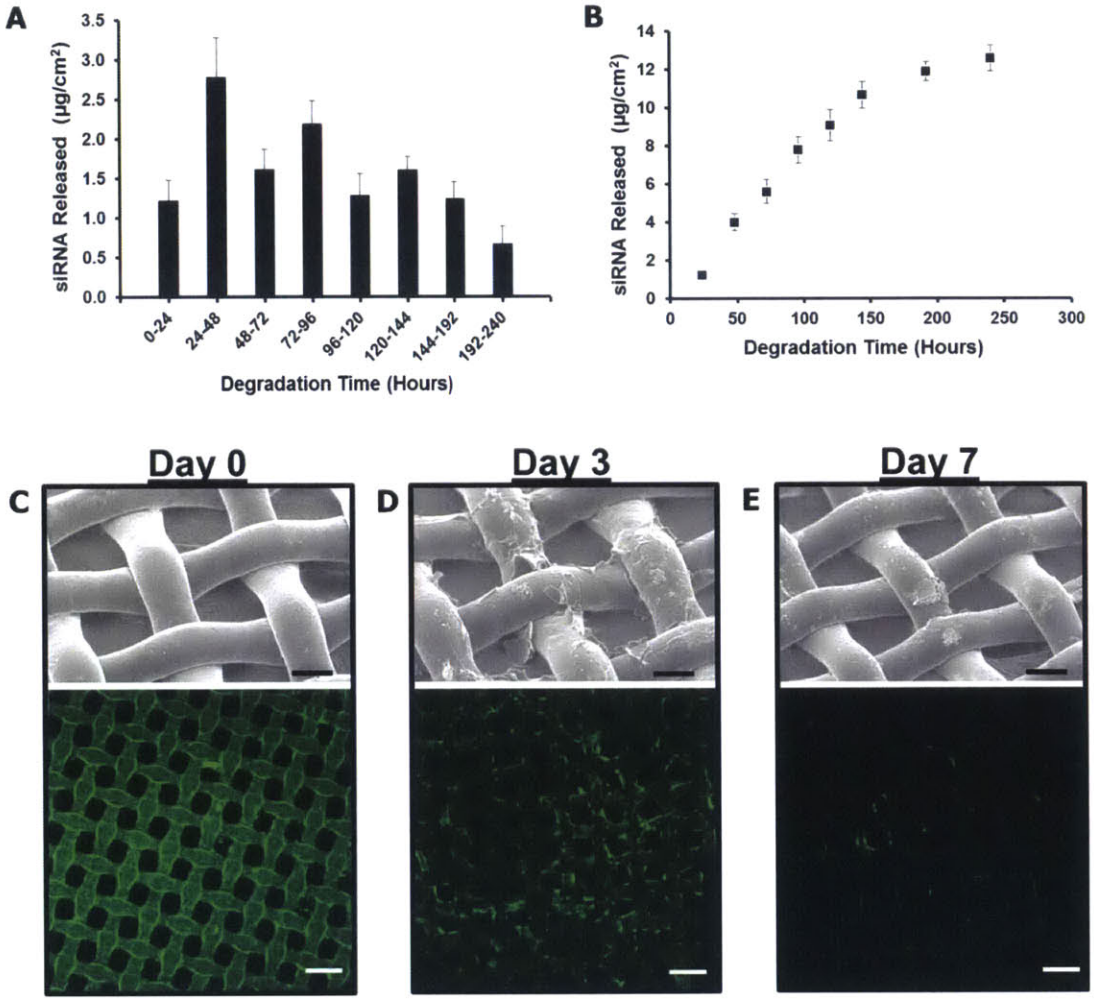

Figure 3-5. LbL film degradation and release of siRNA

(a) Plot of siRNA release measured on a daily (days 1-6) or bi-daily (days 7-10). Release measured during degradation of FITC-labeled siRNA containing film in cell conditioned media. (b) Cumulative release of siRNA over the 10 day period tested. (C-E) Side-by-side comparison of SEM and confocal imaging showing the degradation of the film on day 0 (c), day 3 (d), and day 7 (e), in cell conditioned media. SEM scale bar = 50 µm, Confocal scale bar = 100 µm.

3.3.4 Demonstration of Maintained siRNA Bioactivity

Degradation and release studies showed that siRNA was released from the LbL film for up to 10 days *in vitro*. This release however only followed the fluorescent label attached to the siRNA and does not give any indication of whether the siRNA is intact and active or not. As siRNA is known to undergo rapid nuclease degradation when unprotected[1,2], it was important to demonstrate that the siRNA released at every time points was still bioactive. To investigate this, films were degraded as previously described for 24, 72, or 120 hours in cell conditioned media prior to introduction to GFP-expressing NIH-3T3 cells. These films, having been degraded for predetermined amounts of time, provide us with snap shots of the film at each time and thus allow for evaluation of the activity of the siRNA being released at that time point.

The experiment was carried as follows: cells were seeded at a density of 5,000 cells per well in a 48-well plate and allowed to seed for 24 hours prior to testing. After this period 0.25cm^2 bandages were placed within each well and cells were exposed to these pre-degraded films for 72 hours. After this period of exposure, cells were trypsinized and then assessed for mean cell fluorescence using flow cytometry (**Figure 3-6**). All films tested were demonstrated to reduce GFP expression relative to cells treated with control films. The extent to which the films reduced mean cell fluorescence was comparable to the estimated siRNA release under the test conditions. A slight reduction in function could also be due to degradation of the siRNA released or changes in the way that the siRNA is complexed when it is released from the film at later periods.

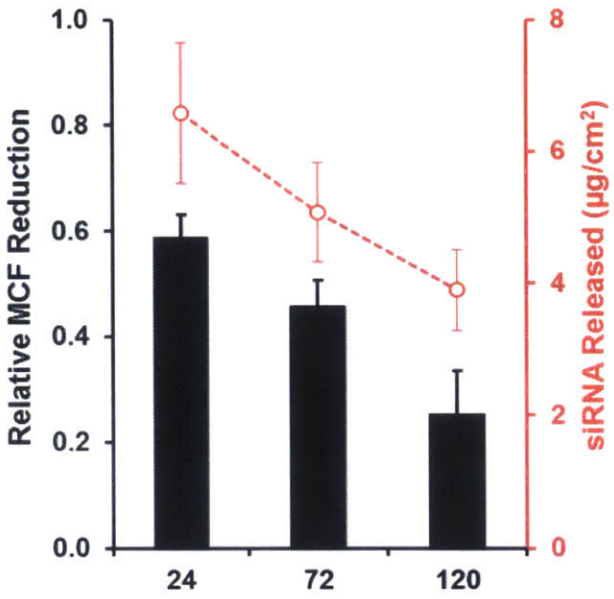

Figure 3-6. Continued function of siRNA released from LbL films assessed over a one week period *in vitro*

Films introduced to cells after degradation in cell conditioned media for up to five days (120 hours) prior to introduction to cells were still able to affect knockdown of GFP in NIH-3T3 cells.

3.3.5 Cellular Uptake of siRNA

The uptake of siRNA released from the degrading film was followed in NIH-3T3 cells using a fluorescently labeled siRNA over a 1 week period. **Figure 3-7** shows images of 3T3 cells after being exposed to the degrading film for 3, 5, and 7 days respectively. At day three the fluorescent signal within the cells was largely localized to punctate spots. By day 5 and 7 cells were more diffusely fluorescent although they still contained many punctate localizations of fluorescent signal.

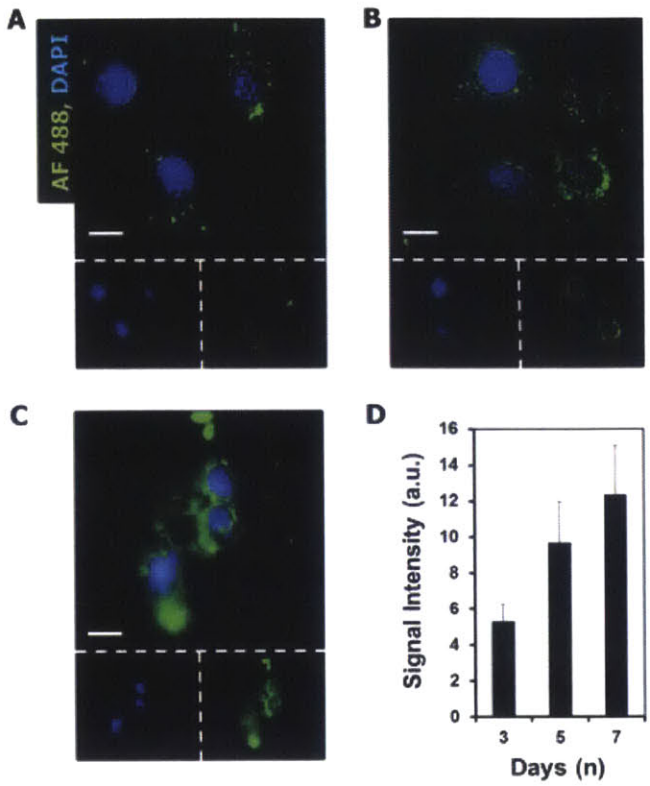

Figure 3-7. siRNA released from LbL assembly continues to transfect cells and remains active over 1 week period *in vitro*

(a-c) Uptake of AlexaFluor488-labeled siRNA by NIH-3T3 cells at 3 (a), 5 (b), and 7(c) days exposure to LbL films containing labeled siRNA. Cells were seen to become more diffusely fluorescent over the one week period. Scale bar = 10 μm. (d) Average fluorescent intensity for cells

To better understand the way that the released siRNA was being presented to the cells in culture we looked to evaluate how film material was accumulating within the wells. To do this we used confocal imaging of cells exposed to the released film material for three days. A number of fascinating features were apparent from this study. Most important of which was a potential answer as to how material was coming into contact with the cells. We had assumed that the released micron sized film material was further being broken down and taken up by cells, but had little evidence to support such assertions. Imaging studies showed however that such a route was possible, as large 3-8 μm diameter particles were seen to come to rest on top of

cells in culture. These cells were observed to contain multiple small punctate localizations of the labeled siRNA.

Many of these particles were seen within cells and outside of the cell bodies. This presentation suggests that the material released from the film coated bandages were accumulating in the bottom of the wells with the cells and were thus presented for cellular uptake. The signal within the cells was observed to be largely contained within small localizations; however many of the cells also had a more diffuse fluorescent signal, suggesting that endosomal escape had been achieved and that these cells were successfully transfected with the released film material **(Figure 3-8)**.

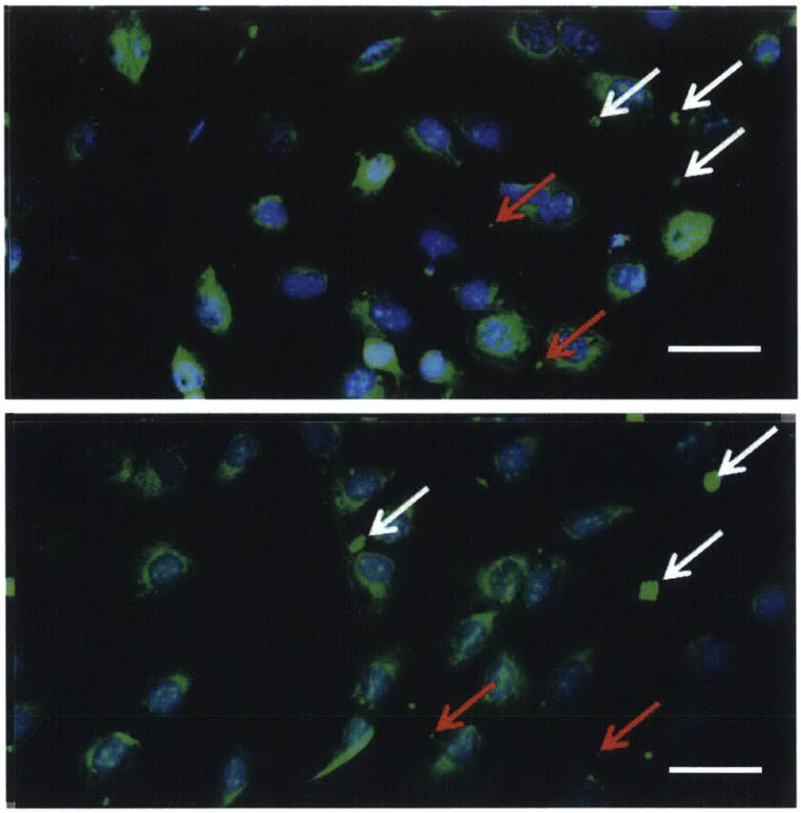

Figure 3-8. Release of siRNA from the surface is in the form of large pieces of LbL film These large multi-micron sized pieces are then further degraded until they can transfect cells effectively. The white arrows point to pieces of the labeled film material that are in excess of 2 μm in diameter, while the red arrows point to foci that are less than 0.5 μm. Scale bar = 20 μm.

3.3.6 Extension to knockdown in MDA-MB-435 and M4A4 Cells

To this point we performed all *in vitro* experiments using NIH-3T3s as a representative cell type. It is known that different cell types, especially cell lines derived from cancers, have very different transfection efficacies. We were interested to evaluate our approach in such cell lines so as to gain insight into the effect that our assembled drug delivery device may have when placed *in vivo* where multiple different cell types from differing cell lineages will most likely be present. To evaluate the effectiveness of this film in achieving knockdown in more cell types we chose to investigate two commonly used cancer cell lines that were made to constitutively express GFP, the MDA-MB-435 and M4A4 cell lines.

Similar to our testing of the LbL coated bandages with NIH-3T3 cells, knockdown of GFP was observed as early as three days after application in both cell lines and was maintained for the entire one week study **(Figure 3-9a)**. Cell viability was seen to be reduced **(Figure 3-9b)** in the M4A4 cells over the one week period, although it remained relatively high (~90%) compared to that of cells treated with uncoated controls. These results suggest that delivery of siRNA from this film can transfect multiple cell types and provide interesting capabilities for this modular platform in future use.

Compared to the NIH-3T3 cells we observed significantly less reduction in gene expression for the M4A4 cell line while comparable reduction in the MDA cell line. These cause for these differences is hard to determine. We believe that as we have screened our candidate films for efficacy in the NIH-3T3 cell line that we may have come to a more optimal formulation in that testing group relative to other cell line. It may also be however that GFP expression in these two cancer cell lines may be higher than expression in the NIH-3T3 cells due to metabolic differences in the cell lines. One last factor to consider is the relative cell density as well, as the cancer cells were much faster proliferating than the 3T3 cell line, perhaps leading to a reduced intra-cellular concentration of the delivered siRNA, thus reducing the RNA interference effects observed. Whatever the cause however, we do see a significant siRNA-specific gene reduction in both of these cell lines with minimal impact on cell viability.

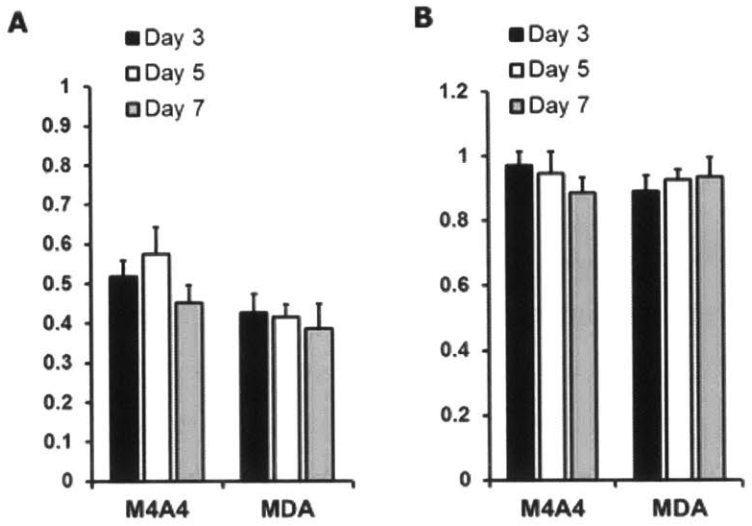

Figure 3-9. Knockdown of GFP characterized in two separate cancer cell lines

(a) Flow cytometry measurement of mean cell fluorescence of either MDA or M4A4 cells that constitutively express GFP exposed to GFP-siRNA containing LbL films followed over a 1 week period. Data shown normalized to mean cell fluorescence of cells exposed to siControl containing film of the same architecture. (b) Viability of cells exposed to coated Tegaderm® substrate normalized to cells exposed to uncoated substrates. Viability measured by metabolic assay AlamarBlue.

3.4 Conclusions

The nano-layered siRNA dressings presented in this work demonstrate an effective method for the incorporation and controlled localized delivery of siRNA. Commercially available nylon bandages when coated with the film developed in this work were able to achieve and maintained significant gene knockdown in multiple cell lines for up to one week *in vitro* without the need for external transfection agents. The films described here are only a few hundred nanometers in thickness and coat the dressings uniformly, leaving the structure of the bandage unaffected.

In total we detailed four distinct siRNA delivering LbL film architectures and evaluated these systems to isolate the best performing for a more focused investigation. The materials used

in creating the films were all biocompatible and all process steps were done in aqueous solution at ambient conditions and at mild pH and ionic strength conditions. This approach demonstrated within this work helps to detail the impact that different multilayer compositions have on drug delivery characteristics, independent of film thickness or drug loading.

The ability to deliver siRNA locally in a controlled and sustained manner is a promising tool in many areas where modulation of local cellular responses could provide benefit. The capability to load siRNA into an ultra-thin polymer coating for safe and effective delivery of siRNA over an extended period of time provides a significant advance in the existing capabilities of RNA interference. The film described in this work has great potential in many applications ranging from coatings for medical implants and tissue engineering constructs to uses in molecular biology and basic research.

3.5 References

1. Whitehead KA, Langer R, Anderson DG. Knocking down barriers: advances in siRNA delivery. Nature Reviews Drug Discovery 2009;8(2): 129-38.

2. Gavrilov K, Saltzman WM. Therapeutic siRNA: principles, challenges, and strategies. The Yale journal of biology and medicine 2012;85(2): 187-200.

3. Vaishnaw AK, Gollob J, Gamba-Vitalo C, et al. A status report on RNAi therapeutics. Silence 2010;1(1): 14.

4. Guo P, Coban O, Snead NM, et al. Engineering RNA for targeted siRNA delivery and medical application. Advanced Drug Delivery Reviews 2010;62(6): 650-66.

5. Ghildiyal M, Zamore PD. Small silencing RNAs: an expanding universe. Nature reviews. Genetics 2009;10(2): 94-108.

6. Burnett JC, Rossi JJ. RNA-based therapeutics: current progress and future prospects. Chemistry & biology 2012;19(1): 60-71.

7. Ballarín-González B, Howard KA. Polycation-based nanoparticle delivery of RNAi therapeutics: Adverse effects and solutions. Advanced Drug Delivery Reviews 2012.

8. Wu ZW, Chien CT, Liu CY, Yan JY, Lin SY. Recent progress in copolymer-mediated siRNA delivery. Journal of drug targeting 2012;20(7): 551-60.

9. Liu J, Guo S, Cinier M, et al. Fabrication of stable and RNase-resistant RNA nanoparticles active in gearing the nanomotors for viral DNA packaging. ACS Nano 2011;5(1): 237-46.

10. Juliano R, Bauman J, Kang H, Ming X. Biological barriers to therapy with antisense and siRNA oligonucleotides. Molecular pharmaceutics 2009;6(3): 686-95.

11. McNamara JO, 2nd, Andrechek ER, Wang Y, et al. Cell type-specific delivery of siRNAs with aptamer-siRNA chimeras. Nature biotechnology 2006;24(8): 1005-15.

12. Takeshita F, Minakuchi Y, Nagahara S, et al. Efficient delivery of small interfering RNA to bone-metastatic tumors by using atelocollagen in vivo. Proceedings of the National Academy of Sciences of the United States of America 2005;102(34): 12177-82.

13. Lorenz C, Hadwiger P, John M, Vornlocher HP, Unverzagt C. Steroid and lipid conjugates of siRNAs to enhance cellular uptake and gene silencing in liver cells. Bioorganic & medicinal chemistry letters 2004;14(19): 4975-7.

14. Schiffelers RM, Ansari A, Xu J, et al. Cancer siRNA therapy by tumor selective delivery with ligand-targeted sterically stabilized nanoparticle. Nucleic acids research 2004;32(19): e149.

15. Shu Y, Cinier M, Shu D, Guo P. Assembly of multifunctional phi29 pRNA nanoparticles for specific delivery of siRNA and other therapeutics to targeted cells. Methods 2011;54(2): 204-14.

16. Alam MR, Ming X, Fisher M, et al. Multivalent cyclic RGD conjugates for targeted delivery of small interfering RNA. Bioconjugate chemistry 2011;22(8): 1673-81.

17. Xiao Z, Farokhzad OC. Aptamer-functionalized nanoparticles for medical applications: challenges and opportunities. ACS Nano 2012;6(5): 3670-6.

18. Che H-L, Bae I-H, Lim KS, et al. Suppression of post-angioplasty restenosis with an Akt1 siRNA-embedded coronary stent in a rabbit model. Biomaterials 2012;33(33): 8548-56.

19. Li JM, Newburger PE, Gounis MJ, Dargon P, Zhang X, Messina LM. Local arterial nanoparticle delivery of siRNA for NOX2 knockdown to prevent restenosis in an atherosclerotic rat model. Gene therapy 2010;17(10): 1279-87.

20. Dimitrova M, Affolter C, Meyer F, et al. Sustained delivery of siRNAs targeting viral infection by cell-degradable multilayered polyelectrolyte films. Proceedings of the National Academy of Sciences 2008;105(42): 16320-25.

21. Nelson CE, Gupta MK, Adolph EJ, Shannon JM, Guelcher SA, Duvall CL. Sustained local delivery of siRNA from an injectable scaffold. Biomaterials 2012;33(4): 1154-61.

22. Nguyen K, Dang PN, Alsberg E. Functionalized, biodegradable hydrogels for control over sustained and localized siRNA delivery to incorporated and surrounding cells. Acta Biomaterialia 2012.

23. Rujitanaroj PO, Wang YC, Wang J, Chew SY. Nanofiber-mediated controlled release of siRNA complexes for long term gene-silencing applications. Biomaterials 2011;32(25): 5915-23.

24. Katz MG, Fargnoli AS, Pritchette LA, Bridges CR. Gene delivery technologies for cardiac applications. Gene therapy 2012;19(6): 659-69.

25. Wolinsky JB, Colson YL, Grinstaff MW. Local drug delivery strategies for cancer treatment: gels, nanoparticles, polymeric films, rods, and wafers. Journal of controlled release : official journal of the Controlled Release Society 2012;159(1): 14-26.

26. Manaka T, Suzuki A, Takayama K, Imai Y, Nakamura H, Takaoka K. Local delivery of siRNA using a biodegradable polymer application to enhance BMP-induced bone formation. Biomaterials 2011;32(36): 9642-8.

27. Rujitanaroj P-o, Jao B, Yang J, et al. Controlling fibrous capsule formation through long-term down-regulation of collagen type I (COL1A1) expression by nanofiber-mediated siRNA gene silencing. Acta Biomaterialia 2012.

28. Chen M. Chitosan/siRNA Nanoparticles Encapsulated in PLGA Nanofibers for siRNA Delivery. ACS Nano 2012;6(6): 4835-44.

29. PT H. Building Biomedical Materials Layer-by-Layer. Materials Today 2012;15(5): 196-206.

30. Jewell CM. Multilayered Polyelectrolyte Assemblies as Platforms for the Delivery of DNA and Other Nucleic Acid-Based Therapeutics. Advanced Drug Delivery Reviews 2008;60(9): 979-99.

31. Shah NJ, Hong J, Hyder MN, Hammond PT. Osteophilic Multilayer Coatings for Accelerated Bone Tissue Growth. Advanced Materials 2012;24(11): 1445-50.

32. Shukla A, Fang JC, Puranam S, Jensen FR, Hammond PT. Hemostatic multilayer coatings. Advanced Materials 2012;24(4): 492-6.

33. Detzel CJ, Larkin AL, Rajagopalan P. Polyelectrolyte Multilayers in Tissue Engineering. Tissue Engineering Part B-Reviews 2011;17(2): 101-13.

34. Zelikin AN. Drug Releasing Polymer Thin Films: New Era of Surface-Mediated Drug Delivery. Acs Nano 2010;4(5): 2494-509.

35. Shukla A, Avadhany SN, Fang JC, Hammond PT. Tunable Vancomycin Releasing Surfaces for Biomedical Applications. Small 2010;6(21): 2392-404.

36. Shah NJ, Hong J, Hyder MN, Hammond PT. Osteophilic multilayer coatings for accelerated bone tissue growth. Advanced Materials 2012;24(11): 1445-50.

37. Zhao Z, Qi Y, Wei M, Zhang F, Xu S. Layer-by-layer assembly and morphological characterizations of DNA/layered double hydroxide thin films. Materials Letters 2012;78: 62-65.

38. Aytar BS, Prausnitz MR, Lynn DM. Rapid Release of Plasmid DNA from Surfaces Coated with Polyelectrolyte Multilayers Promoted by the Application of Electrochemical Potentials. ACS Applied Materials & Interfaces 2012;4(5): 2726-34.

39. Liu S, Liu T, Chen J, Maitz M, Chen C, Huang N. Influence of a layer-by-layer-assembled multilayer of anti-CD34 antibody, vascular endothelial growth factor, and heparin on the endothelialization and anticoagulation of titanium surface. Journal of Biomedical Materials Research Part A 2012: n/a-n/a.

40. AL H. Biorecognition through Layer-by-Layer Polyelectrolyte Assembly: In-Situ Hybridization on Living Cells. BioMacromolecules 2006;7: 2742-50.

41. Wood KC, Chuang HF, Batten RD, Lynn DM, Hammond PT. Controlling interlayer diffusion to achieve sustained, multiagent delivery from layer-by-layer thin films. Proceedings of the National Academy of Sciences of the United States of America 2006;103(27): 10207-12.

42. Hong J. Graphene Multilayers as Gates for Multi-Week Sequential Release of Proteins from Surfaces. ACS Nano 2012;6(1): 81-88.

43. Zhang X, Kovtun A, Mendoza-Palomares C, et al. SiRNA-loaded multi-shell nanoparticles incorporated into a multilayered film as a reservoir for gene silencing. Biomaterials 2010;31(23): 6013-18.

44. Sokolova V, Epple M. Inorganic nanoparticles as carriers of nucleic acids into cells. Angewandte Chemie 2008;47(8): 1382-95.

45. Li J, Chen YC, Tseng YC, Mozumdar S, Huang L. Biodegradable calcium phosphate nanoparticle with lipid coating for systemic siRNA delivery. Journal of controlled release : official journal of the Controlled Release Society 2010;142(3): 416-21.

46. Remington JP. Remington, the science and practice of pharmacy. Easton, Pa.: Mack Pub. Co., 1995:v.

47. Maclachlan I. siRNAs with guts. Nature biotechnology 2008;26(4): 403-5.

48. Chen Y, Bathula SR, Li J, Huang L. Multifunctional nanoparticles delivering small interfering RNA and doxorubicin overcome drug resistance in cancer. The Journal of biological chemistry 2010;285(29): 22639-50.

49. DeLong RK, Akhtar U, Sallee M, et al. Characterization and performance of nucleic acid nanoparticles combined with protamine and gold. Biomaterials 2009;30(32): 6451-9.

50. Paris C, Moreau V, Deglane G, et al. Conjugating Phosphospermines to siRNAs for Improved Stability in Serum, Intracellular Delivery and RNAi-Mediated Gene Silencing. Molecular pharmaceutics 2012.

51. Dawson JI, Kanczler JM, Yang XB, Attard GS, Oreffo ROC. Clay Gels For the Delivery of Regenerative Microenvironments. Advanced Materials 2011;23(29): 3304-08.

52. Jourdainne L, Arntz Y, Senger B, et al. Multiple strata of exponentially growing polyelectrolyte multilayer films. Macromolecules 2007;40(2): 316-21.

53. Zacharia NS, Modestino M, Hammond PT. Factors influencing the interdiffusion of weak polycations in multilayers. Macromolecules 2007;40(26): 9523-28.

Chapter 4
Capillary Flow Layer-by-Layer: A Microfluidic Platform for the High-Throughput Assembly and Screening of Nanolayered Film Libraries

Reproduced in part with permission from "Capillary Flow Layer-by-Layer: A Microfluidic Platform for the High-Throughput Assembly and Screening of Nanolayered Film Libraries" by Castleberry, S.A., Li, W., Deng, D., Mayner, S. & Hammond, P.T. *ACS Nano* (2014).

4.1 Introduction

In Chapter 2 we described our early investigations into LbL films for incorporating and delivering siRNA. These studies helped us to refine our techniques, however they also served as a lesson in the slow pace that such investigations must proceed at due to the available modes of film assembly. This lesson was reinforced in Chapter 3 as our total investigations were unable to broaden beyond four individual films for testing, and even then we needed to focus onto one film for in depth in vitro testing. These important points focused our attention on the way in which we screen LbL assemblies and drove us to develop the technology described in this chapter for high-throughput screening of LbL film libraries.

Layer-by-layer (LbL) assembly is a powerful tool with increasing real world applications in energy, biomaterials, active surfaces, and membranes; however, the current state of the art requires individual sample construction using large quantities of material. Here we describe a technique using capillary flow within a microfluidic device to drive high-throughput assembly of LbL film libraries. This capillary flow layer-by-layer (CF-LbL) method significantly reduces material waste, improves quality control, and expands the potential applications of LbL into new

research spaces. The method can be operated as a simple lab bench top apparatus or combined with liquid handling robotics to extend library size. Here we describe and demonstrate the technique and establish its ability to recreate and expand on known literature for film growth and morphology. We use the same platform to assay biological properties such as cell adhesion and proliferation, and ultimately provide an example of the use of this approach to identify LbL films for surface-based DNA transfection of commonly used cell types.

Layer-by-layer (LbL) assembly is the alternating adsorption of materials onto a surface using complementary interactions, one layer of material at a time, creating nanometer-scale thin films[1-4]. This process enables fine control over the assembly of functional materials into ultra-thin coatings which exhibit a range of interesting properties and have found diverse applications in reactive membranes, drug delivery systems, and electrochemical and sensing devices[5-8]. Over the past decade, exciting new developments have demonstrated the power of LbL assembly in biomedical applications, with examples ranging from bone tissue engineering[9, 10] to vaccine delivery[11] and creating biological interfaces[12, 13].

Several recent advances have led to the adaptation of LbL toward commercial translation, including the use of convection in automated Spray-LbL[14, 15] to coat a broad range of surfaces with accelerated cycle times and the use of Spin-Assisted LbL[16-18] to generate thin films on planar surfaces with control of molecular orientation. These advances enable the implementation of promising LbL systems at the speed and throughput needed for commercial products and processes; however, to date there is no approach capable of assembling libraries of LbL films for research, development, and optimization.

Attempts to create and examine libraries of different LbL film systems can yield understanding of the impact of simple compositional changes in the polymers incorporated on final film structure and property[19-21]. The existing methods for LbL assembly for new materials discovery, however, rely on the individual production of film samples using large reservoirs of material, and must generally be facilitated using specialized or modified lab equipment. The limitations of current LbL techniques are particularly significant when precious, rare, and costly materials are incorporated in the film assembly. For biomaterials applications in particular, optimizing incorporation and/or release of siRNA, DNA, active growth factors, engineered

peptides or other therapeutics would require significant quantities of material, thus severely limiting investigations and potential discoveries in these areas.

As research into LbL film technology continues to expand and researchers pursue new discoveries along with commercial translation in the pharmaceutical industry, several challenges need to be overcome. These include simplifying *in vitro* analysis of films, improving material conservation, and making the LbL process more accessible to a broader scientific community. To address these challenges and enable more thorough investigations of LbL film assemblies, we have developed a simple microfluidic approach for the high-throughput construction of multiple LbL films in parallel. We have termed this approach "Capillary Flow Layer-by-Layer" (CF-LbL) as we harness capillary action to fill microchannels in which LbL films are assembled.

The CF-LbL device consists of an array of these microchannels formed by bonding a polydimethylsiloxane (PDMS) mold to an oxygen plasma treated substrate (*e.g.*, glass, silicon, *etc.*). This approach requires as little as 0.1% as much material per film compared to conventional methods, while enabling the simultaneous assembly of nearly 400 times as many independent films. LbL assemblies of varying compositions, morphologies, and architectures can be rapidly produced in a format that suits a number of physico-chemical and *in vitro* biological assays, and screened for meaningful material properties using this method.

4.2 Methods and Materials

4.2.1 Materials

Linear polyethylenimine (LPEI, M_w of 2.5k, 25k, 250k), and branched polyethylenimine (BPEI, M_w of 1.2k, 10k, 50-100k) were purchased from Polysciences; low molecular weight chitosan (LMW Chitosan, M_w of 15-30k), high molecular chitosan (HMW Chitosan, M_w of 300k), gelatin (pH=2.5), diethylaminoethyl-dextran (DEAE-Dextran), protamine sulfate (PrS), poly-L-lysine (PLL, M_w of 15-30k and 30-70k) and poly(allylamine hydrochloride) (PAH, M_w of 60k) were purchased from Sigma Aldrich; and the degradable poly(beta-aminoesters) (designated Poly 1, and Poly 2) were synthesized using the method that was previously published[48].

4.2.2 Device Fabrication

Masters templates for preparing microfluidic channels were made with an SU-8 photoresist in bas-relief on silicon wafers. The microfluidic device was fabricated in polydimethylsiloxane (PDMS) by using a standard soft-lithography method[49]. In brief, masters with microchannels were prepared with features of SU-8 on silicon wafers with diameter of 4 inches by a photolithography technique. The PDMS elastomer was prepared by mixing pre-polymer with the curing agent (Sylgard 184, Dow Corning) at the weight ratio of 10:1, respectively.

The mixture of the pre-polymer and curing agent was then poured onto the master, and cured in an oven at 75 °C for 4 hours. After curing, the replica was carefully peeled off from the master, and holes with various diameters were made by a Harris micro-punch at the designated positions. The patterned PDMS sheet and a glass slide were plasma treated for 90 s in a plasma cleaner chamber (PDC-3XG, Harrick, USA), and then brought to contact and immediately sealed. The thickness of the formed microchannel is approximately 100 μm. Micro-patterned surfaces inside micro channel were created by using multilayer soft-lithography as previously described[50].

4.2.3 LbL Film Assembly

Material solutions were prepared at a 2 mg/mL concentration and pH adjusted to desired level. All solutions were sterile filtered using a 0.2 μm syringe filter prior to use. Material solutions were introduced to the inlet of a microchannel by pipette. Solutions are drawn into the microchannel *via* capillary force to fill the entire channel within 1-3 seconds. After channel filling the excess material within the inlet is recovered from the inlet. Material in solution is allowed to adsorb for a pre-determined amount of time (*e.g.* 5, 10, or 15 min) and then the channel is cleared either by vacuum or by pressurized air.

The channel is then washed three times with a washing solution to remove material that is not well adsorbed to the channel surface. This process is then repeated with a complimentary species for adsorption and the entire process can be repeated to reach the desired number of layers of LbL film. After film assembly is complete the PDMS sheet can be removed from the substrate, leaving a micro-strip of LbL film on the substrate. Dip LbL films were assembled using a Carl Zeiss HMS DS50 slide stainer. Films were either built on Si wafers or glass slides.

Rinsing steps were performed using UltraPure™ DNase/RNase-Free water (Life Technologies) that was pH adjusted to match with the prior material adsorption step.

4.2.4 Multilayer Film Characterization

Film thickness was measured for films built on Si wafers using a Veeco Dektak (Plainview, NY,USA) surface profilometer. Surface roughness was measured using a Veeco Dimension 3100 atomic force microscope (AFM). Coating of microstructure containing CF-LbL devices was performed using a ZEISS Axiovert 200 fluorescent and brightfield microscope.

4.2.5 Cell Culture and Transfection Studies

NIH-3T3 and HeLa cells were used in this work; both were purchased from ATCC (Manassas VA). NIH-3T3 cells were used to evaluate cell behavior on PAA/PAH LbL films. HeLa cells were used for all transfection studies. Cells were seeded within the CF-LbL assembly device following LbL film construction at an initial density of 0.1M/mL and allowed to settle for 30 minutes, after which media was exchanged to remove unattached cells.

All cell lines were cultured in Advanced-MEM with 5% FBS and 1% Pen-Strep and 2mM L-glutamine. Media was exchanged daily by placing a droplet at the inlet and removing the waste at the exit of the microchannels. Bright field and fluorescent imaging of cells was done with a ZEISS Axiovert 200. Images were analyzed using ImageJ image analysis software. Confocal imaging of cells seeded on microchannel walls was done with a Nikon A1R Ultra-Fast Spectral Confocal Microscope and three-dimensional projection was created using Velocity software. Flow cytometry was performed with FACSCalibur flow cytometer.

4.2.6 Statistical Analysis

Data analysis was performed between groups using Student's *t*-test. These were rectified using ANOVA for comparisons between multiple groups. A value of $p < 0.05$ was used to indicate statistical significance.

4.3 Results

4.3.1 Design of a High-Throughput LbL Device

Each microchannel is comprised of a main channel where material from solution adsorbs onto the substrate, as well as three openings: an inlet well (1), a capillary flow break well (2), and an exit well (3) **(Figure 4-1a)**. Capillary flow within the channel is controlled by covering select regions of the PDMS mold during plasma treatment **(Figure 4-1c and Figure 4-2)**. This leaves these regions hydrophobic, while the uncovered areas receive plasma treatment and become hydrophilic. Material held within the channel is cleared by vacuum which is selectively applied by covering both holes (2) and (3) simultaneously **(Figure 4-1b)**. The layout of channels is modular by design and can be based on 96- and 384-well plate dimensions for high-throughput screening or consist of only a few microchannels for easy bench top use **(Figure 4-3)**. The characterization of films assembled within the microchannels is performed similar to those created by existing LbL methods using ellipsometry, profilometry, light microscopy, and atomic force microscopy.

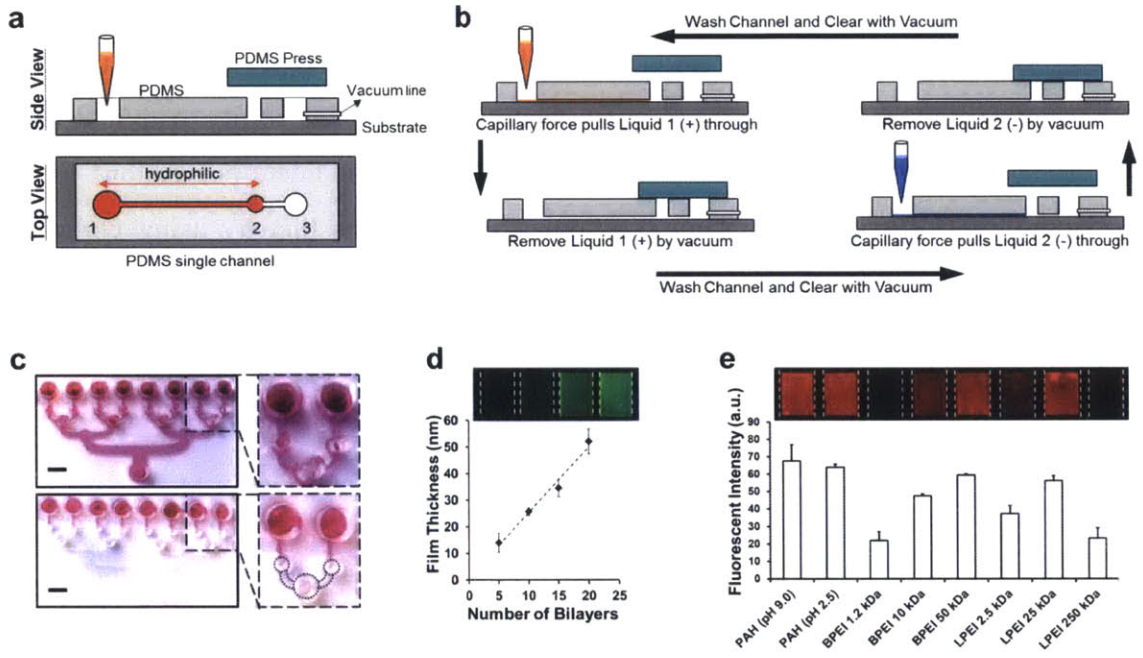

Figure 4-1 Design of capillary flow layer-by-layer (CF-LbL) device

(a) Top and side view of a single channel within a CF-LbL device, the red region is O_2 plasma treated. (b) The process of alternating adsorption of material inside of the microfluidic channels, (+) polycation and (-) polyanion species. (c) Multiple independent channels within a single CF-LbL device. The top image is fully O_2 plasma treated, the bottom image selectively treated, scale

= 3mm. (d) Measurement of film thickness for a sample PAA/PAH_{FITC} LbL film. (e) Screening LbL film architectures for material incorporation. Fluorescently labeled PAA is incorporated into bilayer LbL films with the polycations: PAH, branched polyethylenimine (BPEI), linear polyethylenimine (LPEI). Data shown as mean ± S.D.

To demonstrate the application of this technology in the construction and evaluation of LbL films, we began by assembling a simple bilayer film architecture of poly(acrylic acid) (PAA) and poly(allylamine hydrochloride) (PAH). PAH was labeled with a fluorescent dye and the growth of the film was measured by profilometry. The film grew linearly and resembles similar films assembled on glass slides constructed *via* Dip LbL technique **(Figure 4-1d)** with regard to thickness per bilayer.

For current LbL assembly techniques, investigating libraries of LbL films is a very time and material intensive task, as it requires up to multiple days to construct a single sample while using milliliters of material solution[22-24]. To demonstrate this capability with CF-LbL we assessed the incorporation of a labeled polyanion (PAA) with candidate polycations in simple bilayer assemblies **(Figure 4-1e)**. This experiment demonstrates that by using common lab imaging modalities, such as a gel imager, arrays of LbL films can be assessed for material incorporation. This type of approach could be very useful in determining the best polymer pairing for incorporation of a material of interest, such as a small molecule drug or protein therapeutic.

An important feature for the successful application of the CF-LbL device is the maintained independence of the multiple channels. The separation of the channels can be done in a number of ways, however to facilitate automation of the device a branching manifold system is preferable for material transport as it reduces material streams to only a few outlets, reducing complexity and difficulty for the operator. Such a manifold system then requires some level of inter-connection between the channels. To allow for this interconnection to be variable we determined that creating a large hydrophobic barrier between the channels was important. This barrier is created by selectively plasma treating the PDMS mold prior to adherence to the substrate. Shown in FIGURE 2 is such an application, where the light grey zone is blocked

from the O2 plasma and thus retains the hydrophobic nature of the PDMS as cast. This barrier can be broken when a strong driving pressure is applied across the channel in the direction of the main outlet. Importantly, the material that leaves the channel and goes into the manifold does not return to the depositing channels, as capillary forces are greatly reduced in this hydrophobic zone.

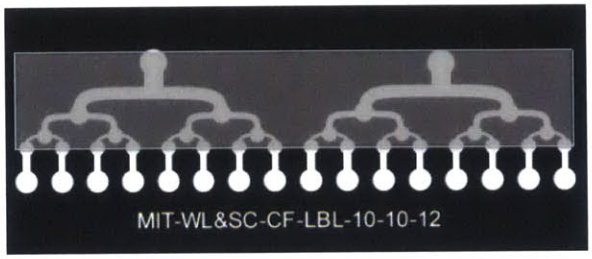

Figure 4-2 Photolithographic Mask Showing Partial O_2 Plasma Treatment
The shaded portion of the design is covered during O_2 plasma treatment so that it remains hydrophobic. This maintains the separation of material between channels to reduce the chance of cross-contamination during assembly.

4.3.2 CF-LbL Array Design

Use of this simple device in liquid robotic systems is most easily achieved by conforming the distribution of inlet wells to common labware, such as 96- or 384-well plates. Such designs are easily created and allow for a great deal of flexibility in the arrays created. Many liquid handling systems operate with a single 8-pipette arm with capabilities to mix in-well and remove material remaining in the well. Such practicalities allow for rapid loading of the microchannels within the device **(Figure 4-3a)**. We designed a number of different microchannel arrays to investigate the practical application of vacuum for material removal through the created manifolds. We found that connecting 16 microchannels with a width of more than 100um was operable with house vacuum. Reducing microchannel width or increasing the number of channels connected lead to unemptied channels due to increased flow resistance.

These arrays as described have some obvious limitations constraining the placement of microchannel inlets so as to facilitate use with common micropipettes; however the design and

layout of channel dimensions is largely up to the creator's discretion. Much of our preliminary work looked at relatively simple straight channel designs. We also designed curved and angled channels as well as channels with varying widths to demonstrate some of the 2-dimensional freedom within the device.

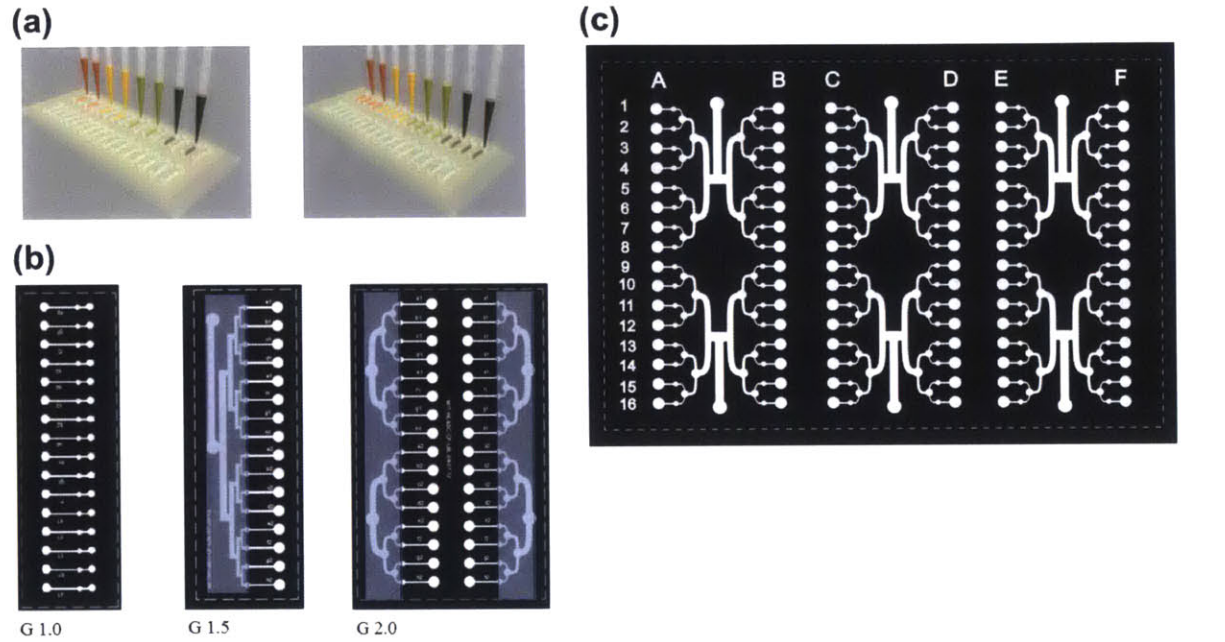

Figure 4-3 CF-LbL device arrangement is modular and customizable

(a) Each channel is independent of neighboring channels. Channel spacing is designed to pair with multichannel pipettes. (b) The device can be operated where channels are connected with an in-device manifold system (G 1.5 & G 2.0) or are held completely separate (G 1.0). Shaded regions denote the portion of the PDMS mold that is covered during plasma treatment so as to remain hydrophobic. (c) The CF-LbL channels can be arranged to 384-well plate spacing with 96 independent channels contained in the space of a common well-plate. This design consists of three modular units (A-B, C-D, and E-F) which can each be placed on individual microscope slides.

4.3.3 Incorporation of Microstructures with the CF-LbL Device

The layout and design of the microchannels within the device are easily customized for different applications. Channel parameters such as length, width, and shape can be modified by

designing different lithographic masks for creating the PDMS mold; however, using more recent advances in soft lithography techniques we can incorporate even more diverse designs. This includes the capability to incorporate microstructures as a part of the PDMS mold that forms the channel, which can be accomplished *via* multilayer soft lithography[25]. Introducing microstructures within the channel opens many interesting avenues for investigation, particularly in the area of *in vitro* experiments where the structures could be used to influence cell behavior.

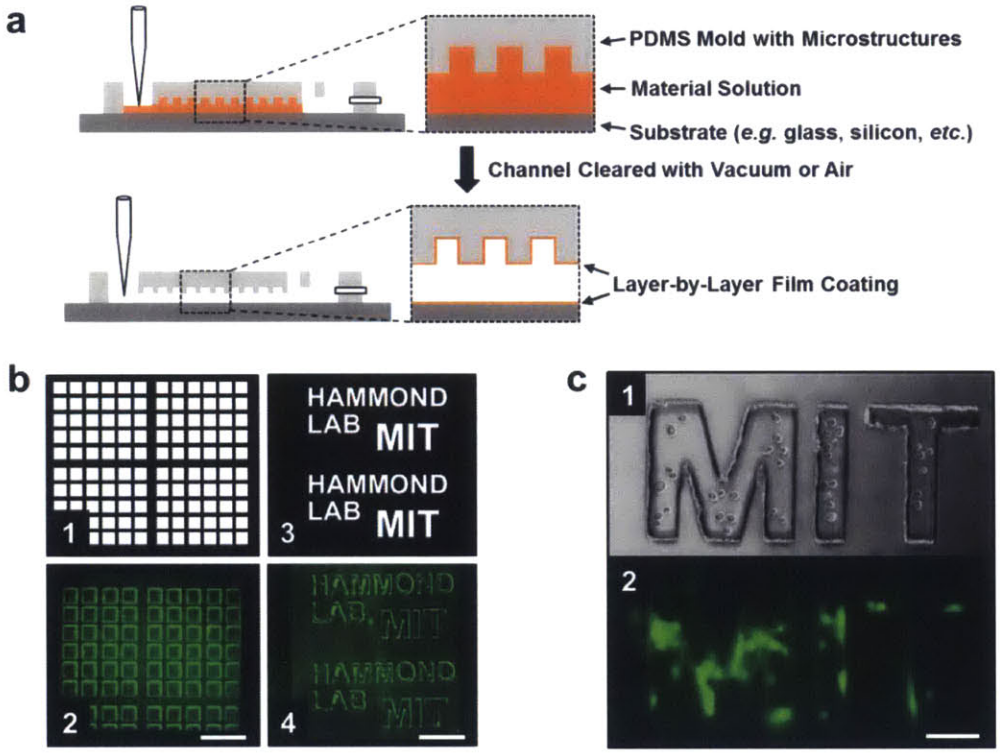

Figure 4-4 CF-LbL coating of microstructures contained within microchannels for diverse customized applications

(a) Schematic for the coating of microstructures within the CF-LbL channels. (b) Demonstration of patterned microstructures included within the microchannels, (1&3) Lithographic mask designs for the micro-wells, (2&4) fluorescent imaging of channels containing microstructures coated with PAA/PAH_{FITC}. Scale bar = 150μm. (c) Micro-patterned surface within the channel used to direct NIH-3T3 cell seeding. (1) Imaged immediately after clearing uncaptured cells from main channel with media. (2) Fluorescent imaging of spread cells after 24 hours. Scale bar = 50μm.

Microstructures contained within the channels of the device can be uniformly coated with LbL films, similar to coating flat surfaces **(Figure 4-4a)**. These structures can be used to increase the active surface area within the channel, and influence cell-surface interactions and adhesion, allowing for the generation of patterned cell surfaces. To demonstrate the capability of CF-LbL to coat these microstructures we assembled a simple bilayer film of PAA/PAH using a fluorescently labeled PAH. Fluorescent imaging of the coated channels shows the uniformity of the film coating, with well reproduced films assembling within and around the microstructure features **(Figure4-4b)**.

The use of microstructures, such as micro-wells, in cell sampling and small-scale cell culture has been well described by other research groups[26-29]. The micro-well features contained within the CF-LbL device are recessed into the PDMS mold and as such are positioned outside of the flow of the main channel and can thus enable cell seeding on the recessed surface features. This is accomplished by first filling the channel with a cell suspension and flipping the device such that gravity directs the cells into the PDMS wells. After thirty minutes fresh media is flowed through the channel by pipette and the cells not contained within the micro-wells are swept away. Using CF-LbL, these micro-wells can be coated with films that contain cell binding moieties or have interesting cell response behaviors to examine cell viability, adhesion, mobility, proliferation, and other cellular activity. To demonstrate this application we used a fluorescent NIH-3T3 cell line and captured cells within a micro-well design **(Figure 4-2c1)**. Cells were observed to preferentially seed within the micro-well structures and to spread within these features after one day in culture **(Figure 4-2c2)**.

4.3.4 High-Throughput Screen of a Weak Polyelectrolyte Bilayer Film

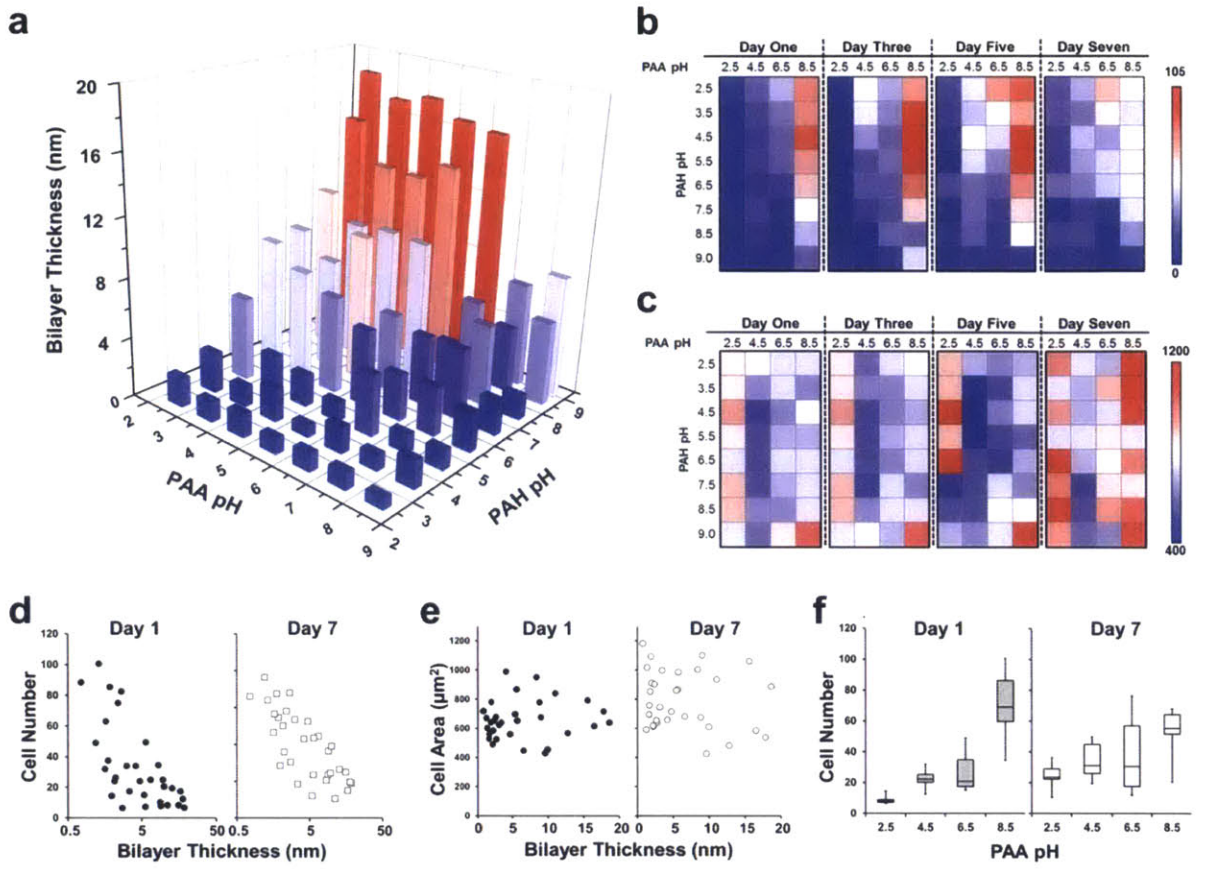

Figure 4-6 High-throughput screening of LbL assemblies

(a) pH-dependent thickness behavior of sequentially absorbed layers of weak polyelectrolytes, 10 bilayers. (b) Cell density on films. Cells were initially seeded at 0.1M/mL. Units = cells/mm^2. (c) The average spread area of cells on the different film architectures. Units = µm^2. (d) Effect of film thickness on cell density. Increasing bilayer thickness negatively impacted the total number of cells which initially seeded on the films. (e) Plot of cell spread area vs. bilayer thickness. No correlation was apparent. (f) Effect of PAA pH on the cell density on the films. Higher PAA pH corresponded with increased cell density, regardless of PAH pH.

To demonstrate the capability of CF-LbL to investigate large LbL film libraries we performed a classic experiment first described by Rubner and coworkers[30, 31], wherein the weak polyelectrolyte bilayer film of (PAA/ PAH) is assembled using polymer solutions that range in pH from 2.5 to 9.0 **(Figure 4-6a)**. Changing the pH of a polyelectrolyte solution alters the

degree of ionization of the adsorbing polymer and as such alters the adsorption of the polyelectrolyte to the surface. It was observed that by increasing the degree of ionization of either PAA or PAH in solution led to a decreased average bilayer thickness, whereas conditions where both polyelectrolytes are weakly ionized lead to the thickest films. These trends in pH and film thickness closely resemble those previously reported[30, 31], demonstrating the applicability of this method to traditional LbL film systems; furthermore, we were able to expand the range of pH values and conditions used in the original study.

Creating biological interfaces that modify cell behavior is an important and growing application for LbL films[32-36]. Investigating the myriad of potential iterative film assemblies around one simple film architecture however can be a very time and material intensive task, especially when considering the need to sterilize each sample prior to *in vitro* evaluation. In addition to preparing the samples for *in vitro* experimentation, actually conducting experiments *in situ* with large sample numbers presents many logistical issues and complicates investigations significantly. A major advantage of the CF-LbL method is that the sterility of the device in which the films are assembled is easily maintained throughout the assembly process. Further, *in vitro* tests can be readily performed directly within the assembled device, greatly simplifying the setup for investigations and limiting complications from film and sample handling.

To demonstrate the application of CF-LbL assembly in performing *in vitro* investigations, we evaluated 32 different film architectures from the previously investigated PAA/PAH bilayer system, covering a wide range of assembly conditions. Cells were seeded directly onto the film and cultured for one week. Response to the different films was evaluated by measuring cell adherence to the surface along with proliferation. Cell density and average cell spread area were measured daily using phase contrast light microscopy (**Figure 4-6 b-c**). Increasing bilayer thickness correlated significantly to decreased cell density, while no trends were apparent in regards to cell spread area (**Figure 4-6 d-e**).

It was also observed that the pH of PAA and PAH had significant impact on cell density (**Figure 4-6f and Figure 4-7**). Plotting the average cell density on the films one day after initial seeding and after 7 days shows some very interesting trends. One important feature that is first apparent is the opposite trends in cell density, where for increasing PAA pH cell density was generally increased, for PAH increased pH lead to decreased cell density. It is difficult to

determine the exact cause for these trends, as a number of possible explanations are possible. First, film thickness undoubtedly plays some role in the cell seeding and proliferation, closely agreeing with previous reports. By reducing the charge density of either polymer we then increase the overall film thickness. A second, auxiliary cause may also be charge density, as charged surfaces are known to play an important role in attracting cells to attach. This is important concept to consider as the total film thickness is an effect of a number of different material and assembly condition choices, charge density of the polymers being used is only one of the choices that effects it.

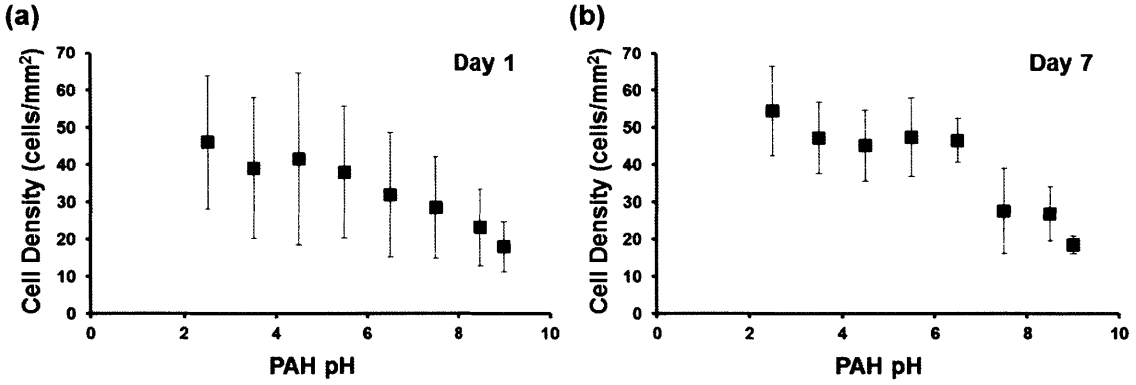

Figure 4-7 The effect of PAH pH on cell density

(a) The impact of PAH assembly pH on initial seeding of cells on a surface. (b) Increasing PAH assembly pH corresponds with decreased cell number after seven days. A clear change is apparent between pH 6.5 and 7.5. This is likely due to a reduction in the degree of ionization of the PAH at these conditions. Error bars represent 95% confidence interval.

4.3.5 Comparison of CF-LbL and Dip LbL Assembled Films

We were interested to determine how well the CF-LbL assembled films approximated LbL films assembled *via* the more traditional dip LbL technique. To do this we chose four films from the previous experiment and assembled them by both dip LbL and the CF-LbL technique. We assessed both the physical characteristics of the assembled films and cell response to them. Atomic force micrographs (AFMs) of the films assembled by either method were seen to have

very similar topographies and surface roughness **(Figure 4-8a)**. The average bilayer thickness and roughness of each film was measured after 10 bilayers were assembled.

There was no significant difference between the films assembled by either technique when comparing the topographic features, roughness, and film thickness **(Figure 4-8 b-c)**. These similarities support our early assertions that these films do closely resemble films created by dip LbL technique. Important to note is that the films are not only physically similar, but that they present very similar surfaces topologically which may play important roles in cell behavior studies.

To assess cellular responses to the coated surfaces we used NIH-3T3 cells. The total number of cells seeded for each group was corrected for the area upon which we were seeding. Cells were observed to respond similarly on both surfaces, with thick films leading to reduced overall cell density. These findings closely resemble those presented in previous reports for PAA/PAH bilayer systems, for which it was found that the mechanical stiffness of the thicker films was a primary determinant of cell adhesion. [37] The statistically similar performance of the films assembled using CF-LbL and dip LbL techniques highlights the usefulness of this approach, as the CF-LbL study not only used less than 1% the material as the dip LbL films, but all of the tested films were able to be easily ran on a single microscope slide, compared to 12 microscope slides for the dip LbL films.

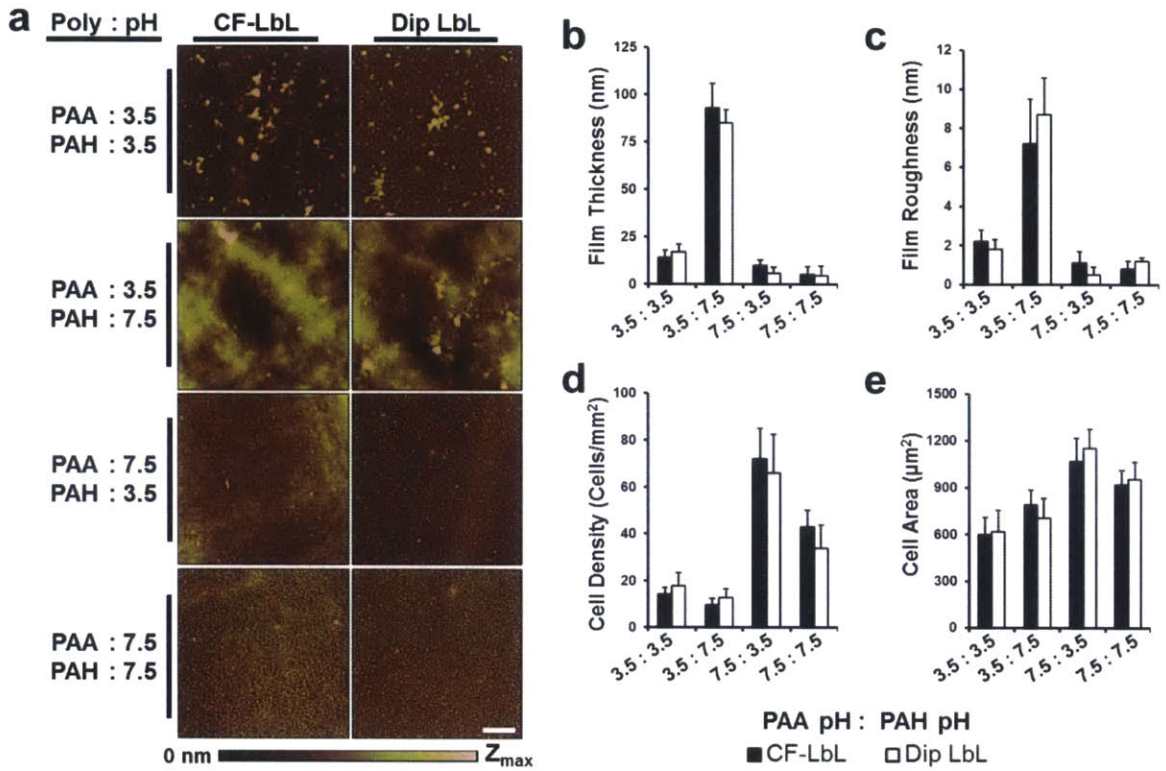

Figure 4-8 Comparison of $(PAA/PAH)_{10}$ films prepared *via* Dip LbL or CF-LbL techniques

(a) AFM micrographs showing the different topographies for each of the LbL films assembled. (b) Film thickness of the assemblies as measured by profilometry. (c) Film roughness as measured by AFM. (d) NIH-3T3 cell density after three days of growth on film coated glass. (e) Average cell spread area for a cell adhered to the film surface. Data shown as mean ± s.d.

4.3.6 Screening LbL Assemblies for DNA Delivery

Locally delivering nucleic acids from surfaces is a relatively simple and highly adaptable approach to alter nearby gene expression that creates significant opportunities in fields ranging from fundamental molecular biology to tissue engineering[23, 38, 39]. There are numerous factors that impact transfection of material, including: nucleic acid packaging, material release, endosomal escape, and if necessary nuclear transport. Due to this complexity, investigations into LbL systems for these applications face very substantial challenges.

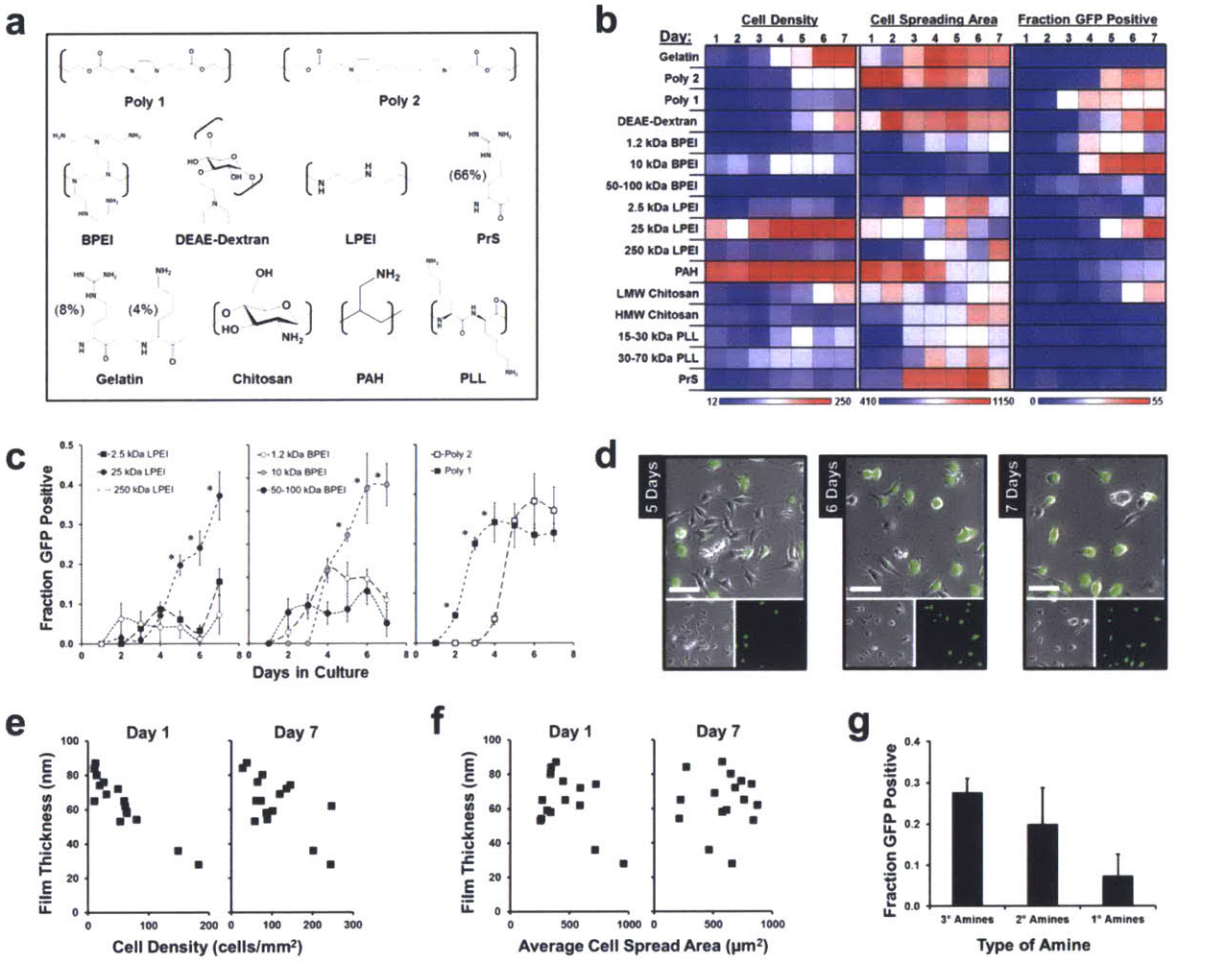

Figure 4-9 Polycation library screen of DNA transfection from LbL films

(a) Chemical structures of polycation repeat units. (b) Heat maps of cell density, cell spreading area, and fraction GFP of DNA transfection of cells cultured on films. (c) Transfection from films containing similar polycations of differing molecular weights. (d) Cells on $(BPEI/pEGFP)_{10}$ film cultured within the microchannels after 5, 6, and 7 days of culture. Scale bar = 50 μm. (e) Effect of film thickness on cell density at one and seven days in culture. (f) Effect of film thickness on average cell spread area. (g) Effect of amine type on DNA transfection after one week in culture. Polycations that contained tertiary amines (3°) achieved significantly higher transfection levels than those that contained only primary amines (1°). Data shown as mean ± s.d.

Previously, research groups have described LbL systems capable of the local delivery of DNA from coated surfaces.[40, 41] These reports provide a great deal of promise for future applications of LbL in combination with medical devices[42, 43] and as DNA vaccines depots.[11, 44] At this time, however, investigations can only reasonably study individual LbL systems, often assembled using only one set of assembly conditions.[40, 41] To demonstrate the use of the CF-LbL assembly for screening film libraries we decided to apply the technique to investigate a focused group of candidate films consisting of a broad range of polycations identified from literature that have been used for DNA transfection **(Figure 4-9a)**. We assembled bilayer films of the polycations with a DNA plasmid for green fluorescent protein (GFP). HeLa cells were seeded directly onto the films within the device and were monitored for GFP expression, cell density, and average cell spread area every day for seven days in culture **(Figure 4-9 b-d).**

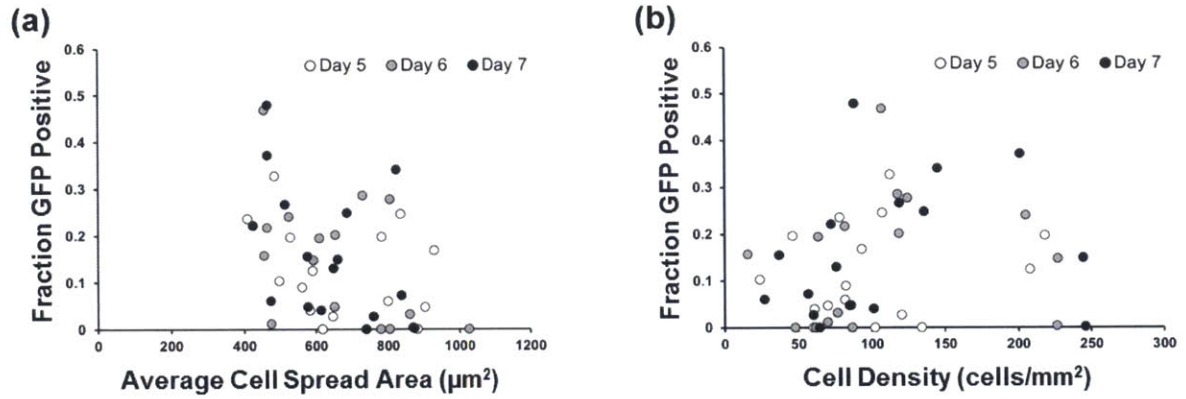

Figure 4-10 Cell spread area and cell number compared to transfection efficacy

(a) Fraction GFP positive cells graphed with the corresponding average cell spread area. No trend can be seen. (b) Fraction GFP positive cells versus the number of cells on a given surface. No trend in transfection was seen for either criteria.

There was no correlation found between cell spread area and transfection efficiency, suggesting that how well the cells engaged with the surface had little impact on delivery of the film material. We were fascinated by this finding as it had been suggested that the more the cell engaged with the surface the greater the likelihood of its transfection, this however was not

observed. It was also a novel finding that the cell density, another sign of the relative biocompatibility of the surface, made no significant impact on GFP expression. These findings may suggest that the cell response to a surface has little impact on transfection from these LbL films or that the relative changes in cell response to these surfaces are not on the order that would force significant changes in behaviors related to transfection.

4.3.6 Scale-Up of LbL Assembly for DNA Delivery

From the screen of 16 films, we found a diversity of cellular response and transfection efficacies that show some interesting trends. Cell density, measured as the number of live cells per square millimeter, was highest on the $(PAH/pEGFP)_{10}$ film, which reached near confluence after only three days of culture. The only two other films to reach confluence within one week were $(Gelatin/pEGFP)_{10}$ and $(LPEI\ 25kDa/pEGFP)_{10}$. Initial cell seeding density was observed to correlate inversely to film thickness, which was largely maintained after one week in culture (**Figure 4-9e**). Film thickness however was not observed to correlate with cell spreading, similar to what was observed for the PAA/PAH systems (**Figure 4-9f**). The primary goal of screening a diverse group of polycations was to elucidate characteristics that correlate with transfection efficacy. The major trait that was seen to correlate with transfection was the type of amine, where films that consisted of polycations which contained tertiary amines achieved the highest average transfection efficacy, while those with only primary amines achieved the lowest on average (**Figure 4-9g**).

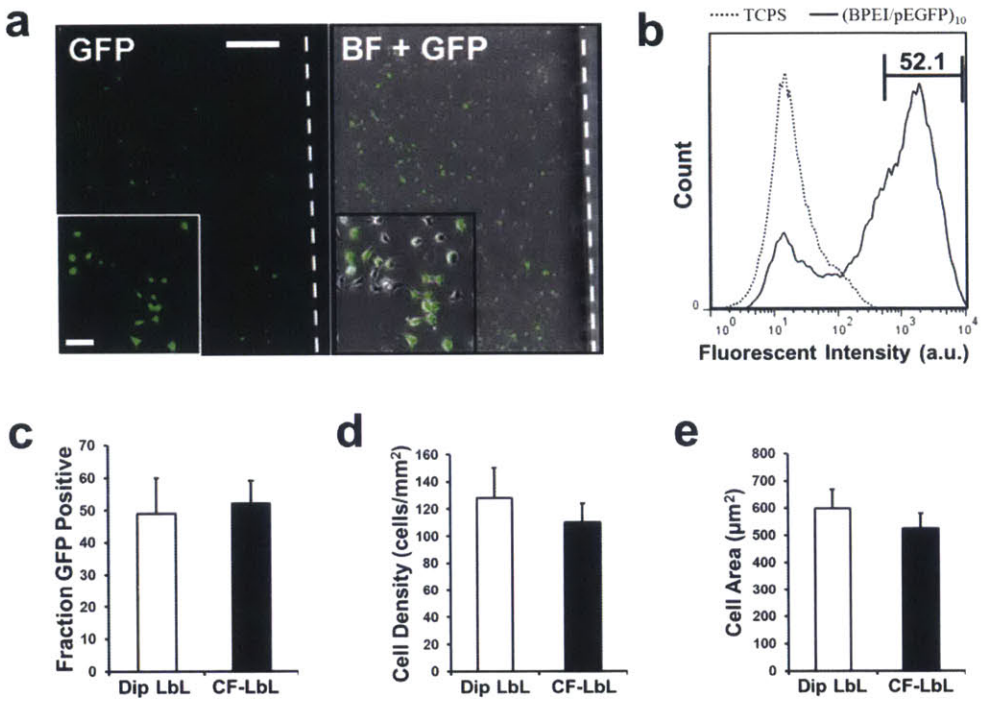

Figure 4-11 Large-scale reproduction of best performing architecture shows similar behavior

(a) Analysis of transfection of HeLa cells cultured on $(BPEI/pEGFP)_{10}$ coated microscope slides. BF = Bright Field. Scale bar = 500 μm, inset scale bar = 50 μm. (b) Flow cytometry analysis of GFP expression for HeLa cells cultured on $(BPEI/pEGFP)_{10}$ for one week. (c) Fraction GFP positive HeLa cells cultured on either Dip LbL or CF-LbL coated glass after one week. (d) Average cell density on film coated substrates after one week in culture. (e) Average cell spread area for HeLa cells seeded on films prepared by either Dip LbL or CF-LbL methods. Data shown as mean ± S.D.

The best performing film architecture from this screen was determined to be $(BPEI/pEGFP)_{10}$ as it reached the highest fraction of GFP expressing cells with relatively high cell density. BPEI, which presents primary, secondary and tertiary amines, is known for its ability to both effectively complex nucleic acids, and to buffer at endosomal pH, which can cause endosomal osmolytic swelling and subsequent nucleic acid release to the cytosol[45-47]. This film was evaluated on a larger scale by assembling it on microscope slides. HeLa cells

were cultured on these large LbL coated slides for seven days **(Figure 4-11 a-b)**. Cell behavior and GFP expression was then analyzed. The fraction of GFP expressing cells as well as average cell density and average cell spread area on the larger film closely resembled that of cells cultured within the CF-LbL microchannels **(Figure 4-11 c-e)**. Together these data provide strong support for the capability of CF-LbL to investigate LbL films for use in applications on larger scales. The films assembled by CF-LbL within microchannels performed identically to their counterparts assembled by Dip LbL on a scale about a thousand times larger in surface area.

4.4 Conclusions

In this work we have described a method for the high-throughput assembly and screening of LbL films. We used this method for three demonstrations: (1) a study on the effect of pH on weak polyelectrolytes in LbL film assembly, (2) the in-situ examination of cell adhesion and viability on LbL assemblies, and (3) the investigation of a library of films for DNA transfection from surfaces. This method is paired with a simple modular microfluidic device that can be used for the simultaneous assembly of hundreds of independent films or for smaller more focused bench top investigations. The device is fabricated *via* common soft lithography techniques and when assembled provides a sterile environment where sensitive biological analysis can be performed on each film independently.

The potential applications of LbL film assemblies are incredibly diverse and growing. Here we have provided a method using a simple microfluidic device that makes possible the high-throughput screening of LbL assemblies while significantly reducing the amount of material used. This method represents a simple yet significant advance for the investigation of LbL films while expanding the ability to study these coatings to laboratories that previously could not. We anticipate that this approach could have enormous impact in a broad range of fields that include developing drug delivery systems and creating biological interfaces.

4.5 References

1. Decher, G., Fuzzy Nanoassemblies: Toward Layered Polymeric Multicomposites. *Science* **1997**, *277*, 1232-1237.

2. Quinn, J. F.; Johnston, A. P.; Such, G. K.; Zelikin, A. N.; Caruso, F., Next Generation, Sequentially Assembled Ultrathin Films: Beyond Electrostatics. *Chem. Soc. Rev.* **2007**, *36*, 707-718.

3. Lavalle, P.; Voegel, J. C.; Vautier, D.; Senger, B.; Schaaf, P.; Ball, V., Dynamic Aspects of Films Prepared by a Sequential Deposition of Species: Perspectives for Smart and Responsive Materials. *Adv. Mater.* **2011**, *23*, 1191-1221.

4. Schlenoff, J. B., Retrospective on the Future of Polyelectrolyte Multilayers. *Langmuir* **2009**, *25*, 14007-14010.

5. Hammond, P. T., Engineering Materials Layer-by-Layer: Challenges and Opportunities in Multilayer Assembly. *AIChE J* **2011**, *57*, 2928-2940.

6. Hammond, P. T., Building Biomedical Materials Layer-by-Layer. *Mater. Today* **2012**, *15*, 196-206.

7. Sukhishvili, S. A., Responsive Polymer Films and Capsules via Layer-by-Layer Assembly. *Curr. Opin. Colloid. In.* **2005**, *10*, 37-44.

8. Lee, J. A.; Krogman, K. C.; Ma, M. L.; Hill, R. M.; Hammond, P. T.; Rutledge, G. C., Highly Reactive Multilayer-Assembled TiO2 Coating on Electrospun Polymer Nanofibers. *Adv. Mater.* **2009**, *21*, 1252-1256.

9. Shah, N. J.; Hyder, M. N.; Moskowitz, J. S.; Quadir, M. A.; Morton, S. W.; Seeherman, H. J.; Padera, R. F.; Spector, M.; Hammond, P. T., Surface-Mediated Bone Tissue Morphogenesis from Tunable Nanolayered Implant Coatings. *Sci. Transl. Med.* **2013**, *5*.191.

10. Facca, S.; Cortez, C.; Mendoza-Palomares, C.; Messadeq, N.; Dierich, A.; Johnston, A. P. R.; Mainard, D.; Voegel, J. C.; Caruso, F.; Benkirane-Jessel, N., Active Multilayered Capsules for *in vivo* Bone Formation. *Proc. Natl. Acad. Sci. U. S. A.* **2010**, *107*, 3406-3411.

11. DeMuth, P. C.; Min, Y.; Huang, B.; Kramer, J. A.; Miller, A. D.; Barouch, D. H.; Hammond, P. T.; Irvine, D. J., Polymer Multilayer Tattooing for Enhanced DNA Vaccination. *Nat. Mater.* **2013**, *12*, 367-376.

12. Jan, E.; Hendricks, J. L.; Husaini, V.; Richardson-Burns, S. M.; Sereno, A.; Martin, D. C.; Kotov, N. A., Layered Carbon Nanotube-Polyelectrolyte Electrodes Outperform Traditional Neural Interface Materials. *Nano Lett.* **2009**, *9*, 4012-4018.

13. Finnemore, A.; Cunha, P.; Shean, T.; Vignolini, S.; Guldin, S.; Oyen, M.; Steiner, U., Biomimetic Layer-by-Layer Assembly of Artificial Nacre. *Nat. Commun.* **2012**, *3*. 966.

14. Krogman, K. C.; Zacharia, N. S.; Schroeder, S.; Hammond, P. T., Automated Process for Improved Uniformity and Versatility of Layer-by-Layer Deposition. *Langmuir* **2007**, *23*, 3137-3141.

15. Izquierdo, A.; Ono, S. S.; Voegel, J. C.; Schaaf, P.; Decher, G., Dipping Versus Spraying: Exploring the Deposition Conditions for Speeding up Layer-by-Layer Assembly. *Langmuir* **2005**, *21*, 7558-7567.

16. Jiang, C.; Markutsya, S.; Tsukruk, V. V., Collective and Individual Plasmon Resonances in Nanoparticle Films Obtained by Spin-Assisted Layer-by-Layer Assembly. *Langmuir* **2004**, *20*, 882-890.

17. Chan, E. P.; Lee, J. H.; Chung, J. Y.; Stafford, C. M., An Automated Spin-assisted Approach for Molecular Layer-by-Layer Assembly of Crosslinked Polymer Thin Films. *Rev. of sci. instruM.* **2012**, *83*, 114102.

18. Cho, J.; Char, K., Effect of Layer Integrity of Spin Self-Assembled Multilayer Films on Surface Wettability. *Langmuir* **2004**, *20*, 4011-4016.

19. Garza, J. M.; Schaaf, P.; Muller, S.; Ball, V.; Stoltz, J. F.; Voegel, J. C.; Lavalle, P., Multicompartment Films Made of Alternate Polyelectrolyte Multilayers of Exponential andLinear Growth. *Langmuir* **2004**, *20*, 7298-7302.

20. Thompson, M. T.; Berg, M. C.; Tobias, I. S.; Lichter, J. A.; Rubner, M. F.; Van Vliet, K. J., Biochemical Functionalization of Polymeric Cell Substrata Can Alter Mechanical Compliance. *Biomacromolecules* **2006**, *7*, 1990-1995.

21. Zhu, Z.; Sukhishvili, S. A., Temperature-Induced Swelling and Small Molecule Release with Hydrogen-Bonded Multilayers of Block Copolymer Micelles. *ACS Nano* **2009**, *3*, 3595-3605.

22. Min, J.; Braatz, R. D.; Hammond, P. T., Tunable Staged Release of Therapeutics from Layer-by-Layer Coatings with Clay Interlayer Barrier. *Biomaterials* **2014**, *35*, 2507-2517.

23. Castleberry, S.; Wang, M.; Hammond, P. T., Nanolayered siRNA Dressing for Sustained Localized Knockdown. *ACS Nano* **2013**, *7*, 5251-5261.

24. Wood, K. C.; Chuang, H. F.; Batten, R. D.; Lynn, D. M.; Hammond, P. T., Controlling Interlayer Diffusion to Achieve Sustained, Multiagent Delivery from Layer-by-Layer Thin Films. *Proc. Natl. Acad. Sci. U. S. A.* **2006**, *103*, 10207-10212.

25. Unger, M. A.; Chou, H. P.; Thorsen, T.; Scherer, A.; Quake, S. R., Monolithic Microfabricated Valves and Pumps by Multilayer Soft Lithography. *Science* **2000**, *288*, 113-116.

26. Williams, C. M.; Mehta, G.; Peyton, S. R.; Zeiger, A. S.; Van Vliet, K. J.; Griffith, L. G., Autocrine-Controlled Formation and Function of Tissue-like Aggregates by Primary Hepatocytes in Micropatterned Hydrogel Arrays. *Tissue Eng. Part A* **2011**, *17*, 1055-68.

27. Yong, J.; Chen, F.; Yang, Q.; Zhang, D.; Bian, H.; Du, G.; Si, J.; Meng, X.; Hou, X., Controllable Adhesive Superhydrophobic Surfaces Based on PDMS Microwell Arrays. *Langmuir* **2013**, *29*, 3274-3279.

28. Chen, Q.; Wu, J.; Zhang, Y.; Lin, Z.; Lin, J. M., Targeted Isolation and Analysis of Single Tumor Cells with Aptamer-Encoded Microwell Array on Microfluidic Device. *Lab Chip* **2012**, *12*, 5180-5185.

29. Zaretsky, I.; Polonsky, M.; Shifrut, E.; Reich-Zeliger, S.; Antebi, Y.; Aidelberg, G.; Waysbort, N.; Friedman, N., Monitoring the Dynamics of Primary T cell Activation and Differentiation Using Long Term Live Cell Imaging in Microwell Arrays. *Lab Chip* **2012**, *12*, 5007-5015.

30. Shiratori, S. S.; Rubner, M. F., PH-Dependent Thickness Behavior of Sequentially Adsorbed Layers of Weak Polyelectrolytes. *Macromolecules* **2000**, *33*, 4213-4219.

31. Yoo. D.; Shiratori, S.; Rubner, M. F., Controlling Bilayer Composition and Surface Wettability of Sequentially Adsorbed Multilayers of Weak Polyelectrolytes *Macromolecules* **1998**, *31*, 4309-4318.

32. Aggarwal, N.; Groth, T., Multilayer Films by Blending Heparin with Semisynthetic Cellulose Sulfates: Physico-Chemical Characterization and Cell Responses. *J Biomed. Mater. Res. A* **2014**, DOI: 10.1002/jbm.a.35095.

33. Gribova, V.; Gauthier-Rouviere, C.; Albiges-Rizo, C.; Auzely-Velty, R.; Picart, C., Effect of RGD Functionalization and Stiffness Modulation of Polyelectrolyte Multilayer Films on Muscle Cell Differentiation. *Acta Biomaterialia* **2013**, *9*, 6468-6480.

34. Wilson, J. T.; Cui, W.; Kozlovskaya, V.; Kharlampieva, E.; Pan, D.; Qu, Z.; Krishnamurthy, V. R.; Mets, J.; Kumar, V.; Wen, J.; *et al.*, Cell Surface Engineering with Polyelectrolyte Multilayer Thin Films. *J. Am. Chem. Soc.* **2011**, *133*, 7054-7064.

35. Wittmer, C. R.; Phelps, J. A.; Saltzman, W. M.; Van Tassel, P. R., Fibronectin Terminated Multilayer Films: Protein Adsorption and Cell Attachment Studies. *Biomaterials* **2007**, *28*, 851-860.

36. Boura, C.; Muller, S.; Vautier, D.; Dumas, D.; Schaaf, P.; Claude Voegel, J.; Francois Stoltz, J.; Menu, P., Endothelial Cell-Interactions with Polyelectrolyte Multilayer Films. *Biomaterials* **2005**, *26*, 4568-4575.

37. Thompson, M. T.; Berg, M. C.; Tobias, I. S.; Rubner, M. F.; Van Vliet, K. J., Tuning Compliance of Nanoscale Polyelectrolyte Multilayers to Modulate Cell Adhesion. *Biomaterials* **2005**, *26*, 6836-6845.

38. Kharlampieva, E.; Kozlovskaya, V.; Sukhishvili, S. A., Layer-by-Layer Hydrogen-Bonded Polymer Films: From Fundamentals to Applications. *Adv. Mater.* **2009**, *21*, 3053-3065.

39. Tang, Z. Y.; Wang, Y.; Podsiadlo, P.; Kotov, N. A., Biomedical applications of layer-by-layer assembly: From biomimetics to tissue engineering. *Adv. Mater.* **2006**, *18*, 3203-3224.

40. Jewell, C. M.; Lynn, D. M., Surface-Mediated Delivery of DNA: Cationic Polymers Take Charge. *Curr. Opin. Colloid In.* **2008**, *13*, 395-402.

41. Jewell, C. M.; Zhang, J. T.; Fredin, N. J.; Lynn, D. M., Multilayered Polyelectrolyte Films Promote the Direct and Localized Delivery of DNA to Cells. *J Control. Release* **2005**, *106*, 214-223.

42. Saurer, E. M.; Jewell, C. M.; Roenneburg, D. A.; Bechler, S. L.; Torrealba, J. R.; Hacker, T. A.; Lynn, D. M., Polyelectrolyte Multilayers Promote Stent-Mediated Delivery of DNA to Vascular Tissue. *Biomacromolecules* **2013**, *14*, 1696-1704.

43. Bechler, S. L.; Si, Y.; Yu, Y.; Ren, J.; Liu, B.; Lynn, D. M., Reduction of Intimal Hyperplasia in Injured Rat Arteries Promoted by Catheter Balloons Coated with Polyelectrolyte Multilayers that Contain Plasmid DNA Encoding PKC Delta. *Biomaterials* **2013**, *34*, 226-236.

44. DeMuth, P. C.; Li, A. V.; Abbink, P.; Liu, J.; Li, H.; Stanley, K. A.; Smith, K. M.; Lavine, C. L.; Seaman, M. S.; Kramer, J. A.; *et al.*, Vaccine Delivery with Microneedle Skin Patches in Nonhuman Primates. *Nat Biotechnol.* **2013**, *31*, 1082-1085.

45. Akinc, A.; Thomas, M.; Klibanov, A. M.; Langer, R., Exploring Polyethylenimine-mediated DNA Transfection and the Proton Sponge Hypothesis. *J. Gene Med.* **2005**, 7, 657-663.

46. Whitehead, K. A.; Langer, R.; Anderson, D. G., Knocking down barriers: advances in siRNA delivery. *Nat. Rev. Drug Discov.* **2009**, *8*, 129-138.

47. Gavrilov, K.; Saltzman, W. M., Therapeutic siRNA: principles, challenges, and strategies. *Yale J. Biol. Med.* **2012**, *85*, 187-200.

48. Lynn, D. M.; Langer, R., Degradable poly(beta-amino esters): Synthesis, Characterization, and Self-assembly with Plasmid DNA. *J. Am. Chem. Soc.* **2000**, *122*, 10761-10768.

49. Xia, Y. N.; Whitesides, G. M., Soft Lithography. *Annu. Rev. Mater. Sci.* **1998**, *28*, 153-184.

50. Mata, A.; Fleischman, A. J.; Roy, S., Fabrication of Multi-layer SU-8 Microstructures. *J Micromech. Microeng.* **2006**, *16*, 276-284.

Chapter 5
Self-Assembled Wound Dressings Silence MMP-9 and Improve Diabetic Wound Healing In Vivo

5.1 Introduction

In Chapter 2 we introduced our preliminary work in developing LbL films for the controlled delivery of siRNA. This work along with that described in Chapter 3 helped us to better define our goals and to identify experimental space for optimization. Using the technology described in Chapter 4 we then worked in combination with more common LbL assembly techniques to screen LbL assemblies for our desired characteristics. In this screen we identified a platform LbL film that allowed us a great deal of flexibility in tuning delivery and knockdown which we describe in this chapter. Here in Chapter 5 we present our *in vivo* investigation into a hierarchical LbL film architecture using a degradable polycation undercoating with an siRNA encapsulating top layer for controlled local delivery of siRNA to treat the chronic upregulation of the extracellular matrix protease MMP-9 in diabetic mouse wounds.

Controlled delivery of short interfering RNA (siRNA) from implants, coatings, and medical devices provides a powerful new approach to modulate local tissue response in a broad range of applications. One such application is in chronic wound healing, where the current clinical standards leave tens of thousands of Americans each year to amputation. In this study, we used nano-layer assembly to create ultra-thin polymer coatings for sustained local siRNA delivery into chronic wounds with tunable release characteristics to improve tissue repair. Using a mouse model of diabetic ulcerative healing we demonstrate that silencing the overexpressed protease MMP-9 within the ulcer improves new tissue formation and subsequent wound closure.

The direct local delivery of short interfering RNA (siRNA) to tissues may present solutions to several complex medical conditions. In particular, chronic wound healing is a serious and painful complication of diabetes mellitus (DM) affecting as many as one in four of these patients with a three year recurrence rate of more than 50% and leaving over 70,000 patients in the United States alone facing amputation. Here we describe the use of siRNA delivered locally into the diabetic ulcer directly and in a sustained fashion to knockdown a chronically upregulated extracellular matrix protease, matrix metalloproteinase-9 (MMP-9), to improve wound healing. A self-assembled polymer thin film coating, when applied conformally to commercially available nylon bandages, sustains the delivery of small interfering RNA (siRNA) into the wound bed while maintaining activity and facilitating transfection. This approach reduces protein expression and enzyme activity within the wound for over two weeks, leading to a significant improvement in chronic wound healing.

Impaired wound healing is a critical concern in the care of diabetic patients. Every year there are more than 750,000 new cases of diabetic foot ulcers (DFUs) in the United States, leading to over 70,000 lower limb amputations[1-3]. In healthy patients, wound healing is a highly orchestrated process of overlapping phases: hemostasis, inflammation, tissue formation, and tissue remodeling[4] which we described in detail in chapter 1 of this thesis. In ulcerative wound healing this process is interrupted and the wound persists in an inflamed state for weeks to months that in many cases never fully resolves.

The pathology of the diabetic ulcer results from this chronic inflammation, due in part to the overexpression of extracellular matrix (ECM) proteases in the wound bed[5-7]. As a result of this overexpression of proteases, ECM accumulation within the DFU is dramatically reduced, impeding epithelial closure of the wound and significantly increasing the risk of infection[8]. Many of the current pharmacologic therapies for DFU have tried to address this issue through either the delivery of super-physiological concentrations of recombinant growth factors or application of lab-grown dermal substitutes[9-12]; however, these have proven to be inconsistent, difficult to maintain, and have led in some cases to serious undesired side effects[9].

Over the past two decades numerous groups have correlated overexpression of matrix metalloproteinase-9 (MMP-9) within chronic ulcers to poor wound healing outcomes in diabetic patients[13-16]. MMP-9 acts as the primary gelatinase expressed within the dermis after wounding

and it plays a crucial role in ECM degradation and tissue reorganization during the healing process[17-21]. However, overexpression impairs the formation of granulation tissue, the early connective tissue that fills a wound, as well as inactivating important growth factors that are critical to the process of wound healing[22-24].

These and other complications of MMP overexpression have spurred substantial research into developing MMP inhibitors. These efforts to develop small molecule inhibitors have been hampered by a number of complicating issues including low specificity, poor bioavailability, and serious musculoskeletal side effects[25-28]. In order to address these issues, we hypothesized that using RNA interference (RNAi) locally to reduce MMP-9 expression in the wound would be an effective approach for increasing ECM accumulation within the wound bed and subsequently improving wound healing.

RNAi using small interfering RNA (siRNA) technology is a promising approach for the sequence-specific targeting of mRNAs for destruction, enabling the knockdown of virtually any expressed protein[29-31]. While the potential applications of RNAi in medicine are numerous, *in vivo* delivery of siRNA remains a major obstacle due to rapid enzymatic degradation of siRNAs and clearance *via* the hepatic and renal systems[32-34]. Local delivery circumvents many of the challenges of delivery, but siRNA must still be protected from enzymatic degradation and effectively enter target cells within the tissues of interest. Only a few systems have been developed for local siRNA delivery; those that have rely on bulky hydrogel formulations that must be injected directly into tissues[35] or re-purposed nanoparticle solutions that must be applied multiple times to achieve efficacy[36]. Neither of these approaches has been demonstrated to treat a known medical condition (i.e., pathologic dysregulation) within tissues.

Furthermore, there are unique challenges that are still to be met in this new area, including the ability to easily combine siRNA delivery and release with existing medical technologies and platforms. Layer-by-Layer (LbL) technology has been demonstrated in a myriad of biomedical applications for delivery from a broad range of material surfaces, including stainless steel and degradable polymer matrices.[37, 38] We have previously demonstrated that LbL incorporation and delivery of siRNA can achieve significant and sustained knockdown of reporter genes *in vitro*[39], although the ability to translate these results to a more complex environment *in vivo* remained unknown. Therefore, developing this technology to effectively

deliver siRNA to a localized area *in vivo* using a meaningful therapeutic gene target presents a significant advancement for the treatment of site-specific disorders, including DFUs as well as cardiovascular diseases, cancers, and transplant rejection.

Here we report the use of LbL to achieve significant knockdown of a target gene within a highly proteolytic wound bed, with the effects sustained for at least two weeks. Using a commercially available nylon bandage as a substrate, we show that self-assembled nanometer-scale coatings can incorporate and release therapeutically relevant quantities of siRNA in a controlled fashion to yield rapid chronic wound closure. This electrostatic assembly not only protects the siRNA from degradation, its release leads to *in situ* polyplex formation that promotes uptake of the material[40, 41]. In the end, this work establishes a method for directly releasing siRNA into wound beds in a sustained manner that achieves sufficient knockdown to address the dysregulation associated with chronic wounds. The modularity of the system and the ability to apply it directly to tissues further suggests that analogous LbL siRNA release systems could be used in a similar fashion to address other types of wound dysregulation. These findings also provide support for further investigations into the role of MMP-9 overexpression in the pathology of chronic diabetic ulcers.

5.2 Material and Methods

5.2.1 Materials

Poly 2 (20 kDa) was synthesized as previously reported. Chitosan (15 kDa) and dextran sulfate (500 kDa) were purchased from Sigma Aldrich company (Manassas, VA). SiRNA sequences were synthesized by Dharmacon (Lafayette, CO). Woven nylon bandages, Tegaderm™ (3M), were purchased through Cardinal Health (Newark, NJ). Phosphate-buffered saline (PBS, 10x), Advanced-MEM, fetal bovine serum, antibiotic-antimycotic solution, and 100 mM L-Glutamine solution were purchased from Invitrogen (Carlsbad, CA). NIH-3T3, HeLa, and MDA-MB-231 cells were purchased from Cell Biolabs (San Diego, CA). All antibodies were purchased from Abcam (Cambridge, MA)

5.2.2 Layer-by-layer film preparation

Films were deposited on oxygen plasma treated bandages. Bandages were cleaned in ethanol and then in RNase free UltraPure™ water (Life Technologies) prior to plasma treatment.

Oxygen plasma treatment was performed for 3 minutes on high setting. Bandages were then immediately immersed in a solution of the polycation Poly 2 for a minimum of one hour. Assembly of LbL films was performed using a Carl Zeiss HMS-DS50 stainer. [Poly 2/DS] base layers were deposited through sequential polymer adsorption steps (2 mg ml^{-1}, pH 5.0) of 10 minutes. Between each polymer deposition step the bandages were washed twice in RNase free water (pH 5.0). Assembly of [CHI/siRNA] film was deposited similarly. Chitosan (1mg ml^{-1}, pH 5.0) was adsorbed for 10 minutes and siRNA (20 μg ml^{-1}, pH 5.0) was adsorbed for 15 minutes. All solutions were prepared in RNase free water, adjusted to a pH of 5.0.

Film growth was characterized for films built on silicon wafers by a Veeco Dektak 150 profilometer. Incorporation of fluorescently labeled siRNA into films built on nylon bandages was followed using a Nikon A1R Ultra-Fast Spectral Scanning confocal microscope. Total siRNA incorporation within films was measured by rapid dissolution in a 1M NaCl solution with vigorous agitation and quantified using a fluorescent plate reader. Release studies were performed in PBS (pH 7.4, 37°C). Release was quantified by fluorescence of the released labeled siRNA read using a fluorescent plate reader.

5.2.3 *In Vitro* LbL Bandage Evaluation

Cells were cultured in Advanced-MEM media with 5% FBS, 1% antibiotic-antimycotic, and 2mM L-glutamine. Cells were seeded at an initial density of 5,000 cells per well in a 48-well plate. After one day LbL coated bandages ($0.25cm^2$ sections) were placed in culture with the cells. The bandages either contained GFP-specific siRNA or a control siRNA sequence or were uncoated. Uncoated bandages were used as the control to test the cytotoxicity of the film. Mean cell fluorescence was measured by flow cytometry, using a BD FACSCalibur flow cytometer. Cell viability was quantified using AlamarBlue assay (Life Technologies). Analysis of GFP expression and cell viability were performed after 3, 5, and 7 days of treatment.

5.2.4 *In Vivo* siRNA Delivery

All animal studies were approved by the MIT Institutional Animal Care and Use Committee (IACUC). Animals were housed and cared for in the USDA-inspected MIT Animal Facility under federal, state, local, and NIH guidelines for animal care. Eight week diabetic (*db/db*) mice (BKS.Cg-Dock7^{m} +/+ Lepr^{db}/J) were purchased from Jackson Labs (Bar Harbor, ME). Daily blood glucose measurements were taken for all mice used. Mice were required to

maintain a blood glucose level in excess of 300mg dl^{-1} to be used for these studies. Three groups of mice were used: (1) MMP-9 siRNA bandage treated, (2) control siRNA bandage treated, and (3) uncoated bandage treated.

Each group had 10 mice total, 5 mice per time point. Hair was removed from the backs of mice using a depilatory cream under anesthesia at least one day prior to surgery. Surgeries were performed under anesthesia and pre-operative analgesic was given to all mice (0.1 mg kg^{-1} Buprenex). Two 6mm full-thickness wounds were excised from the dorsum of mice using a biopsy punch on either side of midline. Bandages were cut to the same size (6mm dia.) as the wound and placed on top of the wound. The bandages were then secured in place using an adherent Tegaderm. This securing bandage holds the test bandage in place as well as keeps cage material from entering the wound. Mice were sacrificed after one and two weeks of treatment. One wound from each mouse was used for histological analysis and one wound was used for RNA isolation and protein analysis.

5.2.5 Histology

Tissues were fixed in zinc fixative without formalin for 48 hours. The excised wounds were then embedded in paraffin and serially sectioned at 250μm levels throughout the wound. At each level an H&E slide was stained and used for 2-D reconstruction of the wound. Unstained slides were also taken for IHC, MT, and PS staining and analysis of the healing tissue. Data analysis was performed using Image J. Orientation of collagen fibers was analyzed using the Image J plugin Orientation J.

5.2.6 Tissue Processing

Isolation of RNA was performed using TRIzol as per the manufacturer's instructions. Synthesis of cDNA was done using iScript cDNA synthesis kit (Bio-Rad Laboratories) and analysis of expression was performed by qRT-PCR using iQ SYBR Green Supermix (Bio-Rad Laboratories) along with selected DNA primer pairs. All experiments were performed in triplicate using a LightCycler 480 (Roche). Relative gene expression was quantified relative to β-actin, a housekeeping gene, using the delta-delta Ct method.

Analysis of MMP-9 activity within wound tissues was performed as previously described[12]. Briefly, total protein concentration of tissue homogenates was measured using BCA

Protein Assay (Pierce Biotechnology) as per the manufacturer's instructions. The concentration of total protein was normalized between groups. MMP-9 activity was then measured using Sensolyte® Plus 520 MMP-9 Assay Kit (AnaSpec) as per the manufacturer's instructions. All experiments were performed in triplicate.

5.2.7 Statistics

Statistical analysis was performed between groups using Student's *t*-test and rectified by ANOVA for comparisons between multiple groups. Values are represented as mean ± s.d. A value of $p < 0.05$ was used to indicate statistical significance.

5.3 Results

5.3.1 Layer-by-Layer Film Characterization

Coatings for siRNA delivery were comprised of two independent film architectures arranged in a hierarchical fashion. In this way one film formed an undercoating, closest to the underlying substrate, and the second film a top coat lying over this undercoating. The first film assembled directly on the woven nylon substrate is a two-component bilayer film of poly(beta-aminoester) 2 (Poly2) and dextran sulfate (DS), referred to as $[\text{Poly 2/DS}]_x$ where x represents the number of architecture repeats. Poly 2 is a well-established hydrolytically degradable polycation that facilitates water-based erosion in multilayer films[42, 43]. This layer serves as a controlled release barrier, promoting the dissociation of the full film from the substrates surface over a prolonged period of time.

On top of this degradable undercoating an siRNA-containing LbL was film assembled using the polycation chitosan (Chi), reported in literature for its capability to complex with siRNA and facilitate cell uptake and delivery of nucleic acids, and siRNA that we refer to as $[\text{Chi/siRNA}]_y$ **(Figure 5-2 a-d)**. Here Y refers to the number of architecture repeats for this siRNA containing film. This film architecture was chosen from an initial broad investigation of LbL film assemblies; exhibiting a range of release profiles ranging from hours to weeks and varying *in vitro* efficacies, many of which were detailed in Chapter 2 of this thesis.

LbL coating were built on nylon Tegaderm® bandages. These bandages have a very regular structure designed to present the wound with a multitude of small pores to allow for wound exudate drainage but resisting cellular infiltration. We were interested to coat this material as it is used extensively in the dressing of ulcerative wounds and is placed in close contact with the wound surface. Coating the bandage required oxygen plasma treatment of the bandages for three minutes. This was observed to create minor changes in the bandages physical characteristics, however longer exposures lead to significant changes at the bandage margins. Coating of the bandages was performed using histological slide stainers specially modified with holder arms to secure the bandages during dipping. The coating as it was applied to the bandage was not observed to obscure the designed structure of the bandage. As seen in **Figure 5-1** the fibers of the bandage and the pore diameters remain the same. It is important to note however that the surface characteristics are changed, as the LbL film presents a very different material than the original nylon.

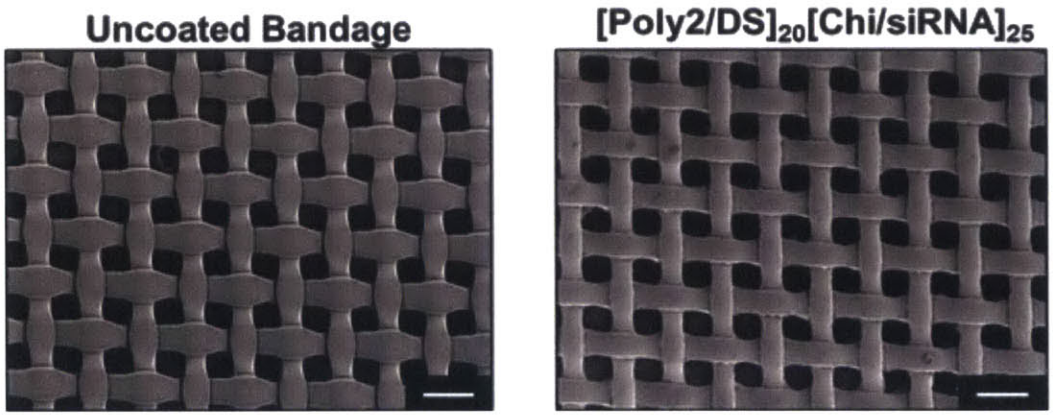

Figure 5-1 Scanning electron micrographs of Tegaderm® bandages
Uncoated bandage is as purchased from Cardinal Health. Oxygen plasma treatment and film assembly does not appreciably alter the structure of the bandage. Pores remain open and coating covers surface uniformly. Scale bar = 100μm.

Confocal imaging using a fluorescently labeled siRNA within the film shows high film uniformity with only minor defects **(Figure 5-2c)**. This image can be directly compared to the films described in Chapter 3 where CaP nanoparticles were used to incorporated labeled siRNA

into a similar construct. The film presented here is much more uniform, with no punctate localizations of fluorescence. Sections of the confocal imaging used to create the projected image demonstrate the uniformity of the coating along the full fiber length.

Assembled films were all sub-micron in thickness (up to approximately 320 nm) and incorporated siRNA at a rate of approximately 0.56 ± 0.11 $\mu g/cm^2$ per layer deposited, reaching 13.9 ± 0.8 $\mu g/cm^2$ after 25 bilayers **(Figure 5-2 e-f)**. The number of layers of the [Poly2/DS] film underlying the siRNA containing film was not observed to cause any significant change in the siRNA loading. Loading of siRNA was evaluated after 5, 10, 15, 20, and 25 layers had been assembled. This showed a near-linear relationship between film growth and siRNA incorporation. Film thickness was seen to accelerate slightly after 15 layers had been assembled; the film growth however was still fairly linear.

In vitro, the film-coated bandages sustain the release of siRNA for up to two weeks and this release can be readily tuned by varying the film architecture **(Figure 5-2 g-h)**. This finding is very exciting as it demonstrates the capability of such a platform for designed therapies. As we can control the amount of siRNA incorporated within the film architecture by changing the number of siRNA incorporating layers assembled, we can independently alter the release profile of that contained siRNA. This control over release is the first step to developing control over delivery.

Increasing the number of degradable layers of [Poly2/DS] under the siRNA incorporating layer created accelerated release profiles for the contained siRNA. When no degradable layers were assembled, the film was observed to release only a small fraction of the loaded siRNA within the first few hours to days of degradation, most likely due to rapid film changes brought on by the change in assembly media to degradation media. I contrast when the number of siRNA incorporating layers was increased the release profile was observed to only moderately change, extending release for approximately four more days between X=0 and X=20 films.

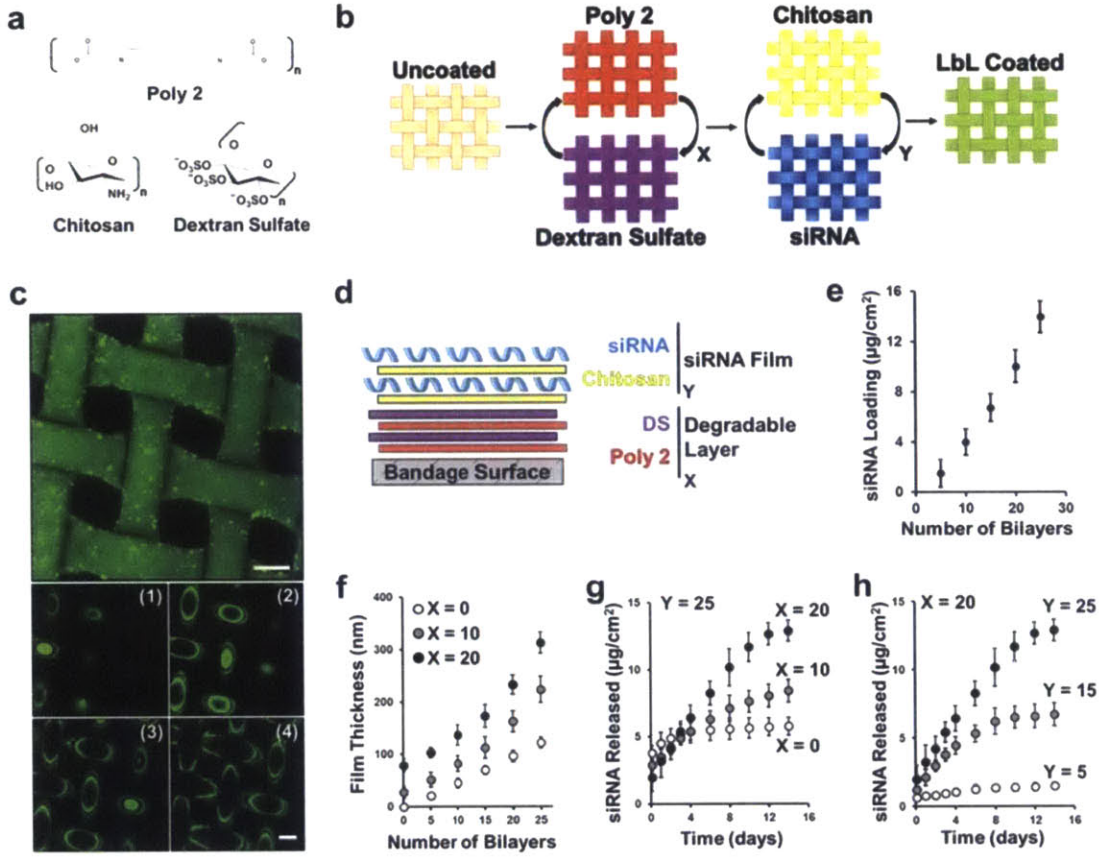

Figure 5-2 LbL coating for sustained release of siRNA

(a) Chemical structures of polymers used in this work. (b) Schematic of the hierarchical structure of LbL films into a single coating. The first (X) film is a hydrolytically degradable undercoating, while the second (Y) film contains the siRNA to be delivered. (c) Fluorescently labeled siRNA is shown to coat the entire woven structure of the nylon bandage. Image used to create the projection (1-4) show the conformal nature of the coating. (d) Side-on schematic of hierarchical LbL film architecture. (e) Incorporation of siRNA was observed to increase in a near-linear fashion over the tested range. (f) Film thickness was observed to increase with the number of layers assembled. Films were assembled on either X = 0, 10, or 20 degradable baselayers. All films tested were sub-micron thick with the thickest reaching nearly 325nm after 25 siRNA containing layers on top of 20 degradable baselayers. (g) Release of siRNA from coated bandages with varying numbers of degradable baselayers. Release was performed out to 14 days in PBS at 37°C. (h) Release of siRNA from coated bandages with varying numbers of

siRNA containing layers assembled on 20 degradable baselayers. All films achieved near complete siRNA release within the 14 day test period. Release performed in PBS at 37°C.

5.3.2 *In Vitro* Evaluation of Coated Bandages

Release of the incorporated siRNA was not observed to be effected by the siRNA sequence to be released. This is important to note, as most research assumes this point. We examined the release of two different siRNA sequences and here demonstrate that their differences were not enough to cause any changes in the release profile observed **(Figure 5-3)**.

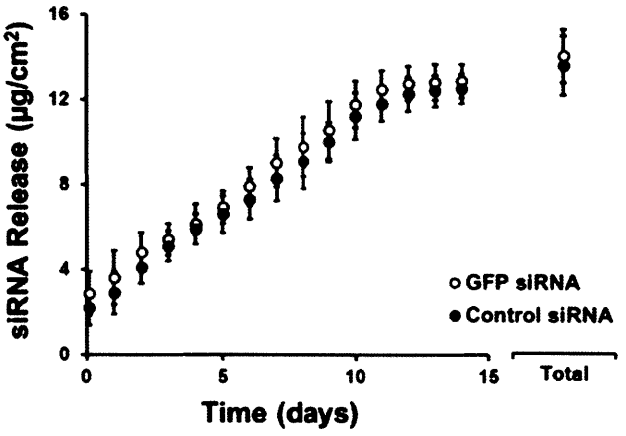

Figure 5-3 Release of siRNA from a coated surface is independent of siRNA sequence
The profile, total release, and total loading of siRNA is not affected significantly by the siRNA sequence. Data is shown as mean ± S.D., n = 3.

Several variations of the film architecture described above were investigated to determine the most effective film *in vitro* for more focused *in vivo* testing. NIH-3T3 cells expressing the reporter gene green fluorescent protein (GFP) were exposed in culture to film-coated bandages containing either a GFP-specific or control siRNA (siControl) sequence. The knockdown of GFP was assessed after five days of treatment by measurement of the mean cell fluorescence (MCF) using flow cytometry. The number of siRNA-containing layers was observed to

significantly impact the extent of GFP knockdown, with the greatest reduction in MCF being achieved by $[Poly2/DS]_{20}[CHI/siRNA]_{25}$ **(Figure 5-4a)**.

These experiments demonstrate the effect of the tuning capabilities of this platform which we observed in our early studies following siRNA release. This capability was used to achieve low to moderate to high levels of gene silencing by only making simple changes to the number of film architecture repeats used. In all cases, film-coated bandages exhibited minimal impact on cell viability relative to uncoated bandages, with all test groups maintaining better than 85 percent relative cell viability **(Figure 5-4b)**. Degradation studies indicated that the rate of release of film material from coated bandages depended on the presence and number of layers of the degradable undercoating. Here we observed that films with 20 degradable layers were able to achieve significant film degradation and material release from the coated surfaces and that this promoted release led to increased gene silencing **(Figure 5-4 a, d)**. Films consisting of 10 or fewer degradable layers however achieved less complete release of siRNA and reduced knockdown compared to the 20 layer films after five days.

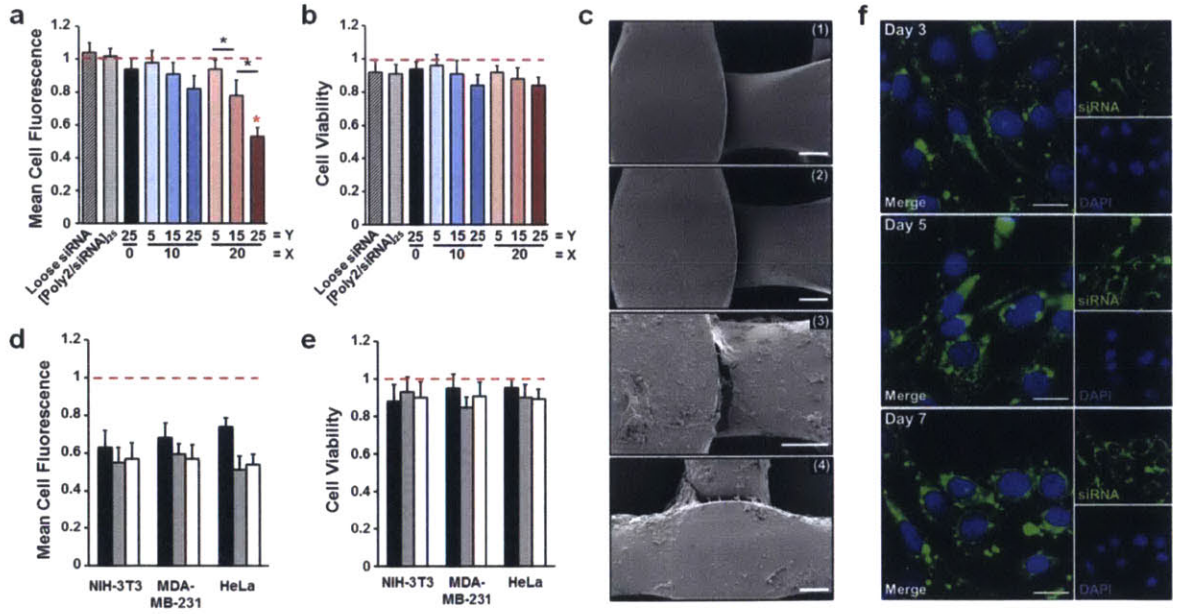

Figure 5-4 *In vitro* analysis of reporter gene knockdown and film behavior

(a) Analysis of mean cell fluorescence (MCF) as measured by flow cytometry after five days of treatment. Values are shown relative to MCF values for cells treated with bandages containing control siRNA (n = 3). (b) Impact of films on cell viability quantified by AlamarBlue assay, shown relative to measurements of cells treated with uncoated bandages(n = 3). (c) Scanning electron micrographs of LbL film coated bandages, (1) no coating, (2) $[Chi/siRNA]_{25}$, (3) $[Poly2/DS]_{10}[Chi/siRNA]_{25}$, (3) $[Poly2/DS]_{20}[Chi/siRNA]_{25}$ after five days degradation in culture with cells. Scale bar = 20μm. (d) Relative MCF of GFP expressing NIH-3T3, MDA-MB-231, and HeLa cell lines after 3, 5, and 7 days of treatment (n = 3). MCF is reduced in all cell lines tested, with the reduction maintained over the one-week test period. (e) Impact on cell viability is minimal for all cell lines tested over one week. (f) Uptake of fluorescently labeled siRNA by NIH-3T3 cells in culture with coated bandages after 3, 5, and 7 days respectively. Scale bar = 15μm. Data is shown as mean ± S.D., * $p<0.05$.

From this early screen of film variants we chose $[Poly2/DS]_{20}[CHI/siRNA]_{25}$ as the best architecture for further study due to the highest level of siRNA incorporation, release, and siRNA-specific gene knockdown. A time course study of knockdown for this architecture in three distinct cell lines expressing GFP found a significant reduction in expression after three days (GFP reduction ranging from 25-35%) **(Figure 5-4d)**. Furthermore, knockdown of GFP in all cell lines persisted throughout the one-week period of testing, with a reduction in GFP expression reaching 45-50% at day seven.

The impact of the film coating on the viability of three different cell lines was minimal, with all cultures maintaining greater than 80 percent viability compared to cells treated with uncoated substrates **(Figure 5-4e)**. The cellular uptake of released film material over time was followed using a fluorescently labeled siRNA for one week *in vitro* **(Figure 5-4f)**. The material was observed to accumulate in punctate localizations within the cell, and at extended times stain the entire cell body, indicating endosomal uptake and escape of siRNA to the cytosol **(Figure 5-5)**. This style of large aggregate release and slow intra-cellular accumulation agrees with our previous findings using CaP nanoparticle films where large multiple micron sized aggregates were observed to accumulate with cells in culture. In this work we see many similarly sized

large particulate containing concentrations of labeled siRNA after only a few days of treatment with the number of such particles increasing over time.

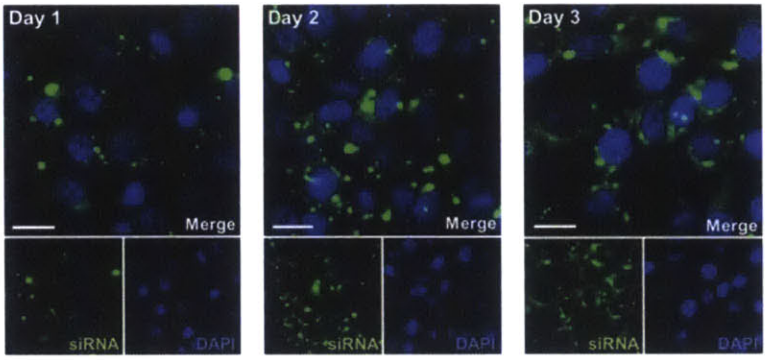

Figure 5-5 Cellular uptake of fluorescently labeled siRNA *in vitro*

Film coated bandages were placed in culture with NIH-3T3 cells and uptake evaluated after 1, 2, and 3 days in culture respectively. Film material is seen to release as film aggregates and slowly be taken up by cells. Scale bar = 15 μm.

5.3.3 *In Vivo* Silencing of MMP-9 in a Diabetic Mouse Model

With the success of the bandages *in vitro*, we next evaluated their efficacy *in vivo* using the *db/db* mouse, a genetically diabetic mouse model that has been well established for chronic ulcerative wound healing[44, 45]. The extracellular matrix protease MMP-9 is known to be overexpressed in this model in agreement with many human DFU patients, making it an ideal animal model for this *in vivo* investigation[46, 47].

Three treatment groups were established; mice either received siMMP-9 (1), siControl (2), or uncoated (3) bandages (two wounds per mouse, n = 5 mice per group per timepoint). The film with maximal knockdown and performance, $[Poly2/DS]_{20}[Chi/siRNA]_{25}$, was chosen for the mouse model studies. The application of the dressings *in vivo* followed the steps outlined in **Figure 5-6a**. Briefly, two 6mm diameter full-thickness wounds were excised from the dorsum of each mouse and a single bandage is placed over each wound site. The bandages were then secured in place using a commercially available adherent bandage. This adherent bandage was important both to secure the test bandage within the wound site and to also protect the wound

from external contaminants and reduce the risk of infection. This testing assembly operated very well for us in these studies, however they did have some notable drawbacks, most important of which was obscuring the wound margins grossly. This issue forced us to only be able to competently image the wound after the bandage was removed. It is unknown if any changes to the wounding or dressing protocols may help in this area, but it is necessary to note here for further consideration.

Wounds were digitally imaged after one and two weeks of treatment at necropsy **(Figure 5-6b)**. After one week, thick tissue bridges the wounds treated with siMMP-9 bandages in contrast to poor tissue growth in the wounds of the control groups. This tissue was dry to the touch compared to the wounds treated with control bandages, with the exudate in the bandage having a more opaque white hue than the translucent look of the controls. Tissue integration into any of the bandages at this point was minimal, however it was noted that the tissue formed underneath the siMMP-9 bandage had an imprint of the bandage design in it, suggesting that the tissue was in close contact to the bandage prior to removal.

After two weeks of treatment the siMMP-9 treated wounds were significantly smaller and appeared to have contracted, with substantial formation of tissue within the wound bed. This tissue had a red shade to it, compared to the light tan color of the control treated wounds. This red color is appropriate in healing wounds, signifying the increased vascularity in the granulation tissue. Of note when removing these bandages the siMMP-9 bandages were heavily infiltrated by the growing tissue, causing issues with bandage removal where the dressing had to be peeled from the granulation tissue, often disrupting the tissue. This behavior was not observed in the control wounds.

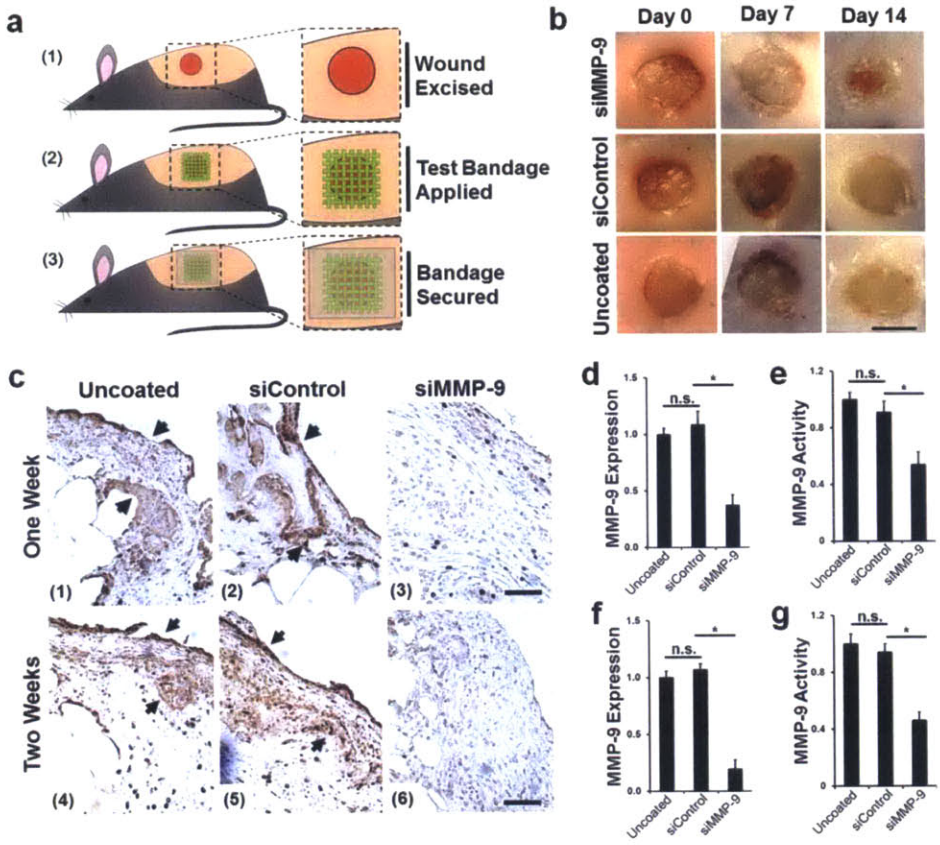

Figure 5-6 ***In vivo*** **application of MMP-9 siRNA coated bandages improves the gross appearance of wounds and reduces MMP-9 expression and activity within the treated wounds**

(a) Schematic of how bandages are applied to the full-thickness excisional wounds on the backs of mice. (1) A six mm diameter wound is excised from the back of the mouse (one on each side). (2) The test bandage is placed over the wound site. (3) The bandage is held in place by an adherent semi-clear bandage. (b) Digital imaging of wounds immediately following surgery (Day 0), and after 7 or 14 days of treatment. Scale bars, 5 mm. (c) IHC staining of MMP-9 within the wound edges of uncoated (1&4), siControl (2&5), and siMMP-9 (3&6) bandage treated wounds. Arrows highlight regions of intense staining. Scale bars, 50 μm. (d&f) Quantitative real time PCR analysis of MMP-9 expression relative to the housekeeping gene β-actin after one week (d) and two weeks (f) of treatment. (e&g) Activity of MMP-9 within wound homogenates as measured by Senso-lyte 520 MMP-9 activity kit after one week (e) and two weeks (g). Data is shown as mean ± S.D., * = $p<0.05$.

Immunohistochemical (IHC) staining for MMP-9 shows a significant reduction within the wounds of mice treated with siMMP-9 films compared to controls. Wounds from mice treated with either uncoated and siControl bandages show deep IHC staining at the wound edge. Wounds treated with siMMP-9 bandages on the other hand have only a diffuse low level of staining at the margins, indicating substantial changes in MMP-9 levels between these groups **(Figure 5-6c)**. MMP-9 staining demonstrated a significant change in the expression levels between the siMMP-9 treated wound and the control groups. MMP-9 staining was especially intense at the wound margins in the control animals, where increased staining could be observed at the edge of the epithelial tongue as well as in the granulation tissue.

The expression of MMP-9 within wounds treated with siMMP-9 bandages was reduced by nearly 60 percent compared to controls after one week, which increased to over 75 percent after two weeks **(Figure 5-6 d&g)**. This substantial change in MMP-9 expression supported the IHC findings we observed in MMP-9 staining. It is difficult to determine whether the sustained reduction in MMP-9 expression is due to continued gene knockdown or if early changes in MMP-9 expression caused a diversion away from the chronic ulcerative state and that this shift leads to the increased relative knockdown.

Similar to the expression analysis we found that the activity of MMP-9 within these wounds was significantly decreased after one week by 46.2% ± 9.1% which increased to 55.0% ± 5.8% after two weeks **(Figure 5-6 e&h)**. This reduced activity is a relative value comparing the average of siControl treated wounds to siMMP-9 treated. Taken together these data demonstrate a significant change in MMP-9 expression within the wound bed and point to a major change in the proteolytic microenvironment during the growth of new tissue.

Analysis of the digital wound imaging demonstrated the stark differences between the healing wounds of the three treatment groups. SiMMP-9 treated wounds were observed to significantly reduce their epithelial gap after one week by up to 64% increasing out to over 80% closure after two weeks. Control groups were observed to act similar to each other, lagging behind the siMMP-9 treated wounds. Use of digital imaging to approximate the epithelial gap

for wounds was performed using ImageJ analysis where the margins were identified based on increased opacity and color change from the wound center **(Figure 5-7)**.

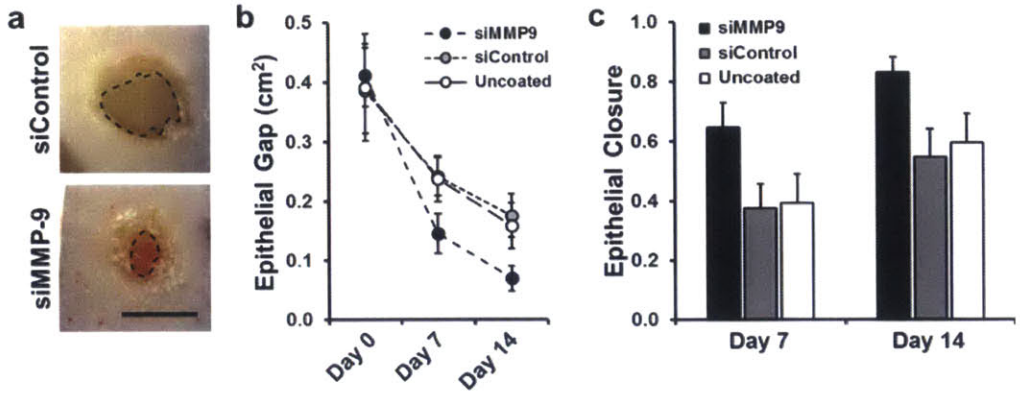

Figure 5-7 Analysis of digital wound imaging

(a) Representative digital imaging for treatment groups after 14 days of treatment. The dashed line represents the approximated epithelial margin as assessed. (b) Quantification of epithelial gap area at time of wounding and after 7 and 14 days of treatment. (c) The fraction closed for each wound after 7 or 14 days of treatment. This fraction is defined as one minus the ratio of the epithelial gap at a given timepoint to the epithelial gap at day of wounding. Data is shown as mean ± s.d., n = 6.

5.3.4 MMP-9 Knockdown Improves Wound Healing

Histological analysis of wound healing was performed using serially sectioned wounds to create a two-dimensional estimate of the epithelial and panniculus carnosus (PC) muscle closure compared to the initial wound. The structure and presentation of normal uninjured mouse dermis is shown in Figure xx. The structure is readily understood by observing the differential staining found in H&E stained slides, where the darker upper layer is the epidermis and the more light pink stained tissue is the dermis, containing the hair follicle and sweat gland structures. Masson's Trichrome (MTC) staining highlights cells and tightly compacted structures in red while the large collagen bundles stain blue. Here the epidermis is a light to deep red in color and the dermis, with its abundance of collagen, a sea of blue with interspersed red dots marking cell bodies. Picrosirius staining assists in the identification of collagen fibers based on their

thickness and natural birefringence. From this imaging orientation of the fibers can be ascertained and used for approximating tissue organization **(Figure 5-8)**.

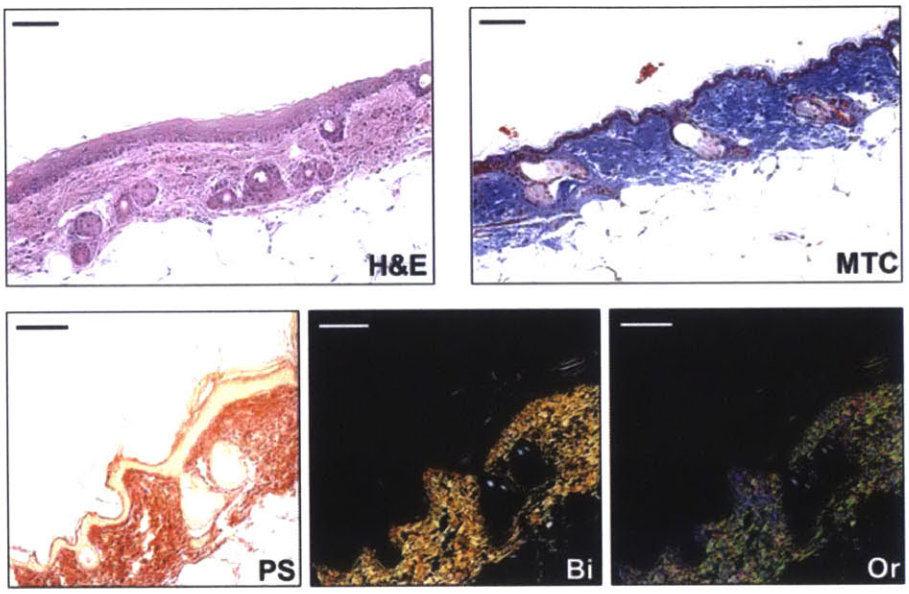

Figure 5-8 Histological analysis of uninjured mouse dermis

Hematoxylin and eosin (H&E), Masson's Trichrome (MTC), and Picrosirius Red (PS) stained sections. PS stained sections we also imaged using polarized light for evaluation of birefrengence (Bi) and then analyzed using OrientationJ™ software for fiber orientation (Or) evaluation. Scale bar = 100 μm.

Representative H&E stained full wound sections are shown in **Figure 5-9 a-b** for each of the treatment groups after one and two weeks respectively. The difference between the degree of epithelial closure and the formation of granulation tissue of the different treatment groups is very pronounced. This is especially true after two week of treatment, where substantial increases in healed tissue within the wound are apparent. As the role of MMP-9 within the injured dermis is to degrade the ECM, we anticipated that its reduction in the wound would promote the accumulation of granulation tissue within the wound bed. Quantification of the granulation tissue thickness in the center of the wound bed shows that wounds treated with MMP-9 siRNA

bandages are nearly twice as thick as controls after one week, which increases to three-fold after two weeks **(Figure 5-9c)**.

The granulation tissue functions as a scaffold for epithelial migration across a wound as well as a substrate for contractile forces to close the wound. We hypothesize that this increase in granulation tissue is then the reason why wounds treated with siMMP-9 bandages exhibit significantly more advanced re-epithelialization and contraction as compared to controls **(Figure 5-9d)**. Important to note here as well is the fact that the granulation tissue formed within wounds treated with siMMP-9 bandages is far more cellular and better vascularized than that of the controls **(Figure 5-9 e-f)**. After two weeks, siMMP-9 wounds contain nearly three times the number of vessels per viewing field as controls, with many vessels apparent in the center of the wound which are not seen in control treated wounds.

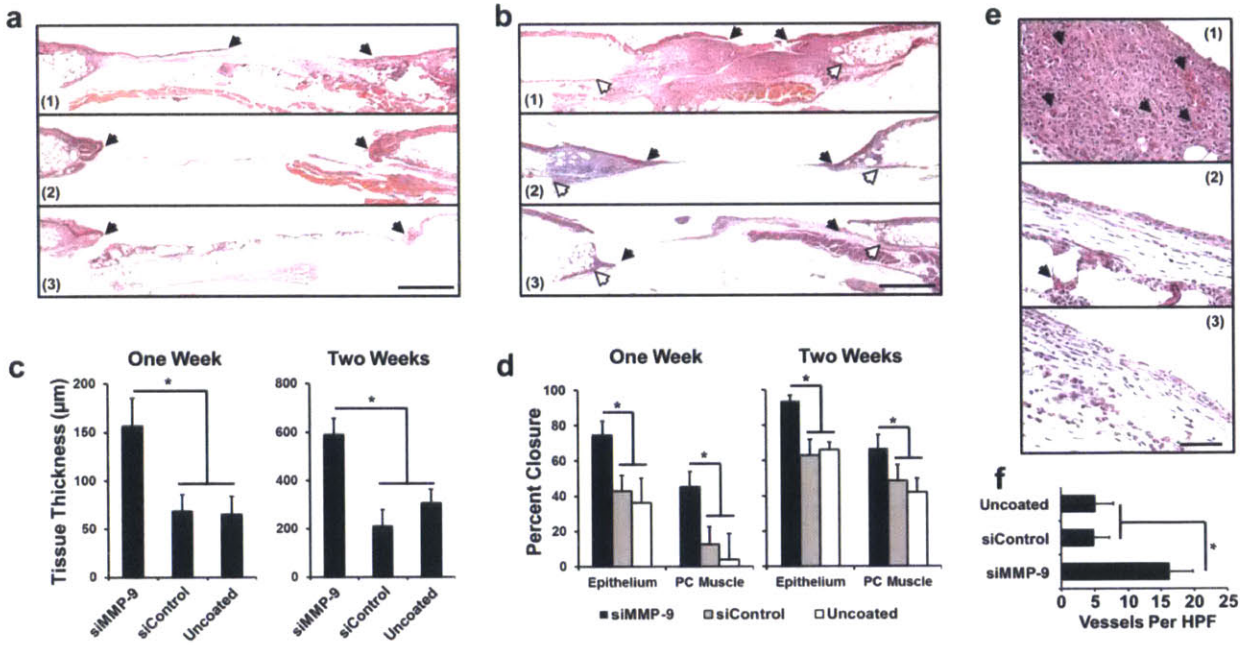

Figure 5-9 Hematoxylin and eosin histological analysis of wound healing

(a-b) H&E stained wound sections after one week (a) and two weeks (b) of treatment with siMMP-9 (1), siControl (2), and Uncoated (3) bandages. Black arrows highlight the epithelial tongue and white arrows point to the end of the PC muscle. Scale bars, 1 mm. (c) Percent closure of the epithelial and PC muscle gaps evaluated at one and two weeks of treatment. (d) Granulation tissue thickness in the center of wounds after one and two weeks. (e) High power

field (HPF) (40x) imaging of the center of wound granulation tissues in siMMP-9 (1), siControl (2), and Uncoated (3) treated wounds. Arrows highlight some of the vessels visible in H&E staining. Scale bar = 100μm (f) Number of vessels per HPF, n = 9 per group. Data is shown as mean ± S.D., * = $p<0.05$.

These dramatic differences in wound healing between the treatment groups can also be appreciated grossly. In Figure 5-10 the one week siControl wound shown in Figure 5-9 is demonstrated to have very little healed tissue contained within the wound site. The tissue that is attached which appears to cross the wound is incredibly thin, and can actually be easily be seen through **(Figure 5-10a)**. Looking closely at this margin one can appreciate the lack of any tissue bridging the wound gap **(Figure 5-10b)**. The edges of the wound have some redness to them, indicating perfusion into the margins, but without any granulation tissue developed within the wound.

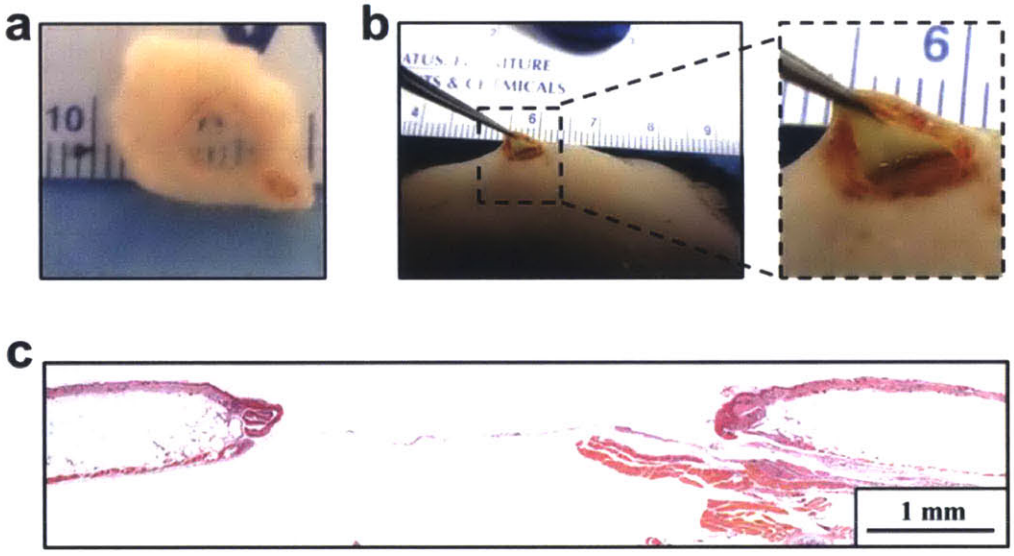

Figure 5-10 Gross examination of siControl wounds after one week demonstrated poor tissue integration and significantly impaired healing

(a) Gross imaging of excised siControl wound. (b) Demonstration of wound site prior to excision, demonstrating little to no tissue accumulation within the wound bed. (c)

Representative histology of wound section demonstrating no granulation tissue formed within the healing wound.

The margin of the one week siControl wound can actually be fully separated from the animals back. This finding is important as this stromal tissue that is observed in the histological preparation that appears to bridge the wound margins is not integrated into the healing dermis at this point. It may serve as a bridge later in the wound healing process and become integrated into the healed wound. This sort of finding makes the behavior of the epidermis, seen on the left of **Figure 5-10c**, to curl into itself, as there is no tissue developed out into the wound for it to migrate on.

5.3.5 siMMP-9 Therapy Increases Granulation Tissue Formation

One of the major substrates for MMP-9 within the healing wound is the early collagen that forms granulation tissue. By reducing the expression of MMP-9, we hypothesized that the granulation tissue would contain more collagen. To evaluate whether this was indeed the case we used Masson's trichrome (MTC) stain, a well-established histological stain for the analysis of collagen within tissues. In tissues stained using this technique, collagen appears blue while cell bodies, muscle, and keratin are red. This allows for the qualitative evaluation of collagen content and cellularity of tissue.

Analysis of MTC staining of wound sections after one week revealed extensive staining for collagen within the granulation tissue of siMMP-9 treated wounds, while control groups have little to no staining **(Figure 5-11)**. The differences mirror that found in the H&E stained wounds, where the siMMP-9 treated tissues contain a robust tissue bridging the wound, with increased cellularity, while control wounds have little tissue growth and sparse cell density within the wound bed. An important finding here in the early stages of wound healing was the apparent integration of the wound margins into the healing tissue in the siMMP-9 treated wounds that is not seen in the controls. This lack of integration contributes to the stagnation of the epithelial closure in the controls, an effect of which is epithelial curling as seen in the siControl section in **Figure 5-11**.

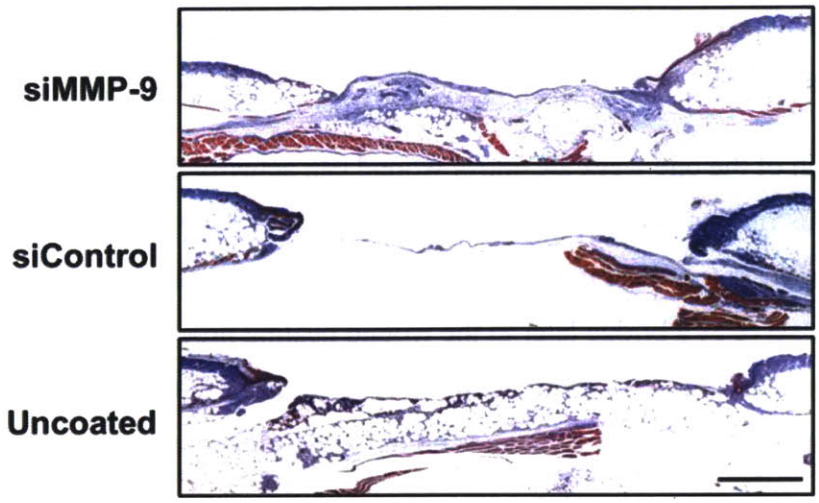

Figure 5-11 Masson's trichrome stained wound sections after one week of treatment
Little connecting tissue is seen to form within the wound beds of siControl and Uncoated treated mice. Mice treated with siMMP-9 bandages developed a thick and collagen rich granulation tissue. Scale bar = 1mm.

After two weeks the wounds treated with siMMP-9 bandages are greatly improved compared to the control wounds. The amount of granulation tissue and its relative cellularity is significantly increased in the siMMP-9 wounds compared to controls. This increased cellularity can be easily seen when looking at the wound centers and appreciating the purple color of that stained tissue, as compared to the lack of stain or faint blue found in the control wounds. Furthermore, the integration of the granulation tissue into the surrounding uninjured dermis that was observed after one week is even more enhanced in the siMMP-9 treatment group versus control after two weeks **(Figure 5-12 c-d)**.

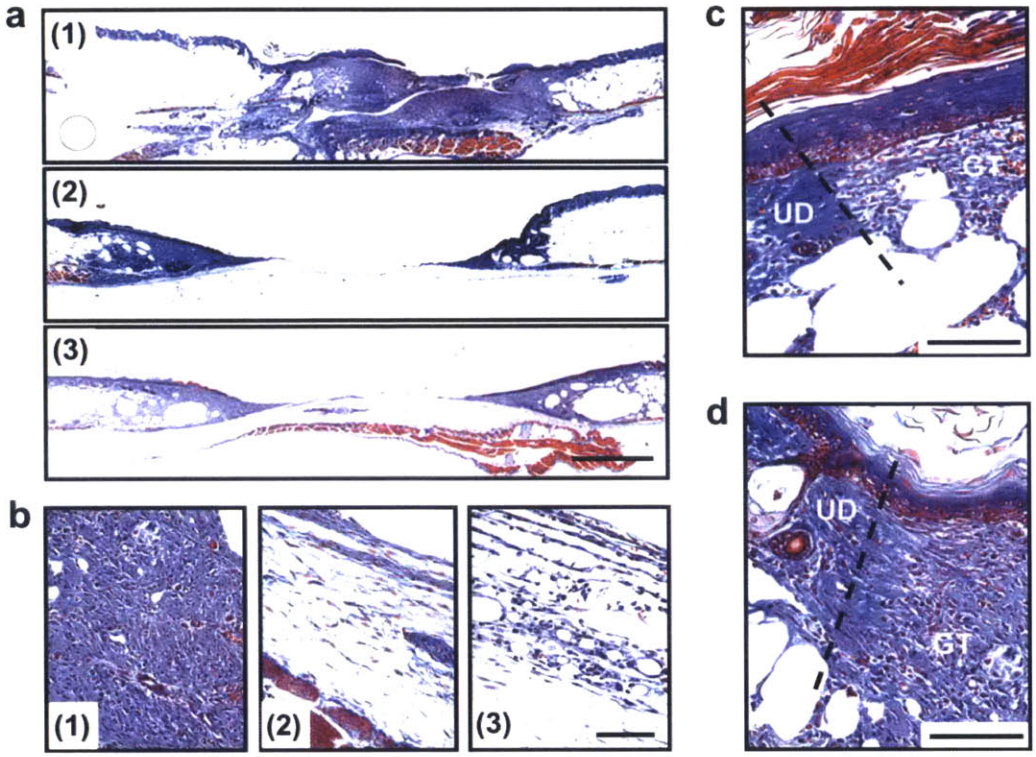

Figure 5-12 Treatment with MMP-9 siRNA increases the collagen content of the formed granulation tissue

(a) Masson's trichrome (MTC) stained wound sections of the center of wounds after two week of treatment of (1) MMP-9 siRNA, (2) Uncoated bandage, (3) Control siRNA treated wounds. Scale bar, 1 mm. (b) MTC stained granulation tissue within the center of the formed tissue shows significantly more collagen (blue stain) within the MMP-9 siRNA treated wounds (1) when compared to either uncoated (2) or control siRNA bandage (3) treated wounds. Scale bar, 100 μm. (c & d) Comparison of the wound edges showed significantly more tissue growth out of the wound edge in MMP-9 siRNA treated wounds (d) than control siRNA (c) treated wounds. Scale bar, 100 μm.

5.3.6 Collagen Content is Increased in siMMP-9 Treated Wounds

To further evaluate collagen accumulation within the wound we used a second independent histological technique: picrosirius (PS) staining of collagen. Collagen within the dermis is a naturally birefringent macromolecule and large collagen fibers can be easily

evaluated using polarized light microscopy. PS staining of collagen greatly enhances this birefringence, allowing for the precise localization of small fibrils of collagen as well as thicker fibers and the distinction between the two[48, 49]. Histological analysis of PS stained tissues has been used widely within the study of wound healing to evaluate the extent and type of collagen present within the healing tissue[50]. The PS stain is bright red in bright field microscopy. When PS stained slides are imaged between crossed-polarizers, however, the thinner early Type III collagen appears blue-green and the thicker and more mature Type I collagen appears orange-red.

Here we use this method to evaluate the maturation of the granulation tissue within the wound bed and its collagen content **(Figure 5-13 a-b)**. After one week of treatment, granulation tissue in MMP-9 siRNA treated mice has nearly twice the collagen content compared to control wounds, as well as twice as much mature collagen **(Figure 5-13 c-d)**. At two weeks of treatment the wounds of MMP-9 siRNA treated mice contain nearly five times the collagen compared to either control group, and the ratio of mature to young collagen is increased over four-fold compared to the control groups.

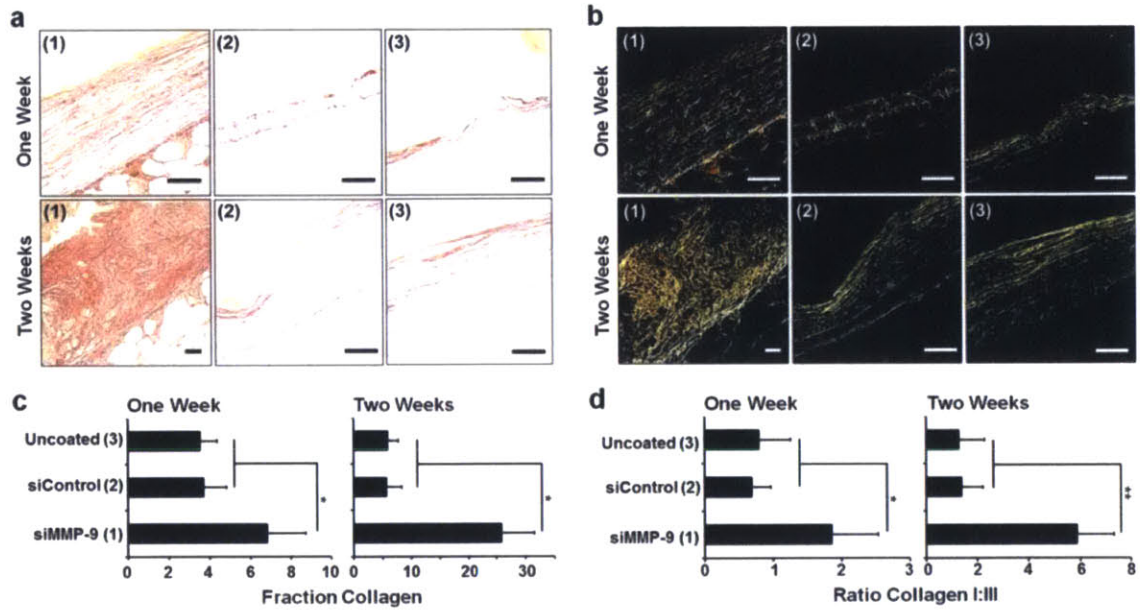

Figure 5-13 Treatment with MMP-9 siRNA increases collagen content and retention within the formed granulation tissue

(a) Picrosiruis red stained wound sections after one and two weeks of treatment with siMMP-9 (1) siControl (2) Uncoated (3) bandages. Scale bars, 75 μm. (b) Imaging of birefringent collagen through crossed-polarizers. Collagen type can be ascertained by the thickness of fibers, with collagen Type I being large orange-red fibers and Type III being thin green filamentous fibers. Scale bars, 75 μm. (c) Fraction of the granulation tissue within the wound that stains red for collagen. (d) The major type of collagen within the formed granulation tissue was significantly different between groups. Groups treated with siMMP-9 saw nearly twice as much Type I collagen after one week compared to controls, which increased to a near five-fold difference after two weeks. Data is shown as mean ± S.D., * = $p<0.05$, ** = $p < 0.01$.

The significant difference between the siMMP-9 treated wounds and those of the control mice is striking. Thick orange-red collagen bundles are seen to stretch though the formed tissue, whereas in the control groups only small blue-green fibers are appreciably present. These data suggest that not only does the knockdown of MMP-9 increase the amount of collagen within the wound bed, but also that its lowered expression allows for larger and more mature collagen fibers to develop within the tissue, more closely resembling uninjured dermis **(Figure 5-14)**.

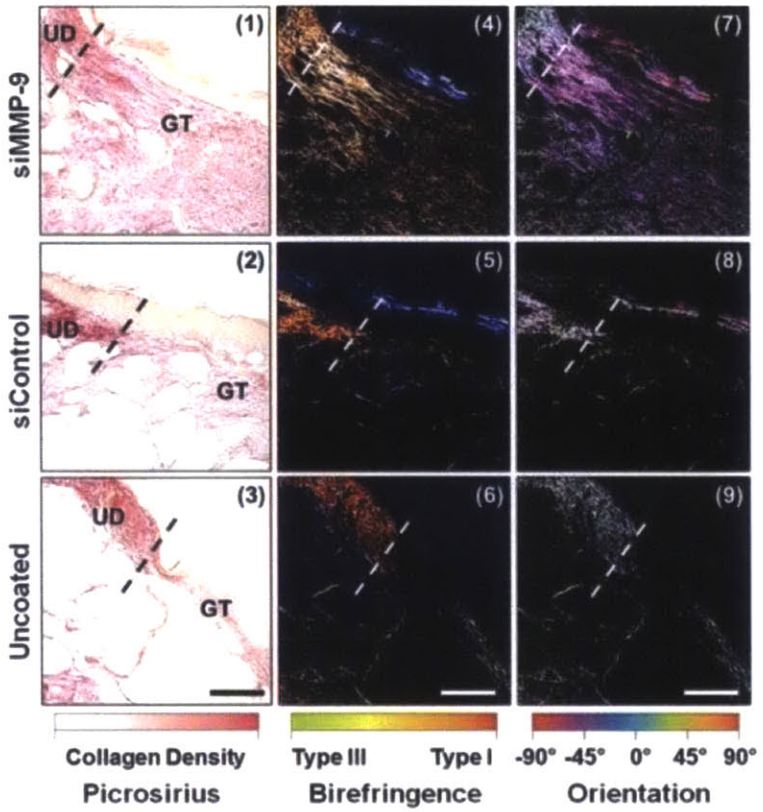

Figure 5-14 Tissue infiltration and wound edge integration is enhanced in wounds treated with siMMP-9 bandages

(1-3) Picrosirius red staining of wound edge. (UD = Uninjured Dermis, GT = Granulation Tissue). (4-6) Birefringent collagen imaging using crossed polarization light microscopy. (7-9) Color map of fiber orientations. This is performed using OrientationJ software[54]. Fiber orientation is only seen in the siMMP-9 treatment group. Scale bars, 75 μm.

When imaging the integration of the granulation tissue into the uninjured surrounding dermis, PS staining helps illuminate the collagen connecting the two tissues. Integration into the surrounding tissue is key in promoting the infiltration of cells into the forming granulation tissue, and in diabetic ulcers this integration is significantly impaired[5, 8]. The wound edges of siMMP-9 treated mice exhibit significantly higher collagen content, with large collagen bundles leading from the uninjured dermis into the granulation tissue. SiControl and uncoated bandage treated mice have no such collagen, with little tissue leading out of the surrounding uninjured dermis **(Figure 5-14)**. Analysis of the orientation of the collagen also highlights the differences.

Collagen within the siMMP-9 treated wound edge is oriented, connecting between the dermis and the granulation tissue while no such alignment is seen in the control groups **(Figure 5-15)**.

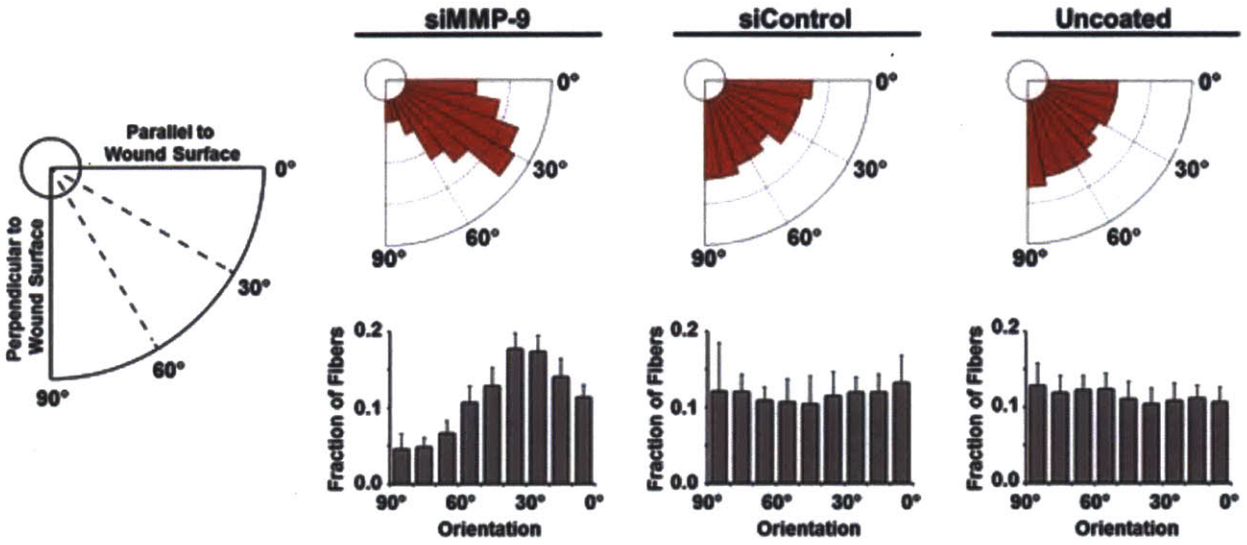

Figure 5-15 Orientation analysis of collagen fibers within wound edges after two weeks
Fibers were seen to have little or no general orientation in siControl and Uncoated bandage treated mice. Mice that were treated with siMMP-9 bandages had a observable orientation of collagen fibers pointing from the uninjured dermis into the forming granulation tissue, falling along 30° angle from the surface of the wound. Data is shown as mean ± S.D., n = 3

5.4 Discussion

Diabetic foot ulcers are the number one cause of non-traumatic lower limb amputations in the United States and contribute an estimated $11 billion in annual cost to the US healthcare system[51]. The current therapeutic options for patients with DFUs have shown only limited success, with nearly half of treated patients unable to achieve full wound closure[9]. With the number of patients suffering from DFUs expected to nearly double in the next 20 years, there is a strong need to develop new therapeutic approaches to better address this disorder[52].

Our motivation for targeting MMP-9 in this work is based on the substantial work of clinicians who have for over two decades correlated its overexpression to poor wound healing outcomes in diabetic patients[6, 8, 17]. However, until now there has been limited research focused on targeting this overexpression as a means of therapy[53], due in large part to the musculoskeletal side effects that has hindered the development of MMP inhibitors. Through the use of layer-by-layer assembly we are able to construct a hydrolytically degradable siRNA depot on top of a commercially available nylon bandage that can deliver siRNA directly into a wound bed and dramatically alter gene expression.

The effect of siMMP-9 therapy closely resembles our initial hypothesis; by reducing the presence of MMP-9 to twenty percent of untreated tissue levels we diminish the overall protease activity by 60 percent. This allows more granulation tissue to form in the wound bed and the new tissue contains up to five-fold more collagen than untreated wounds. Overall, this additional collagen is more mature, and at the edges of the wound is more tightly integrated with the uninjured dermis. We hypothesize that it is this substantial change to the deposited ECM that drives the observed improvement in healing by facilitating faster migration of the epithelial tongue and contraction of the wound.

In summary, this study successfully demonstrates the use of electrostatic assembly to generate ultrathin siRNA coatings capable of direct and effective delivery of siRNA to a highly proteolytic wound environment. This dramatically reduces the expression and activity of a key gelatinase and improves the healing of chronic wounds. Overall, this work begins to lay the groundwork for using localized RNAi to treat a clinically recognized dysregulation within diabetic ulcers and offers a potentially translatable strategy for improving patient care. The strategy outlined here, however, is not limited to treating chronic wounds. This technology is a simple and broadly applicable platform for including localized RNAi from any current medical device and has the potential to address a myriad of applications where altering localized protein express in specific tissue microenvironments may be of use, including cardiovascular diseases, transplant rejection, and cancer.

5.5 References

1. Sen, C.K. et al. Human skin wounds: a major and snowballing threat to public health and the economy. Wound Repair Regen 17, 763-771 (2009).

2. Singh, N., Armstrong, D.G. & Lipsky, B.A. Preventing foot ulcers in patients with diabetes. Jama 293, 217-228 (2005).

3. Boulton, A.J., Vileikyte, L., Ragnarson-Tennvall, G. & Apelqvist, J. The global burden of diabetic foot disease. Lancet 366, 1719-1724 (2005).

4. Gurtner, G.C., Werner, S., Barrandon, Y. & Longaker, M.T. Wound repair and regeneration. Nature 453, 314-321 (2008).

5. Dinh, T. et al. Mechanisms involved in the development and healing of diabetic foot ulceration. Diabetes 61, 2937-2947 (2012).

6. Rayment, E.A., Upton, Z. & Shooter, G.K. Increased matrix metalloproteinase-9 (MMP-9) activity observed in chronic wound fluid is related to the clinical severity of the ulcer. Br J Dermatol 158, 951-961 (2008).

7. Zins, S.R., Amare, M.F., Tadaki, D.K., Elster, E.A. & Davis, T.A. Comparative analysis of angiogenic gene expression in normal and impaired wound healing in diabetic mice: effects of extracorporeal shock wave therapy. Angiogenesis 13, 293-304 (2010).

8. Falanga, V. Wound healing and its impairment in the diabetic foot. Lancet 366, 1736-1743 (2005).

9. Gottrup, F. & Apelqvist, J. Present and new techniques and devices in the treatment of DFU: a critical review of evidence. Diabetes Metab Res Rev 28 Suppl 1, 64-71 (2012).

10. Wieman, T.J., Smiell, J.M. & Su, Y. Efficacy and safety of a topical gel formulation of recombinant human platelet-derived growth factor-BB (becaplermin) in patients with chronic neuropathic diabetic ulcers. A phase III randomized placebo-controlled double-blind study. Diabetes Care 21, 822-827 (1998).

11. Veves, A., Falanga, V., Armstrong, D.G. & Sabolinski, M.L. Graftskin, a human skin equivalent, is effective in the management of noninfected neuropathic diabetic foot ulcers: a prospective randomized multicenter clinical trial. Diabetes Care 24, 290-295 (2001).

12. Marston, W.A., Hanft, J., Norwood, P. & Pollak, R. The efficacy and safety of Dermagraft in improving the healing of chronic diabetic foot ulcers: results of a prospective randomized trial. Diabetes Care 26, 1701-1705 (2003).

13. Moor, A.N., Vachon, D.J. & Gould, L.J. Proteolytic activity in wound fluids and tissues derived from chronic venous leg ulcers. Wound Repair and Regeneration 17, 832-839 (2009).

14. Liu, Y. et al. Increased Matrix Metalloproteinase-9 Predicts Poor Wound Healing in Diabetic Foot Ulcers. Diabetes Care 32, 117-119 (2009).

15. Li, Z., Guo, S., Yao, F., Zhang, Y. & Li, T. Increased ratio of serum matrix metalloproteinase-9 against TIMP-1 predicts poor wound healing in diabetic foot ulcers. J Diabetes Complications 27, 380-382 (2013).

16. Ladwig, G.P. et al. Ratios of activated matrix metalloproteinase-9 to tissue inhibitor of matrix metalloproteinase-1 in wound fluids are inversely correlated with healing of pressure ulcers. Wound Repair Regen 10, 26-37 (2002).

17. Agren, M.S. Gelatinase activity during wound healing. Br J Dermatol 131, 634-640 (1994).

18. Moses, M.A. et al. Temporal study of the activity of matrix metalloproteinases and their endogenous inhibitors during wound healing. J Cell Biochem 60, 379-386 (1996).

19. Brandner, J.M., Zacheja, S., Houdek, P., Moll, I. & Lobmann, R. Expression of matrix metalloproteinases, cytokines, and connexins in diabetic and nondiabetic human keratinocytes before and after transplantation into an ex vivo wound-healing model. Diabetes Care 31, 114-120 (2008).

20. Lobmann, R. et al. Expression of matrix-metalloproteinases and their inhibitors in the wounds of diabetic and non-diabetic patients. Diabetologia 45, 1011-1016 (2002).

21. Dalton, S.J., Mitchell, D.C., Whiting, C.V. & Tarlton, J.F. Abnormal extracellular matrix metabolism in chronically ischemic skin: a mechanism for dermal failure in leg ulcers. J Invest Dermatol 125, 373-379 (2005).

22. Grinnell, F., Ho, C.H. & Wysocki, A. Degradation of fibronectin and vitronectin in chronic wound fluid: analysis by cell blotting, immunoblotting, and cell adhesion assays. J Invest Dermatol 98, 410-416 (1992).

23. Armstrong, D.G. & Jude, E.B. The role of matrix metalloproteinases in wound healing. J Am Podiat Med Assn 92, 12-18 (2002).

24. Hayden, D.M., Forsyth, C. & Keshavarzian, A. The Role of Matrix Metalloproteinases in Intestinal Epithelial Wound Healing During Normal and Inflammatory States. Journal of Surgical Research 168, 315-324 (2011).

25. Brown, S., Meroueh, S.O., Fridman, R. & Mobashery, S. Quest for selectivity in inhibition of matrix metalloproteinases. Curr Top Med Chem 4, 1227-1238 (2004).

26. Coussens, L.M., Fingleton, B. & Matrisian, L.M. Matrix metalloproteinase inhibitors and cancer: trials and tribulations. Science 295, 2387-2392 (2002).

27. Hu, J., Van den Steen, P.E., Sang, Q.X. & Opdenakker, G. Matrix metalloproteinase inhibitors as therapy for inflammatory and vascular diseases. Nat Rev Drug Discov 6, 480-498 (2007).

28. Overall, C.M. & Kleifeld, O. Towards third generation matrix metalloproteinase inhibitors for cancer therapy. Br J Cancer 94, 941-946 (2006).

29. Whitehead, K.A., Langer, R. & Anderson, D.G. Knocking down barriers: advances in siRNA delivery. Nature Reviews Drug Discovery 8, 129-138 (2009).

30. Gavrilov, K. & Saltzman, W.M. Therapeutic siRNA: principles, challenges, and strategies. Yale J Biol Med 85, 187-200 (2012).

31. Ghildiyal, M. & Zamore, P.D. Small silencing RNAs: an expanding universe. Nat Rev Genet 10, 94-108 (2009).

32. Glebova, K.V., Marakhonov, A.V., Baranova, A.V. & Skoblov, M.Y. Therapeutic siRNAs and nonviral systems for their delivery. Molecular Biology 46, 335-348 (2012).

33. Vaishnaw, A.K. et al. A status report on RNAi therapeutics. Silence 1, 14 (2010).

34. Juliano, R., Bauman, J., Kang, H. & Ming, X. Biological barriers to therapy with antisense and siRNA oligonucleotides. Mol Pharm 6, 686-695 (2009).

35. Nelson, C.E. et al. Sustained local delivery of siRNA from an injectable scaffold. Biomaterials 33, 1154-1161 (2012).

36. Zheng, D. et al. Topical delivery of siRNA-based spherical nucleic acid nanoparticle conjugates for gene regulation. Proc Natl Acad Sci U S A 109, 11975-11980 (2012).

37. DeMuth, P.C. et al. Polymer multilayer tattooing for enhanced DNA vaccination. Nat Mater 12, 367-376 (2013).

38. Tang, Z.Y., Wang, Y., Podsiadlo, P. & Kotov, N.A. Biomedical applications of layer-by-layer assembly: From biomimetics to tissue engineering. Advanced Materials 18, 3203-3224 (2006).

39. Castleberry, S., Wang, M. & Hammond, P.T. Nanolayered siRNA Dressing for Sustained Localized Knockdown. ACS Nano 7, 5251-5261 (2013).

40. DeMuth, P.C., Su, X., Samuel, R.E., Hammond, P.T. & Irvine, D.J. Nano-layered microneedles for transcutaneous delivery of polymer nanoparticles and plasmid DNA. Advanced Materials 22, 4851-4856 (2010).

41. Saurer, E.M. et al. Polyelectrolyte Multilayers Promote Stent-Mediated Delivery of DNA to Vascular Tissue. BioMacromolecules 14, 1696-1704 (2013).

42. Lynn, D.M. & Langer, R. Degradable poly(beta-amino esters): Synthesis, characterization, and self-assembly with plasmid DNA. J Am Chem Soc 122, 10761-10768 (2000).

43. Bechler, S.L. & Lynn, D.M. Characterization of Degradable Polyelectrolyte Multilayers Fabricated Using DNA and a Fluorescently-Labeled Poly(beta-amino ester): Shedding Light on the Role of the Cationic Polymer in Promoting Surface-Mediated Gene Delivery. BioMacromolecules 13, 542-552 (2012).

44. Davidson, J.M. Animal models for wound repair. Arch Dermatol Res 290 Suppl, S1-11 (1998).

45. Sullivan, S.R. et al. Validation of a model for the study of multiple wounds in the diabetic mouse (db/db). Plast Reconstr Surg 113, 953-960 (2004).

46. Blakytny, R. & Jude, E. The molecular biology of chronic wounds and delayed healing in diabetes. Diabet Med 23, 594-608 (2006).

47. Neely, A.N., Clendening, C.E., Gardner, J. & Greenhalgh, D.G. Gelatinase activities in wounds of healing-impaired mice versus wounds of non-healing-impaired mice. J Burn Care Rehabil 21, 395-402 (2000).

48. Junqueira, L.C., Cossermelli, W. & Brentani, R. Differential staining of collagens type I, II and III by Sirius Red and polarization microscopy. Arch Histol Jpn 41, 267-274 (1978).

49. Montes, G.S. & Junqueira, L.C. The use of the Picrosirius-polarization method for the study of the biopathology of collagen. Mem Inst Oswaldo Cruz 86 Suppl 3, 1-11 (1991).

50. Cuttle, L. et al. Collagen in the scarless fetal skin wound: detection with picrosirius-polarization. Wound Repair Regen 13, 198-204 (2005).

51. Gordois, A., Scuffham, P., Shearer, A., Oglesby, A. & Tobian, J.A. The health care costs of diabetic peripheral neuropathy in the US. Diabetes Care 26, 1790-1795 (2003).

52. Huang, E.S., Basu, A., O'Grady, M. & Capretta, J.C. Projecting the future diabetes population size and related costs for the U.S. Diabetes Care 32, 2225-2229 (2009).

53. Gooyit, M. et al. A chemical biological strategy to facilitate diabetic wound healing. ACS Chem Biol 9, 105-110 (2014).

54. Rezakhaniha, R. et al. Experimental investigation of collagen waviness and orientation in the arterial adventitia using confocal laser scanning microscopy. Biomech Model Mechanobiol 11, 461-473 (2012).

Chapter 6
Controlled Local Delivery of siRNA *In Vivo* for the Treatment of Chronic Inflammation in Diabetic Wound Healing

6.1 Introduction

In Chapter 3 we described the use of calcium phosphate nanoparticle films for the sustained controlled delivery of siRNA *in vitro*. This work provided a great deal of excitement for us as it was the first reported application of LbL for the successful delivery of siRNA. Pairing this material system with other LbL films however was significantly restrained due to the pH constraints that the CaP particles put on the film assembly. For this reason we chose to pursue the material system outlined in Chapter 5 using chitosan. In this chapter we present a different approach than Chapter 5, where we target tumor necrosis factor alpha (TNFα) within the chronic wounds of genetically diabetic mice using the calcium phosphate LbL film from Chapter 3.

Chronic wound healing is a major complication in type two diabetes mellitus (T2DM), affecting over 750,000 American's each year.[1-3] Impaired wound healing presents an important health concern for T2DM patients as these wounds can linger for months, increasing the risk of serious infection and subsequent requirement for amputations.[3-5] Indeed, diabetic foot ulcers are the number one non-traumatic cause for lower limb amputations in the United States, with over 70,000 such operations each year.[6-9] Recent assessments for the economic burden of chronic wound healing in diabetic patients has estimated that it costs healthcare providers over 11 billion dollars in direct and indirect medical expenses each year.[5, 10-12]

There are a myriad of reasons why patients with T2DM suffer from chronic wound healing, including: prolonged inflammation,[13] altered protease activity,[14, 15] increased risk of vascular abnormalities,[16] poor cell proliferation within the wound bed,[17] decreased growth factor production,[18] and an altered host response,[19] just to name a few. In Chapter 5 we targeted one of

these factors, proteolytic activity, by knocking down matrix metalloproteinase-9 (MMP-9) within the wound site. MMP-9 operates as the primary gelatinase during the dermal wound healing process, and is known to be chronically upregulated within the wound beds of poor healing diabetic ulcers.[20-22] This focused target however may not be enough on its own to correct for the many complications that lead to diabetic ulcers.

As we described in the first chapter of this thesis, wound healing is a highly orchestrated and complex process involving many different stages each with its various cell types evolving over time.[23, 24] The wound healing process is regulated by a number of growth factors and cytokines which can be altered in different disease states, which is true in the case of T2DM.[25, 26] In type two diabetes mellitus the impaired wound healing is first observed by the reduced proliferative response within the healing tissue. This is seen as a lack of sufficient granulation tissue formation to close the wound.[27, 28] Granulation tissue is the early tissue that fills a wound and provides the scaffold for later tissue regeneration. Important in the formation of granulation tissue are the rapid proliferation of fibroblasts and their expression of collagen, a key protein component in the extracellular matrix. Interference with fibroblast proliferation and protein production can be caused by a number of factors including reduced pro-proliferative signaling within tissue and high levels of fibroblast apoptosis, both of which can be due to chronic inflammation.[29, 30]

Over the past three decades a number of different reports have identified the role of chronic inflammation within diabetic wounds as contributing to their pathology.[8, 31-33] A primary mediator of this inflammation within these tissues that has been identified as potentially pathologic numerous times is tumor necrosis factor alpha (TNFα).[34-36] TNFα is produced both as a soluble cytokine and as a cell membrane bound protein by activated macrophages.[37] Its role in wound healing is expansive, as its expression and signaling determines much of the tissues inflammatory response and drives a great deal of the immunologic activity involved in wounding.[26, 38, 39] During the normal wound healing process TNFα expression is at its highest between 12 to 24 hours post-wounding.[40, 41] During this early phase of wound healing TNFα is expressed primarily by neutrophils and macrophages and acts to stimulate fibroblast and keratinocyte proliferation, migration, and production of growth factors.[42, 43]

It has been previously demonstrated that prolonged increased TNFα expression is linked to persistent inflammation and tissue destruction[38] and that the levels of TNFα expression are chronically elevated in non-healing ulcers, including diabetic foot ulcers.[29, 34, 44] It has also been reported that the overexpression of TNFα is associated with impaired wound healing in mouse models of T2DM, including the $Lepr^{db/db}$ mouse which we will use in this work.[36, 45] In type two diabetes TNFα levels are chronically elevated due in part to increased oxidative stress in peripheral tissues as a result of poor perfusion.[46] This chronic increased expression of TNFα has also been demonstrated to slow cutaneous wound healing *in vivo* and impair native collagen production in response to wounding.[47-49] To this end the exogenous application of TNFα to wounds results in significantly reduced mechanical stability of the healed tissues and slows the rate of wound closure.[50]

The chronic upregulated expression of TNFα impairs cell migration through increased Smad7 activity levels, inhibiting the activation of Smad2/3.[51] This inhibition reduces the downstream signaling of TGFβ receptors for the production of type 1 collagen, which is a fundamental component of the dermis that must be produced in the wound bed in significant quantities for appropriate wound healing to occur.[52] TGFβ1 is a potent pro-fibrotic cytokine that is primarily responsible for the induction of collagen synthesis within wound healing,[53] TNFα expression has been demonstrated to not only inhibit this signaling pathway but also to reduce TGFβ1 expression within the dermis at the pre-translational level.[40] This inhibition of TGFβ1 expression is believed to play a key role in the slowed formation of granulation tissue within the wound bed. In addition to its effect on TGFβ signaling, TNFα also stimulates the expression of many pro-inflammatory cytokines through the NF-κB pathway, upregulating the production of MMP-9, IL-1β, and TNFα.[54-56]

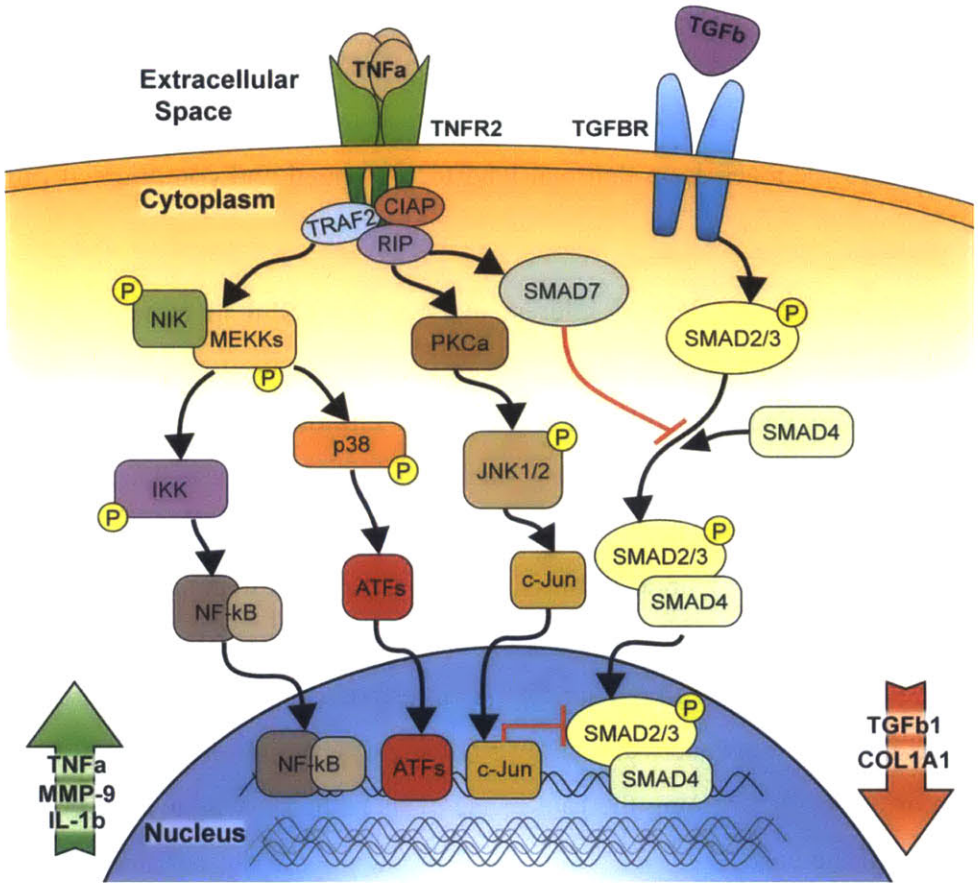

Figure 6-1 Cartoon schematic of selected TNFα signaling pathways

These pathways are known to contribute to a number of pathologic roles in chronic wound healing.[40]

In Chapter 5 we focused on the targeted knockdown of one of these factors, MMP-9, within diabetic wounds. Expression of MMP-9 within ulcers is in part driven by TNFα expression and its chronic upregulation within diabetic ulcers is thought to be as a consequence of increased TNFα expression. In cutaneous wound healing MMP-9 operates as the primary gelatinase, degrading the early collagen within the wound bed that forms the granulation tissue.[22, 57, 58] Beyond MMP-9, TNFα also stimulates the expression of an important pro-inflammatory cytokine, interleukin-1 beta (IL-1β).[59] IL-1β is known to be upregulated in chronic ulcers, especially in poor healing diabetic wounds, and plays an important role in inducing a pro-inflammatory macrophage phenotype. Previous research has demonstrated that the inhibition of

IL-1β was able to improve wound healing outcomes in a mouse model of diabetic wound healing, and was observed to reduce the expression of MMP-9 and TNFα.[60] In addition to stimulating MMP-9 and IL-1β, TNFα also stimulates its own expression, creating a complex pro-inflammatory positive feedback loop that can lead to prolonged and complicated inflammatory conditions.

There has been a great deal of interest in targeting TNFα in numerous inflammatory diseases such as psoriasis, irritable bowel syndrome, and rheumatoid arthritis.[38] To date all of the approved anti-TNFα therapies rely on monoclonal antibodies to target TNFα in solution. These approaches have demonstrated amazing successes in treating these diseases by combating the effect of chronic TNFα overexpression. There are substantial drawbacks to this approach however including a number of undesirable side effects such as liver toxicity, risk of serious infections, and malignancy, as well as being exceptionally cost-intensive therapies.[39, 61] Reducing TNFα expression locally with RNA interference (RNAi), however presents a potentially more versatile approach that may reduce the systemic side effects of anti-TNFα therapy while more directly targeting the root cause of its pathology, its overexpression, at what could be a fraction of the cost.

Localized RNAi presents a great number of potential benefits over traditional small molecule therapies due to its specificity and gene targeted design. Compared to biologics currently on the market, short interfering RNAs do not require cell culture for manufacturing, can be readily purified from a highly concentrated reaction mixture, and the siRNA sequence can be readily adapted to target many different sequences for quick optimization.[62-64] Here we look at localized delivery of RNAi as it can circumvent many complications of systemic delivery that we have covered in detail in the previous chapter. Layer-by-layer (LbL) is a surface modification technology that takes advantage of complimentary interactions between material species for the controlled assembly of ultrathin polymer film coatings on activated surfaces.[65-67] This technique has been well-reported for the controlled incorporation and delivery of many bioactive materials including small molecules, biologics, DNA, and RNA.[68-71] Here we use this technology similarly to what we reported in Chapters 3 and 5 of this thesis for the controlled localized delivery of siRNA.

We chose to focus this chapter on the film architecture that was first explored in Chapter 3, the tetralayer of [PrS/CaP/PrS/Lap]. This film was chosen based on the great *in vitro* results we saw as presented previously and in this Chapter as well as our preliminary findings that this film architecture seemed better tolerated than the chitosan containing films. In this chapter we will describe the thorough *in vitro* investigation of our [PrS/CaP/PrS/Lap] film and then test this film in an excisional wounding model of diabetic foot ulcers in a genetically diabetic mouse.[72-75] To this effect we demonstrate the siRNA-specific sustained knockdown of TNFα within the wounds of diabetic mice, and demonstrate that this knockdown led to improved wound healing outcomes including accelerated re-epithelialization, increased granulation tissue formation, improved vascularization of the healed tissue, and increased collagen deposition and maturation within the healing tissue.

6.2 Methods and Materials

6.2.1 Materials

LPEI (25 kDa) was purchased from Polysciences (Warrington, PA). SiRNA sequences were synthesized by Dharmacon (Lafayette, CO). Alexafluor 488-labeled siRNA was purchased from Qiagen (Valencia, CA). Tegaderm™ (3M) Woven nylon bandages were purchased through Cardinal Health (Newark, NJ). Antibiotic-antimycotic solution, 100 mM L-Glutamine solution, phosphate buffered saline (PBS, 10x), Advanced-MEM, AlamarBlue, TriZol, and fetal bovine serum were purchased from Invitrogen (Carlsbad, CA). NIH-3T3, HeLa, and MDA-MB-231 cells were purchased from ATCC (Manassas VA). $CaCl_2$, NH_3PO_4, Protamine Sulfate, and Picrosiruius stain material were purchased from Sigma-Aldrich Company (Manassas, VA). DNA primers were purchased from IDT (Coralville, Iowa). All antibodies were purchased from Abcam (Cambridge, MA). Laponite silicate clay was purchased from Southern Clay Products Inc. (Gonzalez, TX).

6.2.2 Layer-by-layer film preparation

Films were deposited on oxygen plasma treated bandages. Bandages were cleaned in ethanol and then in RNase free UltraPure™ water (Life Technologies) prior to plasma treatment. Oxygen plasma treatment was performed for 3 minutes on high setting. Bandages were then immediately immersed in a solution of the polycation Poly 2 for a minimum of one hour. Assembly of LbL films was performed using a Carl Zeiss HMS-DS50 stainer. Assembly of

[PrS/CaP/PrS/Lap] film was deposited similarly. PrS (2 mg ml^{-1}, pH 8.0) was adsorbed for 10 minutes and CaP (siRNA concentration = 20 μg ml^{-1}, pH 8.0) was adsorbed for 30 minutes. Laponite clay (10 mg ml^{-1}, pH 9.0) was absorbed for 2 minutes. All solutions were prepared in RNase free water, adjusted to a pH of 8.0.

Film growth was characterized for films built on silicon wafers by a Veeco Dektak 150 profilometer. Incorporation of fluorescently labeled siRNA into films built on nylon bandages was followed using a Nikon A1R Ultra-Fast Spectral Scanning confocal microscope. Total siRNA incorporation within films was measured by rapid dissolution in a 1M NaCl solution with vigorous agitation and quantified using a fluorescent plate reader. Release studies were performed in cell conditioned media at 37°C. Release was quantified by fluorescence of the released labeled siRNA read using a fluorescent plate reader.

6.2.3 *In Vitro* LbL Bandage Evaluation

Cells were cultured in Advanced-MEM media with 5% FBS, 1% antibiotic-antimycotic, and 2mM L-glutamine. Cells were seeded at an initial density of 5,000 cells per well in a 48-well plate. After one day LbL coated bandages (0.25cm^2 sections) were placed in culture with the cells. The bandages either contained GFP-specific siRNA or a control siRNA sequence or were uncoated. Uncoated bandages were used as the control to test the cytotoxicity of the film. Mean cell fluorescence was measured by flow cytometry, using a BD FACSCalibur flow cytometer. Cell viability was quantified using AlamarBlue assay (Life Technologies). Analysis of GFP expression and cell viability were performed after 3, 5, and 7 days of treatment.

6.2.4 *In Vivo* siRNA Delivery

All animal studies were approved by the MIT Institutional Animal Care and Use Committee (IACUC). Animals were housed and cared for in the USDA-inspected MIT Animal Facility under federal, state, local, and NIH guidelines for animal care. Eight week diabetic (*db/db*) mice (BKS.Cg-Dock7^{m} +/+ Lepr^{db}/J) were purchased from Jackson Labs (Bar Harbor, ME). Daily blood glucose measurements were taken for all mice used. Mice were required to maintain a blood glucose level in excess of 300mg dl^{-1} to be used for these studies. Three groups of mice were used: (1) TNFα siRNA bandage treated, (2) control siRNA bandage treated, and (3) uncoated bandage treated.

Each group had 6 mice total, 3 mice per time point. Hair was removed from the backs of mice using a depilatory cream under anesthesia at least one day prior to surgery. Surgeries were performed under anesthesia and pre-operative analgesic was given to all mice (0.1 mg kg^{-1} Buprenex). Two 6mm full-thickness wounds were excised from the dorsum of mice using a biopsy punch on either side of midline. Bandages were cut to the same size (6mm dia.) as the wound and placed on top of the wound. The bandages were then secured in place using an adherent Tegaderm. This securing bandage holds the test bandage in place as well as keeps cage material from entering the wound. Mice were sacrificed after one and two weeks of treatment. One wound from each mouse was used for histological analysis and one wound was used for RNA isolation and protein analysis.

6.2.5 Histology

Tissues were fixed in zinc fixative without formalin for 48 hours. The excised wounds were then embedded in paraffin and serially sectioned at 250μm levels throughout the wound. At each level an H&E slide was stained and used for 2-D reconstruction of the wound. Unstained slides were also taken for IHC, MTC, and PS staining and analysis of the healing tissue. Data analysis was performed using Image J. Orientation of collagen fibers was analyzed using the Image J plugin Orientation J.

6.2.6 Tissue Processing

Isolation of RNA was performed using TRIzol as per the manufacturer's instructions. Synthesis of cDNA was done using iScript cDNA synthesis kit (Bio-Rad Laboratories) and analysis of expression was performed by qRT-PCR using iQ SYBR Green Supermix (Bio-Rad Laboratories) along with selected DNA primer pairs. All experiments were performed in triplicate using a LightCycler 480 (Roche). Relative gene expression was quantified relative to β-actin, a housekeeping gene, using the delta-delta Ct method. All experiments were performed in triplicate.

6.2.7 Statistics

Statistical analysis was performed between groups using Student's *t*-test and rectified by ANOVA for comparisons between multiple groups. Values are represented as mean ± S.D. A value of $p < 0.05$ was used to indicate statistical significance.

6.3 Results

6.3.1 *In Vitro* Analysis of the CaP Tetralayer Film

We described this film in detail in Chapter 3 of this thesis and we were interested to further test the film for its tunability so as to compare it to the chitosan containing film we investigated in chapter 5. Calcium phosphate nanoparticles were created as previously reported (ref) and were found to have an average diameter of approximately 216 nm with a zeta potential of -27 mV, which was in good agreement to what we had found previously.

Films were assembled on cleaned silicon substrates and thickness was measured by profilometry. The surface appeared very rough, Ra = 24.2 ± 6.6 nm, which is similar to what we had found for the same film in our previous investigations. Release studies were conducted in cell conditioned media at 37°C, as described previously, for films prepared with 5, 15, or 25 architecture repeats. Release of siRNA from the films was followed for up to two weeks. Release was quantified using commercially available fluorescently labeled siRNAs. Each film was observed to release siRNA, films assembled with 15 or more tetralayers released siRNA until the end of the study period, while films with only 5 layers were observed to not release any more siRNA after approximately one week.

In vitro analysis of the effective knockdown of a reporter gene was performed as follows: $[PrS/CaP/PrS/Lap]_{25}$ film coated Tegaderm® (3M) samples were assembled using siRNA for GFP targeting and were placed in culture with HeLa cells that constitutively express green fluorescent protein (GFP). Cells were analyzed by flow cytometry after 3 or 5 days of treatment to assess mean cell fluorescence which was compared to cells treated with similarly coated bandages containing a control siRNA sequence. The impact that the coated bandages had on cell viability was evaluated by comparing the metabolic activity of cells treated with LbL coated bandages to cells treated with uncoated control bandages. This was done using AlamarBlue assay as per the manufacturer's protocol.

SiRNA-specific knockdown of GFP in HeLa cells correlated well with the release of siRNA from each architecture. As controls in this experiment we investigated 100 pmol of siRNA delivered either in naked form with PBS or formulated with Lipofectamine 2000 as per

the manufacturer's protocol. Treatment with naked siRNA was observed to only minimally impact either GFP expression or cell viability. Lipofectamine achieved the greatest reduction in mean cell fluorescence, nearly 80% reduction after three days, however cell viability in these cultures was reduced by over 55%. In comparison, the best LbL film system achieved nearly 35% reduction with no significant impact on cell viability. After five days cells treated with lipofectamine were observed to increase in mean cell fluorescence, while cells treated with LbL coated substrates all saw continued reduction in MCF, where the best architecture again was the 25 tetralayer film, reaching an MCF reduction of approximately 55%. Cells treated with the $[PrS/CaP/PrS/Lap]_{25}$ film were observed to accumulate labeled siRNA over a one week period, demonstrating the continued uptake of released material from the degrading films *in vitro*.

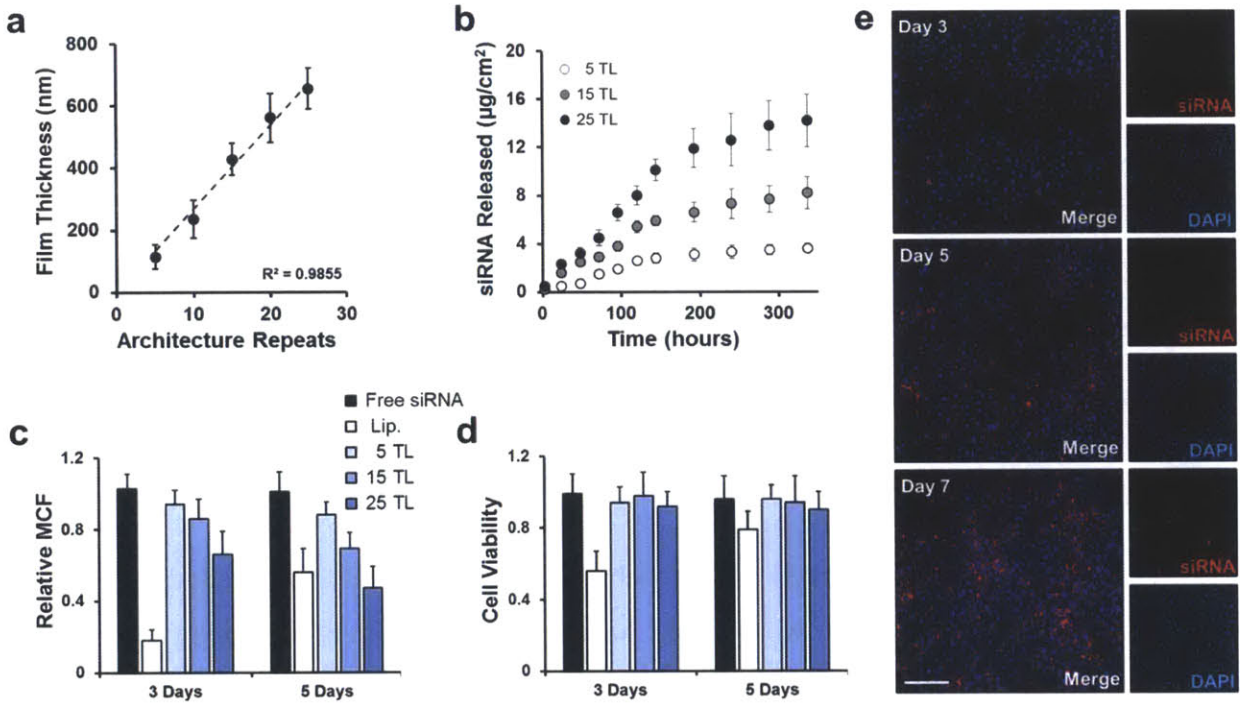

Figure 6-2 *In vitro* investigations of [PrS/CaP/PrS/Lap] film architecture

(a) Film growth as measured by profilometry for films assembled on silicon substrates. (b) Quantification of siRNA release from film coated bandages over two weeks in cell conditioned media at 37°C. (c) Flow cytometry analysis of mean cell fluorescence for cells treated with free siRNA, lipofectamine encapsulated siRNA, and LbL film coated substrates with 5, 15, or 25 layers of LbL film. (d) Cell viability of cells treated with controls compared to PBS, or film

coated substrates compared to uncoated, as measured by AlamarBlue metabolic assay. (e) Fluorescent imaging of HeLa cell uptake of LbL film material in vitro using AlexaFluor-546 labeled siRNA. Cell nucleus is stained with Dapi nuclear stain. Scale bar = 75 μm. Data is mean ± S.D., n = 3.

6.3.2 *In Vivo* Analysis of the [PrS/CaP/PrS/Lap]$_{25}$ Film

Based on our thorough *in vitro* investigation we determined that the [PrS/CaP/PrS/Lap]$_{25}$ film was the best performing architecture. Similar to our approach in Chapter 5 we followed our *in vitro* study by investigating its performance *in vivo* using the Lepr$^{db/db}$ mouse, a genetically diabetic mouse model that is well established for the study of chronic ulcerative wound healing[72, 73]. The pro-inflammatory cytokine TNFα is expressed at increased levels in this model, in agreement with studies of patients with diabetic foot ulcers, making it an ideal animal model for our *in vivo* investigations.[18, 75]

To fully investigate the impact of the localized delivery of siTNFα therapy from LbL film we studied three different treatment groups (1) siTNFα, (2) siControl, or (3) uncoated bandages (two wounds per mouse, n = 3 mice per group per timepoint). Dressings were applied *in vivo* as described in Chapter 5. Briefly, two 6mm diameter full-thickness wounds were created by biopsy punch in the dorsum of each mouse. One bandage was placed into each wound and secured in the wound with a commercially available adherent bandage.

This adherent bandage served to keep debris out of the wound and to reduce subsequent risk of infection. We found in our work from Chapter 5 that this form of a dressing worked well for the Lepr$^{db/db}$ mouse model. These mice are unable to reach their backs due to their obese state; as such the bandages remained unmolested throughout the two week study. Similar to our finding in Chapter 5, wounds could only be clearly imaged after necropsy, as the dressing obscured the wound margins and removal of the bandage for daily imaging presented a risk of infection that we felt was too high.

Digital images were acquired at necropsy after one and two weeks of treatment. Visually, the changes in wound healing between the three treatment groups were striking. These images were analyzed for epithelial margin closure (**Figure 6-3**). Grossly, after one week

siTNFα wounds were observed to be redder within the wound bed than controls and the margins of the epithelium was noticeably advanced from the original wound margins. When inspecting the control treated wounds this reddening of the wound bed and epithelial changes were not observed. In strong contrast however, control treated wounds appeared to have remained largely unchanged from the original wounds.

After two weeks of treatment these difference are even more dramatic. The siTNFα treated wounds were on average less than 10% their original area, while the controls remained at almost 50% of the original wound size. These striking differences can be easily appreciated in the gross digital images in Figure 6-4a, while two-dimensional cartoon representation of the average wound area are presented in Figure 6-4b. Appreciably, after two weeks the un-epithelialized wound gap is a deep red color, indicating significant vascular perfusion of the wound bed, while the control wounds appear white to tan in color and noticeably shallow regions in the backs of the animals. Similarly to what we observed in the siMMP-9 treated wound described in Chapter 5, the wounds treated with siTNFα bandages were integrated into their bandages. This was to a noticeably lesser degree than the siMMP-9 treated wounds from before, but it was common for all of the siTNFα treated wounds and contributed to at least three of the wounds appearing to have not fully regenerated their epithelium. This behavior was not observed for any of the control bandage treated wounds.

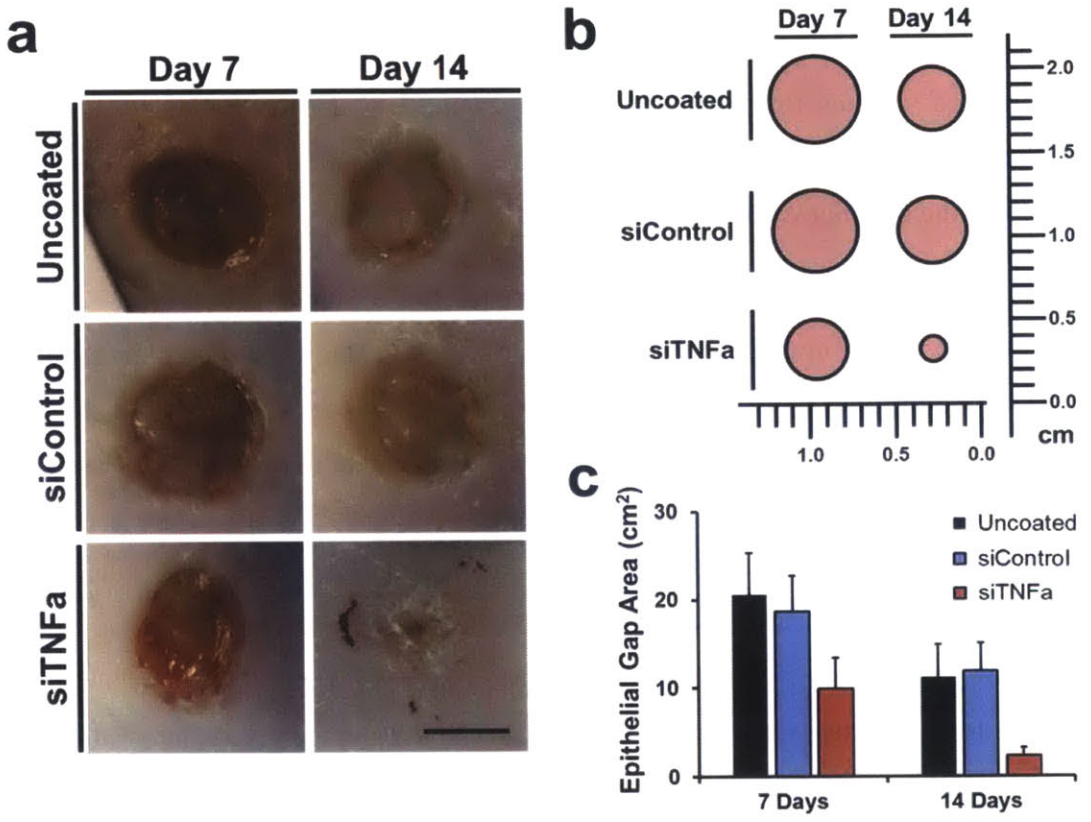

Figure 6-4 Gross digital imaging analysis of wound healing

(a) Representative digital images of wounds treated with uncoated Tegaderm and LbL coated bandages containing siControl or siTNFα siRNA sequences. Scale bar = 5 mm. (b) Two-dimensional representation of approximate epithelial gap areas as measured from digital wound analysis. (c) Epithelial gap area. Data is mean ± S.D., n = 6.

6.3.3 *In Vivo* Knockdown of TNFα in a Mouse Model of Chronic Wound Healing

For each mouse one wound was selected for histological processing and one was prepared for protein and RNA isolation for subsequent analysis. Immunohistochemical (IHC) staining for TNFα demonstrated a significant reduction of its expression both within the granulation tissue and at the wound margin of mice treated with siTNFα films compared to controls. Wounds from mice treated with either uncoated and siControl bandages showed especially deep IHC staining for TNFα in the granulation tissue formed near the wound margins after two weeks. Wounds treated with siTNFα-9 bandages, however, exhibited a significantly lower level of staining for TNFα, primarily localized in only a few cells. Quantification of the

number of TNFα positive cells within the stained wound sections supported this finding, where siTNFα treated wounds had fewer TNFα positive cells after one week, which was even more dramatically reduced after two weeks to approximately one-sixth the number observed in the control sections.

The expression of TNFα in wounds treated with siTNFα containing bandages was reduced by almost 52 ± 11% after one week, increasing to 74 ± 9% at two weeks **(Figure 6-5b)**. This dramatic change in TNFα expression supports the findings we observed by immunohistochemical staining for TNFα in wound sections. As TNFα signaling is known to operate in a positive feedback loop, it is difficult to determine whether the dramatic changes in TNFα expression observed at two weeks is more a consequence of early TNFα expression reduction or the continued reduction of TNFα due to our intervention.

Analysis of the IHC staining for TNFα in the sections from treated wounds demonstrates a stark difference between the siTNFα treatment group and the two controls. Wounds treated with uncoated and siControl bandages were observed to stain deeply for TNFα throughout the granulation tissue and around the wound margins. The number of TNFα staining cells was nearly four times as high in the control wounds as compared to the siTNFα treated wounds. This finding is in agreement with the known operation of TNFα to function as a pro-inflammatory cytokine, driving its own expression as well as driving the recruitment of inflammatory cells to the tissue which express TNFα. Staining at the wound margins in the control treated wounds demonstrated significant enhancement in TNFα expressing cells over the two week period, whereas wounds treated with the siTNFα bandages saw the total number of TNFα positive cells drop by over 80% in wound margin tissues.

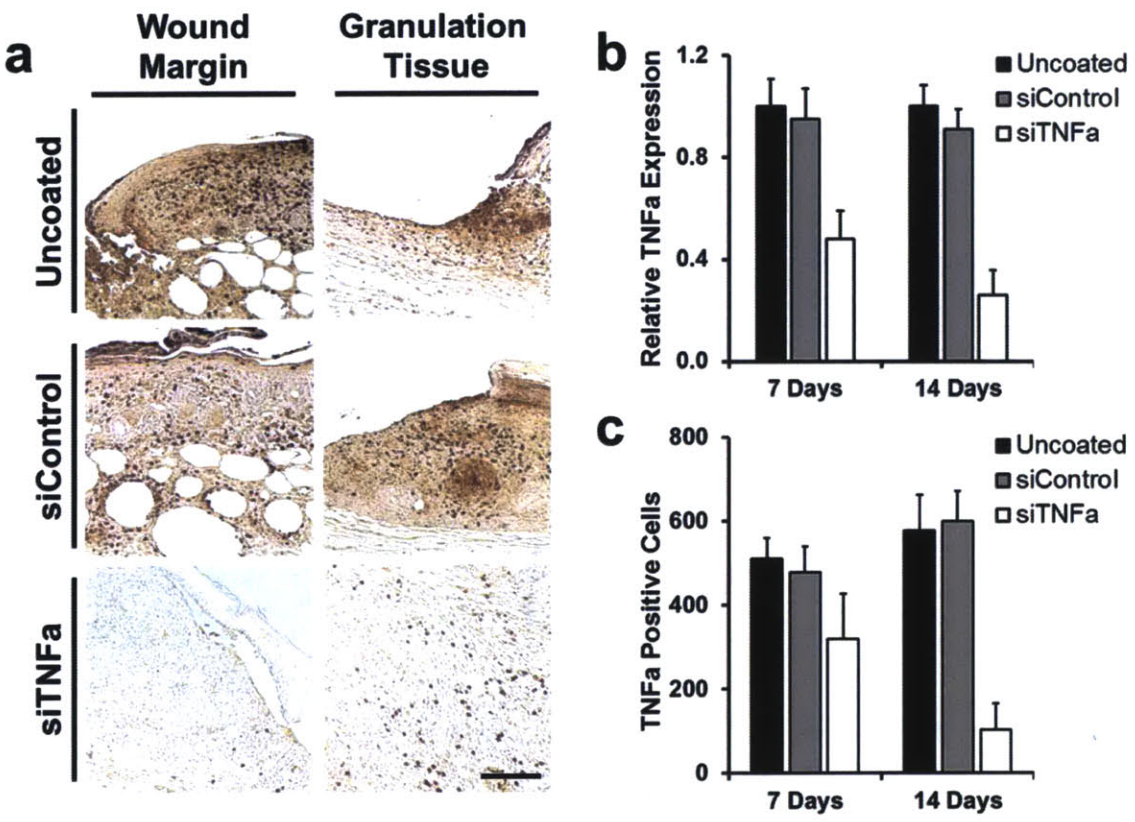

Figure 6-5 Analysis of tumor necrosis factor alpha expression within wounds treated wounds of Lepr$^{db/db}$ mice

(a) Representative images of IHC staining for TNFα in sections of wounds treated with either uncoated, siControl, or siTNFα bandages. Scale bar = 100 μm. (b) qRT-PCR analysis of TNFα expression, all values are relative to uncoated control wounds, β-actin is used for reference. (c) Quantification of TNFα positive cells per wound section. Data is mean ± S.D., n = 3.

Concentration of TNFα expressing cells in the granulation tissue is indicative of an ongoing inflammatory process in the control treated wounds that is not present in the siTNFα treated wounds. This is important as cells that are expressing TNFα drive other inflammatory cells within the tissue as well as signal for many of the cells important in the wound healing process to undergo apoptosis and to not contribute to the creation of new tissue. This is especially important in the case of fibroblasts and keratinocytes within the granulation tissue, as TNFα signaling can depress their mobility and proliferative ability, while also reducing their production of important ECM proteins.

It has been previously described that the pro-inflammatory cytokine interleukin-1 beta (IL-1β) is an important mediator in the inflammatory process underlying diabetic chronic wound healing. TNFα signaling is known to stimulate the expression of IL-1β, which is believed to contribute to the pathology of TNFα overexpression in these wounds. We investigated how the knockdown of TNFα altered IL-1β expression to evaluate its potential impact on the wound healing processes we observed. After one week there was no statistically significant difference between the IL-ab expression for the three different treatment groups. After two weeks however, the siTNFα treated wound expression of IL-1β was approximately 40% of that in either of the control groups. This reduction is quite substantial, but it is difficult to determine if this reduction is directly due to reduced TNFα stimulated IL-1β production, or due to larger changes in the wound environment including altered cellular populations between the three treatment groups.

6.3.4 Histological Evaluation of Wound Healing

Wounds selected for histological processing were serially sectioned with levels at every 250 um with H&E, MTC, and unstained sections taken at every level for full histological characterization of the treated wounds. H&E sections at each level were used to generate two-dimensional projections of the wound areas to quantify epithelial closure and wound contraction. Epithelial margins are readily identified in H&E stained sections, denoted in **Figure 6-5a** by black arrows. Wound contraction can be quantified from the displacement of the panniculus carnousis (PC) muscle, a muscle underlying the dermis in rodents, which does not regenerate and thus can be used to approximate the original wound margin in histological sections.

Wounds treated with siTNFα bandages exhibited significantly accelerated re-epithelialization without significant changes in wound contraction. Similar to what we observed grossly after one week, the siTNFα treated wounds had an epithelial gap of only 40% of the original wound area, while control treated wounds were up to 75% of the original wound size. After two weeks this difference was even more pronounced, with three of the wounds appearing to have completely re-epithelialized in the siTNFα treated wounds, whereas all of the control wounds were still around 40% of the original wound area. Rapid re-epithelialization is important in successful wound healing as it closes the healing tissue off from the outside, greatly reducing the risk of infection and helping to reduce related chronic inflammation.

Evaluation of the histological sections of the different treated wounds demonstrates the striking differences due to siTNFα knockdown. After two weeks, the siControl and uncoated bandages treated wounds had only managed to generate a thin flimsy tissue connecting the wound edges. This tissue is only a few cell layers thin in regions, with very light eosin staining. The tissue formed in the control wounds is largely not integrated with the uninjured dermis. The majority of the tissue appears to be connected more to the underside of the skin, with the fibrotic tissue formed around the cut margins of the PC muscle, than the damaged edge of the healing dermis. The siTNFα treated wounds in contrast are exceptionally well integrated into both the PC muscle and the dermis, with thick granulation tissue extension reaching out to the wound margins.

The granulation tissue in all of the treated wounds stains lighter with eosin than the uninjured dermis. The granulation tissue in the siTNFα treated wounds, however, stains more consistently across the wound bed and appears more similar to the uninjured dermis staining than either of the controls. In addition to the level of connective tissue staining, the siTNFα treated wounds are also much more cellular than the tissue formed in the control wounds. The tissue in the center of the siTNFα treated wounds had distinct epidermal and dermal cell layers, exhibiting the native structure of the skin, while control wounds had only a thin poorly organized fibrous tissue.

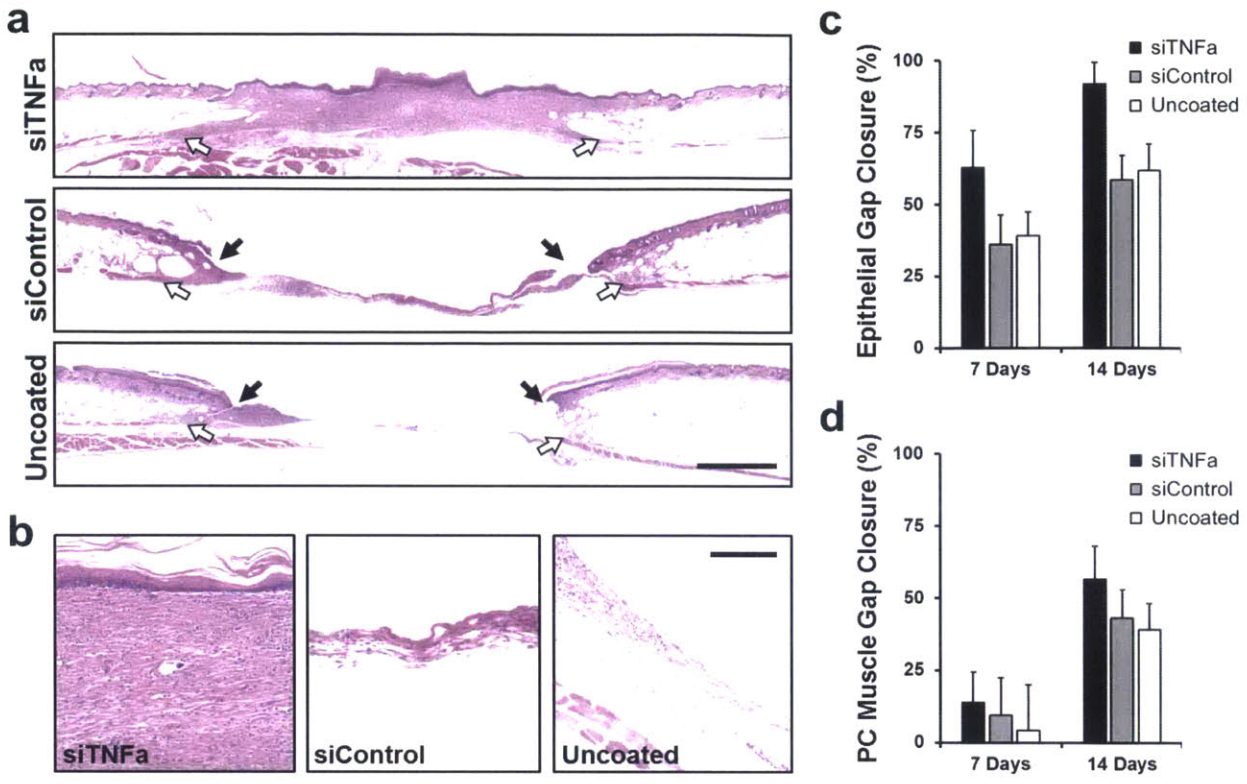

Figure 6-5 Histological evaluation of wound healing

(a) Representative H&E stained wound sections of different treatment groups. Black arrows identify epithelial margins, white arrows identify panniculus carnosus (PC) muscle margins. Scale bar = 1 mm. (b) High power field images of granulation tissue in the center of wounds. Scale bar = 75 μm. (c) Percent closure of epithelial gap from two-dimensional projection of serially sectioned wounds as compared to initial wound area. (d) Percent closure of PC muscle gap from original wound size. Data is mean ± S.D., n = 3.

6.3.5 Evaluating the Impact of TNFα Knockdown on ECM Deposition

TNFα stimulates both the increased expression of MMP-9, the key gelatinase in cutaneous wound healing, as well as reduced expression of collagen. As a result diabetic ulcers, which chronically overexpress TNFα, are known to produce little granulation tissue with significantly reduced collagen density. To investigate this aspect of these chronic wounds we analyzed the treated wounds for connective tissue deposition using Masson's Trichrome stain

(MTC). In the dermis, this stain highlights collagen in blue while cells, keratin, and muscle are deep red in color. The intensity of the blue staining can also be used to draw qualitative assessments of the level of collagen deposition and its relative organization.

Evaluating the MTC stained sections grossly, the differences between the siTNFα treated wounds and the siControl and uncoated wounds is easily apparent. Similar to what was observed for H&E staining, the overall state of wound healing in the siTNFα treated wounds is significantly more advanced than the controls, with near-complete re-epithelialization observed in many of the wound sections. Control treated wounds have significantly impaired epithelial closure with very little granulation tissue formation in the wound center. The collagen staining in the granulation tissue of the siControl and uncoated bandage treated wounds is very similar, with very light blue staining and very low cell density compared to the uninjured dermis in the same section. The siTNFα treated wound in contrast is very cellular, while also containing significantly more collagen then control wounds.

The granulation tissue of the siTNFα treated wound is significantly more cellular than its uninjured dermis. This is expected in normally healing wounds, as the tissue is undergoing rapid proliferation and ECM production. Comparing the granulation tissue found at the wound centers for each treatment group highlights this stark contrast, as the siTNFα treated wounds appear as a densely populated sea of red cells surrounded in deep staining blue collagen, while the control wounds appear light blue to clear with only a few cells visible lying on these thin blue strands **(Figure 6-6b)**. The striking differences in the thickness of the granulation tissue, first appreciated in the H&E stained sections, is also readily observed in the MTC stained sections. The siTNFα treated wounds have a thick and robust wound bed, with a deep red staining keratin-rich epidermis stretching out over the entire wound. Control wounds on the other hand have little keratin staining on the granulation tissue, with little advancement of the epithelial margins visible.

Analysis of the wound margins for the three different treatment groups supports our early findings that were based on H&E staining, where the siTNFα treated wounds are far more advanced than the control wounds. The granulation tissue at the margins in siTNFα treated wounds is over 150um thick, with increased cellularity and comparable collagen staining to the uninjured dermis. The margins in the control wounds in comparison are thin, with a stark change

from the tissue directly adjacent to the wound site and the granulation tissue in the wound bed. The change at the margins in the controls is abrupt, occurring within less than a 300um of the original wound edge. The epidermis appears continuous in the siTNFα treated wounds, while in the controls it abruptly ends near the original wound margins, after two weeks just beginning to contact the healing granulation tissue and attempting to close off the wound.

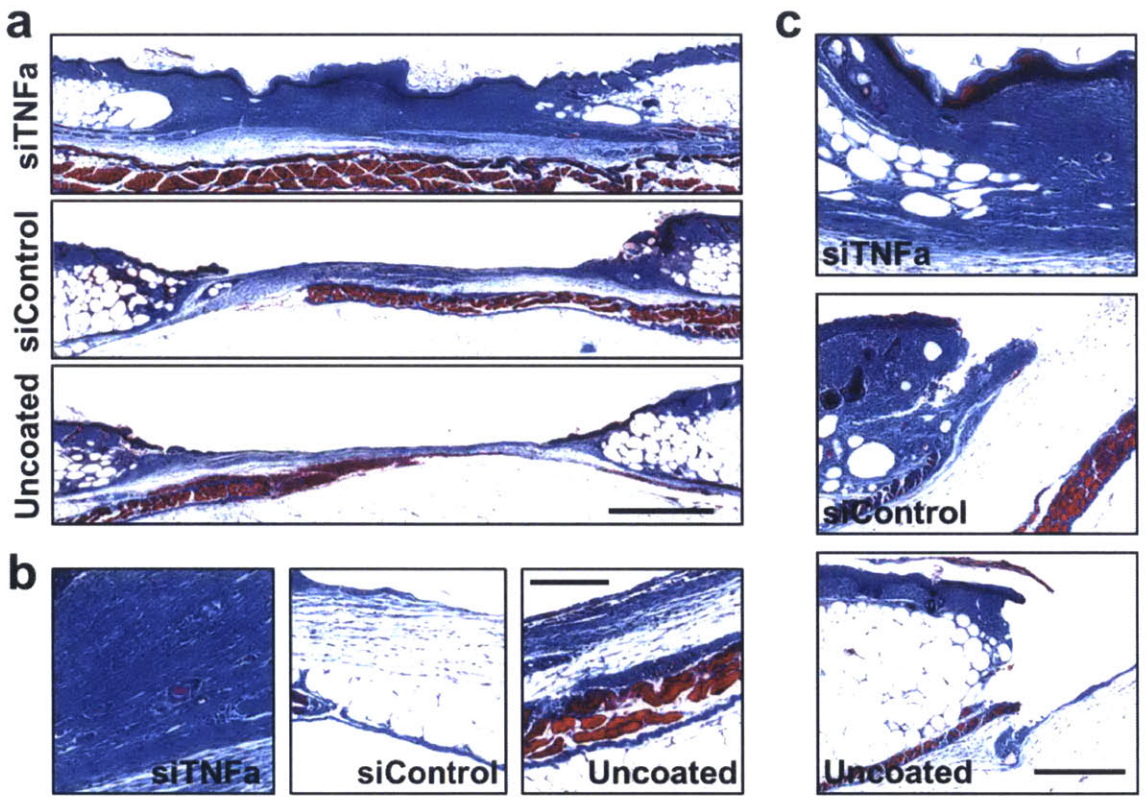

Figure 6-6 Histological analysis of connective tissue in wound healing

(a) Representative full wound sections stained with Masson's Trichrome stain. Scale bar = 1 mm. (b) Representative wound center images, demonstrating the significant differences between the cellularity and level of connective tissue deposition between the different treatments. Scale bar = 100 μm. (c) Representative images of the wound margins for each treatment group. The images are oriented such that the uninjured dermis is on the left and the healing granulation tissue is on the right. Scale bar = 100 μm.

The histological changes in connective tissue deposition were dramatic, however we were interested to see to what extent the change in TNFα expression impacted the expression of collagen in the wounds. Collagen type 1 is the primary form of mature collagen in the dermis, and expression of the alpha 1 subunit of this type of collagen (Col1a1) is known to be negatively impacted by TNFα signaling.[76] Comparing the expression of Coll1a1 in siTNFα treated wounds after one week demonstrated a near 3.4-fold increase in expression compared to uncoated bandages. Interestingly, we noted that the siControl bandages achieved a significant increase in Coll1a expression versus uncoated bandages, nearing 1.6 times the expression as the uncoated. After two weeks this difference diminished to the point of not being significant, while the difference between siTNFα and the controls grew to approximately 5.8-fold increased expression. This substantial increase in collagen expression within the siTNFα treated wounds supports the increased deposition we observed histologically, however it may also be in part due to alterations in cell populations present within the granulation tissue.

6.3.6 Effect of TNFα Knockdown on MMP-9 Expression

We were interested to evaluate the deposition of granulation tissue in the differently treated wounds as it is well-known that overexpression of TNFα contributes to poor ECM deposition and increased proteolytic activity as a consequence of chronic inflammation. TNFα signaling is known to upregulate the expression of MMP-9, which we previously studied the detrimental impact of its overexpression in Chapter 5. In Chapter 5 we detailed how the controlled knockdown of MMP-9 led to improved wound healing in this same mouse model of diabetic chronic wound healing. As such we were very interested to investigate the potential connection here, so as to understand if the improvements we have seen from siTNFα therapy in these wounds may in some part be due to changes in MMP-9 expression.

Immunohistochemical staining for MMP-9 expression demonstrated significantly lower background staining in siTNFα treated wounds than in either control group **(Figure 6-7a)**. The number of MMP-9 positive cells was also significantly reduced in siTNFα treated wounds after two weeks, compared to relatively steady numbers in either of the two control bandage treated wounds **(Figure 6-7c)**. Quantitative PCR analysis of MMP-9 expression in the wounds demonstrated significantly lowered MMP-9 expression in siTNFα treated wounds compared to controls. After one week of treatment, the siTNFα wounds observed an approximate 41 ± 8%

relative reduction in MMP-9 expression compared to uncoated bandage treated wounds. This difference was observed to increase after two weeks, to only 35 ± 13% of that found in the controls **(Figure 6-7b)**.

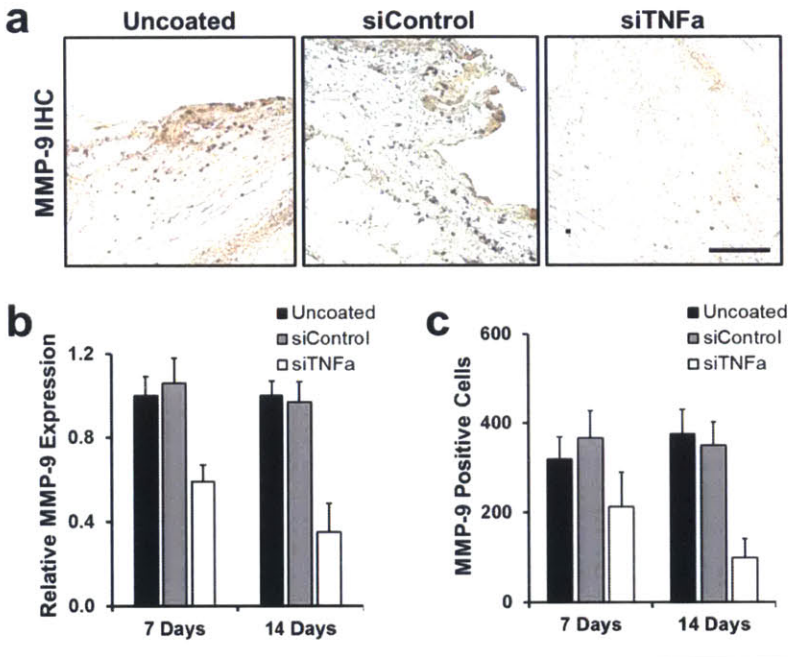

Figure 6-7 Expression of matrix metalloproteinase-9 (MMP-9) within the treated wounds of Lepr$^{db/db}$ mice

(a) Representative images of IHC staining for MMP-9 expression within the granulation tissue of each treatment group. Scale bar = 100 µm. (b) qRT-PCR analysis of MMP-9 expression after one and two weeks of treatment for each group, relative quantification using b-actin for control. (c) Quantitative analysis of MMP-9 positive cells per wound section for each treatment group. Data is mean ± S.D., n = 3.

From these observations it is apparent that the knockdown of TNFα expression within the healing wounds reduces the expression of MMP-9 and the number of MMP-9 positive cells within the wound bed. Due to the complex signaling of TNFα within wound healing as a major contributor in inflammation, it is difficult to know whether this reduced MMP-9 expression is

due to reduced TNFα signaling or due to reduced inflammatory cell recruitment. Our findings suggest that TNFα plays an important role in MMP-9's activity within the healing wounds, however, detailing where in the biological network its impact is greatest is difficult to determine with certainty.

6.3.7 Knockdown of TNFα Reduces Macrophage Population in Wound Bed

The expression of TNFα in healing wounds is largely performed by activated macrophages within the tissue. Evaluating the number of macrophages within healing wounds gives a quantitative assessment for both the level of inflammation within the tissue and for the driving forces for the recruitment of macrophages. It has been previously demonstrated that targeting TNFα systemically using monoclonal antibody therapy reduces the recruitment of macrophages to diabetic ulcer wounds in mice. Here we observe a similar phenomenon, that the knockdown of TNFα within this tissue also reduces the recruitment of macrophages, from approximately 50% of control at one week to 30% at two weeks of treatment.

Macrophages within the uncoated and siControl wounds were observed to densely populate the wound margin **(Figure 6-8a)**. Wounds treated with siTNFα bandages were observed to contain significantly lower numbers of F4/80 positive macrophages at the wound margin. Similarly, the granulation tissue of the control wounds were heavily populated with IHC stained macrophages, while the siTNFα treated wounds held significantly fewer stained cells **(Figure 6-8b)**.

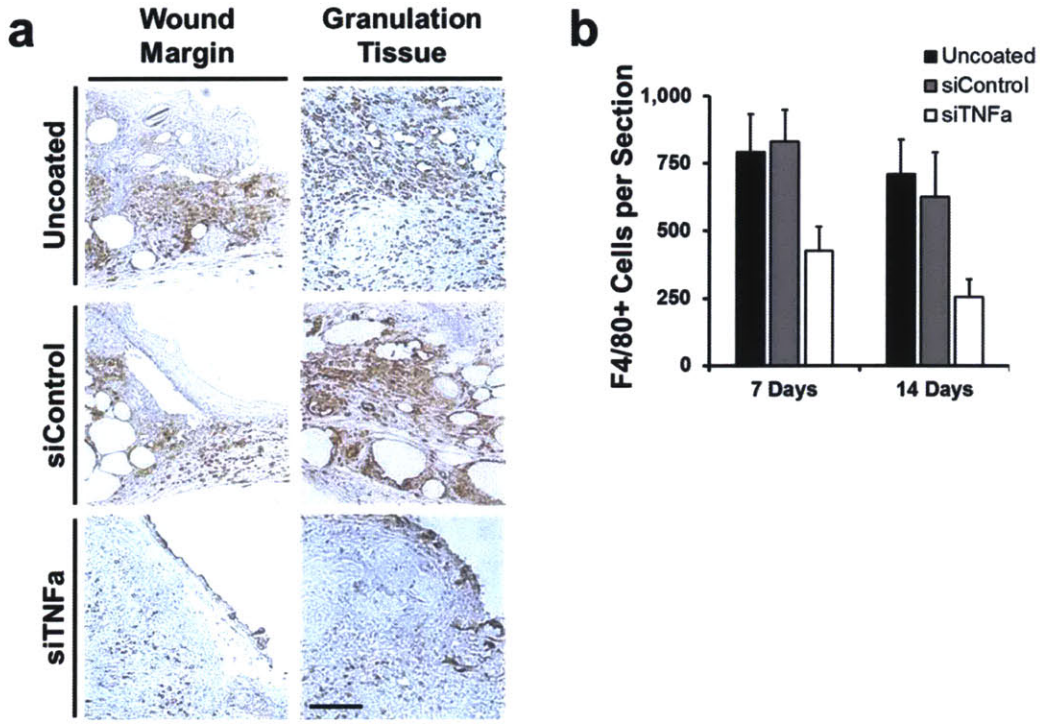

Figure 6-8 IHC analysis of healing wounds for F4/80 positive macrophages

(a) Representative high power images of wound margins and granulation tissue for each treatment group. Scale bar = 75 μm. (b) Quantification of F4/80 positive cells per wound section. Data is mean ± S.D., n = 3.

6.3.8 Reduced Pro-Inflammatory Signaling Improves Vascularity

A very important characteristic of poor healing diabetic ulcers that is clinically very confounding is the decreased vascularity of the healing tissues in these wounds. Chronic TNFα expression and inflammation are known to impair vessel formation.[43] This decreased vascularity is well represented in this mouse model of chronic healing. Grossly, we had observed increased redness in the siTNFα treated wounds, compared to relative pallor in the controls wounds. This finding is indicative of increased vascular perfusion in the siTNFα tissues, however to thoroughly investigate this finding we performed CD31 staining of wound sections to quantify the number of vessels within the healing granulation tissues.

Immunohistochemical staining of vessels with CD31 demonstrated significant differences in the level of vascularity between the granulation tissues of the siTNFα treated wounds and the control wounds **(Figure 6-9a)**. After one week there was approximately twice the density of

vessels in the siTNFα treated wounds compared to controls, and this difference increased after two weeks to nearly three times the control **(Figure 6-9b)**. The number of vessels observed in the siControl and uncoated bandage treated wounds was statistically similar at one week and two weeks. In normal wound healing, the granulation tissue would be growing rapidly through this period, demanding increased blood flow from more vessels. The fact that there is little change observed in the number of vessels in these wounds suggests that the slow growing granulation tissue is potentially hypoxic, a common finding in ulcerative healing.

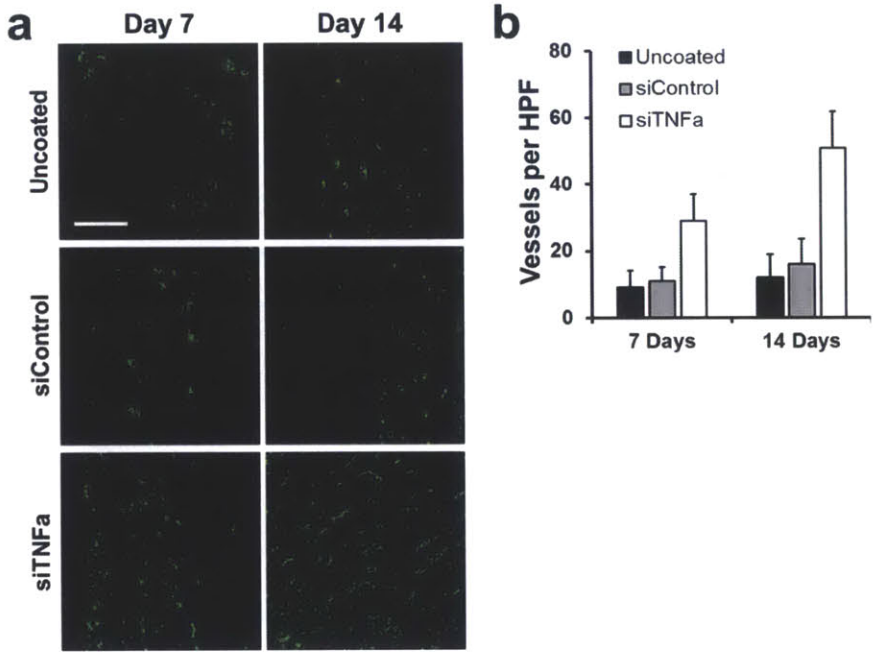

Figure 6-9 Quantification of vascular differences for each treatment group

(a) Representative images of IHC staining for CD31+ endothelial cells outlining vessels within the healed tissue. Scale bar = 50 μm. (b) Quantification of the stained vessels per high power field. Data is mean ± S.D., n = 6.

It is important to note here that increased vascularity can be due to a number of factors in the wound healing process. The siTNFα treated wounds contained significantly more granulation tissue, increasing both the driving force for vascularity, as well as the scaffold for it. As the control treated wounds contained significantly less dense granulation tissue, it is understandable that there would be less demand for perfusion, and as such fewer vessels. Here again it is difficult to discern that intervention with TNFα knockdown increased vascularity in

the healing tissue or that due to the increased granulation tissue more vessels were created. It is most likely a combination of these two forces, as TNFα overexpression is known to impair neovascularization *in vitro* and *in vivo* when applied exogenously, and as we have detailed within this chapter it also plays a crucial role in the degenerative effects of inflammation on ECM production and accumulation in the wound.[77]

6.3.9 Epidermal Closure is Accelerated in siTNFα Treated Wounds

One of the most important milestones in healthy wound healing is complete epithelial closure of the wound bed. This shields the healing tissue from outside irritants and greatly reduces the risk for bacterial colonization and infection. The epidermis serves a protective role for the healing granulation tissue, allowing for the time intensive remodeling phase of wound healing to occur. The epidermis is a striated structure, where the proliferative cells that populate it remain as a basal layer. These proliferative cells are constantly dividing and creating more cells that travel upwards, generating the stratum spinosum and granulosum layers until finally creating the stratum corneum layer with the cellular debris and keratin.[23]

KI-67 stain is a highly specific nuclear marker for cell proliferation.[78] Immunohistochemical analysis of KI-67 expression is the gold standard to estimate the level of proliferative activity within tissues, which is commonly used in the evaluation of neoplasms in the clinic. Here we can use KI-67 IHC staining to approximate the level of proliferation within the healing tissue as well as to evaluate the viable epidermal margins. As the structure of the epidermis contains a highly proliferative basal cell layer, KI-67 staining in the dermis highlights this line of proliferative cells beautifully, giving great insight into the exact margin of the proliferating epidermis.

IHC staining for KI-67 in wound section from the three different treatment groups lends strong support in favor of our previous histological analysis. The proliferating epidermis is seen to stretch out across the entire wound section in siTNFα treated wounds after two weeks, fully closing the wound bed off from the outside environment. In either of the control sections, no such advancement is observed **(Figure 6-10 a&d)**. Investigating the epidermis at the original wound margins demonstrates the dramatic differences between the control wounds and those

treated with siTNFα bandages. Black arrows highlight the end point of the proliferating epidermis. In the siTNFα treated wounds, no distinct epidermal margin was easily discernable, demonstrating the level of epidermal migration and remodeling that had already occurred in these wounds **(Figure 6-10b)**.

The center of wound sections stained for KI-67 demonstrates another important distinction between the siTNFα treated wounds and the siControl or uncoated bandage groups **(Figure 6-10c)**. The number of proliferating cells in the granulation tissue at the center of the wound is significantly increased in the siTNFα wounds. The proliferating epidermis is seen to stretch out into the wound center, albeit with some level of disorganization at the very center of the wound. This is not observed in either of the control groups, with very few KI-67 positive cells seen in any of the wound sections at the center of the granulation tissue. The siTNFα treated wounds were observed to have nearly four times the number of KI-67 positive cells as compared to control wounds. This striking difference was maintained even after two weeks of treatment **(Figure 6-10e)**.

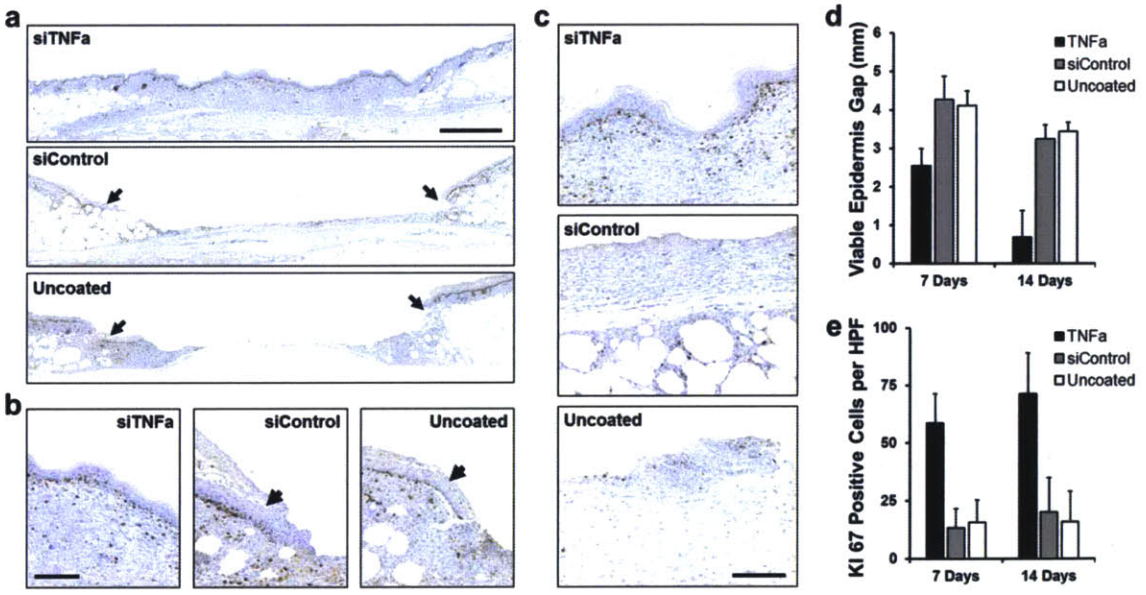

Figure 6-10 Analysis of cell proliferation within the treated wounds using KI-67 immunohistochemical staining

(a) Representative full wound sections for each treatment group. KI-67 stains proliferative cells, including the basal endothelial cells that are continuously proliferating to generate the epidermis

and stratum corneum. Scale bar = 1 mm. (b) Representative high power images of the wound margins. Black arrows highlight the end of the proliferative epidermis. The proliferative epidermis is seen to extend beyond the wound margin in the siTNFα treated wounds. Scale bar = 50 μm. (c) Representative images of the wound centers for the different treatment groups. The proliferative epidermis is seen to extend out to the wound center, with many KI-67 positive proliferative cells observed in the granulation tissue, few such cells are observed in the granulation tissue of the control wounds. Scale bar = 75 μm. (d) Quantification of the gap observed in the proliferating epidermis at the wound center section. (e) Number of KI-67 positive cells observed in the granulation tissue for each treatment group. Data is mean ± S.D., n = 3.

6.3.10 Knockdown of TNFα Improves Wound Collagen Content and Maturation

TNFα signaling within the wound is known to decrease collagen expression within the healing tissue as well as upregulate the expression of metalloproteinases that degrade the accumulating extracellular matrix. These two important factors contribute significantly to the lack of granulation tissue formation within the healing wound and impair the wound healing process. By reducing the expression of TNFα, we observed increased expression of collagen type I, the mature form of collagen within the dermis. We had also observed reduced expression of MMP-9 within the wound, creating a parallel with our previous studies in Chapter 5. Here we used picrosirius red staining, similar to what we presented in Chapter 5, to analyze the accumulation and maturation of collagen content within the healing tissue.

Collagen is a naturally birefringent macromolecule within the dermis. When stained using picrosirius red this natural characteristic is enhanced, so that even thin fibrils of collagen, collagen type III, within the dermis can be easily identified. Using polarizing light microscopy we can quantify both the total amount of collagen as a fraction of the tissue volume and the relative ratio of mature collagen type I to early fibular collagen type III. Evaluating the three treatment groups in this way, we observed dramatic differences in these measurable criteria. The siTNFα treated wounds were seen to accumulate significantly more collagen over the two week study period, reaching nearly a five-fold increase in total collagen within the wound versus

controls. The control treated wounds on the other hand were observed to increase in collagen content at a much slower rate, with little change observed over the study period.

The relative composition of the collagen within the wound was also significantly different between the treatment groups. The siTNFα treated wounds contained much more mature collagen type I compared to control wounds. This characteristic of the siTNFα treated wounds was present after one week of treatment, and increased through week two. Control treated wounds appeared stagnant, with a steady balance of collagen I to collagen III at both one and two weeks of treatment. The amount of collagen type I within these control treated wounds was observed to increase slightly over the study period.

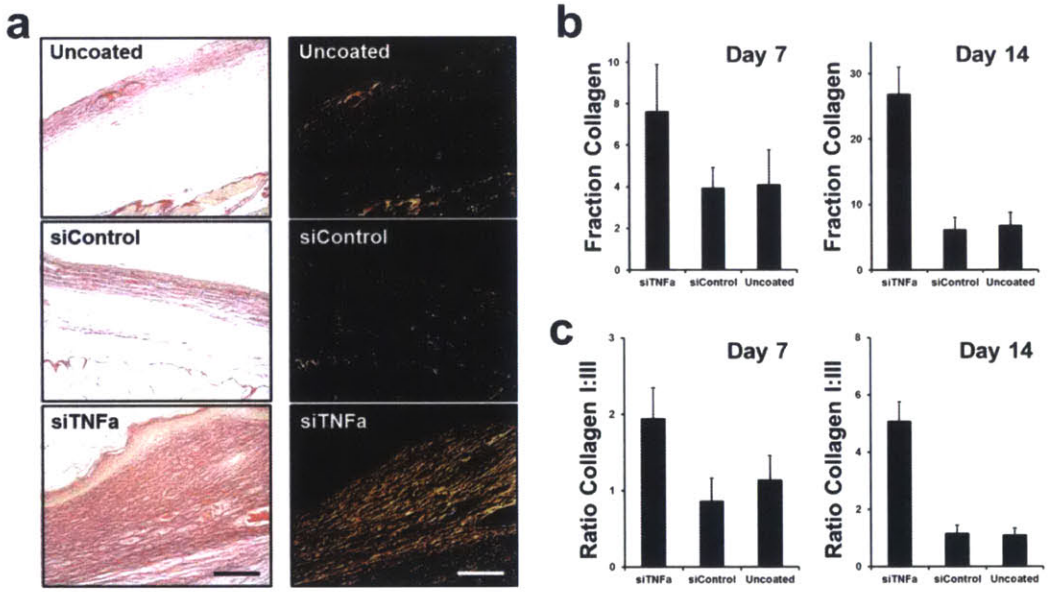

Figure 6-11 Analysis of collagen within the granulation tissue

(a) Representative brightfield and polarized light microscope images of uncoated, siControl, and siTNFα treated wounds. Scale bar = 200 μm. (b) Quantification of total fraction collagen of the granulation tissue as measured by ImageJ digital image analysis. (c) Ratio of orange collagen type I and green collagen type 3 areas within the healing granulation tissues. Image analysis performed using ImageJ.

These data together suggest that the treatment of these chronically impaired wounds with siTNFα therapy greatly accelerated collagen accumulation and maturation within the wound bed compared to either siControl or uncoated bandage treated wounds. Importantly, this

accumulation of collagen within the granulation tissue forms the scaffold on which the epidermis can migrate to achieve wound closure. In our analysis of wound closure we found that siTNFα treated wounds also achieved significantly more advanced wound closure than controls. These findings then support the hypothesis that by improving the accumulation of granulation tissue within the healing wound bed, considering the increase in mature collagen type I content, may contribute to this improved wound healing we have observed in siTNFα treated wounds.

6.4 Discussion

Diabetic foot ulcers are the most common cause of non-traumatic lower limb amputations in the United States. They cost an approximate $11 billion to the US healthcare system every year.[10] Current options for DFU patients have only demonstrated limited success, with almost half of these patients unable to achieve 100% wound closure.[79, 80] As the prevalence of diabetic foot ulcers is expected to nearly double in the next two decades, there is a great unmet need to create new approaches to better address this condition.[11]

Tumor necrosis factor alpha is chronically overexpressed in diabetic ulcers and has been previously demonstrated to play a pathologic role in chronic ulcers. The role of TNFα has been extensively explored in a number of pathologies related to chronic inflammation including rheumatoid arthritis, Crohn's disease, and psoriasis. These investigations have developed a number of clinically viable biologic approaches to reduce TNFα signaling within a myriad of tissues. These approaches however have devastating side effects and are incredibly cost-intensive. A number of previous researches have investigated the potential application of such technologies to target TNFα overexpression within chronic wounds with some success in a related mouse model. Here we present a new paradigm in this approach, unlike previous approaches that focus on the delivery of monoclonal antibodies to target and isolate TNFα, we target the overexpression of TNFα locally within the tissue of interest to directly reduce its expression and thus its pathologic role.

The film we describe in this work, [PrS/CaP/PrS/Lap], when applied to a commercially available nylon bandage was able to deliver tunable quantities of siRNA over a two week period. *In vitro* we demonstrated how this approach allowed for the controlled delivery of siRNA for the

specific knockdown of the reporter gene GFP with little impact on cell viability, supporting our previously published work as described in Chapter 3.

The approach we took in this work parallels that which we described in Chapter 5, where we targeted MMP-9 overexpression using a different ultrathin coating. These two chapters together begin to form a more complete understanding of the complex physiology underlying the pathologies of this chronic wound model. Whereas earlier we looked to directly influence the expression of the ECM protease MMP-9 within the ulcer, here we looked further up in the inflammatory pathway to target a key upregulated mediator of chronic inflammation believed to be important in this disease. As we described in this chapter, the role of TNFα in promoting inflammation and subsequently impairing wound healing is supported by our findings that the siRNA-specific knockdown of TNFα improved these features.

It was observed that reducing the expression of TNFα within the healing tissues accelerated wound closure and significantly improved granulation tissue formation. The tissue that was formed within the wound bed contained significantly increased quantities of mature collagen, had nearly three times the number of vessels, and was seen to be significantly more proliferative. The biology underlying the pathologic role of TNFα is a complex interconnected network of positive feedback loops which touch many of the important aspects of inflammation. Knockdown of TNFα within these chronic wounds resulted in significant reductions in MMP-9 expression and IL-1β expression, while increasing the expression of collagen. Taken together these findings suggest a substantial shift in the inflammatory state of these wounds, supported by the significant reduction in the number of macrophages seen in the wounds, due to TNFα knockdown.

We believe that the approach outlined here represents a second supporting argument for the use of LbL technology in localized RNAi. We targeted a known primary mediator of inflammation within a well-established animal model of chronic diabetic wound healing and successfully reduced its expression by up to 74% after two weeks. Using local controlled delivery of siRNA is a powerful technology that we believe can have an enormous impact in a variety of areas outside of wound healing, including other forms of regenerative medicine, cancer therapy, and molecular biology.

6.5 References

1. Apelqvist, J., Ragnarson-Tennvall, G. & Larsson, J. Topical treatment of diabetic foot ulcers: an economic analysis of treatment alternatives and strategies. Diabet Med 12, 123-128 (1995).

2. Apelqvist, J., Ragnarson-Tennvall, G., Larsson, J. & Persson, U. Long-term costs for foot ulcers in diabetic patients in a multidisciplinary setting. Foot Ankle Int 16, 388-394 (1995).

3. Boulton, A.J., Vileikyte, L., Ragnarson-Tennvall, G. & Apelqvist, J. The global burden of diabetic foot disease. Lancet 366, 1719-1724 (2005).

4. Apelqvist, J., Castenfors, J., Larsson, J., Stenstrom, A. & Agardh, C.D. Wound classification is more important than site of ulceration in the outcome of diabetic foot ulcers. Diabet Med 6, 526-530 (1989).

5. Larsson, J. & Apelqvist, J. Towards less amputations in diabetic patients. Incidence, causes, cost, treatment, and prevention--a review. Acta Orthop Scand 66, 181-192 (1995).

6. Jeffcoate, W.J. & Harding, K.G. Diabetic foot ulcers. Lancet 361, 1545-1551 (2003).

7. Zimmet, P., Alberti, K.G. & Shaw, J. Global and societal implications of the diabetes epidemic. Nature 414, 782-787 (2001).

8. Wellen, K.E. & Hotamisligil, G.S. Inflammation, stress, and diabetes. The Journal of clinical investigation 115, 1111-1119 (2005).

9. Singh, N., Armstrong, D.G. & Lipsky, B.A. Preventing foot ulcers in patients with diabetes. Jama 293, 217-228 (2005).

10. Gordois, A., Scuffham, P., Shearer, A., Oglesby, A. & Tobian, J.A. The health care costs of diabetic peripheral neuropathy in the US. Diabetes Care 26, 1790-1795 (2003).

11. Huang, E.S., Basu, A., O'Grady, M. & Capretta, J.C. Projecting the future diabetes population size and related costs for the U.S. Diabetes Care 32, 2225-2229 (2009).

12. Ramsey, S.D. et al. Incidence, outcomes, and cost of foot ulcers in patients with diabetes. Diabetes Care 22, 382-387 (1999).

13. Pierce, G.F. Inflammation in nonhealing diabetic wounds: the space-time continuum does matter. Am J Pathol 159, 399-403 (2001).

14. Ladwig, G.P. et al. Ratios of activated matrix metalloproteinase-9 to tissue inhibitor of matrix metalloproteinase-1 in wound fluids are inversely correlated with healing of pressure ulcers. Wound Repair Regen 10, 26-37 (2002).

15. Moor, A.N., Vachon, D.J. & Gould, L.J. Proteolytic activity in wound fluids and tissues derived from chronic venous leg ulcers. Wound Repair and Regeneration 17, 832-839 (2009).

16. Komesu, M.C., Tanga, M.B., Buttros, K.R. & Nakao, C. Effects of acute diabetes on rat cutaneous wound healing. Pathophysiology 11, 63-67 (2004).

17. Hehenberger, K., Heilborn, J.D., Brismar, K. & Hansson, A. Inhibited proliferation of fibroblasts derived from chronic diabetic wounds and normal dermal fibroblasts treated with high glucose is associated with increased formation of l-lactate. Wound Repair Regen 6, 135-141 (1998).

18. Blakytny, R. & Jude, E. The molecular biology of chronic wounds and delayed healing in diabetes. Diabet Med 23, 594-608 (2006).

19. Siqueira, M.F. et al. Impaired wound healing in mouse models of diabetes is mediated by TNF-alpha dysregulation and associated with enhanced activation of forkhead box O1 (FOXO1). Diabetologia 53, 378-388 (2010).

20. Lobmann, R. et al. Expression of matrix-metalloproteinases and their inhibitors in the wounds of diabetic and non-diabetic patients. Diabetologia 45, 1011-1016 (2002).

21. Hayden, D.M., Forsyth, C. & Keshavarzian, A. The Role of Matrix Metalloproteinases in Intestinal Epithelial Wound Healing During Normal and Inflammatory States. Journal of Surgical Research 168, 315-324 (2011).

22. Liu, Y. et al. Increased Matrix Metalloproteinase-9 Predicts Poor Wound Healing in Diabetic Foot Ulcers. Diabetes Care 32, 117-119 (2009).

23. Gurtner, G.C., Werner, S., Barrandon, Y. & Longaker, M.T. Wound repair and regeneration. Nature 453, 314-321 (2008).

24. Longaker, M.T. & Gurtner, G.C. Introduction: wound repair. Semin Cell Dev Biol 23, 945 (2012).

25. Werner, S. & Grose, R. Regulation of wound healing by growth factors and cytokines. Physiol Rev 83, 835-870 (2003).

26. Navarro-Gonzalez, J.F. & Mora-Fernandez, C. The role of inflammatory cytokines in diabetic nephropathy. J Am Soc Nephrol 19, 433-442 (2008).

27. Claxton, M.J., Armstrong, D.G. & Boulton, A.J. Healing the diabetic wound and keeping it healed: modalities for the early 21st century. Curr Diab Rep 2, 510-518 (2002).

28. Falanga, V. Wound healing and its impairment in the diabetic foot. Lancet 366, 1736-1743 (2005).

29. Brem, H. & Tomic-Canic, M. Cellular and molecular basis of wound healing in diabetes. The Journal of clinical investigation 117, 1219-1222 (2007).

30. Graves, D.T., Liu, R., Alikhani, M., Al-Mashat, H. & Trackman, P.C. Diabetes-enhanced inflammation and apoptosis--impact on periodontal pathology. J Dent Res 85, 15-21 (2006).

31. Cheng, T.L. et al. Thrombomodulin Promotes Diabetic Wound Healing by Regulating Toll-Like Receptor 4 Expression. J Invest Dermatol (2015).

32. Martin, P. & Leibovich, S.J. Inflammatory cells during wound repair: the good, the bad and the ugly. Trends Cell Biol 15, 599-607 (2005).

33. Rosner, K. et al. Immunohistochemical characterization of the cutaneous cellular infiltrate in different areas of chronic leg ulcers. Apmis 103, 293-299 (1995).

34. Ashcroft, G.S. et al. Tumor necrosis factor-alpha (TNF-alpha) is a therapeutic target for impaired cutaneous wound healing. Wound Repair Regen 20, 38-49 (2012).

35. Goren, I., Kampfer, H., Podda, M., Pfeilschifter, J. & Frank, S. Leptin and wound inflammation in diabetic ob/ob mice: differential regulation of neutrophil and macrophage influx and a potential role for the scab as a sink for inflammatory cells and mediators. Diabetes 52, 2821-2832 (2003).

36. Goren, I. et al. Systemic anti-TNFαlpha treatment restores diabetes-impaired skin repair in ob/ob mice by inactivation of macrophages. J Invest Dermatol 127, 2259-2267 (2007).

37. Khanna, S. et al. Macrophage dysfunction impairs resolution of inflammation in the wounds of diabetic mice. PLoS ONE 5, e9539 (2010).

38. Taylor, P.C. Anti-TNF therapy for rheumatoid arthritis and other inflammatory diseases. Mol Biotechnol 19, 153-168 (2001).

39. Taylor, P.C. Anti-tumor necrosis factor therapies. Curr Opin Rheumatol 13, 164-169 (2001).

40. Xu, F., Zhang, C. & Graves, D.T. Abnormal cell responses and role of TNF-alpha in impaired diabetic wound healing. Biomed Res Int 2013, 754802 (2013).

41. Han, Y.P., Tuan, T.L., Wu, H., Hughes, M. & Garner, W.L. TNF-alpha stimulates activation of pro-MMP2 in human skin through NF-(kappa)B mediated induction of MT1-MMP. J Cell Sci 114, 131-139 (2001).

42. Barrientos, S., Stojadinovic, O., Golinko, M.S., Brem, H. & Tomic-Canic, M. Growth factors and cytokines in wound healing. Wound Repair and Regeneration 16, 585-601 (2008).

43. Tellechea, A. et al. Angiogenic and Inflammatory Markers in Diabetic Wound Healing. Diabetes 59, A325-A325 (2010).

44. Wetzler, C., Kampfer, H., Stallmeyer, B., Pfeilschifter, J. & Frank, S. Large and sustained induction of chemokines during impaired wound healing in the genetically diabetic mouse: prolonged persistence of neutrophils and macrophages during the late phase of repair. J Invest Dermatol 115, 245-253 (2000).

45. Goren, I., Muller, E., Pfeilschifter, J. & Frank, S. Severely impaired insulin signaling in chronic wounds of diabetic ob/ob mice: a potential role of tumor necrosis factor-alpha. Am J Pathol 168, 765-777 (2006).

46. Uemura, S. et al. Diabetes mellitus enhances vascular matrix metalloproteinase activity: role of oxidative stress. Circ Res 88, 1291-1298 (2001).

47. So, T., Ito, A., Sato, T., Mori, Y. & Hirakawa, S. Tumor necrosis factor-alpha stimulates the biosynthesis of matrix metalloproteinases and plasminogen activator in cultured human chorionic cells. Biol Reprod 46, 772-778 (1992).

48. Solis-Herruzo, J.A., Brenner, D.A. & Chojkier, M. Tumor necrosis factor alpha inhibits collagen gene transcription and collagen synthesis in cultured human fibroblasts. J Biol Chem 263, 5841-5845 (1988).

49. Regan, M.C. et al. Tumor necrosis factor-alpha inhibits in vivo collagen synthesis. Surgery 113, 173-177 (1993).

50. Rapala, K. et al. Tumor necrosis factor alpha inhibits wound healing in the rat. Eur Surg Res 23, 261-268 (1991).

51. Bitzer, M. et al. A mechanism of suppression of TGF-beta/SMAD signaling by NF-kappa B/RelA. Genes Dev 14, 187-197 (2000).

52. Arancibia, R. et al. Tumor necrosis factor-alpha inhibits transforming growth factor-beta-stimulated myofibroblastic differentiation and extracellular matrix production in human gingival fibroblasts. J Periodontol 84, 683-693 (2013).

53. Penn, J.W., Grobbelaar, A.O. & Rolfe, K.J. The role of the TGF-beta family in wound healing, burns and scarring: a review. Int J Burns Trauma 2, 18-28 (2012).

54. Lee, C.W. et al. TNF-alpha induces MMP-9 expression via activation of Src/EGFR, PDGFR/PI3K/Akt cascade and promotion of NF-kappaB/p300 binding in human tracheal smooth muscle cells. Am J Physiol Lung Cell Mol Physiol 292, L799-812 (2007).

55. Vaday, G.G. et al. Fibronectin-bound TNF-alpha stimulates monocyte matrix metalloproteinase-9 expression and regulates chemotaxis. J Leukoc Biol 68, 737-747 (2000).

56. Lee, I.T., Lin, C.C., Wu, Y.C. & Yang, C.M. TNF-alpha induces matrix metalloproteinase-9 expression in A549 cells: role of TNFR1/TRAF2/PKCalpha-dependent signaling pathways. J Cell Physiol 224, 454-464 (2010).

57. Rayment, E.A., Dargaville, T.R., Shooter, G.K., George, G.A. & Upton, Z. Attenuation of protease activity in chronic wound fluid with bisphosphonate-functionalised hydrogels. Biomaterials 29, 1785-1795 (2008).

58. Rayment, E.A., Upton, Z. & Shooter, G.K. Increased matrix metalloproteinase-9 (MMP-9) activity observed in chronic wound fluid is related to the clinical severity of the ulcer. Br J Dermatol 158, 951-961 (2008).

59. Stewart, R.J. & Marsden, P.A. Biologic control of the tumor necrosis factor and interleukin-1 signaling cascade. Am J Kidney Dis 25, 954-966 (1995).

60. Mirza, R.E., Fang, M.M., Ennis, W.J. & Koh, T.J. Blocking interleukin-1beta induces a healing-associated wound macrophage phenotype and improves healing in type 2 diabetes. Diabetes 62, 2579-2587 (2013).

61. Taylor, P.C., Williams, R.O. & Maini, R.N. Immunotherapy for rheumatoid arthritis. Curr Opin Immunol 13, 611-616 (2001).

62. Sawant, R.R. et al. Polyethyleneimine-lipid conjugate-based pH-sensitive micellar carrier for gene delivery. Biomaterials 33, 3942-3951 (2012).

63. Guo, P. et al. Engineering RNA for targeted siRNA delivery and medical application. Advanced Drug Delivery Reviews 62, 650-666 (2010).

64. Yin, H. et al. Non-viral vectors for gene-based therapy. Nat Rev Genet 15, 541-555 (2014).

65. PT, H. Building Biomedical Materials Layer-by-Layer. Materials Today 15, 196-206 (2012).

66. Castleberry, S.A., Li, W., Deng, D., Mayner, S. & Hammond, P.T. Capillary Flow Layer-by-Layer: A Microfluidic Platform for the High-Throughput Assembly and Screening of Nanolayered Film Libraries. ACS Nano (2014).

67. Decher, G. Fuzzy nanoassemblies: Toward layered polymeric multicomposites. Science 277, 1232-1237 (1997).

68. Matsusaki, M., Ajiro, H., Kida, T., Serizawa, T. & Akashi, M. Layer-by-layer assembly through weak interactions and their biomedical applications. Advanced Materials 24, 454-474 (2012).

69. Su, X.F., Kim, B.S., Kim, S.R., Hammond, P.T. & Irvine, D.J. Layer-by-Layer-Assembled Multilayer Films for Transcutaneous Drug and Vaccine Delivery. ACS Nano 3, 3719-3729 (2009).

70. Becker, A.L., Johnston, A.P.R. & Caruso, F. Layer-By-Layer-Assembled Capsules and Films for Therapeutic Delivery. Small 6, 1836-1852 (2010).

71. Macdonald, M.L., Rodriguez, N.M., Shah, N.J. & Hammond, P.T. Characterization of tunable FGF-2 releasing polyelectrolyte multilayers. BioMacromolecules 11, 2053-2059 (2010).

72. Sullivan, S.R. et al. Validation of a model for the study of multiple wounds in the diabetic mouse (db/db). Plast Reconstr Surg 113, 953-960 (2004).

73. Davidson, J.M. Animal models for wound repair. Arch Dermatol Res 290 Suppl, S1-11 (1998).

74. Trengove, N.J. et al. Analysis of the acute and chronic wound environments: the role of proteases and their inhibitors. Wound Repair Regen 7, 442-452 (1999).

75. Neely, A.N., Clendening, C.E., Gardner, J. & Greenhalgh, D.G. Gelatinase activities in wounds of healing-impaired mice versus wounds of non-healing-impaired mice. J Burn Care Rehabil 21, 395-402 (2000).

76. Buck, M., Houglum, K. & Chojkier, M. Tumor necrosis factor-alpha inhibits collagen alpha1(I) gene expression and wound healing in a murine model of cachexia. Am J Pathol 149, 195-204 (1996).

77. Liu, R., Bal, H.S., Desta, T., Behl, Y. & Graves, D.T. Tumor necrosis factor-alpha mediates diabetes-enhanced apoptosis of matrix-producing cells and impairs diabetic healing. Am J Pathol 168, 757-764 (2006).

78. Yerushalmi, R., Woods, R., Ravdin, P.M., Hayes, M.M. & Gelmon, K.A. Ki67 in breast cancer: prognostic and predictive potential. Lancet Oncol 11, 174-183 (2010).

79. Gottrup, F. & Apelqvist, J. Present and new techniques and devices in the treatment of DFU: a critical review of evidence. Diabetes Metab Res Rev 28 Suppl 1, 64-71 (2012).

80. Wieman, T.J., Smiell, J.M. & Su, Y. Efficacy and safety of a topical gel formulation of recombinant human platelet-derived growth factor-BB (becaplermin) in patients with chronic neuropathic diabetic ulcers. A phase III randomized placebo-controlled double-blind study. Diabetes Care 21, 822-827 (1998).

Chapter 7
Silencing Connective Tissue Growth Factor *In Vivo* Reduces Contraction in a Rat Model of Burn Scar Wound Healing

7.1 Introduction

In Chapters 5 & 6 we described the application of two different LbL films assembled on a commercially available bandage for the controlled local delivery of siRNA into diabetic chronic wounds. Both of these approaches were demonstrated to accelerate wound closure and improve outcomes out to two weeks *in vivo*. This was done by targeting two different upregulated proteins that are believed to be pathologic in chronic wounds, one an important ECM proteinase expressed in the dermis and the other a powerful pro-inflammatory cytokine. Here we use the same film as described in Chapter 5 to coat a commercially available silk suture and demonstrate closely maintained in vitro properties of the film coating. We then test this suture *in vivo* in a well-established third-degree burn dermal scarring model in rats to knockdown connective tissue growth factor, a known mediator of scar formation in dermal wounding.

Wound healing is an incredibly complex process that we have described in detail throughout the majority of this thesis. Much of this focus has been aimed at improving impaired chronic wound healing. Here we target a very different pathology that affects almost every patient with a wound, which is scar formation. Be it from serious trauma, plastic surgery, or playground roughhousing, scars can detrimentally impact our quality of life.[1-3] Importantly, scar formation from serious trauma can often be debilitating by reducing range of motion and joint mobility and subsequently impairing function.[4-6] The current treatment options for scars offers little comfort for patients, often consisting of topical steroids which have serious undesirable side-effects, surgical resection which has a low success rate and a considerable risk of infection, and simple silicone-based gel wraps.[7, 8]

The goal of normal cutaneous wound healing is to regenerate the naturally protective structures of the skin quickly so as to reduce the risk of infection.[9-11] This process is made up of a number of different stages including hemostasis, inflammation, proliferation, and remodeling.[12] The last two of these stages, proliferation and remodeling, are especially important in determining scar formation as they pertain to the production of the healing extracellular matrix (ECM) and its reorganization.[13-16] In scarring, this healing process does not regenerate all of the native structures of the skin, leaving a poorly organized dense collagen-rich matrix that is often highly contracted by myofibroblasts.[2, 17-19] This is often the case in hypertrophic scarring, which can result from traumatic injuries such as burn wounds.[20-23]

As scarring is such an omnipresent occurrence in daily life, a great deal of research has been focused on understanding the underlying pathologic causes for it. Much of this research has focused on the dysregulated signaling of transforming growth factor-beta (TGFβ) within wounds,[15, 24-28] as it has been shown that upregulated expression of TGFβ is correlated to increased fibrosis in animal models of cutaneous scarring.[14, 29-33] Proper signaling of TGFβ within wounds, however, is necessary for healthy wound healing, as it orchestrates a number of disparate pathways integral in effective tissue regeneration and remediation of inflammation.[24, 27, 34] To this end it has been demonstrated that the inhibition of TGFβ *in vivo* significantly reduces scar formation but also greatly impairs wound healing.[35] For this reason efforts to target TGFβ signaling directly raise concerns about the total impact of such therapies.

Connective tissue growth factor (CTGF) is a key downstream mediator of TGFβ signaling that has been demonstrated to regulate many of its pro-fibrotic effects.[36-43] CTGF has been shown to play an important role in regulating many key cellular processes within wound healing, including cell proliferation and migration as well as myofibroblasts differentiation and ECM production.[39-41, 44, 45] CTGF also functions to assist in TGFβ-based stimulation of collagen and tissue inhibitor of metalloprotenase-1 (TIMP-1) expression.[46-49] A number of previous reports have described the potentially pathologic overexpression of CTGF within fibrotic diseases, including dermal scarring, where its increased expression has been well-characterized within keloids.[46, 50-53]

As CTGF has been demonstrated to function as a key mediator of scar formation in vivo, targeting its expression as a means of reducing scar formation is logical.[25, 26, 30, 54, 55] Previous

research has demonstrated some success in this approach using anti-sense RNA therapy; however, these approaches have focused on direct bolus injection of un-encapsulated siRNA.[56-60] This leaves the delivered siRNA open to rapid degradation and clearance from the target tissue, significantly reducing its efficacy. Even with these drawbacks, these reports have demonstrated significant siRNA-specific reduction in CTGF expression leading to substantial changes in scar formation. These works as a whole build a compelling case for targeted anti-CTGF therapies in the treatment of scar production, but also give evidence for the need to develop more effective techniques for controlled siRNA delivery.

We have previously described the use of layer-by-layer (LbL)[61-65] assembly to construct ultrathin polymer films for the controlled localized delivery of siRNA into chronic wounds to significantly accelerate wound healing *in vivo*. These reports have focused on the delivery of siRNA from a commercially available woven nylon bandage applied directly into healing wounds. To apply this technology to anti-scar therapy we first need to decide on an animal model to use. We chose to conduct this research in a rat third-degree burn model as it has been demonstrated to form highly reproducible scars[66-68] which are known to overexpress CTGF.[69, 70] Burn scars however do not present open wounds, as is the case for excisional models, thus requiring us to make adjustments to what substrate we coat for implantation into the healing burn wound. For this purpose we used a commercially available silk suture. Coating sutures for anti-scar therapy has the added benefit of being widely applicable in the arena of scar therapy, as many scars are the result of surgical procedures or traumatic injury, where sutures would already be used.

In this work we describe the application of an ultrathin polymer film coating applied to a commercially available silk suture for the controlled local delivery of siRNA into healing third-degree burns. This coating was first thoroughly investigated *in vitro* to demonstrate efficacy of siRNA delivery from the coated substrate, achieving sustained levels of siRNA-specific gene knockdown for up to five days with a controlled siRNA release profile. In vivo these coated sutures were directly placed into healing burns on the dorsum of rats and produced significant siRNA-specific reductions in targeted gene expression. The controlled knockdown of CTGF within the healing burns resulted in greatly reduced scar contraction, improved tissue

remodeling, and the regeneration of important native tissue structures such as papillae which are lost in all other control groups.

7.2 Methods and Materials

7.2.1 Materials

Poly 2 (20 kDa) was synthesized as previously reported.[71] Chitosan (15 kDa) and dextran sulfate (500 kDa) were purchased from Sigma Aldrich company (Manassas, VA). SiRNA sequences were synthesized by Dharmacon (Lafayette, CO); alexafluor 488-labeled and 546-labeled siRNA was purchased from Qiagen (Valencia, CA). Ethicon 4-0 Perma-Hand Silk suture were purchased from Santa Cruz Biotechnology Inc. (Dallas, TX). Phosphate-buffered saline (PBS, 10x), Advanced-MEM, fetal bovine serum, antibiotic-antimycotic solution, and 100 mM L-Glutamine solution were purchased from Invitrogen (Carlsbad, CA). NIH-3T3, HeLa, and MDA-MB-231 cells were purchased from Cell Biolabs (San Diego, CA). All antibodies were purchased from Abcam (Cambridge, MA).

7.2.2 Layer-by-layer film preparation

Films were deposited on oxygen plasma treated sutures. Sutures were cleaned in ethanol and then in RNase free UltraPure^{TM} water (Life Technologies) prior to plasma treatment. Oxygen plasma treatment was performed for 3 minutes on high setting. Sutures were then immediately immersed in a solution of the polycation Poly 2 for a minimum of one hour. Assembly of LbL films was performed using a Carl Zeiss HMS-DS50 stainer. [Poly 2/DS] base layers were deposited through sequential polymer adsorption steps (2 mg ml^{-1}, pH 5.0) of 10 minutes. Between each polymer deposition step the bandages were washed twice in RNase free water (pH 5.0). Assembly of [CHI/siRNA] film was deposited similarly. Chitosan (1mg ml^{-1}, pH 5.0) was adsorbed for 10 minutes and siRNA (20 μg ml^{-1}, pH 5.0) was adsorbed for 15 minutes. All solutions were prepared in RNase free water, adjusted to a pH of 5.0.

Film growth was characterized for films built on silicon wafers by a Veeco Dektak 150 profilometer. Incorporation of fluorescently labeled siRNA into films built on nylon bandages was followed using a Nikon A1R Ultra-Fast Spectral Scanning confocal microscope. Total siRNA incorporation within films was measured by rapid dissolution in a 1M NaCl solution with vigorous agitation for films assembled on sutures and quantified using a fluorescent plate reader.

Release studies were performed in PBS (pH 7.4, 37°C) and in cell conditioned media (37°C). Release was quantified by fluorescence of the released labeled siRNA read using a fluorescent plate reader.

7.2.3 *In Vitro* LbL Bandage Evaluation

Cells were cultured in Advanced-MEM media with 5% FBS, 1% antibiotic-antimycotic, and 2mM L-glutamine. Cells were seeded at an initial density of 5,000 cells per well in a 48-well plate. After one day LbL coated sutures (3 cm, cut to 1 cm lengths) were placed in culture with the cells. The suture coatings either contained GFP-specific siRNA or a control siRNA sequence or were uncoated. Uncoated suture was used as the control to test the cytotoxicity of the film. Mean cell fluorescence was measured by flow cytometry, using a BD FACSCalibur flow cytometer. Cell viability was quantified using AlamarBlue assay (Life Technologies). Analysis of GFP expression and cell viability were performed after 3 and 5 days of treatment.

7.2.4 *In Vivo* siRNA Delivery

All animal studies were approved by the MIT Institutional Animal Care and Use Committee (IACUC) and by the Subcommittee on Research Animal Care (IACUC) of the Massachusetts General Hospital. Animals were housed and cared for in the USDA-inspected MIT Animal Facility under federal, state, local, and NIH guidelines for animal care. Six week old Sprague-Dawley rats (~200g, n=3) were purchased from Charles River Laboratories (Wilmington, MA). Three groups of rats were used: (1) CTGF siRNA (siCTGF) suture treated, (2) control siRNA (siControl) suture treated, and (3) uncoated suture treated.

Prior to wounding, rats were anesthetized with isoflurane. Hair was removed from the backs of rats using an electric clipper. Six burn wounds were created on the dorsum of each rat by applying the end of a pre-heated brass block ($\geq$ 95°C) for 10 seconds. Each wound was created with a single application of a pre-heated brass block. This protocol results in a non-lethal, full-thickness, third-degree burn measuring approximately 1cm^2. Burns were spaced evenly down the midline of the rat starting from the top of the back and going down to 2 cm above the tail. Each rat received all three treatment groups, with two burn wounds for each group per rat. Sutures were placed immediately after burn creation. They were placed running laterally across the burn in a vertical mattress suture, with four total passes through each burn. Sutures were placed through the dermis so as to not impair skin movement. Digital imaging of

burns was performed after 15 and 30 days of treatment. Rats were sacrificed after 30 days. Each wound was cut so tissue for RNA isolation was taken from the treated scar. These wounds were then used for histological analysis.

7.2.5 Histology

Tissues were fixed in zinc fixative without formalin for 48 hours. The excised wounds were cut on center and then embedded cut-face down in paraffin. Sections were taken at the wound center and at two further levels of 250μm reaching a total of 1mm sampling length through the scar. At each level an H&E slide was stained. Unstained slides were also taken for IHC, MTC, and PS staining and analysis of the healing tissue. All sections were 5μm thick. Image analysis was performed using Image J. Orientation of collagen fibers was analyzed using the Image J plugin Orientation J.

7.2.6 Tissue Processing

Isolation of RNA was performed using TRIzol as per the manufacturer's instructions. Synthesis of cDNA was done using iScript cDNA synthesis kit (Bio-Rad Laboratories) and analysis of expression was performed by qRT-PCR using iQ SYBR Green Supermix (Bio-Rad Laboratories) along with selected DNA primer pairs. All experiments were performed in triplicate using a LightCycler 480 (Roche). Relative gene expression was quantified relative to β-actin, a housekeeping gene, using the delta-delta Ct method.

7.2.7 Statistics

Statistical analysis was performed between groups using Student's *t*-test and rectified by ANOVA for comparisons between multiple groups. Values are represented as mean ± s.d. A value of $p < 0.05$ was used to indicate statistical significance.

7.3 Results

7.3.1 Description of LbL Film Architecture

In this report we use the identical film architecture as was described in detail in Chapter 5 of this thesis. The film consists of a hierarchical structure of two simple bilayer films. The first film applied to the surface is a hydrolytically degradable film using Poly2, a poly(beta-

aminoester), and dextran sulfate. On top of this film the siRNA incorporating layer of low molecular weight chitosan and siRNA are applied **(Figure 7-1)**. This film structure was extensively detailed in chapter 5 of this thesis for the ability to independently tune siRNA release rate from total siRNA release. The films efficacy was demonstrated *in vitro* with three different cell lines for the siRNA-specific knockdown of GFP. Further, the film was assembled on a commercially available nylon bandage and demonstrated sustained gene silencing in vivo in a mouse model of chronic diabetic wound healing.

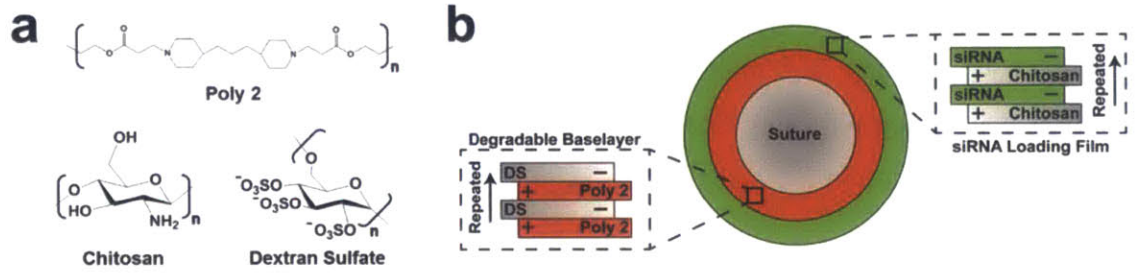

Figure 7-1 Layer-by-layer film architecture for the controlled local delivery of siRNA
(a) Chemical structure of repeating unit of polymers used in film assembly. (b) Schematic cartoon of LbL assembly as constructed on the suture surface.

Here we investigate the application of this film architecture to deliver siRNA into healing burn wounds for scar remediation. As layer-by-layer assembly is an equilibrium driven process that has been reported to be effectively reproducible on a variety of surfaces we began our work by demonstrating this feature of the LbL assembly. Films were assembled on cleaned silk suture, as described in the methods section of this work, that were oxygen plasma treated on high for three minutes. Films were assembled as previously described. Total film incorporation of siRNA was evaluated based on a per centimeter basis as estimating the surface area of the coated silk suture is impractical for the measuring of doses or testing purposes.

7.3.2 Evaluation of LbL Film Coating on Silk Sutures

It was observed that siRNA incorporation on the suture was near-linear, similar to what had been observed for coated nylon bandage and silicon substrates. After 25 layers of the [Chi/siRNA] film were assembled onto the $[Poly2/DS]_{20}$ coated suture a total of 2.1 ± 0.3 μg/cm

of siRNA was incorporated. We evaluated the release of the siRNA form this coated surface in two different release media. The first was PBS at 7.4 and 37°C, this is a common release media for hydrolytically degradable LbL films as it effectively reproduces the body's salt concentration and pH. It however does not capture the biological protein interactions that may also contribute in facilitating material release. To better estimate release in biologic media we used cell conditioned media at 37°C, as described in the methods and materials section of this chapter.

Film coated sutures in both media were observed to sustain the release of siRNA for over nine days, while the PBS testing saw release carried out to nearly 12 days. These findings suggest an impact of release media on the release of the siRNA. This release was followed using a fluorescently labeled siRNA, imaging of the film coating the suture containing the labeled siRNA prior to release is shown in **Figure 7-2c**. The coating is observed to uniformly cover the surface of the woven silk suture with only a few defects observed. A few punctate localizations of fluorescent signal are observed in the coating, primarily lying in the recesses between individual fibers. This is likely aggregation of the accumulating film material between the fibers. After seven days of degradation in the cell conditioned media much of the labeled siRNA is observed to be released from the surface **(Figure 7-2d)**. This release is observed to occur in patches across the coated surface. Large areas of fluorescence are still apparent after the seven days of degradation, but the total level of fluorescence is seen to be significantly reduced.

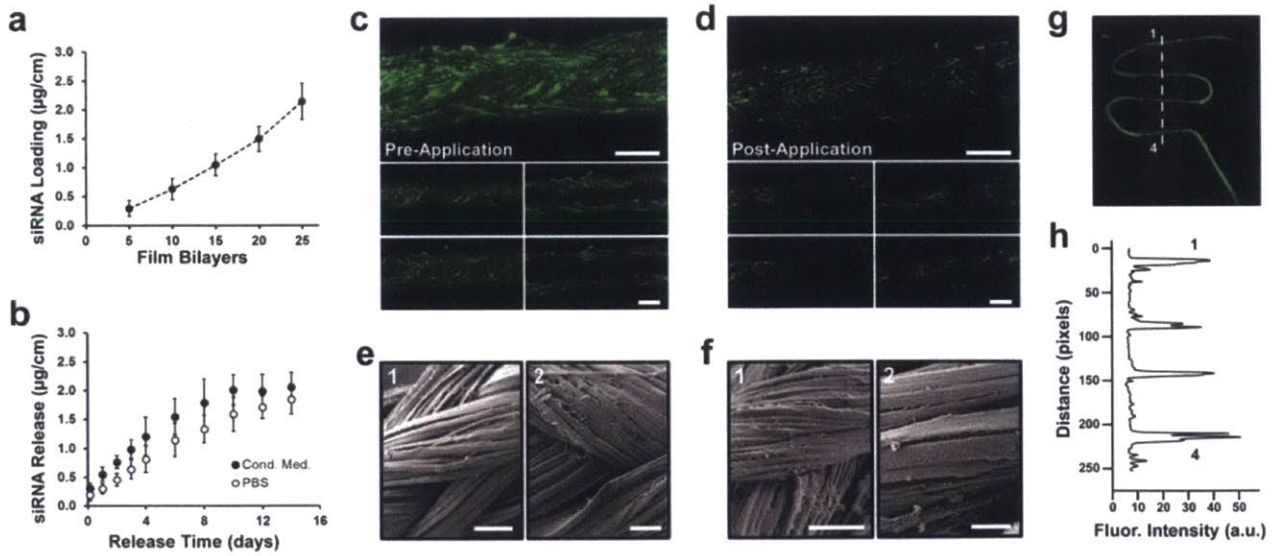

Figure 7-2 *In vitro* characterization of LbL coating applied to a commercially available silk suture

(a) siRNA incorporation per cm of coated suture at 5, 10, 15, 20, and 25 architecture repeats. (b) Release of siRNA over 14 days in vitro in either PBS or cell conditioned media at 37oC. (c) Confocal imaging of fluorescently labeled siRNA incorporated within the film coating prior to degradation. (d) Confocal imaging of fluorescently labeled siRNA incorporated within the film coating five days into degradation in cell conditioned media. (e) SEM images of LbL coated silk suture prior to degradation. Scale bar = 100μm (1), 25μm (2). (f) SEM images of LbL coated silk suture after five days degradation in cell conditioned media. Scale bar = 100μm (1), 15μm (2). (g) LbL coated silk suture drawn through PDMS block and then imaged using a Typhoon 9400 Variable Mode Imager. The number of times the suture has passed through the block is marked from 1-4. (h) Quantification of relative fluorescent signal along the dashed line in (g) with locations 1 and 4 marked as such. Data shown are mean ± S.D., n=3.

Scanning electron micrograph (SEM) images of film coated sutures demonstrate the uniform level of coating across the suture. A few areas of bridging are visible across the woven network of fibers **(Figure 7-2e2)**, but many of the individual fibers are still apparent upon observation **(Figure 7-2e1)**. SEM images of the coated suture after seven days of degradation in cell conditioned media showed significant deterioration in the coating surface. Many noticeable defects are observed along the surface of the coated fibers, with the fibers now appearing to have pieces of swollen film crossing between them **(Figure 7-2f1)**. Close examination of the fibers shows an increasingly rough surface with noticeable flaking off of the coating **(Figure 7-2f2)**. This presentation is similar to what we had observed in our previous studies using this film architecture assembled on nylon bandages in Chapter 3.

The LbL coating on the suture after assembly appeared uniform over the surface; however, we were concerned that the application of the suture would damage the coating so as to remove the siRNA from the surface. To investigate this concern we assembled the LbL film on the surface of the silk suture containing a labeled siRNA and drew the suture through a PDMS block four times **(Figure 7-2g)**. We then imaged the suture *in situ* to evaluate the level of remaining fluorescent material on the suture **(Figure 7-2h)**. What we observed was little to no

detrimental loss of the labeled signal from suture from being drawn though the PDMS. We repeated this test using excised pig dermis and observed a similar phenomenon when we compared fresh suture to that which had been drawn through the skin four times. These findings lend support to the application of such a suture *in vivo*, as we now know that the materials assembled on the surface should be expected to stay with the suture at the site of implantation.

7.3.3 *In Vitro* Investigation of siRNA Delivery from LbL Coated Sutures

We next wanted to investigate the activity of the incorporated siRNA. As we had observed in our previous work that this film was able to effectively achieve significant siRNA-specific gene knockdown, we were interested to validate these finding from the new substrate. To do this we determined that 3cm of the coated suture would be a comparable sample size to test as in our previous experiments in Chapter 5. The sutures were cut to 1cm long lengths and were allowed to settle in the wells. This experimental setup is not ideal, as it could potentially lead to higher levels of siRNA delivery to cells closer to the sutures as well as increased risk of cytotoxicity due to direct physical contact with the suture. We did not observe either of these issues within this work, but we were particularly careful in the slow and deliberately even placement of the cut suture throughout the well.

In vitro studies for the knockdown of the reporter gene GFP were carried out in two cell lines, HeLa and NIH-3T3 that constitutively express GFP. After three days of treatment significant siRNA-specific gene knockdown was observed in both cell lines. GFP reduction after three days was approximately 37% in HeLa cells and 31% in NIH-3T3 cells. This knockdown was observed to increase at five days to nearly 55% in HeLa cells and 48% in NIH-3T3 cells **(Figure 7-3a)**. No significant cytotoxicity was observed for the LbL coated sutures versus sutures that were as purchased **(Figure 7-3b)**.

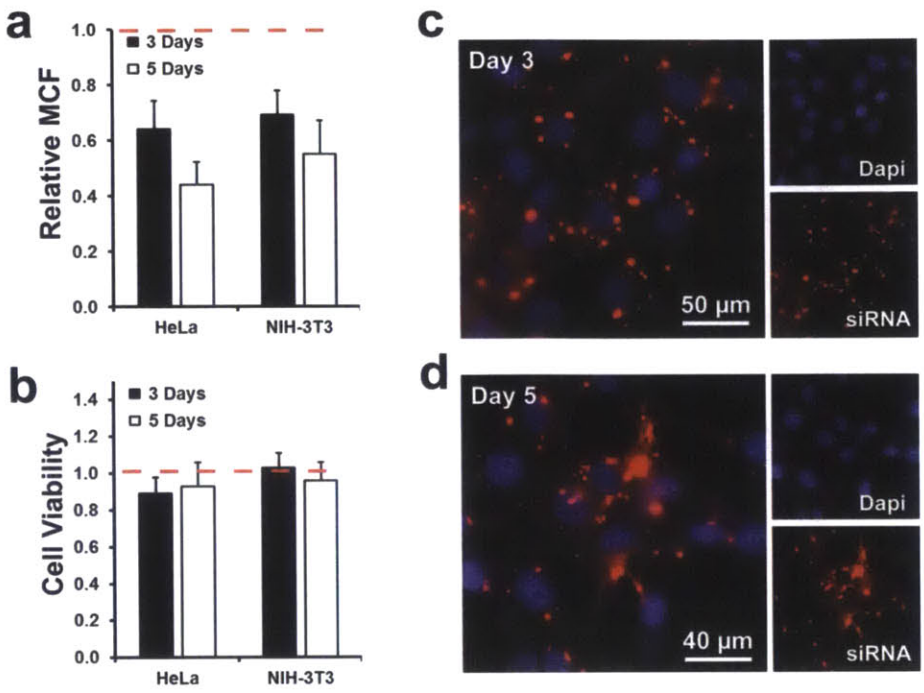

Figure 7-3 ***In vitro*** **evaluation of siRNA delivery from LbL coated sutures**

(a) Flow cytometry analysis of mean cell fluorescence for HeLa and NIH-3T3 cells treated with siGFP containing LbL coated sutures relative to cells treated with siControl containing sutures. (b) Relative cell viability for cells treated with LbL coated sutures and those treated with uncoated sutures. (c) HeLa cell uptake of labeled siRNA film material after three days in culture. (d) HeLa cell uptake of labeled siRNA film material after five days in culture. Data shown are mean ± S.D., n=3.

Uptake of the labeled siRNA in HeLA cells demonstrated a similar pattern as to what was observed in our previous work. Multiple large micron sized particles were seen to accumulate around cells while more diffusely labeled sub-micron localizations were observed intra-cellularly **(Figure 7-3c-d)**. The level of diffuse labeling within the cells increased from day three to day five. This sort of pattern fits well with our imaging studies of the releasing LbL coated suture as we can clearly visualize these multi-micron sized particles flaking off of the coated surface as a product of the coating defects we can observe remaining on the coated surface.

7.3.4 *In Vivo* Application of LbL Coated Sutures

Six week old Sprague-Dawley rats were prepared for surgery under anesthesia. The dorsum of each rat was shaven with an electric clipper and cleaned immediately prior to wounding. Burn wounds were created along the midline of the dorsum using heated (≥ 95°C) brass blocks **(Figure 7-4c)** applied to the skin of the rat for 10 seconds. Wounds were created evenly down the back of each rat starting at the top of the back and ending approximately 2 cm above the tail. Sutures were placed through each burn wound laterally crossing the burn four times in a vertical mattress suture style. The excess suture was clipped near the skin surface leaving as little as possible for the rat to interact with. Sutures were placed such that they ran through the scar but entered and exited through the uninjured margins approximately 1-2mm outside of the burn wound at either margin **(Figure 7-4a)**.

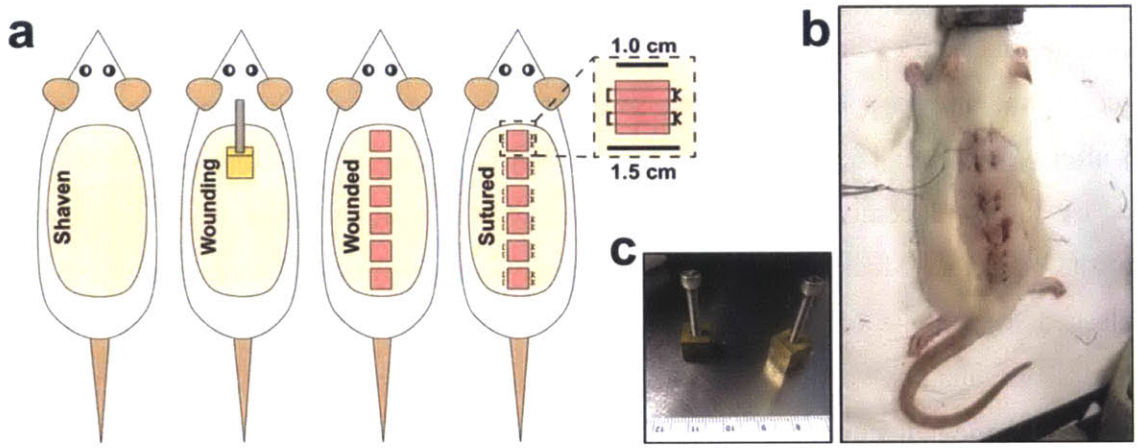

Figure 7-4 The application of LbL coated sutures in a third-degree burn model in rats
(a) Cartoon schematic of the preparation the rats. Rats were shaven with an electric clipper, wounded with a heated (≥ 95°C) brass block, and then four (4) sutures were placed laterally crossing the burn entering and exiting the dermis approximately 1-2mm at the margin. (b) Image of the sutured rat post-operation closely resembles our goal. (c) Image of two of the brass blocks used to create burn injuries.

The wounding and suture placement was carried out as described in **Figure 7-4a** and resulted in a well reproducible model where rats are largely unable to interfere with their sutured burns and the sutures remain intact within the burn wounds **(Figure 7-4b)**. Through the one month study we did not observe any removal of suture from by the rats and the sutures appeared

well tolerated with only limited discomfort noticed in the first few days after wounding. Suture placement is important in this model, as the wounded tissue will quickly become necrotic and lose much of its mechanical stability. This wounded tissue is known to fall off of the burn wounds after approximately two weeks and as such if sutures exit the dermis inside of the burn they will be much easier for the rat to remove. Wounds were treated with one of three types of suture: (1) siCTGF, (2) siControl, and (3) uncoated. Each rat had two wounds treated with each type of suture. Suture location along the back was changed for each rat to control for potential differences in contraction along the back.

7.3.5 CTGF Knockdown Reduces Contraction of Burn Wounds *In Vivo*

Digital imaging of burn wounds was performed at the day of wounding, so called day 0 and after 15 and 30 days post-wounding **(Figure 7-5a)**. Grossly, the wounds are identical initially after wounding. The brass blocks create a uniform $1cm^2$ square burn that is only slightly obscured by suture placement. After 15 days the siCTGF wounds appear less contracted than either of the controls. Measuring the total scar area was complicated by the eschar having not fully released from some of the wounds **(Figure 7-5b)**. Quantification of the scar area was performed from analysis of digital wound images using ImageJ. The scar margin was determined from the hair line margins. After 15 days of treatment the scar area was significantly reduced in both siControl and uncoated suture treated wounds, indicating increased contraction within these burns compared to the siCTGF burns.

After 30 days of treatment the siCTGF treated scars appear significantly wider than the control treated burns, maintaining nearly twice the average scar width **(Figure 7-5c)**. Many of the control wounds appeared dramatically contracted, with an exaggerated hourglass characteristic to them. Total scar area in siCTGF treated wounds was approximately 167% that in burns treated with siControl sutures and 150% that of uncoated sutures. Interestingly it was observed that contraction within the siCTGF burns was especially impaired around the site of suture placement while regions of the scar far away from the suture appear significantly more contracted. This is distinct from what was observed in control wounds, where the area of suture placement was where the highest degree of contraction was observed.

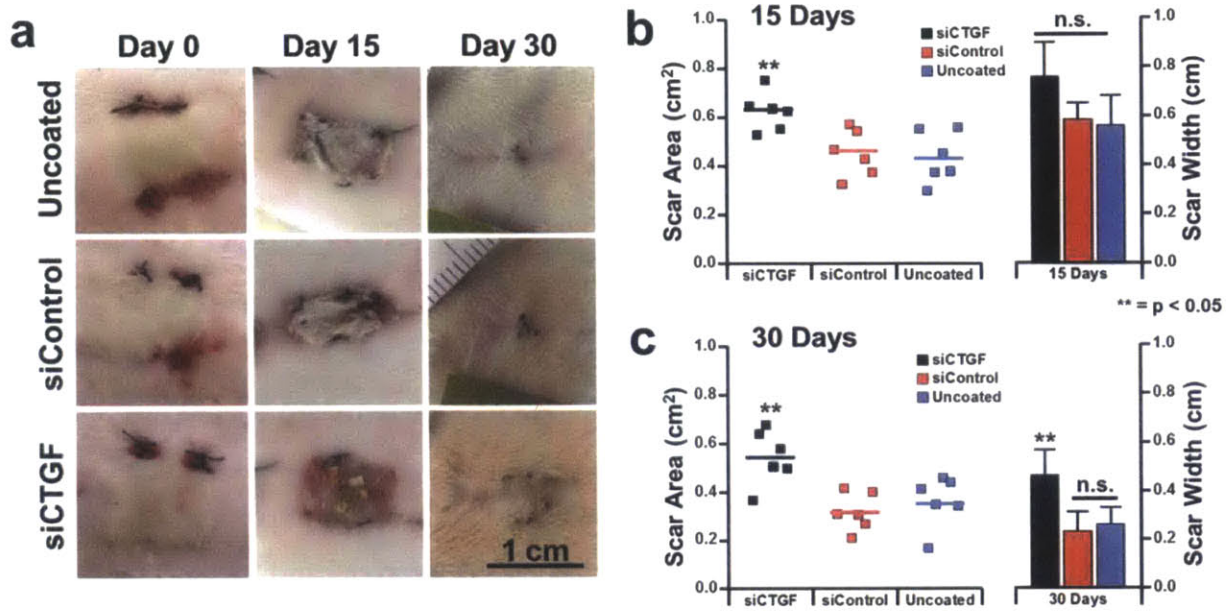

Figure 7-5 Wound analysis by digital image quantification

(a) Representative digital images of wounds immediately after suture placement, after 15 days of treatment and after 30 days of treatment. (b) Quantification of wound images after 15 days. Both scar area and lateral width are elevated in the siCTGF wounds, indicating reduced contraction. (c) Quantification of wound images after 30 days of treatment. Both scar area and lateral width are elevated in the siCTGF wounds compared to controls, demonstrating significantly reduced contraction. Data shown are mean ± S.D., n=6.

7.3.6 *In Vivo* Silencing of CTGF and Its Effects on Fibrosis Related Gene Expression

Connective tissue growth factor is a key mediator of the pro-fibrotic wound healing response to TGFβ signaling in cutaneous wound healing. Its expression *in vivo* has been previously connected to upregulated expression of a number of important proteins in scar production, including: alpha-smooth muscle actin (αSMA), tissue inhibitor of metalloproteinase-1 (TIMP-1), and collagen (Col1a1) **(Figure 6)**. It has been previously demonstrated that the knockdown of CTGF during dermal wound healing results in significantly reduced expression of these proteins and subsequently reduced local fibrosis. In this work we hypothesized that the

controlled local delivery of siRNA targeting CTGF would have a similar response, by reducing local CTGF expression we could also reduce the expression of these known downstream mediators of scar formation.

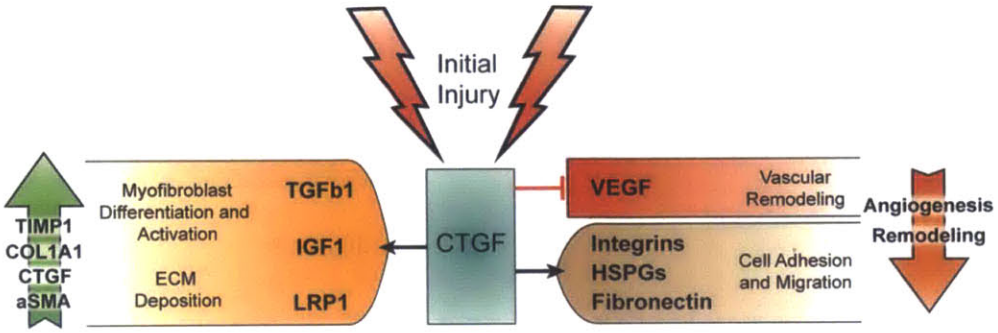

Figure 6 Cartoon schematic of selected CTGF mediated pathways important in fibrosis
CTGF is known to mediate a number of diverse interactions between cell surface receptors, ECM proteins, and soluble growth factors and cytokines. These interactions influence a wide range of cellular behavior during wound healing.

Gene expression was determined by qRT-PCR for mRNA expression in tissues isolated from within the sutured burn wounds and compared to expression from unwounded dermis of the same rat. The expression of CTGF within the burn wound treated with siCTGF sutures was reduced by approximately 36% percent compared to controls after 30 days of treatment **(Figure 7-7a)**. CTGF expression was significantly elevated within all burn wounds when compared to the uninjured dermis; however, the relative level of upregulation was significantly different between the treatment groups. No difference was observed between the siControl and uncoated treatment groups.

Alpha smooth muscle actin is expressed by myofibroblasts within healing wounds, which act to drive wound contraction. For this reason overexpression of αSMA within wounds is considered detrimental, as wound contraction often contributes to scar formation, poor tissue mobility, and subsequent functional impairments. Reduced αSMA expression has been previously demonstrated to reduce wound contraction in animal models and in *in vitro* studies. The expression of αSMA was significantly reduced within wounds treated with the siCTGF delivering sutures compared to either control group. Wounds treated with siControl containing

sutures were observed to express αSMA at approximately 1.6 times that found in siCTGF treated wounds **(Figure 7-7b)**. We believe this increased expression of αSMA within the control wounds is a contributing factor to the decrease we observed in total scar area and scar width for these wounds.

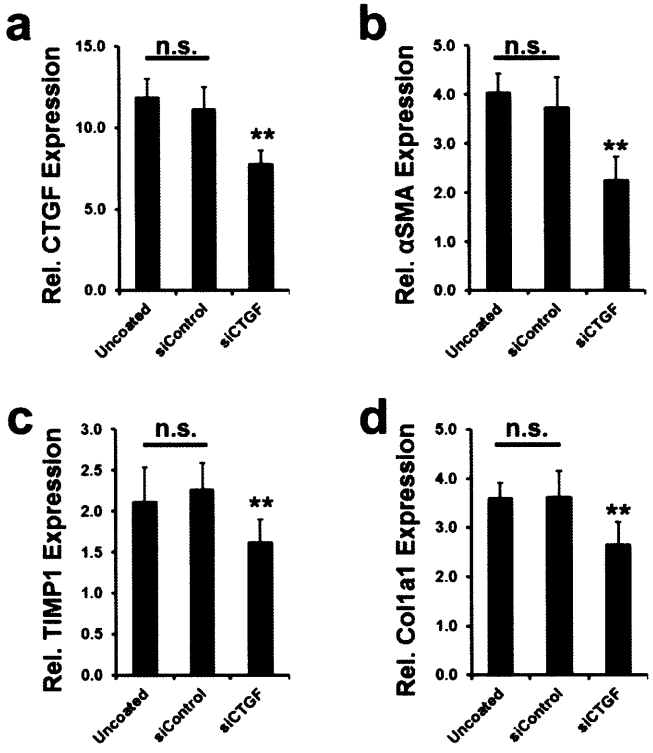

Figure 7-7 Analysis of *in vivo* gene expression

(a) qRT-PCR analysis of CTGF expression in treated wounds relative to uninjured dermis from matched rats. (b) Relative expression of αSMA in treated wounds compared to uninjured dermis. (c) TIMP1expression in sutured wounds relative to uninjured dermis from matched rats. (d) Collagen expression within treated burn wounds relative to uninjured dermis. Data shown are mean ± S.D., n=6.

Another important factor in scar formation is collagen production and its reorganization. Collagen is produced by fibroblasts within the healing tissue and is reorganized by matrix metalloproteinases (MMPs). The balance of collagen expression and MMP activity within a healing wound contributes significantly to the speed of healing and the quality of the tissue

produced. In chapter 5 of this thesis we described how upregulated MMP expression and activity along with lagging collagen production produced slow healing poorly organized granulation tissue. In the case of scar formation this situation is reversed, where overproduction of collagen and slow reorganization contribute to poor tissue function and scaring.

Importantly, CTGF overexpression within healing tissues is known to play an important role in TGFβ stimulated collagen production in cutaneous wound healing as well as its stimulation of TIMP1 expression. TIMP1 acts to inhibit MMPs that are crucial in the reorganization of dermal collagen. We found that in the case of siCTGF treated wounds, collagen and TIMP1 expression were both significantly reduced. Col1a1 was reduced by approximately 29% versus siControl wounds, while TIMP1 expression was reduced by approximately 23% **(Figure 7-7c-d)**.

7.3.7 Knockdown of CTGF Results in Histological Changes

Histological evaluation of treated scars was performed after 30 days of treatment. Wound sections were taken in the direction of suture placement from the center of each sutured burn wound and at two consecutive levels spaced 250μm out from the center of the tissue. H&E histological analysis of the burn wounds focused primarily on tissue organization, scar characteristic dimensions, and general appearance. In H&E staining cutaneous scar tissue appears more cellular and has a less reticular tissue structure. Staining of the parenchyma is lighter in early scar tissue as compared to uninjured dermis. As the scar tissue matures and remodels the staining within the stroma increases to match the uninjured tissues. Beyond only staining, structural differences between uninjured tissue and scar tissue are dramatic and can be readily appreciated in H&E histology. Scar tissue lacks many of the natural structures found in the skin, including hair follicles, papillary structures, and sweat glands. The loss of these structures contributes to some of the complications of scar.

Qualitative analysis of the burn wounds demonstrated a number of noticeable differences between the siCTGF treated wounds and the control groups **(Figure 7-8a)**. The epidermal thickness of siCTGF wounds appeared increased in many of the wound sections, however it was not statistically significant when quantifies. Also concerning the epidermal layer of the skin, the

first signs of papillary structures can be seen in siCTGF treated wounds. This is important as these structures are often lost in scar tissue and they function to improve the integration of the epidermis and the dermis, strengthening the bond between these layers of skin.[72, 73] These structures were not seen in any of the control treated wounds. Another important observation to note was the epidermis was seen to break free from the dermis within a number of the control wounds, demonstrating the lack of such a strong connection. The appearance of this junction in control wounds is flat with little variegation **(Figure 7-8b)**.

A common presentation in scars is hypertrophy, where the production of the healing tissue and wound contraction together lead to a scar that grows above the surrounding uninjured tissue. This presentation is very important to many of the aesthetic aspects of healing, as these raised scars can be undesirable. Grossly, we did not appreciate any significant hypertrophy within any of the burn wounds, and did not observe any correlation between treatment group and a raised or bumpy appearance. Histologically we observed this raised feature in a number of the treated wounds, however it was not consistently observed in any specific group. The relative vascularity of the scars was also of interest to us as good perfusion of the healing tissue is important to the overall health of the tissue. It has also been reported that CTGF may play a role in neovascularization.[74-76] To evaluate this we performed CD31 staining of wound sections and quantified both the number of vessels and average vessel diameter per high powered field. We found significantly increased vessel number in the siCTGF treated wounds with no observable differences between the control treated wounds. The average vessel diameter in all treatment groups was statistically similar.

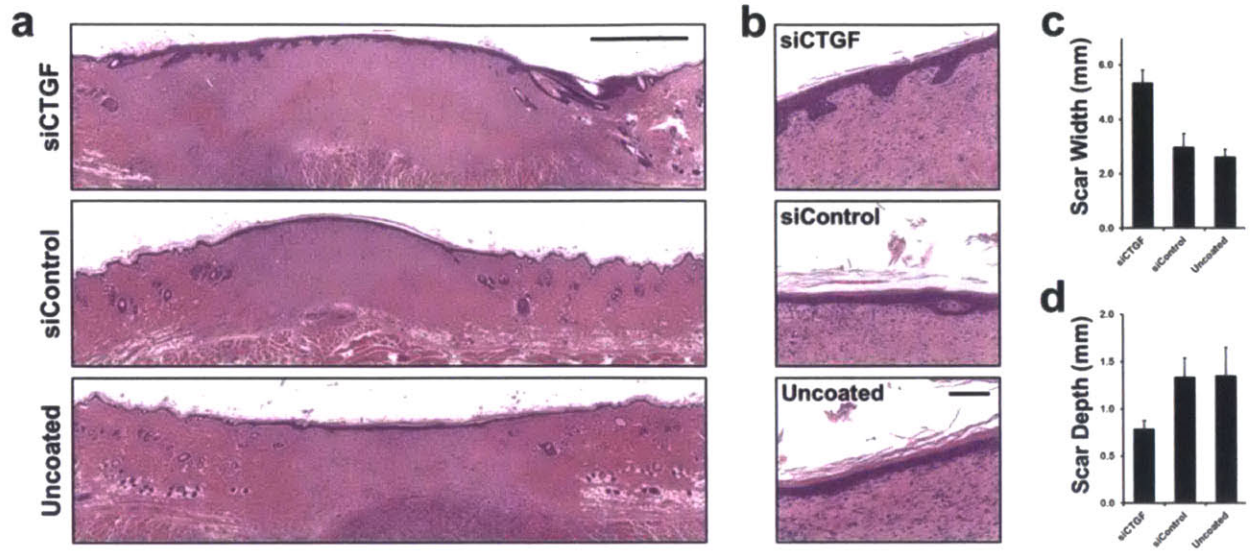

Figure 7-8 H&E histology of scar tissue formation in treated burn wounds

(a) Representative full wound sections for each of the treatment groups. Scale bar = 1 mm. (b) High power images of the epidermis-dermis junction demonstrating papillary structures in siCTGF treated wounds that are absent in controls. Scale bar = 100 μm. (c) Average scar width as determined by histological analysis. (d) Average scar depth as determined from qualitative histological analysis. Data shown are mean ± S.D., n=6.

As we had observed grossly, the siCTGF treated burns were wider than either the siControl or uncoated suture treated burns **(Figure 7-8c)**. The depth of the scar however is reduced by nearly half in the siCTGF treated wounds compared to controls **(Figure 7-8d)**. This dramatic reduction in scar depth is fascinating as it demonstrates the potential for improved long term reorganization of these wounds. Most of the siControl and uncoated suture treated burns were observed to have scars reaching down to skeletal muscle that could readily be identified in H&E staining after the 30 days of treatment. In the siCTGF burns, scars were far more topical, penetrating down to the skeletal muscle in small projections but not uniformly as seen in the control wounds. Overall, the appearance of the siCTGF treated burn wounds is much more remodeled than that seen in the control burns. This is evidenced by the presence of the darker staining parenchyma, which is more similar to uninjured dermis in appearance, within the scar body in the siCTGF treated wounds, while control burn wounds appear to uniformly consist of light staining scar tissue. This is a very promising finding in conjunction with the appearance of

papillary structures in these burns, as the scar tissue treated with siCTGF sutures may be remodeling more effectively to recapitulate the uninjured dermis.

7.3.8 Knockdown of CTGF Improves Tissue Remodeling

Masson's trichrome stain (MTC) is an important connective tissue stain for analyzing collagen deposition within tissues. In the dermis, MTC stains collagen blue while cells, muscle, and keratin appear red. In healing tissue increases in collagen content can be appreciated in MTC stained sections for deeper staining blue color, while lower collagen content is a lighter shade of blue. Cellularity of tissues can also be appreciated, similar to H&E staining, as the cell body within the tissue appears red. This is particularly useful in identifying the epidermal layers of cells as they stain a deep red with little blue staining. In MTC staining early scars are observed to stain lighter shade of blue than the uninjured dermis or healthy remodeled tissues due to the smaller size of the collagen fibers bundles within the scar and the relative increased cellularity.

Comparing the three treatment groups used in this work, MTC demonstrates a number of key differences between the siCTGF treated wounds and controls. Importantly, inspection of the full wound sections supports our previous findings from H&E histological analysis for increased scar width in the siCTGF burns **(Figure 7-9a)**. It also demonstrates increasing levels of reorganization within the healing scar. This can be appreciated in **Figure 7-9a** by the dark blue staining regions crossing through the siCTGF scar. This increased staining above the skeletal muscle and through the scar demonstrates a significant level of remodeled tissue that appears much more similar to the uninjured dermis than the scars observed in the siControl or uncoated suture treated burns.

A second important finding observed in the MTC staining is the existence of papillary structures interconnecting the epidermis with the dermis **(Figure 7-9b)**. As we described in the previous section, these papillae serve to better integrate the epidermis with the dermis. Here we see that the epidermal tissue is well circumscribed and has a consistent variegated appearance. Inspecting the controls we see only a flat thin layer of cells lying on top of the dermis with no observable structures reaching into it from the epidermis. Looking closely at the border between the epidermis and dermis we can also appreciate the different organization of the dermal

collagen. Taking on a more whirled appearance in the siCTGF treated wounds, with controls are uniformly flat up to and including this border region.

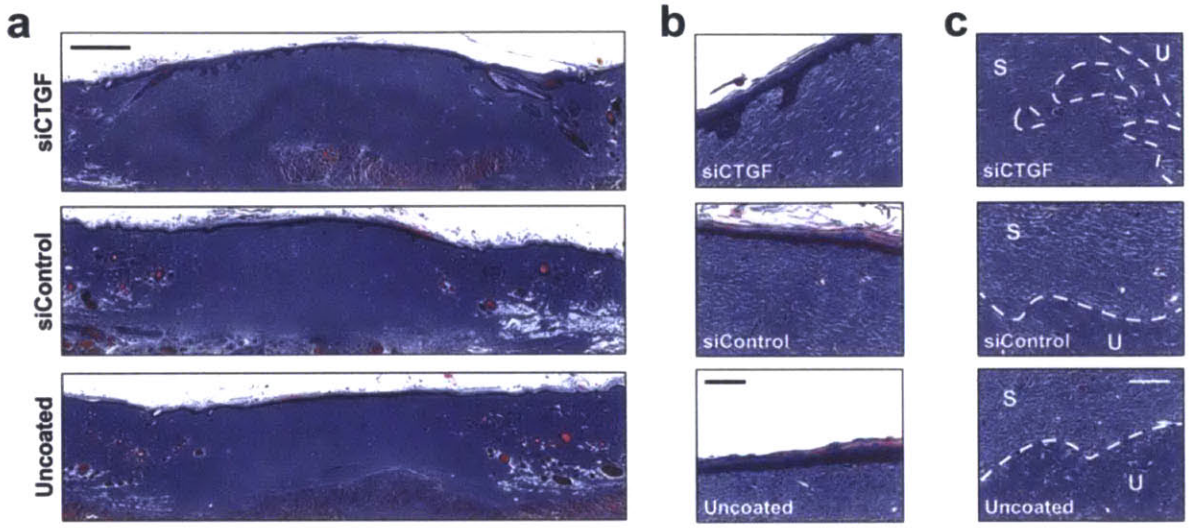

Figure 7-9 Masson's trichrome staining of treated rat burn sections

(a) Representative full wound sections for gross histological comparison. Scale = 0.8 mm. (b) Representative high powered images of epidermal-dermal border demonstrating interdigitating epidermal papillae in siCTGF treated wounds not seen in controls. Scale bar = 100 μm (c) Representative high powered images of wound margins demonstrating the level of tissue reorganization observed in siCTGF treated wounds.

Grossly, the MTC stained full wound sections demonstrated increased tissue reorganization in the siCTGF treated wounds. This reorganizing is especially important at the wound margins to ensure a healthy integration of the healing tissue into the uninjured surrounding tissue. Qualitatively evaluating the scar margins of the different treatment groups we observe a number of important differences between them **(Figure 7-9c).** Burns treated with siCTGF sutures have a much less clear margin, obscured by large variations in the margin edge and regions of tissue that stain similarly to the uninjured dermis in the surrounding scar. Uncoated and siControl suture treated burns have fairly consistent clear margins with only small areas of remodeling at the margins.

7.3.9 Reduced Total Scar Area and Contraction

To evaluate collagen accumulation and organization further within the burn wound we used a second independent histological technique, picrosirius red (PS) staining of collagen. Collagen is a naturally birefringent macromolecule and as such can be readily evaluated using polarized light microscopy of histological sections. PS staining of collagen enhances this birefringence, allowing for more precise characterization collagen.[77, 78] Histological analysis of PS stained tissues has been widely reported in the study of wound healing and scar formation to evaluate the extent and orientation of collagen present within the healing tissue.[79] In birefringence imaging thin Type III collagen has a blue-green appearance while thicker and more mature Type I collagen appears orange-red.

Here we use picrosirius red staining to evaluate the collagen content within burn wounds and the level of collagen orientation observed at the burn margin. Collagen content within scars is known to be increased. This collagen is often poorly organized and does not recapitulate the basket-weave structure that is observed in the uninjured dermis. Grossly analyzing the full wound sections, a dramatic difference between the siCTGF suture treated wounds and the siControl and uncoated suture treated wounds is easily apparent **(Figure 7-10a)**. The siCTGF scar region contains much larger collagen fibers that are evenly distributed and organized into a cross-hatching network. Similar to what we had observed in both H&E and MTC staining, the topical aspect of the scar is most consistent to the control wounds, however the depth of this region is less than half of that observed in the controls. It is also interesting to note here that regions we had noted were clearly scar tissue from H&E and MTC appear much more similar in collagen structure to the uninjured dermis than any such identifiable regions within the control burn wounds.

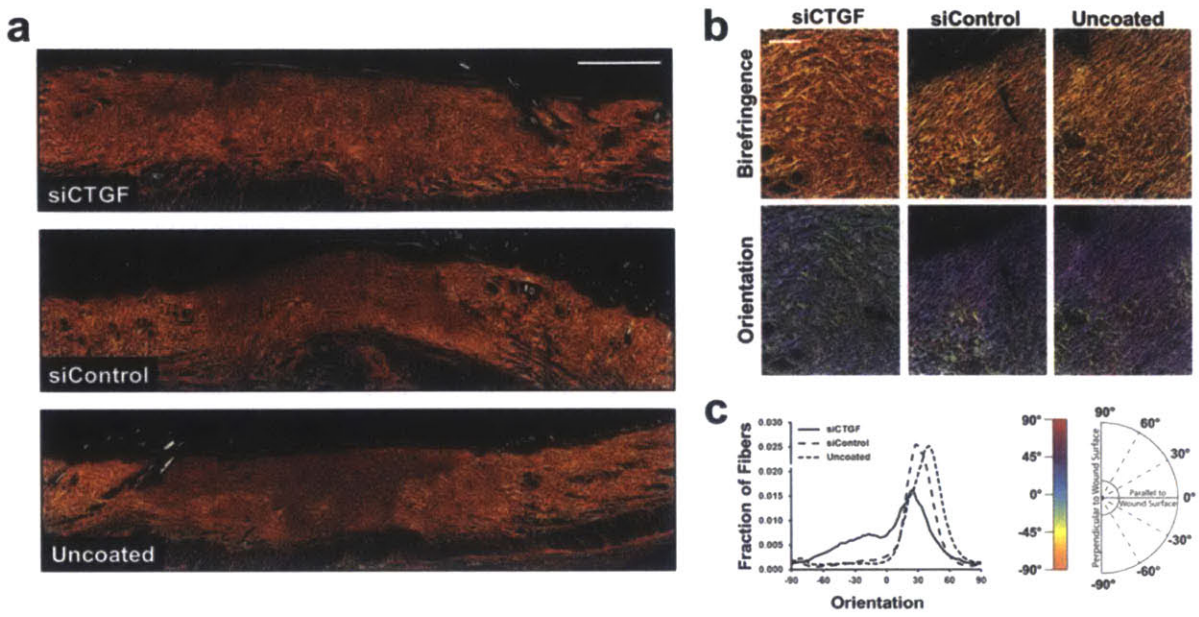

Figure 7-10 Picrosirius red staining analysis of collagen content and orientation within the healing burn wounds

(a) Representative full wound sections imaged for birefringence for each treatment group. Scale bar = 1mm. (b) Representative high power images of burn margins for each group and their respective orientation analysis color maps. Scale bar = 50 μm (c) Plot of average fiber orientation fractions for each treatment group. Data shown are mean, n=3.

An important aspect of the pathology of scar tissue is contraction. Physiologically contraction occurs as a result of mechanical forces transmitted across the ECM within the scar. Collagen is a primary component of that ECM. Orientation of collagen fibers is an important factor in evaluating scar characteristics as it gives insight into the level of mechanical forces being transmitted across the fibers. Highly aligned collagen in the orientation of contraction, which in this animal model would be laterally across the wound sections, helps characterize the level of contraction ongoing within the scar.

Here we performed orientation analysis of the large to medium collagen fibers within at the scar margin to assess the extent of contraction within these wounds. This was performed using the ImageJ plugin Orientation J.[80] This analysis demonstrates the high degree of orientation with the collagen fibers at the scar margin of siControl and uncoated suture treated burns. The siCTGF treated burns however demonstrate significantly less alignment, and have a

much more woven characteristic to their appearance. This is important as it demonstrates the extent to which contractile forces are present within the control wounds, and how they are still present in the siCTGF treated wounds, but to a lesser degree. In the color maps the purple-blue shaded collagen fibers are oriented in the direction of the scar center and are abundant in the control wounds. These fibers are visible within the siCTGF treated burn but not to the same degree and mixed in with a substantial population of fibers seen going in opposing directions **(Figure 7-10b-c)**.

7.4 Discussion

Scars are an everyday part of life, but in the case of large traumatic injuries, burns, and surgery they can created a great deal of discomfort for patients both physically and aesthetically.[2, 7, 8] In the case of burn wounds, contractions can lead to serious complications including range of motion issues and loss of function for the tissues involved.[6, 81] The current treatment options available to patients largely consist of silicone gel sheeting and topical steroids, which can slow wound healing and increase the risk of serious infection.[7] To date a great deal of research has been done to identify key biological mediators of scar production, however being able to specifically target these actors has been limited due to the lack of technology to effectively deliver targeted therapies locally at the site of interest. In this chapter we describe using layer-by-layer delivery of RNA interference as one approach to this goal.

In this report we describe the application of an ultrathin polymer film coating for the sustained local delivery of siRNA into healing third-degree burns in a rat model. The film architecture used in this work is similar to that reported previously for delivery of siRNA to chronic wounds in a mouse model of diabetes. In our previous work we focused on the controlled knockdown of MMP-9 from a commercially available nylon bandage to improve granulation tissue formation and accelerate wound closure. Here we used a commercially available silk suture that once coated with the LbL film could be placed through the burn wound to provide a siRNA delivering depot into the healing tissue to effect scar formation.

Here we targeted a known mediator of TGFβ stimulated fibrosis, connective tissue growth factor. CTGF is known to be upregulated within hypertrophic scars and its expression is

associated with the increased expression of collagen, TIMP1, and alpha-smooth muscle actin within scars. Previous reports have demonstrated that anti-sense RNA therapy against CTGF expression within wounds leads to reduced scar production. These reports however have focused on the bolus administration of RNA to the wound site, leaving the RNA open to rapid clearance and poor bioavailability, thus achieving lower potential efficacies. Using LbL coatings to sustain the local delivery of siRNA into the healing wound is an approach that we believe addresses both of these concerns. In this work we demonstrate how one might approach the controlled delivery of siRNA from a coated substrate common in the wound sites where scars form, targeting this key mediator which resulted in significant changes in scar formation in a third-degree burn model in rats.

Ultrathin coatings were observed to uniformly coat the surfaces of commercially available silk sutures and were demonstrated to sustain the release of siRNA out to nearly two weeks. These film coated sutures were tested for *in vitro* siRNA-specific gene knockdown and were shown to reduce the expression of the reporter gene GFP in two different cell lines for up to five days with minimal impact on cell viability. This film coated suture when placed through third-degree burn wounds was able to achieve significant siRNA-specific reduction of CTGF expression *in vivo*. This reduction in CTGF expression was connected to reduced expression of many related TGFβ stimulated pro-fibrotic genes, including collagen, TIMP1, and αSMA. Macroscopically siCTGF treated wounds were significantly less contracted than wounds treated with either siControl coated sutures or uncoated sutures.

Histologically the siCTGF scars were significantly less contracted than control scars, and were significantly shallower. The healed tissue within the siCTGF treated burn wound contained papillary structures, which play a crucial role in providing a strong connection between the epidermis and the dermis. These structures were not observed in any of the control scars. In addition to these findings, the level of remodeling within the siCTGF treated wounds was also increased compared to controls. MTC staining of wound sections provided evidence of increased reorganization of the healing tissue and more advanced remodeling of the scar margins. Finally, picrosirius red staining of the treated wound sections provided a great deal of insight into the organization of collagen within the healing tissues and the level of contractile forces acting on them. It was observed that reducing CTGF expression improved collagen

remodeling within the burn wound and significantly reduced the level of collagen orientation at the scar margin indicating significantly reduced contractile forces within the tissue.

In summary, we have presented the local application of an ultrathin polymer coating that can be uniformly assembled onto a commercially available silk suture for the sustained effective knockdown of a key mediator in cutaneous scar formation *in vivo*. This targeted therapy resulted in a significantly reduced fibrotic response within healing burn tissue. The work detailed in this report is one of the first demonstrations of controlled local RNA delivery into healing burns to improve outcomes. This work also substantiates the previously reported findings that CTGF is a potential therapeutic target within wounds to reduce fibrosis while not impairing normal wound healing. The approach outlined within this report has the potential to significantly impact a myriad of diverse fields, from treating liver, renal, and pulmonary fibrosis to developing regenerative medicines, cancer therapies, and providing a tool in fundamental scientific research.

7.5 References

1. Baker, R., Urso-Baiarda, F., Linge, C. & Grobbelaar, A. Cutaneous scarring: a clinical review. Dermatol Res Pract 2009, 625376 (2009).

2. Mustoe, T.A. Scars and keloids. Bmj 328, 1329-1330 (2004).

3. Widgerow, A.D. & Chait, L.A. Scar management practice and science: a comprehensive approach to controlling scar tissue and avoiding hypertrophic scarring. Adv Skin Wound Care 24, 555-561 (2011).

4. Gurtner, G.C., Werner, S., Barrandon, Y. & Longaker, M.T. Wound repair and regeneration. Nature 453, 314-321 (2008).

5. Gurtner, G.C., Rohrich, R.J. & Longaker, M.T. From bedside to bench and back again: technology innovation in plastic surgery. Plast Reconstr Surg 124, 1355-1356 (2009).

6. Nedelec, B., Ghahary, A., Scott, P.G. & Tredget, E.E. Control of wound contraction. Basic and clinical features. Hand Clin 16, 289-302 (2000).

7. Mustoe, T.A. et al. International clinical recommendations on scar management. Plast Reconstr Surg 110, 560-571 (2002).

8. Mustoe, T.A. Evolution of silicone therapy and mechanism of action in scar management. Aesthetic Plast Surg 32, 82-92 (2008).

9. Walmsley, G.G. et al. Scarless wound healing: chasing the holy grail. Plast Reconstr Surg 135, 907-917 (2015).

10. Wong, V.W., Gurtner, G.C. & Longaker, M.T. Wound healing: a paradigm for regeneration. Mayo Clin Proc 88, 1022-1031 (2013).

11. Nauta, A., Gurtner, G. & Longaker, M.T. Wound healing and regenerative strategies. Oral Dis 17, 541-549 (2011).

12. Park, J.E. & Barbul, A. Understanding the role of immune regulation in wound healing. Am J Surg 187, 11S-16S (2004).

13. Goldschmeding, R. et al. Connective tissue growth factor: just another factor in renal fibrosis? Nephrol Dial Transplant 15, 296-299 (2000).

14. Border, W.A., Brees, D. & Noble, N.A. Transforming growth factor-beta and extracellular matrix deposition in the kidney. Contrib Nephrol 107, 140-145 (1994).

15. Border, W.A. & Noble, N.A. Transforming growth factor beta in tissue fibrosis. N Engl J Med 331, 1286-1292 (1994).

16. Birkedal-Hansen, H. Proteolytic remodeling of extracellular matrix. Curr Opin Cell Biol 7, 728-735 (1995).

17. Grinnell, F. Fibroblasts, myofibroblasts, and wound contraction. J Cell Biol 124, 401-404 (1994).

18. Mackool, R.J., Gittes, G.K. & Longaker, M.T. Scarless healing. The fetal wound. Clin Plast Surg 25, 357-365 (1998).

19. Sen, C.K. et al. Human skin wounds: a major and snowballing threat to public health and the economy. Wound Repair Regen 17, 763-771 (2009).

20. Rock, C.L., Dechert, R.E., Khilnani, R., Parker, R.S. & Rodriguez, J.L. Carotenoids and antioxidant vitamins in patients after burn injury. J Burn Care Rehabil 18, 269-278; discussion 268 (1997).

21. DeCherney, A.H. et al. Expression of cyclin protein after thermal skin injury in a guinea pig model. J Burn Care Rehabil 18, 292-298 (1997).

22. Rodgers, K.E. et al. Histologic alterations in dermal repair after thermal injury effects of topical angiotensin II. J Burn Care Rehabil 18, 381-388 (1997).

23. Fraser, J.F. et al. Deep dermal burn injury results in scarless wound healing in the ovine fetus. Wound Repair Regen 13, 189-197 (2005).

24. Penn, J.W., Grobbelaar, A.O. & Rolfe, K.J. The role of the TGF-beta family in wound healing, burns and scarring: a review. Int J Burns Trauma 2, 18-28 (2012).

25. Pena, R.A., Jerdan, J.A. & Glaser, B.M. Effects of TGF-beta and TGF-beta neutralizing antibodies on fibroblast-induced collagen gel contraction: implications for proliferative vitreoretinopathy. Invest Ophthalmol Vis Sci 35, 2804-2808 (1994).

26. Cordeiro, M.F. et al. Novel antisense oligonucleotides targeting TGF-beta inhibit in vivo scarring and improve surgical outcome. Gene Ther 10, 59-71 (2003).

27. Wahl, S.M. Transforming growth factor beta (TGF-beta) in inflammation: a cause and a cure. J Clin Immunol 12, 61-74 (1992).

28. O'Kane, S. & Ferguson, M.W. Transforming growth factor beta s and wound healing. Int J Biochem Cell Biol 29, 63-78 (1997).

29. Border, W.A. Transforming growth factor-beta and the pathogenesis of glomerular diseases. Curr Opin Nephrol Hypertens 3, 54-58 (1994).

30. Border, W.A. & Noble, N.A. TGF-beta in kidney fibrosis: a target for gene therapy. Kidney Int 51, 1388-1396 (1997).

31. Montesano, R. & Orci, L. Transforming growth factor beta stimulates collagen-matrix contraction by fibroblasts: implications for wound healing. Proc Natl Acad Sci U S A 85, 4894-4897 (1988).

32. Massague, J. & Wotton, D. Transcriptional control by the TGF-beta/Smad signaling system. Embo J 19, 1745-1754 (2000).

33. Desmouliere, A., Geinoz, A., Gabbiani, F. & Gabbiani, G. Transforming growth factor-beta 1 induces alpha-smooth muscle actin expression in granulation tissue myofibroblasts and in quiescent and growing cultured fibroblasts. J Cell Biol 122, 103-111 (1993).

34. Branton, M.H. & Kopp, J.B. TGF-beta and fibrosis. Microbes Infect 1, 1349-1365 (1999).

35. Sisco, M. et al. Antisense oligonucleotides against transforming growth factor-beta delay wound healing in a rabbit ear model. J Am Coll Surgeons 201, S60-S60 (2005).

36. Lipson, K.E., Wong, C., Teng, Y. & Spong, S. CTGF is a central mediator of tissue remodeling and fibrosis and its inhibition can reverse the process of fibrosis. Fibrogenesis Tissue Repair 5, S24 (2012).

37. Wang, X., McLennan, S.V., Allen, T.J. & Twigg, S.M. Regulation of pro-inflammatory and pro-fibrotic factors by CCN2/CTGF in H9c2 cardiomyocytes. J Cell Commun Signal 4, 15-23 (2010).

38. Esson, D.W. et al. Expression of connective tissue growth factor after glaucoma filtration surgery in a rabbit model. Invest Ophthalmol Vis Sci 45, 485-491 (2004).

39. Dammeier, J., Brauchle, M., Falk, W., Grotendorst, G.R. & Werner, S. Connective tissue growth factor: a novel regulator of mucosal repair and fibrosis in inflammatory bowel disease? Int J Biochem Cell Biol 30, 909-922 (1998).

40. Duncan, M.R. et al. Connective tissue growth factor mediates transforming growth factor beta-induced collagen synthesis: down-regulation by cAMP. FASEB journal : official publication of the Federation of American Societies for Experimental Biology 13, 1774-1786 (1999).

41. Gore-Hyer, E. et al. TGF-beta and CTGF have overlapping and distinct fibrogenic effects on human renal cells. Am J Physiol Renal Physiol 283, F707-716 (2002).

42. Grotendorst, G.R. Connective tissue growth factor: a mediator of TGF-beta action on fibroblasts. Cytokine Growth Factor Rev 8, 171-179 (1997).

43. Igarashi, A., Okochi, H., Bradham, D.M. & Grotendorst, G.R. Regulation of connective tissue growth factor gene expression in human skin fibroblasts and during wound repair. Mol Biol Cell 4, 637-645 (1993).

44. Abreu, J.G., Ketpura, N.I., Reversade, B. & De Robertis, E.M. Connective-tissue growth factor (CTGF) modulates cell signalling by BMP and TGF-beta. Nat Cell Biol 4, 599-604 (2002).

45. Holmes, A. et al. CTGF and SMADs, maintenance of scleroderma phenotype is independent of SMAD signaling. J Biol Chem 276, 10594-10601 (2001).

46. Ito, Y. et al. Expression of connective tissue growth factor in human renal fibrosis. Kidney Int 53, 853-861 (1998).

47. Leask, A., Holmes, A., Black, C.M. & Abraham, D.J. Connective tissue growth factor gene regulation. Requirements for its induction by transforming growth factor-beta 2 in fibroblasts. J Biol Chem 278, 13008-13015 (2003).

48. Leask, A. et al. The control of ccn2 (ctgf) gene expression in normal and scleroderma fibroblasts. Mol Pathol 54, 180-183 (2001).

49. Ignotz, R.A. & Massague, J. Transforming Growth-Factor-Beta Stimulates the Expression of Fibronectin and Collagen and Their Incorporation into the Extracellular-Matrix. Journal of Biological Chemistry 261, 4337-4345 (1986).

50. Yokoi, H. et al. Role of connective tissue growth factor in profibrotic action of transforming growth factor-beta: a potential target for preventing renal fibrosis. Am J Kidney Dis 38, S134-138 (2001).

51. Frazier, K., Williams, S., Kothapalli, D., Klapper, H. & Grotendorst, G.R. Stimulation of fibroblast cell growth, matrix production, and granulation tissue formation by connective tissue growth factor. J Invest Dermatol 107, 404-411 (1996).

52. Okada, H. et al. Connective tissue growth factor expressed in tubular epithelium plays a pivotal role in renal fibrogenesis. J Am Soc Nephrol 16, 133-143 (2005).

53. Khoo, Y.T. et al. Upregulation of secretory connective tissue growth factor (CTGF) in keratinocyte-fibroblast coculture contributes to keloid pathogenesis. J Cell Physiol 208, 336-343 (2006).

54. Daniels, J.T. et al. Understanding and controlling the scarring response: the contribution of histology and microscopy. Microsc Res Techniq 42, 317-333 (1998).

55. Washio, H. et al. Transcriptional inhibition of hypertrophic scars by a gene silencer, pyrrole-imidazole polyamide, targeting the TGF-beta1 promoter. J Invest Dermatol 131, 1987-1995 (2011).

56. O'Shaughnessy, K.D., Kim, P., Roy, N.K. & Mustoe, T.A. Antisense oligonucleotides to TGF-beta and CTGF decrease hypertrophic scarring in a rabbit ear model. Wound Repair and Regeneration 15, A20-A20 (2007).

57. Sisco, M. et al. Antisense inhibition of connective tissue growth factor (CTGF/CCN2) mRNA limits hypertrophic scarring without affecting wound healing in vivo. Wound Repair Regen 16, 661-673 (2008).

58. Sriram, S., Robinson, P., Pi, L., Lewin, A.S. & Schultz, G. Triple combination of siRNAs targeting TGFbeta1, TGFbetaR2, and CTGF enhances reduction of collagen I and smooth muscle actin in corneal fibroblasts. Invest Ophthalmol Vis Sci 54, 8214-8223 (2013).

59. Gibson, D.J. et al. Conditional knockout of CTGF affects corneal wound healing. Invest Ophthalmol Vis Sci 55, 2062-2070 (2014).

60. Crean, J.K., Lappin, D., Godson, C. & Brady, H.R. Connective tissue growth factor: an attractive therapeutic target in fibrotic renal disease. Expert Opin Ther Targets 5, 519-530 (2001).

61. Wood, K.C., Boedicker, J.Q., Lynn, D.M. & Hammond, P.T. Tunable drug release from hydrolytically degradable layer-by-layer thin films. Langmuir : the ACS journal of surfaces and colloids 21, 1603-1609 (2005).

62. Wood, K.C., Chuang, H.F., Batten, R.D., Lynn, D.M. & Hammond, P.T. Controlling interlayer diffusion to achieve sustained, multiagent delivery from layer-by-layer thin films. Proc Natl Acad Sci U S A 103, 10207-10212 (2006).

63. Decher, G. Fuzzy nanoassemblies: Toward layered polymeric multicomposites. Science 277, 1232-1237 (1997).

64. Decher, G. et al. Layer-by-Layer Adsorbed Films of Polyelectrolytes, Proteins or DNA. Abstr Pap Am Chem S 205, 334-POLY (1993).

65. Hammond, P.T. Building biomedical materials layer-by-layer. Materials Today 15, 196-206 (2012).

66. Golberg, A. et al. Non-thermal, pulsed electric field cell ablation: A novel tool for regenerative medicine and scarless skin regeneration. Technology (Singap World Sci) 1, 1-8 (2013).

67. Golberg, A. et al. Pulsed electric fields for burn wound disinfection in a murine model. J Burn Care Res 36, 7-13 (2015).

68. Golberg, A. et al. Eradication of multidrug-resistant in burn wounds by antiseptic pulsed electric field. Technology (Singap World Sci) 2, 153-160 (2014).

69. Alfaro, M.P. et al. A physiological role for connective tissue growth factor in early wound healing. Lab Invest 93, 81-95 (2013).

70. Wang, J.F. et al. Fibrocytes from burn patients regulate the activities of fibroblasts. Wound Repair Regen 15, 113-121 (2007).

71. Lynn, D.M. & Langer, R. Degradable poly(beta-amino esters): Synthesis, characterization, and self-assembly with plasmid DNA. J Am Chem Soc 122, 10761-10768 (2000).

72. Lin, C.M. et al. Microencapsulated human hair dermal papilla cells: a substitute for dermal papilla? Arch Dermatol Res 300, 531-535 (2008).

73. Elliott, K., Stephenson, T.J. & Messenger, A.G. Differences in hair follicle dermal papilla volume are due to extracellular matrix volume and cell number: implications for the control of hair follicle size and androgen responses. J Invest Dermatol 113, 873-877 (1999).

74. Kondo, S. et al. Connective tissue growth factor increased by hypoxia may initiate angiogenesis in collaboration with matrix metalloproteinases. Carcinogenesis 23, 769-776 (2002).

75. Hashimoto, G. et al. Matrix metalloproteinases cleave connective tissue growth factor and reactivate angiogenic activity of vascular endothelial growth factor 165. J Biol Chem 277, 36288-36295 (2002).

76. Inoki, I. et al. Connective tissue growth factor binds vascular endothelial growth factor (VEGF) and inhibits VEGF-induced angiogenesis. FASEB journal : official publication of the Federation of American Societies for Experimental Biology 16, 219-221 (2002).

77. Junqueira, L.C., Cossermelli, W. & Brentani, R. Differential staining of collagens type I, II and III by Sirius Red and polarization microscopy. Arch Histol Jpn 41, 267-274 (1978).

78. Montes, G.S. & Junqueira, L.C. The use of the Picrosirius-polarization method for the study of the biopathology of collagen. Mem Inst Oswaldo Cruz 86 Suppl 3, 1-11 (1991).

79. Cuttle, L. et al. Collagen in the scarless fetal skin wound: detection with picrosirius-polarization. Wound Repair Regen 13, 198-204 (2005).

80. Rezakhaniha, R. et al. Experimental investigation of collagen waviness and orientation in the arterial adventitia using confocal laser scanning microscopy. Biomech Model Mechanobiol 11, 461-473 (2012).

81. Daniels, J.T. et al. Mediation of transforming growth factor-beta(1)-stimulated matrix contraction by fibroblasts: a role for connective tissue growth factor in contractile scarring. Am J Pathol 163, 2043-2052 (2003).

Chapter 8
Transdermal Delivery of siRNA In Vivo from LbL Coated Microneedle Arrays

8.1 Introduction

In Chapters 5, 6, and 7 we described the application of LbL coated medical devices for the local delivery of siRNA into wounds. These applications ranged from accelerating impaired wound healing in chronic ulcerative wounds to reducing scar formation in third-degree burns. Two of these reports, Chapters 5 and 7 used the same hierarchical LbL film architecture of $[Poly2/DS]_{20}[Chi/siRNA]_{25}$. Here we use a similar film, minus the hydrolytically degradable undercoating film architecture, applied to microneedles for transdermal delivery of siRNA. Release of the siRNA from these coated microneedles was facilitated by the rapid solvation of a dip-coated layer of the pH-responsive polymer poly(o-nitrobenzyl-methacrylate-co-methyl-methacrylate-co-poly(ethylene-glycol)-methacrylate) (PNMP) that was deposited on the microneedles and photoactivated prior to LbL film assembly. In this chapter we used these LbL coated microneedles to effect significant gene knockdown *via* transdermal delivery. This work was focused as a proof of concept study to demonstrate the flexibility of the LbL film system in this application.

Controlled local delivery of RNA interference is a growing area of research that has wide ranging potential applications from tissue engineering and cancer therapy to molecular biology.[1-10] In our previous research we have described the application of the Layer-by-layer (LbL) assembly technique for the construction of ultrathin polymer coatings for the sustained delivery of siRNA *in vivo*. These applications have focused on treating known pathologies in cutaneous wound healing and have taken the form of coated bandages and coated sutures. Both of these medical devices are common in the wound healing field, however depending on the circumstance such devices may not be desirable for implementation at a target site. For this reason we began to consider more broadly applicable approaches for the delivery of siRNA LbL films into the dermis.

One approach that has been widely reported over the past two decades for local transdermal delivery is the application of microneedle technology.[11-18] Microneedles can be constructed *via* soft lithography, printing technologies, or a number of methods.[17, 19-24] They can be made of any number of materials from a myriad of polymers to silicon to materials more common to the operating theatre, such as stainless steel.[25-31] These structures when assembled can be used as an array of very small syringes that pierce the skin for local administration of contained doses of drugs. Microneedles have a number of advantages over other modes of transdermal delivery. Compared to syringes there is a much lower risks of blood born pathogen transmission and accidental needle sticks as well as generating less medical waste that could potentially be improperly re-used.[15, 27, 32-37]

Previous reports from our group and others have demonstrated the capability to coat poly-(l-lactide) (PLLA) microneedle arrays for sustained transdermal delivery of DNA.[38-45] Applying microneedle-based cutaneous delivery of LbL film coated material to siRNA has potential applications in a myriad of complex diseases. In the arena or wound healing, one could imagine the temporary implantation of siRNA delivering microneedles at the wound margin of diabetic ulcers to reduce MMP-9 or TNFα expression, or directly applying such microneedles into forming scars to reduce contraction through the silencing of CTGF. Here we were interested to approach this investigation as a proof-of-concept to demonstrate that similar to what had been observed for DNA delivery with microneedles,[46-49] we could deliver siRNA. In this way we could expand the application of the LbL films developed throughout this thesis to be much more broadly applicable as we would no longer need to concern ourselves with the preparation and implantation of a solid substrate support.

In doing this work we built upon the previous reported works published from our group using LbL coated microneedles with important additions to improve transdermal delivery of LbL coatings.[50] Important in these additions is the requirement for dermal pre-perforation of application sites for LbL film deposition into the dermis. This small protocol addition greatly improved dermal penetrance and led to a significant enhancement of transdermal delivery of the LbL coated materials.[51-53] Additionally, we also describe a more efficient approach for the deposition of PNMP on microneedle surfaces, using a dip-coating technique that reduces polymer waste by over an order of magnitude.

Herein we present the application of a simple bilayer film architecture assembled over a rapidly soluble dip-coated polymer film which we demonstrate to deliver significant quantities of siRNA transdermally to affect the sustained knockdown of a reporter gene *in vivo*. This report begins with a thorough *in vitro* analysis of the LbL bilayer film architecture, demonstrating the capability to effectively incorporate and deliver microgram quantities of siRNA within minutes of reaching release conditions. This work is then followed by extensive *in vivo* analysis of siRNA delivery and subsequent profiling of reporter gene knockdown. In summary within this work we present the first report of controlled transdermal of siRNA form LbL coated microneedles *in vivo*.

8.2 Methods and Materials.

8.2.1 Materials

PNMP (31:59:10, poly(o-nitrobenzyl-methacrylate-co-methyl-methacrylate-co-poly(ethylene-glycol)-methacrylate), 17kDa) was assembled through free radical polymerization of o-nitrobenzyl methacrylate, methyl methacrylate, and poly(ethylene glycol) methacrylate as previously described.[54] SiRNA sequences were synthesized by Dharmacon (Lafayette, CO). Alexafluor 546-labeled siRNA was purchased from Qiagen (Valencia, CA). Antibiotic-antimycotic solution, 100 mM L-Glutamine solution, phosphate buffered saline (PBS, 10x), Advanced-MEM, AlamarBlue, and fetal bovine serum were purchased from Invitrogen (Carlsbad, CA). HeLa cells were purchased from ATCC (Manassas VA).

8.2.2 PLLA Microneedle Fabrication

PDMS molds (Sylgard 184, Dow-Corning) were prepared as previously described.[43] PLLA (1.9 dl g^{-1}) purchased from Lakeshore Biomaterials (Essen, DE) was melt-molded into PDMS molds under vacuum (-25inches Hg) at 140°C for 30 minutes, 200°C for 60 minutes, and -20°C for 30 minutes. PLLA microneedles were heat treated (140°C for 4 hours) for conferring dioxane solvent resistance.[50]

8.2.2 PNMP Film Deposition

Samples were coated with PNMP using a dip-coating technique where samples were dip coated (6 cycles of 5 sec dip and 30 sec dry) in PNMP containing 1,4-dioxane (2mg/ml). PNMP

coated samples were then immediately exposed to vacuum (-25inches Hg) at 25°C for 12 hours. PNMP coated samples were activated by photos-witching using ultraviolet radiation (254nm, 2.25 mW cm-2) for 20min.

8.2.3 Layer-by-layer film preparation

Films were deposited on PNMP coated PLLA microneedles. Microneedles were cleaned with three 30 second rinses in pH 5.0 RNase free UltraPure™ water (Life Technologies) prior to film assembly. Microneedles were first immersed in a solution of the polycation Chitosan for a minimum of one hour prior to film assembly. Assembly of LbL films was performed using a Carl Zeiss HMS-DS50 stainer. Assembly of [Chi/siRNA] film was deposited similarly. Chitosan (1 mg ml^{-1}, pH 5.0) was adsorbed for 15 minutes and siRNA (20 μg ml^{-1}, pH 5.0) was adsorbed for 30 minutes. All solutions were prepared in RNase free water, adjusted to a pH of 5.0.

Film growth was characterized for films built on silicon wafers by a Veeco Dektak 150 profilometer. Incorporation of fluorescently labeled siRNA into films built on coated surfaces was followed using a Nikon A1R Ultra-Fast Spectral Scanning confocal microscope. Total siRNA incorporation within films was measured by rapid dissolution in a 1M NaCl solution with vigorous agitation and quantified using a fluorescent plate reader. Release studies were performed in PBS (pH 7.4) at 37°C. Release was quantified by fluorescence of the released labeled siRNA read using a fluorescent plate reader.

8.2.4 *In Vivo* siRNA Delivery

All animal studies were approved by the MIT Institutional Animal Care and Use Committee (IACUC). Animals were housed and cared for in the USDA-inspected MIT Animal Facility under federal, state, local, and NIH guidelines for animal care. Eight week old BALB/cJ were purchased from Jackson Labs (Bar Harbor, ME). Eight week old C57BL/6-Tg(UBC-GFP)30Scha/J were obtained from a collaborator. Three groups of mice were used: (1) GFP siRNA microneedle treated, (2) control siRNA microneedle treated, and (3) uncoated microneedle treated. Each group consisted of 3 mice total with both ears receiving the same treatment. Microneedle application surgeries were performed under anesthesia.

Implantation of the microneedle arrays was performed in a three step process: (1) PLLA microneedles were used to generate reproducible defects in the skin so that the LbL coated microneedles could be implanted without resistance (2) ears were treated with approximately 50μL of PBS (pH 7.4) for ten seconds to wet the application site (3) LbL coated microneedles were applied into the pre-made perforations and attached to the mice using labeling tape. These microneedles were held in the implant site for thirty minutes. After which time the tape backing was removed, being careful to keep the microneedles within the ear and the microneedles were gently massaged in a circular pattern for thirty seconds. After this period the microneedles were removed and the mice were allowed to recover on warming pads until they were back at baseline.

8.2.5 Histology

Tissues were fixed in zinc fixative without formalin for 48 hours. The excised wounds were then embedded in paraffin and serially sectioned at 250μm levels throughout the microneedle application region. At each level an H&E slide was stained and used for 2-D reconstruction of the wound. Unstained slides were also taken for tissue analysis. Data analysis was performed using Image J.

8.2.6 Statistics

Statistical analysis was performed between groups using Student's *t*-test and rectified by ANOVA for comparisons between multiple groups. Values are represented as mean ± S.D. A value of $p < 0.05$ was used to indicate statistical significance.

8.3 Results

8.3.1 Microneedle Array and Film Assembly

Our group and others have previously reported methods for the controlled delivery of therapeutics into the dermis using LbL coated polymer microneedles. Here we took a similar approach and investigated the application of our previously described LbL film coated onto poly-(l-lactide) (PLLA) microneedle arrays. These microneedle arrays were fabricated via melt-molding PLLA into poly(dimethylsiloxane) PDMS molds as previously described. Each microneedle was approximately 650 μm tall and 250 μm wide at its base, in a pyramid shape.

PNMP was dip-coated onto these microneedle arrays and quickly dried under vacuum to form a conformal thin film over the surface of the microneedles. These PNMP coated microneedles were then exposed to UV light for 30 minutes to facilitate the cleavage the o-nitrobenzyl groups from the PNMP, converting the organic-soluble PNMP into a weak polyelectrolyte that is water soluble at biologic conditions pH > 6.5. The pH solubility derived from the photo-activation of PNMP provides the primary means of release of the LbL coating into the dermis from the microneedles. This release is triggered by coming into contact with biologic fluids, namely the interstitial fluid within the dermis which is at a pH of approximately 7.4. The UV activated PNMP quickly dissolves under these conditions within minutes of implantation, releasing the above coated LbL film into the dermis.

Layer-by-layer films were assembled onto the microneedles as previously described. Briefly, the PNMP coated microneedle arrays were attached to silicon supports with silicone glue and allowed to dry overnight. These arrays were then cleaned for RNA deposition by rinsing in three baths of RNase free water at pH 5.0 for one minute each. LbL assembly was carried out *via* the dip LbL method using a re-purposed histology slide stainer. Arrays were dipped into alternating baths of low molecular weight chitosan (1 mg mL^{-1}) and siRNA (20 μg mL^{-1}) with three 30 second wash steps between each polyelectrolyte deposition. All solutions were used at pH 5.0.

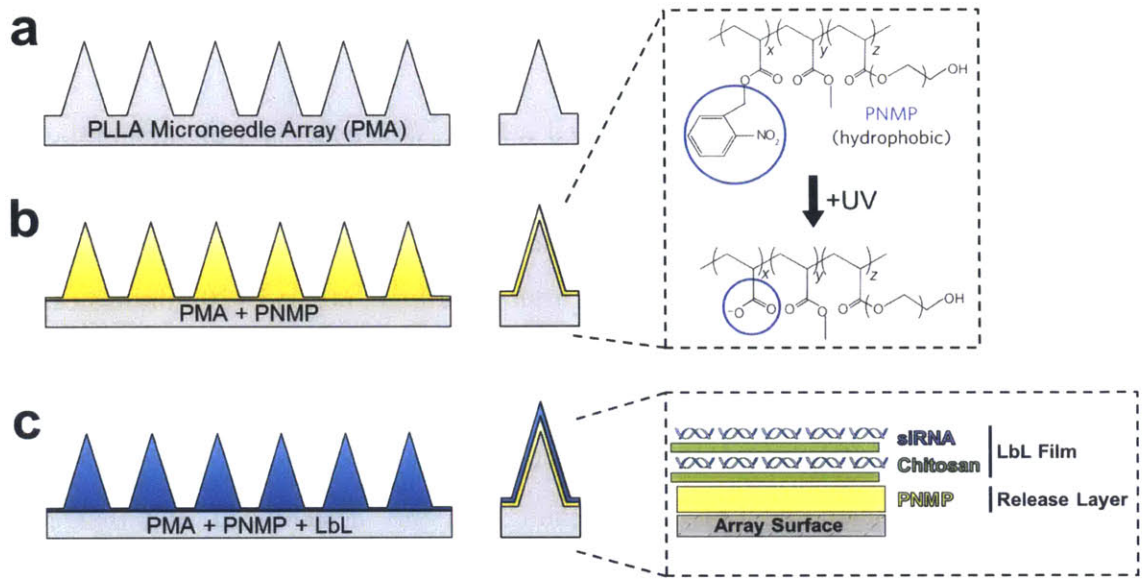

Figure 8-1 Cartoon schematic of quick releasing microneedle assemblies for transdermal delivery of siRNA

(a) PLLA microneedle arrays (PMAs) are assembled *via* a melt-molding technique within PDMS molds. (b) PMAs are coated in a uniform PNMP layer by dip-coating PNMP and then placing under vacuum. (c) LbL films are assembled over the PNMP layer.

8.3.2 Preliminary Investigations into LbL Film Assembly and Release

Preliminary *in vitro* studies were conducted on films prepared on silicon and glass slides to investigate film assembly and release characteristics. This work also looked at the uniformity of the coating, as the PNMP layer is deposited in a manner that may lead to non-uniform surfaces on which the LbL film was to be assembled. Films were observed to uniformly assemble over the PNMP coated surfaces with slight variation in film thickness only observed at the sample margins, which is most likely due to drying effects. Incorporation of siRNA was observed to be somewhat similar to what we have previously observed for other coated substrates, though reduced significantly by about 30%. Profiling the incorporation demonstrates that a great deal of this difference is due to the early layers of the LbL film not incorporating as much siRNA as in other studied substrates, suggesting that the PNMP surface we are coating is less ideal for LbL assembly. In total, after 25 layers of the [Chi/siRNA] film were assembled on the PNMP coated

surfaces approximately 11.3 ± 1.2 μg/cm^2 siRNA was incorporated into the LbL coating **(Figure 8-2a)**.

For release studies, fluorescently labeled siRNA was used in LbL assemblies. The release of the siRNA was studied at pH 7.4 in PBS at 37°C with agitation. In brief, films assembled on glass substrates were immersed into PBS at 37°C and placed on a rocking platform. The amount of siRNA was quantifies after 10, 20, 30, 60, and 120 minutes of release. After 30 minutes of being submerged in PBS at 37°C nearly 80% of the incorporated siRNA was observed to release from the coated surface. These films when submitted to violent agitation were observed to completely release siRNA from their surfaces, suggesting that the PNMP was largely dissolved underneath the LbL film creating a highly destabilized film that could be readily removed from the surface **(Figure 8-2b)**. .From these findings we determined that a 30 minute incubation period within the dermis would be most appropriate, with the addition of a physical massage step to facilitate this complete release of the LbL film.

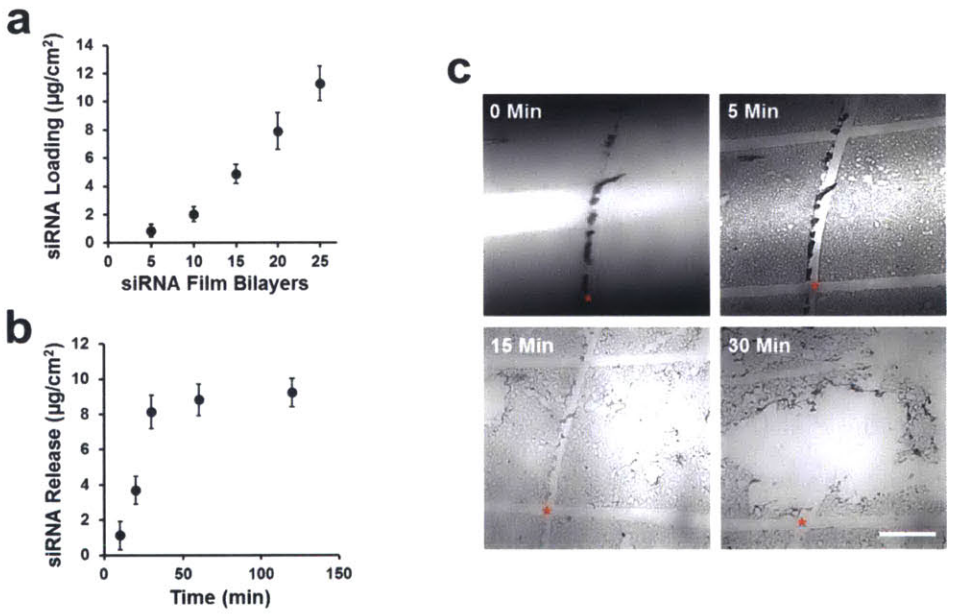

Figure 8-2 Rapid release of coating from surfaces from changes to physiologic conditions
(a) Incorporation of siRNA quantified throughout film assembly on top of PNMP coated glass slides. (b) Release of siRNA from LbL and PNMP coated glass slides. (c) Phase contrast

imaging of LbL films releasing from the coated surface after application of PBS (pH 7.4). Scale bar = 350 μm. (*) Denotes the same region throughout all of the images.

Visual appreciation of the rapid destabilization and release of the siRNA containing LbL film was important to understand how this process occurs **(Figure 8-2c)**. Immediately after application of the warmed PBS the surface, which was dried after LbL film assembly, begins to wet. These images were taken using phase contrast microscopy, and the initially very thin films were optically clear and light in color. After only 5 minutes at the release conditions this appearance had dramatically changes, with many small blebs in the surface becoming visible and the overall appearance of the film becoming darker and rougher. After 15 minutes large defects within the film coating are apparent. These defects originate in the middle of the unperturbed film and not necessarily at the cut margins. Thirty minutes after the PBS was applied to the coated surface enormous defects within the coating are observed. The film is seen to be loosely associated with the surface, and is seen to stretch and flake off from the glass substrate. After this point physical disturbance of the surface was observed to fully remove the coating from the surface.

8.3.3 *In Vivo* Application of siRNA Microneedle Arrays

The application of LbL coated microneedles for transdermal delivery of siRNA *in vivo* was performed similar to what has been previously described. Mice were anesthetized prior to any operation. For this study we chose to look at the knockdown of the reporter gene GFP in a ubiquitously GFP expressing mouse model. We chose to target GFP expression within the ears of these mice for a number of reasons; first as this tissue is relatively thin the level of tissue autofluorescence will be minimized. Second, the microneedles should penetrate the majority of the ears thickness, delivering siRNA into the full thickness of tissue to be analyzed so as to reduce complicating background fluorescence. Third, blood supply to distal portion of the ear is low, reducing the impact of the GFP positive blood cells on fluorescent measurements.

Implantation of the microneedle arrays was performed in a three step process. The first step was pre-perforation, where PLLA microneedles were used to generate reproducible defects in the skin so that the LbL coated microneedles could be implanted without resistance. Second,

ears were treated with approximately 50μL of PBS (pH 7.4) for ten seconds to wet the application site. Third, LbL coated microneedles were applied into the pre-made perforations and attached to the mice using labeling tape **(Figure 8-3a)**. These microneedles were held in the implant site for thirty minutes. After which time the tape backing was removed, being careful to keep the microneedles within the ear and the microneedles were gently massaged in a circular pattern for thirty seconds **(Figure 8-3b)**. After this period the microneedles were removed and the mice were allowed to recover on warming pads until they were back at baseline.

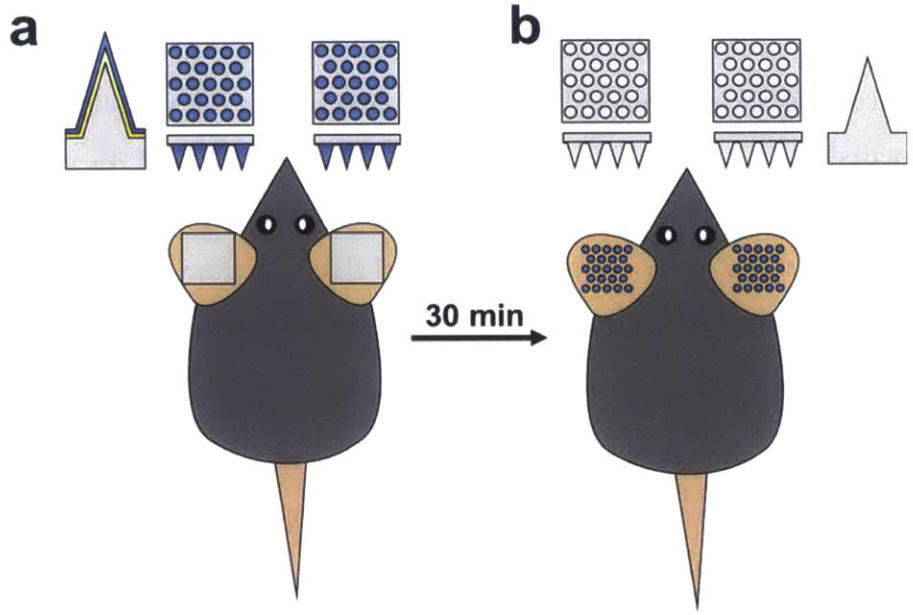

Figure 8-3 Cartoon schematic of in vivo microneedle array implantation
(a) Fully assembled microneedle arrays are placed into pre-perforated mouse ears that have been wetted with PBS (pH7.4) and remain in place for 30 minutes. (b) Microneedle arrays are removed from the mouse ears following 30 second massage to facilitate deposition of loosely attached film material. LbL coatings are intended to remain within the perforations and the PLLA microneedles are removed.

A new finding that influenced this protocol was the determination that PNMP treated microneedles could not effectively puncture the skin of mice. We believe this may be a new

phenomenon due to the way in which PNMP is deposited onto the microneedles via dip-coating technique and not spray drying. Dioxane, the solvent used in PNMP deposition, solubilizes PLLA. We believe that this step reduces the mechanical stability of the PLLA and results in the poor penetration. Using a non-PNMP coated microneedle array to puncture the ears resulted in highly reproducible perforation s that allowed for relatively simple implantation of the LbL coated microneedles into these sites.

8.3.4 *In Vivo* Release of SiRNA LbL Films

Microneedle arrays coated with siRNA containing LbL films were first tested *in vivo* for successful release of incorporated siRNA. To do this fluorescently labeled siRNA was used in the film assembly. LbL films were observed to coat the microneedle arrays in a near-uniform pattern, with some increased fluorescence observed at the microneedle margins **(Figure 8-4a)**. This is most likely due to slight aggregation at the dipping edge during film assembly. Post-application in vivo the level of fluorescent signal was observed to be greatly reduced **(Figure 8-4b)**. The labeled siRNA was observed to be fully released from the microneedle surface, even at the base of the array after the 30 minute application into the mice ears.

Quantification of the level of siRNA release from the coated microneedles demonstrated an approximate 84% reduction in average radiant efficiency **(Figure 8-4c)**. This suggests substantial delivery of the incorporated siRNA into the dermis. Visually inspecting the fluorescent imaging we can observe significant reductions in fluorescent intensity within the area of the microneedle array. When these LbL coated microneedles are imaged *via* confocal imaging the labeled siRNA is observed to coat the entire length of the microneedle from base to tip **(Figure 8-4d)**. After *in vivo* application and subsequent siRNA release, this coating is observe to be largely removed from the microneedles and only remains in small fragments at the base. This is in agreement with our previous fluorescent imaging of the microneedle arrays, as well as our preliminary studies on the release of these coatings from coated glass substrates.

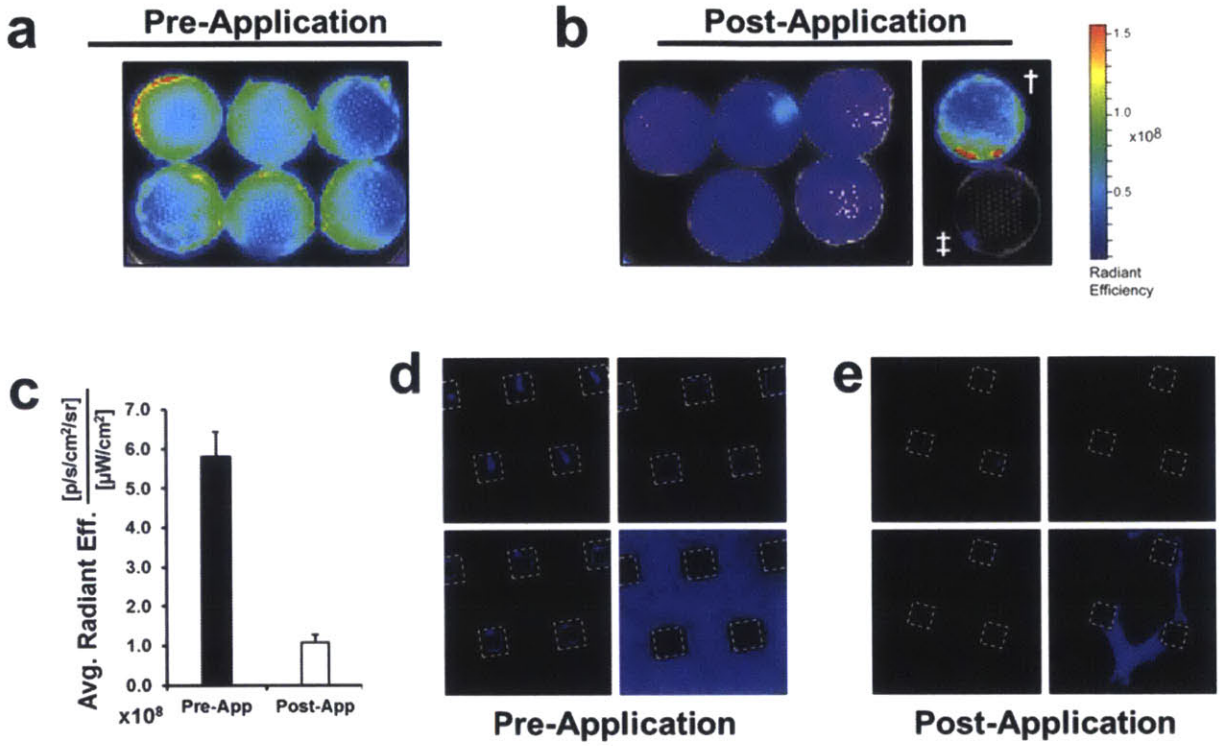

Figure 8-4 ***In vivo*** **delivery of fluorescently labeled siRNA**

(a) Pre-application fluorescent imaging of siRNA coated microneedles. (b) Post-application fluorescent imaging of siRNA coated microneedles demonstrate significantly reduced fluoresce. † Simultaneously imaged microneedle array not implanted. ‡ PLLA microneedle array without any PNMP or siRNA. (c) Quantification of average radiant efficiency for siRNA microneedle arrays before and after in vivo application. (d) Confocal imaging of labeled siRNA coated microneedle arrays demonstrating uniform coating out to the microneedle tips prior to application. (d) Post-application confocal imaging of microneedle arrays demonstrating the significant release of labeled siRNA film from the surface.

8.3.5 Penetrating the Skin with LbL Coated Microneedles

Application of PLLA microneedle arrays has been demonstrated in reports to effectively penetrate a range of skin from mouse to macaque. Here we have described the application of these arrays to mouse ears. Important to note, the microneedles we used were approximately 650 μm in length, while the distal portions of mouse ears are only around 400 μm thick. We

observed no full penetration of mouse ears in these experiments; however, it is a definite risk with using microneedles in such thin skin. For this reason the pre-perforation step was performed with the utmost of care in applying even slow pressure to the ears.

Evaluating the efficacy of the microneedles in puncturing the mouse ears we observe that the arrays do effectively penetrate the epidermis and dermis in the ear in a regular pattern. They are even seen to reach through the cartilage of the ear. This is perhaps not ideal, but it does suggest that the microneedles are reaching a sufficient depth into the skin so as to gain access to the tissues we are interested to deliver siRNA to. Inspecting the H&E stained histology we can observe a regular disruptive pattern through the ear, suggesting the regular puncturing of the skin with the evenly spaced microneedles **(Figure 8-5a)**. **Figure 8-5a** is histology from immediately post-application, where the mouse was sacrificed after siRNA release was finished. Importantly, the damage to this tissue is not insignificant, as this level of tissue disruption will necessitate an inflammatory response and subsequent wound healing **(Figure 8-5b)**. This response can be easily observed in Figure 86-c, two days post-application **(Figure 8-5c)**. Many neutrophils and even some macrophages can be seen remodeling the damage tissue, digesting the damaged muscle. This sort of response was observed in all treatment groups.

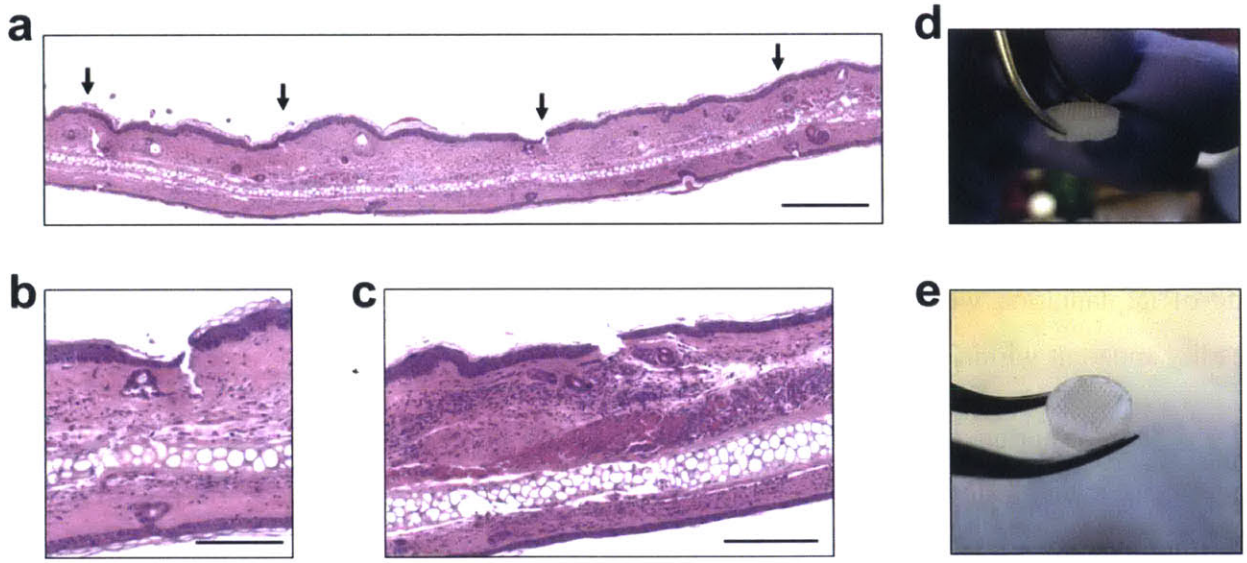

Figure 8-5 Application of LbL coated microneedle arrays *in vivo*

(a) H&E stained histological section of mouse ear demonstrating regular puncture pattern immediately after wounding. Scale bar = 700 μm. (b) Microneedle puncture is seen to reach through the epidermis into the dermis and abut the cartilage within the ear. Scale bar = 300 μm. (c) Microneedle puncture site two days after application, inflammation and tissue response is easily visible. Scale bar = 300 μm. (d) Microneedle array prior to application. (e) Microneedle array after 30 minute application *in vivo*.

Grossly, microneedles prior to application have a pyramid shape with a sharp point. Microneedles are straight and have little deviation in their structure, keeping a regular appearance (Figure 8-6d). Post-application to the mouse ears microneedles have a less clean appearance, with the tips of the microneedles often appearing bent and curled over. A few of the microneedles are folded over; however, most of them appear largely the same as they were pre-application. This suggests that the microneedles were properly placed within the perforation and most likely did reach into the dermis to deliver their coated siRNA films.

8.3.6 Transdermal Delivery of siRNA by LbL Microneedles

Delivery of siRNA into the ears of mice was followed using a fluorescently labeled siRNA incorporated into the LbL films. Uptake of the labeled siRNA was followed for the first two days in vivo. Immediately after delivery two mice were sacrificed and their ears fixed and prepared for histology. Delivery of the labeled siRNA can be clearly seen in **Figure 8-6a**. The full microneedle length can be observed to pierce the skin, reaching from the epidermis through the dermis and into the muscle. The delivered siRNA is not observed to travel very far from the site of implantation within the 30 minute application window. Few siRNA positive cells are readily apparent within these sections.

One day after application of the siRNA coated microneedles, the tissue appears much more contracted at the implant site. The fluorescent signal is largely still localized surrounding the microneedle site **(Figure 8-6b)**. A few siRNA positive cells appear to be distinguishable in the nearby tissue. Within this image we can also appreciate the depth that the microneedle was able to travel within the ear, reaching through the cartilage. No muscle is seen in the between the

dermis and the cartilage, suggesting that the presence of the muscle may have played a role in the microneedle from Figure 8-7a not reaching into the cartilage.

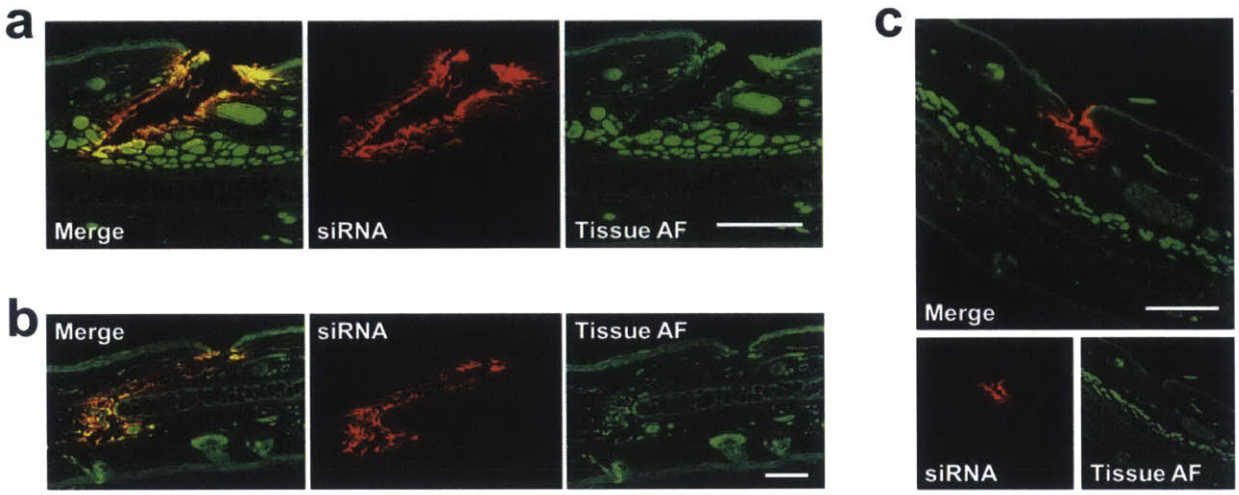

Figure 8-6 Tracking siRNA delivery at the site of application *in vivo*

(a) Fluorescent imaging of labeled siRNA immediately after application. Scale bar = 200 μm. (b) Imaging of siRNA delivery one day post-application. Scale bar = 150um. (c) Local uptake of siRNA two days after delivery. Scale bar = 200 μm. Tissue AF = Tissue Autofluorescence.

After two days many more siRNA positive cells are visible in the area adjacent to the site of application **(Figure 8-6c)**. The wound is observed to be much smaller than observed previously, however at this point it becomes much easier to distinguish cells that have taken up the labeled siRNA. There remains a significant quantity of the labeled material within the implant site, but it would be expected that this material would continue to be taken up and provide a sustained delivery within this site.

8.3.7 Controlled Localized Knockdown of GFP *In Vivo*

We were interested to determine the activity of our delivered siRNA in vivo. As we have demonstrated through this work, we are able to effectively release siRNA contained within an LbL film into microneedle implant sites. Whether this siRNA is able to effectively transfect cells to effect gene knockdown has yet to be demonstrated. To do this we chose to target the

reporter gene GFP expressed ubiquitously throughout a mouse model. The study was performed as described, with application of microneedle arrays into the ears of the mice for the siRNA-specific knockdown of GFP.

In this work we focused on three groups of mice. The first received microneedles containing siRNA for GFP knockdown (siGFP), the second receives microneedles containing a control siRNA sequence (siCon), and the third group receives microneedles with only PNMP and no LbL film (uncoated). Each group consisted of 3 mice, with both ears receiving the same treatment. After application of microneedle arrays mice were imaged daily out to one week to follow GFP expression, using whole-animal fluorescence imaging **(Figure 8-7a)**. Knockdown of GFP expression within the application site was observed in the siGFP treated mice after only two days, with the greatest relative difference occurring between four to five days post-application **(Figure 8-7b-c)**.

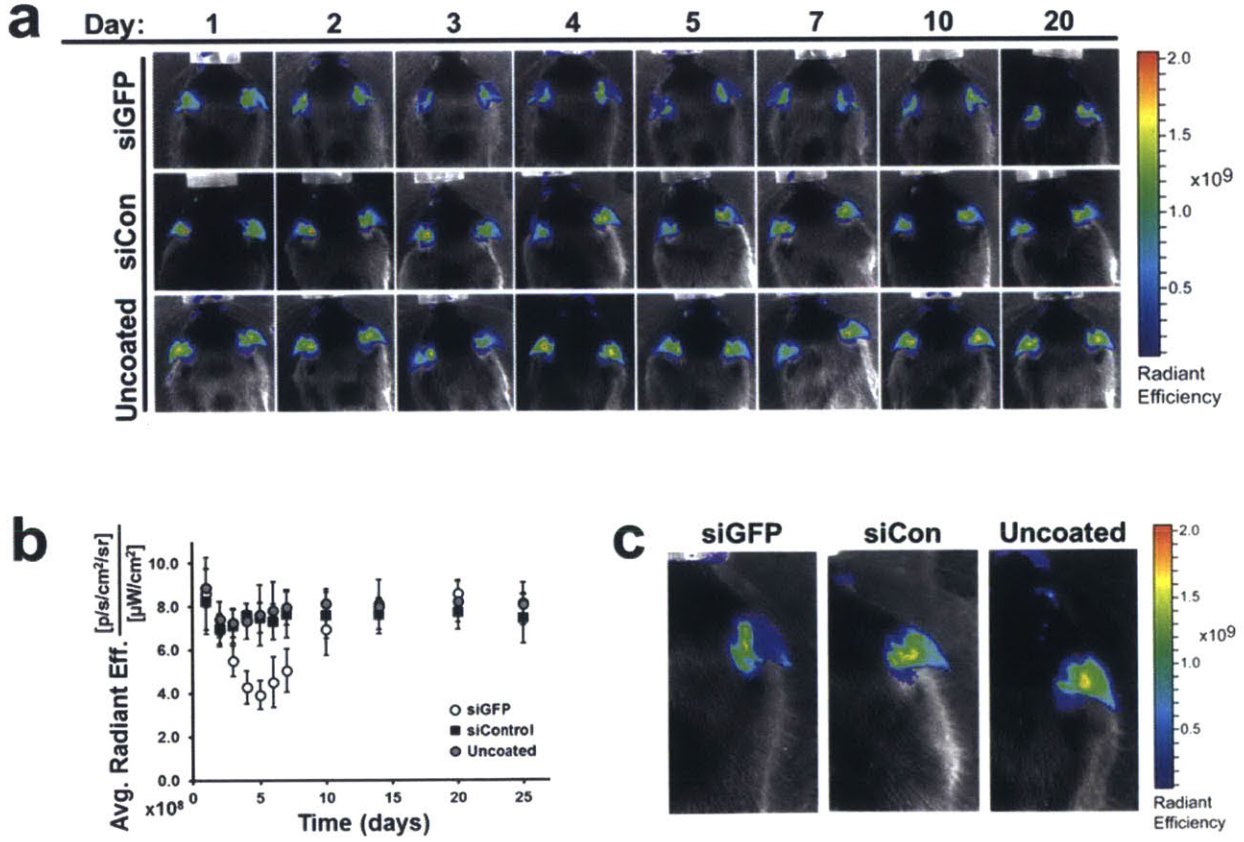

Figure 8-7 Controlled local knockdown of the reported gene GFP *in vivo*

(a) Representative in vivo imaging of GFP fluorescence for each treatment group over 20 days. (b) Plot of average relative fluorescence within the application site for each treatment group. (c) The greatest siRNA-specific knockdown was observed 4-5 days after application, seen here is day 4 representative images for each treatment group. Data shown are mean ± S.D., n=6.

The knockdown of GFP expression saw an approximate 50% reduction in siGFP treated ears compared to siCon or uncoated groups. There was no observed significant difference between the control groups, suggesting that the LbL coating itself was not acting to alter GFP expression *in vivo*. Knockdown of GFP was observed to be significant out to seven days, recovering to baseline after this period. It is important to note that within this animal model, blood cells are GFP positive and that tissue autofluorescence creates a complicating factor in evaluating GFP expression.

GFP knockdown was observed to be locally constrained within the site of microneedle application **(Figure 8-7c)**. This observation is in agreement with our earlier histological finding of the delivered siRNA being retained within the implant site and uptake by cells in the surrounding tissue to be enhanced. GFP expression within the tissue adjacent to the application site was observed to remain statistically similar to the same tissue in the control treated ears. These findings suggest that our delivery of siRNA was able to effectively achieve a sustained localized significant reduction in GFP expression within this mouse model.

8.4 Discussion

The localized controlled transdermal delivery of RNA interference has potential application in a myriad of different settings.[4, 5, 8] Within this thesis we have been primarily focused on wound healing, which is one such situation where controlled RNAi delivery has been demonstrated successful. The combination of LbL and microneedles provides a fascinating platform for simple and effective direct delivery to the skin. To achieve this we needed to design new delivery protocols however, both *in vitro* and *in vivo*.

Within this work we assembled a previously reported LbL film system onto PNMP coated microneedles for controlled local siRNA-specific knockdown *in vivo*. We performed this work as a proof of concept approach to determine if the LbL film which we have previously observed to successfully deliver siRNA from wound dressing and sutures could be effectively implemented using microneedle arrays as a substrate. Through some slight modifications of previously reported protocols we were able to effectively coat microneedle arrays with the LbL film and demonstrated the local delivery of the siRNA film.

The first such important change was the move from spray coating PNMP over the surface of the microneedles, to dip-coating the solution. This change resulted in significant material savings, which is very important as the PNMP polymer is a difficult to synthesize in large quantities that are required for spray deposition. This process allowed for the reproducible creation of a thin PNMP layer that conformally coated the microneedle array while also making possible more extensive in vitro studies within a reasonable timeframe. Our second major protocol development was use of an uncoated PLLA microneedle array to pre-puncture the mouse ears for placement of LbL coated microneedles. This approach resulted in improved delivery of the LbL coatings within the mouse dermis.

The siRNA delivering LbL coating was first investigated in vitro to establish the capability for the PNMP undercoating to affect rapid release of the siRNA. It was observed that up to 11.3 ± 1.2 $\mu g/cm^2$ of siRNA were incorporated on top of the PNMP coating. This siRNA film was observed to rapidly shed from the coated surface when immersed in PBS at 7.4 and 37oC. Imaging the release of the film demonstrated how the film began to bleb and swell within minutes of exposure to the release conditions. When films were assembled on microneedles and applied in vivo we observed similar extensive LbL film release from the coated surface.

In vivo investigations demonstrated the regular pattern of microneedle punctures into the dermis. In many of the sections the damage was observed to reach into the skeletal muscle and even through the cartilage. The response to such injury was as would be expected; causing a significant inflammatory response that resulted in tissue damage and contraction around the site of implant.[55-57] The delivery of the coated siRNA was seen to be largely concentrated to the tissue directly in contact with the microneedle, while after a few days numerous siRNA positive cells were observed in the surrounding tissue. To demonstrate the effective knockdown of a

gene in vivo we chose to target the reporter gene GFP in a mouse model with ubiquitous GFP expression. We observed significant GFP reduction in a siRNA-specific manner for up to one week. This knockdown was observed to be largely contained within the site of application without significant changes in the fluorescence of the surrounding tissues.

The general approach we have outlined within this report has numerous potential applications ranging from tissue engineering and regenerative medicine to cancer therapy. This sort of approach could have potential in any number of applications where the local delivery of siRNA may be of benefit. In the context of this thesis we have demonstrated again that the LbL film first developed in Chapter 5 can be broadly applied to myriad of different substrates. Here we focused on the knockdown of a reporter gene that has no impact on a meaningful pathology, but the implications of this work is easily extrapolated to efforts that could make a real difference in the treatment of complex diseases.

8.5 References

1. Yin, H. et al. Non-viral vectors for gene-based therapy. Nat Rev Genet 15, 541-555 (2014).

2. Zhang, Y., Satterlee, A. & Huang, L. In vivo gene delivery by nonviral vectors: overcoming hurdles? Mol Ther 20, 1298-1304 (2012).

3. Thanik, V.D. et al. Topical matrix-based siRNA silences local gene expression in a murine wound model. Gene Ther 14, 1305-1308 (2007).

4. Pan, M., Ni, J., He, H., Gao, S. & Duan, X. New Paradigms on siRNA Local Application. BMB Rep (2014).

5. Segovia, N. et al. Hydrogel Doped with Nanoparticles for Local Sustained Release of siRNA in Breast Cancer. Adv Healthc Mater 4, 271-280 (2015).

6. Vandegrift, M.T. et al. Acellular dermal matrix-based gene therapy augments graft incorporation. J Surg Res (2015).

7. Nelson, C.E., Gupta, M.K., Adolph, E.J., Guelcher, S.A. & Duvall, C.L. siRNA Delivery from an Injectable Scaffold for Wound Therapy. Adv Wound Care (New Rochelle) 2, 93-99 (2013).

8. Nelson, C.E. et al. Sustained local delivery of siRNA from an injectable scaffold. Biomaterials 33, 1154-1161 (2012).

9. Nelson, C.E. et al. Tunable delivery of siRNA from a biodegradable scaffold to promote angiogenesis in vivo. Advanced Materials 26, 607-614, 506 (2014).

10. Ghildiyal, M. & Zamore, P.D. Small silencing RNAs: an expanding universe. Nat Rev Genet 10, 94-108 (2009).

11. Huzil, J.T., Sivaloganathan, S., Kohandel, M. & Foldvari, M. Drug delivery through the skin: molecular simulations of barrier lipids to design more effective noninvasive dermal and transdermal delivery systems for small molecules, biologics, and cosmetics. Wires Nanomed Nanobi 3, 449-462 (2011).

12. McAllister, D.V. et al. Microfabricated needles for transdermal delivery of macromolecules and nanoparticles: Fabrication methods and transport studies. Proc Natl Acad Sci U S A 100, 13755-13760 (2003).

13. Henry, S., McAllister, D.V., Allen, M.G. & Prausnitz, M.R. Microfabricated microneedles: A novel approach to transdermal drug delivery. Journal of Pharmaceutical Sciences 87, 922-925 (1998).

14. Mukerjee, E., Collins, S.D., Isseroff, R.R. & Smith, R.L. Microneedle array for transdermal biological fluid extraction and in situ analysis. Sensor Actuat a-Phys 114, 267-275 (2004).

15. Miyano, T. et al. Sugar micro needles as transdermic drug delivery system. Biomed Microdevices 7, 185-188 (2005).

16. Davis, S.P., Martanto, W., Allen, M.G. & Prausnitz, M.R. Hollow metal microneedles for insulin delivery to diabetic rats. Ieee T Bio-Med Eng 52, 909-915 (2005).

17. Park, J.H. et al. Polymer particle-based micromolding to fabricate novel microstructures. Biomed Microdevices 9, 223-234 (2007).

18. Matriano, J.A. et al. Macroflux (R) microprojection array patch technology: A new and efficient approach for intracutaneous immunization. Pharm Res 19, 63-70 (2002).

19. Chabri, F. et al. Microfabricated silicon microneedles for nonviral cutaneous gene delivery. Brit J Dermatol 150, 869-877 (2004).

20. Paik, S.J. et al. In-plane single-crystal-silicon microneedles for minimally invasive microfluid systems. Sensor Actuat a-Phys 114, 276-284 (2004).

21. Ito, Y., Kashiwara, S., Fukushima, K. & Takada, K. Two-layered dissolving microneedles for percutaneous delivery of sumatriptan in rats. Drug Dev Ind Pharm 37, 1387-1393 (2011).

22. Chandrasekaran, S., Brazzle, J.D. & Frazier, A.B. Surface micromachined metallic microneedles. J Microelectromech S 12, 281-288 (2003).

23. Gill, H.S. & Prausnitz, M.R. Pocketed microneedles for drug delivery to the skin. J Phys Chem Solids 69, 1537-1541 (2008).

24. Andrianov, A.K., Marin, A. & DeCollibus, D.P. Microneedles with intrinsic immunoadjuvant properties: microfabrication, protein stability, and modulated release. Pharm Res 28, 58-65 (2011).

25. Gill, H.S. & Prausnitz, M.R. Coated microneedles for transdermal delivery. Journal of Controlled Release 117, 227-237 (2007).

26. Saurer, E.M., Flessner, R.M., Sullivan, S.P., Prausnitz, M.R. & Lynn, D.M. Layer-by-Layer Assembly of DNA- and Protein-Containing Films on Microneedles for Drug Delivery to the Skin. BioMacromolecules 11, 3136-3143 (2010).

27. Prausnitz, M.R. Microneedles for transdermal drug delivery. Advanced Drug Delivery Reviews 56, 581-587 (2004).

28. Migalska, K. et al. Laser-engineered dissolving microneedle arrays for transdermal macromolecular drug delivery. Pharm Res 28, 1919-1930 (2011).

29. Wang, P.M., Cornwell, M., Hill, J. & Prausnitz, M.R. Precise microinjection into skin using hollow microneedles. J Invest Dermatol 126, 1080-1087 (2006).

30. Ji, J., Tay, F.E.H., Miao, J.M. & Iliescu, C. Microfabricated microneedle with porous tip for drug delivery. J Micromech Microeng 16, 958-964 (2006).

31. Cui, Q.F., Liu, C.L. & Zha, X.F. Study on a piezoelectric micropump for the controlled drug delivery system. Microfluid Nanofluid 3, 377-390 (2007).

32. Bal, S.M., Caussin, J., Pavel, S. & Bouwstra, J.A. In vivo assessment of safety of microneedle arrays in human skin. Eur J Pharm Sci 35, 193-202 (2008).

33. Bal, S.M., Ding, Z., van Riet, E., Jiskoot, W. & Bouwstra, J.A. Advances in transcutaneous vaccine delivery: Do all ways lead to Rome? Journal of Controlled Release 148, 266-282 (2010).

34. Zahn, J.D., Trebotich, D. & Liepmann, D. Microdialysis microneedles for continuous medical monitoring. Biomed Microdevices 7, 59-69 (2005).

35. Arora, A., Prausnitz, M.R. & Mitragotri, S. Micro-scale devices for transdermal drug delivery. Int J Pharm 364, 227-236 (2008).

36. Sivamani, R.K., Liepmann, D. & Malbach, H.I. Microneedles and transdermal applications. Expert Opin Drug Deliv 4, 19-25 (2007).

37. Raphael, A.P. et al. Targeted, needle-free vaccinations in skin using multilayered, densely-packed dissolving microprojection arrays. Small 6, 1785-1793 (2010).

38. Demuth, P.C., Garcia-Beltran, W.F., Ai-Ling, M.L., Hammond, P.T. & Irvine, D.J. Composite dissolving microneedles for coordinated control of antigen and adjuvant delivery kinetics in transcutaneous vaccination. Adv Funct Mater 23, 161-172 (2013).

39. DeMuth, P.C. et al. Vaccine delivery with microneedle skin patches in nonhuman primates. Nat Biotechnol 31, 1082-1085 (2013).

40. Demuth, P.C., Min, Y., Irvine, D.J. & Hammond, P.T. Implantable Silk Composite Microneedles for Programmable Vaccine Release Kinetics and Enhanced Immunogenicity in Transcutaneous Immunization. Adv Healthc Mater (2013).

41. DeMuth, P.C., Moon, J.J., Suh, H., Hammond, P.T. & Irvine, D.J. Releasable layer-by-layer assembly of stabilized lipid nanocapsules on microneedles for enhanced transcutaneous vaccine delivery. ACS Nano 6, 8041-8051 (2012).

42. DeMuth, P.C., Su, X., Samuel, R.E., Hammond, P.T. & Irvine, D.J. Nano-layered microneedles for transcutaneous delivery of polymer nanoparticles and plasmid DNA. Advanced Materials 22, 4851-4856 (2010).

43. Park, J.H., Allen, M.G. & Prausnitz, M.R. Biodegradable polymer microneedles: Fabrication, mechanics and transdermal drug delivery. Journal of Controlled Release 104, 51-66 (2005).

44. Donnelly, R.F. et al. Design, Optimization and Characterisation of Polymeric Microneedle Arrays Prepared by a Novel Laser-Based Micromoulding Technique. Pharm Res 28, 41-57 (2011).

45. Park, J.H., Allen, M.G. & Prausnitz, M.R. Polymer microneedles for controlled-release drug delivery. Pharm Res 23, 1008-1019 (2006).

46. DeMuth, P.C. et al. Polymer multilayer tattooing for enhanced DNA vaccination. Nat Mater 12, 367-376 (2013).

47. Chen, X.F. et al. Dry-coated microprojection array patches for targeted delivery of immunotherapeutics to the skin. Journal of Controlled Release 139, 212-220 (2009).

48. Jiang, J. et al. Coated microneedles for drug delivery to the eye. Invest Ophthalmol Vis Sci 48, 4038-4043 (2007).

49. Lee, K., Kim, J.D., Lee, C.Y., Her, S. & Jung, H. A high-capacity, hybrid electro-microneedle for in-situ cutaneous gene transfer. Biomaterials 32, 7705-7710 (2011).

50. DeMuth, P.C. et al. Polymer multilayer tattooing for enhanced DNA vaccination. Nat Mater 12, 367-376 (2013).

51. Yang, M. & Zahn, J.D. Microneedle insertion force reduction using vibratory actuation. Biomed Microdevices 6, 177-182 (2004).

52. Davis, S.P., Landis, B.J., Adams, Z.H., Allen, M.G. & Prausnitz, M.R. Insertion of microneedles into skin: measurement and prediction of insertion force and needle fracture force. J Biomech 37, 1155-1163 (2004).

53. Verbaan, F.J. et al. Improved piercing of microneedle arrays in dermatomed human skin by an impact insertion method. Journal of Controlled Release 128, 80-88 (2008).

54. Doh, J. & Irvine, D.J. Photogenerated polyelectrolyte bilayers from an aqueous-processible photoresist for multicomponent protein patterning. J Am Chem Soc 126, 9170-9171 (2004).

55. Gurtner, G.C., Werner, S., Barrandon, Y. & Longaker, M.T. Wound repair and regeneration. Nature 453, 314-321 (2008).

56. Park, J.E. & Barbul, A. Understanding the role of immune regulation in wound healing. Am J Surg 187, 11S-16S (2004).

57. Longaker, M.T. & Stern, R. Wound environment: parallels between healing and tumorigenesis. Surgery 107, 715 (1990).

Chapter 9
Polymer Conjugated Retinoids for Controlled Transdermal Delivery

9.1 Introduction

In Chapter 8 we described the development of ultrathin polymer coatings for transdermal delivery of siRNA from LbL coated microneedles. This technique uses the physical disruption of the skin to deliver LbL contained materials into the dermis. Here we took an orthogonal approach to transdermal delivery, using a polymer conjugated hydrophobic drug that could be applied topically to the skin for controlled delivery. This work is very different than the rest of the work presented in this thesis as it does not concern RNA interference, but was inspired by a conflagration of motivating factors, including the need for improved acne treatments for patients and my disdain for bad television commercials.

All-trans retinoic acid (ATRA), a metabolite of Vitamin A, is a key component in the topical treatment of numerous different skin disorders, including: acne, psoriasis, and UV-induced photoaging.[1-8] ATRA therapy acts by reducing abnormal follicular epithelial hyper-keratinization as well as repressing UV-induced cell signaling pathways that lead to upregulated expression of metalloproteinases.[9-14] Use of ATRA however is limited by its serious side-effects such as skin irritation and hair loss as well as its poor chemical stability.[15-20] Previous investigations have looked to control these undesirable characteristics through controlled release formulations such as creams, microparticles, and emulsions.[17, 21-24] These strategies however rely on bolus delivery of active ATRA that in the case of creams and emulsions can become immediately available. This rapid increase in local concentration causes a number of adverse side-effects.[10, 25] While on the other hand, microparticle approaches require injection across the dermis, increasing the potential for immunologic response and infection. To date there has been limited research into polymer-conjugated forms of ATRA, with their focus on application in cancer therapies.[26-28]

Poly(vinyl alcohol) (PVA) is an excipient of choice in many pharmacologic formulations and is commonly used in the preparation of biodegradable particles.[29-32] PVA is well tolerated and has demonstrated a very good safety profile *in vivo*.[33-36] Applications for PVA in drug delivery primarily focus on it as a surfactant, providing excellent drug loading while allowing control over particle size and stability.[37-40] Recent reports have highlighted the mucoadhesive nature of PVA coated particles, suggesting that the hydrogen bonding ability of PVA promotes interaction with mucosal proteins.[41-44] This adhesive nature of PVA to mucosal components suggests a broader potential use, one that can take advantage of the hydrogen bonding to increase the residence time of drugs within tissues. Conjugating the hydrophobic ATRA to the very hydrophilic PVA through a hydrolytically degradable ester linkage, creates a new approach to formulate ATRA into a controlled release nanomaterial with potentially enhanced tissue residence.

Controlling ATRA release presents many substantial improvements over the current techniques for ATRA delivery. Currently ATRA is placed as a bolus at the sight of interest, immediately activating retinoic acid receptors and generating a strong pro-inflammatory response that can cause serious pain, irritation, and damage to the dermis. Bolus delivery also requires constant re-application to the sight of interest, often multiple times per day. By delivering ATRA as a controlled-release conjugate we can avoid these side effects and promote a more healthy response from the tissue with better control over ATRA action.

In this report we describe the synthesis and evaluation of a PVA-ATRA polymer-drug conjugate (PATRA) for topical controlled delivery of ATRA. When hydrated, PATRA forms a nanoparticle micelle which is soluble in water and provides protection from UV degradation of ATRA. Release of ATRA from the polymer conjugate was sustained for up to ten days *in vitro*. Delivery into skin was evaluated first using explant pig dermis which showed a near four-fold increase in ATRA accumulation within the dermis and a ten-fold reduction in permeated ATRA after 12 hours compared to bolus ATRA administration. When tested *in vivo* PATRA was observed to elicit minimal inflammatory response compared to ATRA therapy, while remaining present for up to nearly five days post-application.

9.2 Materials and Methods

9.2.1 Materials

PVA and ATRA were purchased form Sigma-Aldrich (St. Louis, MO). Phosphate-buffered saline (PBS, 10x), Advanced-MEM, fetal bovine serum, antibiotic-antimycotic solution, and 100 mM L-Glutamine solution were purchased from Life Technologies (Grand Island, NY). AlexaFluor 647 NHS ester was purchased from Life Technologies (Grand Island, NY). NIH-3T3 cells were purchased from ATCC (Manassas, VA).

9.2.2 Fabrication of PATRA

0.138g DMAP and 1.0g PVA were added to a stirred solution of ATRA (0.341 g) in 80 mL of anhydrous DMF. The reaction temperature was cooled to 0°C, and DCC was added to the reaction mixture. The reaction was allowed to run for 12-24h (depending on chromatographic measurement), during which the reaction temperature was allowed to reach room temperature. After the stipulated reaction period, DCU precipitate was filtered off, and the filtrate was concentrated *in vacuo* at low pressure, and precipitated in ether.

After centrifugation of the ether suspension at 5000 rpm for 15 minutes, the residue was collected, dissolved in water, and dialyzed against water for 12h to remove any insoluble polar impurities. The compound was characterized by UV-Vis spectroscopy, ^{1}H NMR and ^{13}C NMR.

9.2.3 *In Vitro* Analysis of PATRA

Release studies were carried out in a hydroalcoholic solution at two physiologically relevant temperatures, 20°C and 37°C. The impact of ATRA on cell proliferation was assessed by supplementing the media of sub-confluent NIH-3T3 cells with ATRA, PATRA, PVA, and PBS in 24-well plates at concentrations equivalent to 10μM ATRA. ATRA was prepared in a concentrated hydroalcoholic solution of 10 μL. A similar dose of ethanol (5 μL) was added to each treatment group immediately after addition of the testing agents. The cell number calculated from imaging of those wells is used as the reference in the calculation of relative cell density.

Uptake, retention, and penetration of ATRA in pig skin were investigated using a Franz diffusion cell as previously described. Skin was harvested from the flanks of adult female Yorkshire pigs 1 hour after sacrifice with subcutaneous fat removed. Skin was sectioned and frozen at -80°C for up to six months prior to use. Skin was prepared for diffusion experiments

by thawing in PBS for one hour after which time all hair on the skin was shaven off. Test samples of skin were cut to 30mm x 30mm square samples that were placed into the diffusion cell such that the top of the dermis faced a 3mL testing retention reservoir and the underside faced a 15mL penetration reservoir. All studies were run at room temperature.

Samples were placed into the retention reservoir at a concentration of 0.1 mg/mL and followed for up to 12 hours. ATRA concentration was evaluated in both the retention and penetration reservoirs every four hours during this period *via* UV absorbance measurements. ATRA was first solubilized in a concentrated alcohol solution prior to being diluted into the retention well. A similar amount of ethanol was added to the PATRA retention well to control for ethanol concentration. For both groups, the penetration reservoir was filled with a hydroalcoholic solution so that the ATRA that could penetrate the skin would be soluble for UV absorbance measurement.

9.2.4 *In Vivo* PATRA Application

All animal studies were approved by the MIT Institutional Animal Care and Use Committee (IACUC). Animals were housed and cared for in the USDA-inspected MIT Animal Facility under federal, state, local, and NIH guidelines for animal care. Six week old Balb/CJ mice (n=18) were purchased from Jackson Laboratories (Bar Harbor, ME). Mice were either used for irritation assessment or for IVIS PATRA retention testing.

Mice used for the assessment of irritation were given each of the two different treatments on 1cm^2 regions of their dorsum, these included PATRA, ATRA, PVA, and PBS. A total of twelve mice were used in this assessment. 50μL of 10 μM ATRA solution was placed on two 1 cm^2 shaved areas on the flanks of a Balb/CJ mouse on either side of midline. PATRA (0.092 mg mL^{-1}) and PVA (0.089 mg mL^{-1}) concentrations were controlled for 10 μM ATRA dosing. These solutions were rubbed into the skin using a cotton-tipped applicator for 30 seconds.

Mice used for PATRA retention testing were given two applications of one material, either PATRA or the unconjugated AF-647 dye, on two 1 cm^2 regions on their dorsum on midline. The material was allowed to adsorb into the skin for 30 minutes and then the mice were cleaned with a wetted towel to remove excess. Mice were imaged daily for up to seven days.

9.2.5 Histology

Tissues were fixed in zinc fixative without formalin for 48 hours. The excised tissues were cut on center and then embedded cut-face down in paraffin. Sections were taken at the wound center and at one further level of 500 μm reaching a total of 1mm sampling length through the application site. At each level an H&E slide was stained. Unstained slides were also taken for potential IHC analysis of the tissue. All sections were 5μm thick. Image analysis was performed using Image J.

9.2.7 Statistics

Statistical analysis was performed between groups using Student's *t*-test and rectified by ANOVA for comparisons between multiple groups. Values are represented as mean ± S.D. A value of $p < 0.05$ was used to indicate statistical significance.

9.3 Results

9.3.1 Chemical Synthesis of PVA Conjugated ATRA (PATRA)

Retinoids are a powerful and broadly used class of therapeutics.[8, 12, 45-47] In particular, all-trans retinoic acid (ATRA) is used in numerous cosmetic formulations for anti-aging and wrinkle reduction, while also being a first line cancer therapy in lymphoblastic leukemia.[6, 10, 48, 49] Delivering ATRA is difficult however as it is incredibly hydrophobic, making it practically insoluble in water. The current formulations of ATRA rely on solubilizing emulsifiers that are greasy and can damage or dehydrate areas of application.[11, 50-52] These formulations are unstable *in vivo*, leading to rapid bolus release of ATRA into the tissues in which they are dosed, which significantly contributes to the side-effects of ATRA therapy.[10, 25, 53]

These formulation concerns create complications as it is difficult to maintain ATRA at a therapeutic level within tissues. This complication is exacerbated by the relatively narrow therapeutic index for ATRA and the significant risk of side-effects. Indeed, the formulation constraints create the necessity for repeated applications, increasing the risk of such complications. These complications are of significant interest to the commercial applications of ATRA as it is the primary agent of my anti-acne creams.[12, 13, 54, 55] In this role ATRA acts as an anti-proliferative (similar to its use in cancer therapy) to reduce the formation of commodomes.[7]

By conjugating ATRA to a highly water soluble FDA approved polymer through an ester-bond linkage we can produce a water soluble polymer-drug conjugate for the controlled release of ATRA. The choice of polymer is important in this work as it will determine a great deal of the conjugates final characteristics. We chose to focus our work on poly(vinyl alcohol) (PVA) as it has been used extensively as a drug excipient and is very well tolerated *in vivo*.[31, 33-35, 56] PVA has been described in numerous previous reports for its highly mucoadhesive nature, due to the number of hydrogen bonds it can form with mucosal polysaccharides. In a similar role, we hope to take advantage of this adhesive nature of PVA to form a topical glue that would hold the conjugate within the administration site for the controlled delivery of ATRA.

Conjugating ATRA to PVA was performed *via* the Steglich esterification process using DCC (N,N'-dicyclohexycarbodiimide) chemistry in a one-pot synthesis as described in the methods section of this chapter **(Figure 9-1)**. Initially, DMSO was used as solvent which resulted in a heterogeneous reaction condition for carrying out the esterification. This purified product was weighed and the UV absorbance for ATRA was quantified. It was determined that as per the directions described in the methods section PVA functionalization with ATRA reached approximately 3.25 weight percent. We have also found that the solubility of PVA can be increased by using DMAc/5% LiCl as the solvent system.

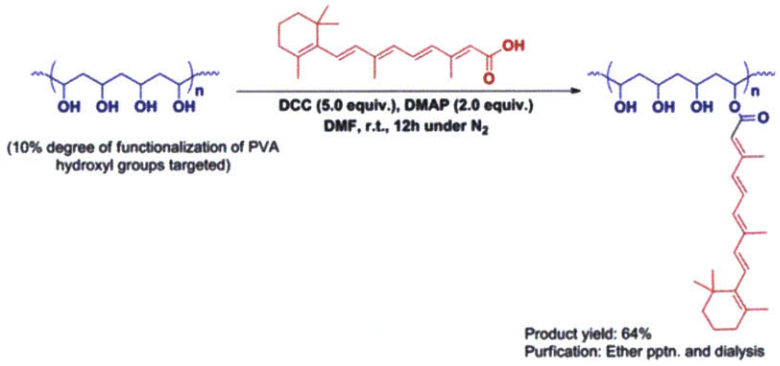

Figure 9-1 Chemical synthesis of PATRA

Conjugation of ATRA to PVA was performed using DCC chemistry in DMF overnight at room temperature under nitrogen.

Conjugating the hydrophobic ATRA to the highly water-soluble PVA through an ester-bond linkage produces an amphiphilic material. In aqueous solution it would then make sense that the

hydrophobic ATRA moieties along the PVA backbone would isolate themselves away from the polar solvent, forming a micellar structure. We hypothesized that this micelle structure would allow for significantly increased water solubility of the ATRA so long as it was conjugated to the PVA in PATRA.

This increased water solubility could then be used to investigate new formulations and novel means of delivery into the target tissues. It is important to note here that micelles can be easily disrupted by non-specific interactions with proteins and other biomolecules; we would then expect that while the PATRA may form a micelle in an uncluttered aqueous solution, it would lose this structure *in vivo*. Unlike emulsified formulations of ATRA however, by covalently conjugated the ATRA to the much large PVA, along with PVAs mucoadhesive nature, we should be able to retain the conjugate within the application site to achieve controlled release of ATRA **(Figure 9-2)**.

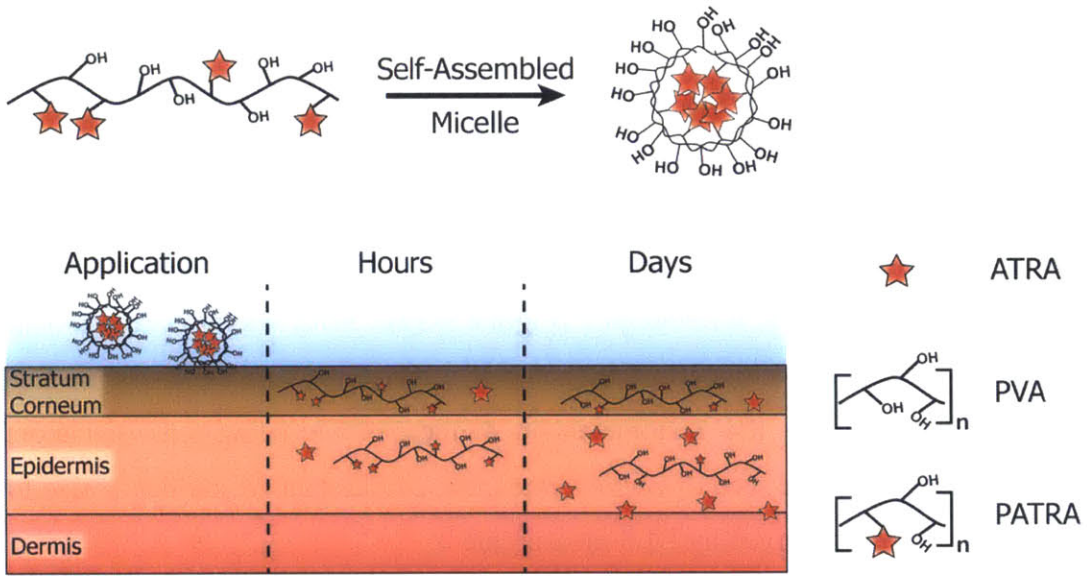

Figure 9-2 Cartoon schematic of the adsorption of micellar PATRA into the dermis
Release of ATRA from the PATRA conjugate occurs in the hydrated dermis.

9.3.2 Characterization of PATRA *In Vitro*

We hypothesized that the covalent conjugation of ATRA to PVA would result in the creation of a water soluble drug-polymer conjugate that would naturally form a micellar structure in aqueous solution. To investigate these hypotheses we performed a series of *in vitro* analyses on the PATRA molecule. We began by gross examination of the purified product, which was a light yellow in color, a lighter shade than the pure ATRA product. PATRA was solubilized in water for ten minutes and then analyzed for the formation of nanoparticles as well as for its general appearance **(Figure 9-3a&c)**. At the highest concentration of PATRA we attempted (100mg/mL) we observed no particles, and the color of the solution gave the suggestion that much of the PATRA was not fully solubilized as semi-translucent portions of the dried powder were observed to remain visible in the mixture. Nanoparticle structures were observed by dynamic light scattering (DLS) at concentrations starting at 50mg/mL and lower. These particles were in the range of 120 to 150 nm in diameter. The appearance of these particle containing solutions was a light yellow, and was observed to vary in intensity with the relative dilution of the PATRA.

We believed that the logical structure of the PATRA material in aqueous solution was a micelle, however we were unsure what type of a micelle would be formed. To investigate this important characteristic we performed transmission electron microscopy of the PATRA using uranyl acetate negative staining to mark the hydrophobic ATRA-rich regions of the structure, which appear dark in the TEM micrographs **(Figure 9-3b)**. What we observe is a nano-fibular structure, where ATRA is occluded in the center of a thin fiber. These fibers are high aspect ratio structures, with only a few nanometers in diameter while being tens of nanometers in length. These nano-fibers are seen to agglomerate into particles that are similar in size to the 120 to 150 nm structures we observed by DLS measurement.

A

Polymer (mg/mL)	ATRA (mg/mL)	Particle Diameter (nm)	Appearance
100.0	2.45	N/A	Opaque Yellow
50.0	1.23	126.6 ± 4.1	Clear Yellow
25.0	0.61	131.1 ± 3.2	Clear Yellow
5.0	0.12	138.2 ± 5.1	Clear Yellow
1.0	0.02	148.1 ± 7.2	Clear Light Yellow

B

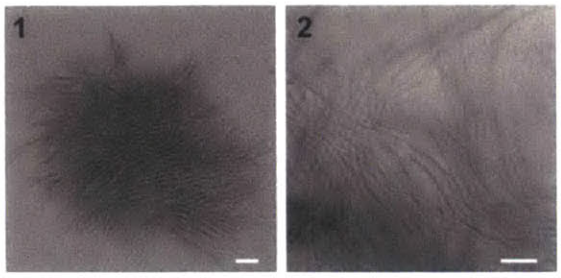

C

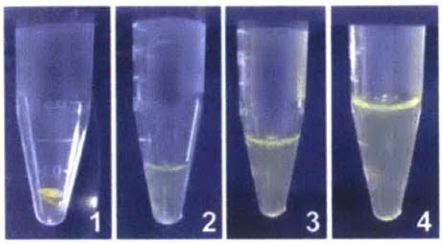

D

Solvent	ATRA Solubility (mg/mL)	PATRA Solubility (mg/mL)
Hydroalcoholic	0.67 ± 0.05	0.58 ± 0.07
Water	< 0.01	0.33 ± 0.08
PBS	< 0.01	0.35 ± 0.04

Figure 9-3 Nano-fiber PATRA solubility and characterization

(a) Characterization of particle size and solution appearance for different concentrations of PATRA in water. (b) TEM images of nano-fiber PATRA formed in water. In water PATRA forms thin (3-5 nm) fibers (2) that agglomerate into nanoparticles (1). (c) Digital images of solubilization of PATRA dry powder (1) at 50mg/mL (2), 25mg/mL (3), and 5mg/mL (4) concentrations. (d) Solubility of ATRA and PATRA in different solutions. Data shown is mean ± S.D., n=3.

As the PATRA polymer appeared to better solubilize the ATRA molecule in water we were interested in determining the extent of this increased solubility. We thus investigated the solubility of free ATRA and PATRA conjugated ATRA in three different solutions: (1) hydroalcoholic (50:50), (2) deionized water, and (3) PBS 1x (pH7.4). Solubility was evaluated by bringing 2mg/mL of ATRA either free or conjugated to PVA into equilibrium at room temperature for 1 hour, followed by centrifugation of the solution at 1,500 rpm for five minutes to remove undissolved precipitate **(Figure 9-3d)**. The supernatant from this process was then used for the testing of ATRA concentration *via* UV absorbance as previously described.[25]

We were surprised to find that ATRA solubility in the hydroalcoholic solution was statistically identical to PATRA conjugated ATRA. We had understood that ATRA was soluble to some extent in ethanol, but were impressed that the PATRA conjugate would also be soluble in this mixed solvent. ATRA was observed to be insoluble in either deionized water and PBS

solutions; however, PATRA was observed in significant quantities in these solutions. PATRA was seen to carry approximately 0.33 ± 0.08 mg/mL ATRA stably into deionized water and 0.35 ± 0.04 mg/mL into PBS. These quantities were notably less than what we had previously observed from our solubility studies, suggesting that those findings may have included material that was able to be removed by centrifugation. These materials could include partially solubilized polymers as well as large micro-aggregates of the micelles.

We also investigated the relative stability of the micelle structure by evaluating its in simulated body fluids. We did this by the addition of 5% fetal bovine serum (FBS) into deionized water or PBS solutions of PATRA. What we observed was a complete loss of the particle signal within the solution, generating a wide heterogeneous signal that was uninterpretable by DLS. This suggests that the presence of the proteins within the FBS could drive the disassembly of the micelle structure. This is important as one would assume that upon entry into the skin the presence of proteins and other macromolecules would operate similarly and drive the disassembly of the micelle structure *in vivo*. A similar loss of particle structure was observed with the addition of ethanol to PATRA solubilized in water. By DLS the particle distribution was very broad from multiple microns to tens of nanometers in scale for PATRA in the hydroalcoholic solution.

9.3.3 Controlled Release of ATRA

Release of ATRA from the PATRA polymer was evaluated by dialysis. The PVA polymer is 10 kDa and the ATRA molecule is only 300 Da; therefore, carrying out the release of ATRA within a dialysis bag with a 10 kDa cutoff enabled retention of the PATRA and PVA while equilibrating the ATRA. Release was carried out in hydroalcohol solution as this solvent mixture created a similar loss of particle structure as what we would hypothesize to happen *in vivo* and solubilizes the released ATRA so that we can continuously track its release *in situ*.

Release studies were carried out a two physiologically relevant temperatures as it is known that just like any reaction ester hydrolysis is affected by temperature **(Figure 9-4a)**. We chose to consider 20°C and 37°C as these would approximately represent room temperature and body temperature for the application of the PATRA formulation. Daily measurements of the

released ATRA demonstrated a continuous liberation of the ATRA into solution over approximately eight days.

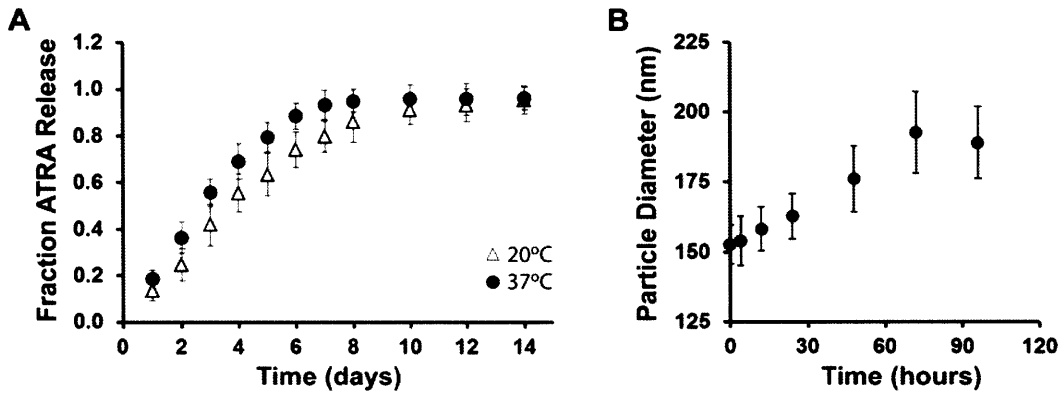

Figure 9-4 Controlled release of ATRA from PATRA and changes in particle size
(a) ATRA release followed daily at 20°C and at 37°C in hydroalcoholic solution out to two weeks. (b) Average particle size after degrading in water for specified periods of time.

We were interested to evaluate the in vitro stability of the PATRA micelles in water, as storage of the formed micelles in water would likely lead to the release of the ATRA. We evaluated this by simply solubilizing PATRA within deionized water and evaluating the average particle diameter over time. It was observed that the average particle diameter increased with storage significantly over a 100 hour study period **(Figure 9-4b)**. During this time it was also observed that the size distribution of particles widened.

9.3.4 *In Vitro* Activity of PATRA

The *in vitro* activity of ATRA was measured by evaluating its effect as an anti-proliferative, as has been previously reported.[18, 20, 57] This was done by supplementing the media of sub-confluent NIH-3T3 cells with ATRA, PATRA, PVA, and control solution in 24-well plates at concentrations equivalent to 10 μM ATRA. ATRA is not soluble in water, and as such must be solubilized in a concentrated hydroalcoholic solution which is then added to cell culture. Ethanol, even in a very low concentration, can be detrimental to cell survival and proliferation. For this reason a similar dose of ethanol was added to each treatment group immediately after

addition of the testing agents. The control solution is deionized water with a small control volume of ethanol, and the cell number calculated from imaging of those wells is used as the reference in the calculation of relative cell density.

Cell proliferation was measured by daily brightfield phase contrast imaging for up to four days as well as with metabolic activity assay after the four days in culture. PATRA was observed to achieve a similar decrease in proliferation as ATRA, while PVA treatment caused negligible changes in proliferation **(Figure 9-5)**. The level of anti-proliferative activity observed in PATRA treated cultures suggests that the activity of ATRA *in vitro* is not inhibited by its conjugation to PVA. It is also possible that PATRA may operate in a different fashion that free ATRA. A third option is that in the presence of cells hydrolysis of the PATRA ester bond may be accelerated, liberating bound ATRA.

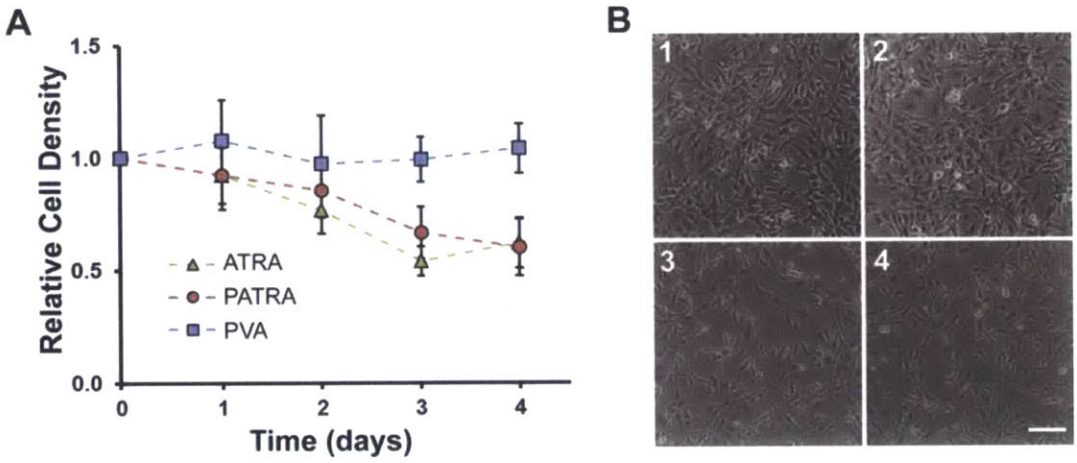

Figure 9-5 Comparison of impact of ATRA and PATRA on cell viability

(a) Relative cell density of cell cultures treated with ATRA, PATRA, or PVA. ATRA in-well concentration was set at 10μM and PATRA concentration was set at an equivalent ATRA concentration. The concentration of PVA was determined by the PVA concentration in PATRA treated wells. (b) Brightfield imaging after four days in culture of NIH-3T3 cells that are either untreated (1) or treated with (2) PVA, (3) PATRA, (4) ATRA. Scale bar = 50 μm.

Importantly, the activity of ATRA bound to PATRA was not observed to be significantly reduced. Further study in this area may elucidate the fundamental reason why the anti-proliferative activity of PATRA appears increased over out predicted released ATRA. It is our belief that the most likely explanation for this finding is a combination of the relatively low unbound concentration of ATRA within the cell culture and the accelerated liberation of ATRA from PATRA under cell culture conditions.

9.3.5 *In Vitro* Delivery of PATRA

Uptake, retention, and penetration of ATRA in pig skin were investigated using a Franz diffusion cell using previously described. In brief, skin was harvested from the flanks of adult female Yorkshire pigs 1 hour after sacrifice with subcutaneous fat removed. Skin was sectioned and frozen at -80°C for up to six months prior to use. Skin was prepared for diffusion experiments by thawing in PBS for one hour after which time all hair on the skin was shaven off. Test samples of skin were cut to 30mm x 30mm square samples that were placed into the diffusion cell such that the top of the dermis was pointed to a 3mL testing retention reservoir and the underside towards a 15mL penetration reservoir. All studies were run at room temperature.

Samples to be tested were placed into the retention reservoir at a concentration of 0.1 mg/mL and followed for up to 12 hours. ATRA concentration was evaluated in both the retention and penetration reservoirs every four hours during this period *via* UV absorbance measurements. Similar to what had been done for *in vitro* studies; ATRA was first solubilized in a concentrated alcohol solution prior to being diluted into the retention well. A similar amount of ethanol was added to the PATRA retention well to control for this. For both groups the penetration reservoir was filled with a hydroalcoholic solution so that the ATRA that could penetrate the skin would be soluble for UV absorbance measurement.

The structure of the pig skin is shown in **Figure 9-6a**. The uppermost layer is the stratum corneum, followed by the epidermis and then the dermis. Each of these layers presents a different environment for ATRA and PATRA accumulation. We labeled the PATRA with a fluorescent dye to evaluate where within the skin the PATRA would localize. What we observed was an increasing concentration of PATRA within the epidermis over the testing period **(Figure 9-6b)**. After four hours the tissue largely look unremarkable, with some fluorescent signal appearing in the stratum corneum, after 12 hours though, an intense clear signal throughout the epidermis is observed, indicating a significant enrichment of this portion of the skin for the labeled PATRA.

Following the ATRA concentration within the receiving reservoir on the underside of the pig skin, we observed a much higher level of ATRA accumulation at every time point tested for free ATRA than PATRA **(Figure 9-6c)**. Logically this makes sense as the diffusion of the much larger PATRA molecule would be much slower than the small ATRA molecule. In addition to this significant property change, the nature of PVA to form hydrogen bonds within the tissue may also be contributing to this impaired penetration.

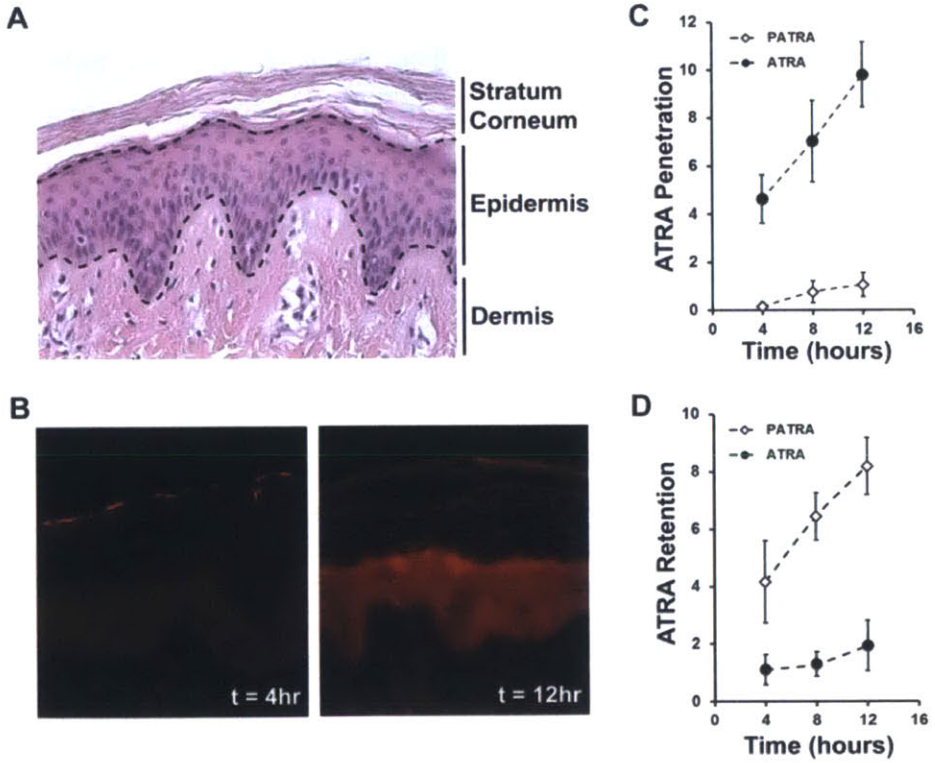

Figure 9-6 Uptake and transport of ATRA in explant pig skin

(a) Histological appearance of pig dermis. (b) Uptake of fluorescently labeled PATRA after 4 and 12 hours of exposure. Uptake is seen to significantly increase over this time and accumulate within the epidermis. (c) Fraction penetration of ATRA through pig dermis followed over 12 hours. (d) Quantification of fraction of ATRA accumulated within the pig dermis over 12 hours of exposure.

Quantification of the ATRA concentration within the retention and penetration reservoirs allows us to perform a mass balance analysis for the ATRA in the testing system. This analysis showed that there was a significantly higher accumulation of the PATRA bound ATRA within the pig skin than was observed for free ATRA **(Figure 9-6d)**. After 12 hours of exposure, approximately 8.2% of the ATRA placed in the retention reservoir was recovered within the treated skin, with the amount increasing over the test period. This finding is in agreement with our previous findings from labeled PATRA, which we had observed accumulating within the epidermis over this period of time.

9.3.6 *In Vivo* PATRA Causes Less Irritation

One of the most reported side effects of topical ATRA therapy is irritation within the application region. This is due in large part to the bolus administration of ATRA, which can often reach super-therapeutic levels easily, especially when treatments require multiple daily administrations of the ATRA formulation. To investigate the relative irritative nature of PATRA in comparison to ATRA we tested each on the flanks of mice. Irritation was evaluated by digital imaging of the application site of ATRA, PATRA, or control solutions for up to five days post-application as well as by histological evaluation after 5 days. In brief, 50μL of 10 μM ATRA solution was placed on a 1 cm^2 shaved area on the flank of a Balb/CJ mouse. PATRA (0.092 mg mL^{-1}) and PVA (0.089 mg mL^{-1}) concentrations were controlled for 10 μM ATRA dosing. This solution is rubbed into the skin using a cotton-tipped applicator for 30 seconds. Each mouse received one of the four different material solutions applied in two locations. Inflammation and dermal changes subsequent to ATRA application were evaluated by both by digital imaging and by H&E histology.

Grossly, the ATRA treated skin begins to appear inflamed after three days. The skin has a thick and rough appearance **(Figure 9-7a)**. The stratum corneum is beginning to flake off, giving a rash like appearance to the site application. The PATRA and PVA treated have no such change in appearance. After five days of treatment the ATRA skin looks less irritated, fewer red spots are observed pockmarking the skins surface. The skin however still has a rash-like quality with a thick and calloused presentation. Neither the PATRA nor the PVA treated skin has any such changes. These application sites appear the same as they were prior to application and are very similar to skin that was treated with PBS and only a small amount of ethanol.

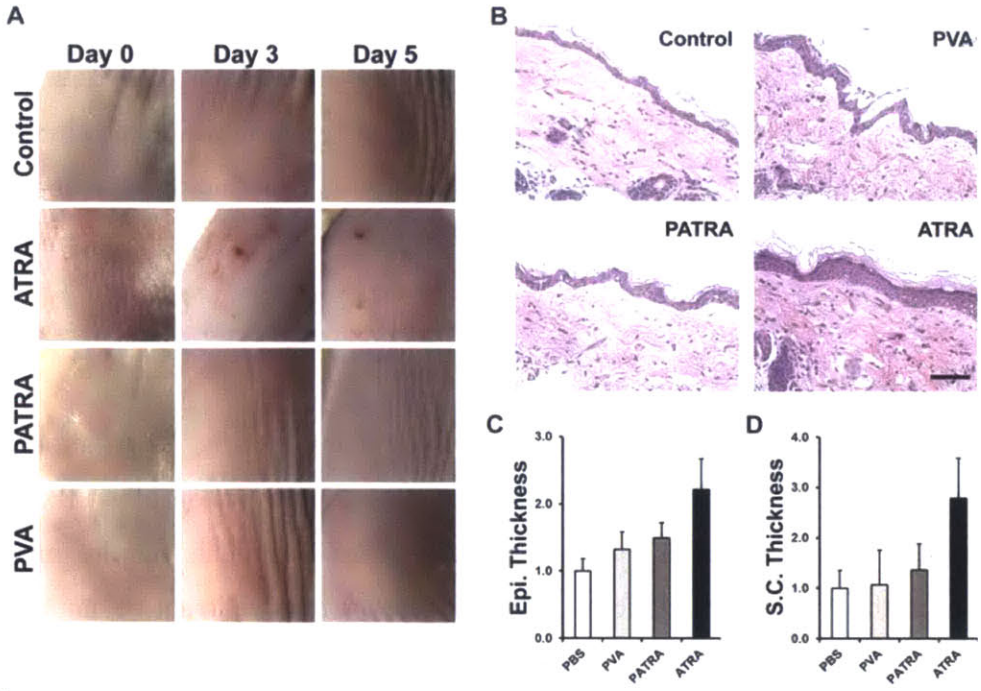

Figure 9-7 Reaction to ATRA application to the dermis

(a) Digital imaging of mouse dermis 0, 3, and 5 days post-application. (b) Histological sections of treated mouse dermis. Changes in epidermal and stratum corneum thickness are clearly observed due to bolus administration of ATRA. These changes are not observed in other treatment groups. (c-d) Quantification of histological findings for the treatment groups after five days. Data shown are mean ± S.D., n = 4.

Histologically, the differences between the treatment groups can be easily appreciated **(Figure 9-7b-d)**. Significantly increased stratum corneum (SC) and epidermal thickness was observed in ATRA treated mice, while not seen in PATRA or control group subjects, indicating

increased inflammation within these tissues. *In vivo* evaluation of PATRA-induced irritation showed a significant reduction in both the irritation and inflammation as seen in similar ATRA applications. We believe this is due to the controlled manner in which the ATRA is released from PATRA, reducing the likelihood of over-stimulating the dermis with ATRA upon administration.

9.3.7 Improved In Vivo Retention of PATRA

The application and retention of the PATRA material was followed using a dye-conjugated form of PATRA. This material was prepared similarly to the base PATRA with the inclusion of an alexafluor-647 dye that was bound to PVA through an ester-linkage, similar to the ATRA molecule. Whole-animal *in vivo* imaging for the tracking of the labeled conjugate was performed on a daily basis for seven days. As a control for the dye-conjugated PATRA we also similarly deposited the free dye on the dorsum of mice to track the loss of the free dye signal.

PATRA and the small molecule dye were both applied to the backs of mice in two locations on the midline on day 0. The materials were allowed to absorb into the skin for 30 minutes and then the backs of the mice were washed twice using a wet cloth. Average radiant efficiency was quantified within the area of application **(Figure 9-8a-b)**. It was observed that the labeled PATRA showed a 3-fold longer half-life within the skin versus the unconjugated small molecule fluorescent dye. The signal from the dye-conjugated PATRA could be seen to persist for out to five days with the average time to 95% clearance lasting almost 6 days **(Figure 9-8c)**.

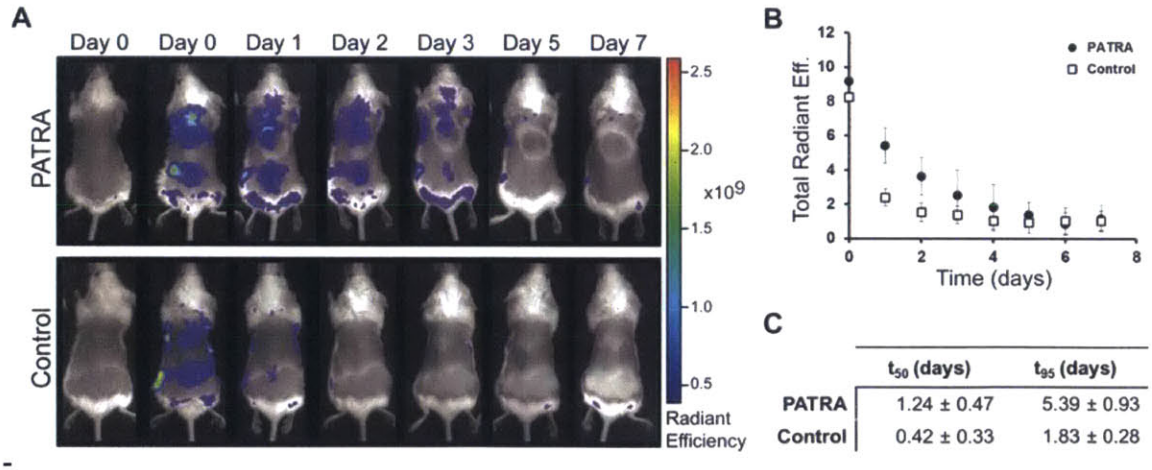

Figure 9-8 Retention of PATRA in the skin of mice

(a) IVIS imaging of fluorescently labeled PATRA over 7 days. Unconjugated dye is seen to disappear after only two days while PATRA conjugated dye stays for up to 5 days. Material was added at two locations on the midline of the backs of mice. (b) Quantification of total radiant efficiency for each application site for PATRA and dye treated mice. (c) Half-life and t_{95} measured from first-order exponential fits of fluorescent data.

9.4 Discussion

Topical application of all-trans retinoic acid is commonly used to treat severe acne and psoriasis as well as being used in many cosmetic applications for its anti-photoaging effects.[6, 14, 46, 58] Administration of ATRA however, presents many difficulties due to its hydrophobic nature and poor stability. A number of different approaches to delivering ATRA to the dermis have been previously investigated.[25, 27, 50, 59] These approaches have focused on formulating ATRA with emulsifiers and lipids to improve solubility or on entrapping it within polymer-based particles to provide sustained release. Achieving both high solubility and controlled release of ATRA from a single platform is a difficult task.

In this work we have presented a new approach to address these issues by directly conjugating ATRA to PVA through a hydrolytically degradable ester-bond linkage. This conjugate formulation helps to solubilize ATRA in water while improving retention of the small molecule at the application site. *In vitro* evaluation of ATRA release demonstrated sustained release for over ten days. We hypothesize that similar to other approaches using ester-bond conjugation the rate of hydrolysis could be manipulated using linking groups or by secondary modification to the PVA backbone.

The approach developed within this work is a simple and robust method using DCC chemistry to form a polymer-drug conjugate which can sustain the release of ATRA over approximately 5 days *in vitro* with little to no reduction in activity over that time. When hydrated the material forms nanometer scale nano-fibers that agglomerate into larger nanoparticles. Conjugation of ATRA to PVA was demonstrated to increase the solubility of ATRA up to nearly 0.35 mg/mL in water. We believe that this increased solubility is achieved due to the amphiphillic nature of PATRA forming nano-micelle fibular structures that are water-soluble.

This polymer conjugate was evaluated cutaneous delivery and was demonstrated to significantly increase the amount of ATRA that was retained within the dermis over a 12 hour period. Fluorescent imaging of the treated tissues showed that the PATRA conjugate was concentrated within the epidermal layer of the skin, which increased throughout the study period. Applying the PATRA conjugate in vivo we observed a significant reduction in gross inflammation as well as insignificant histological findings for inflammation. Further, we also investigated the retention of PATRA within the application site, and demonstrated that this conjugated formulation was observed to be present (t_{95}) for up to nearly six days.

This data taken together presents a substantial argument for the capability of this described method to effectively control the delivery of ATRA into the dermis for topical applications. This approach is broadly useful in a multitude of the applications for ATRA including topical treatments as well as in nanoparticle formulations for cancer therapy. ATRA release from the formulation was observed to be controlled over approximately one week *in vitro* with a resident half-life in the dermis of nearly two days. Activity of ATRA released from the PATRA conjugate was as active as commercially available ATRA measured *in vitro*. Formulating ATRA into PATRA also significantly reduced the negative side effects of ATRA topical therapies, namely irritation and dermal inflammation. We believe that this approach of nano-fiber PATRA for the controlled topical application of ATRA presents many advantages over common formulations for ATRA delivery and is a new approach to this area.

9.5 References

1. Gollnick, H. & Schramm, M. Topical drug treatment in acne. Dermatology 196, 119-125 (1998).

2. Orfanos, C.E., Ehlert, R. & Gollnick, H. The Retinoids - a Review of Their Clinical-Pharmacology and Therapeutic Use. Drugs 34, 459-503 (1987).

3. Mills, O.H. & Kligman, A.M. Treatment of Acne-Vulgaris with Topically Applied Erythromycin and Tretinoin. Acta Derm-Venereol 58, 555-557 (1978).

4. Olsen, E.A. et al. Tretinoin Emollient Cream - a New Therapy for Photodamaged Skin. J Am Acad Dermatol 26, 215-224 (1992).

5. Lehman, P.A., Slattery, J.T. & Franz, T.J. Percutaneous-Absorption of Retinoids - Influence of Vehicle, Light Exposure, and Dose. Journal of Investigative Dermatology 91, 56-61 (1988).

6. Fisher, G.J. et al. Molecular basis of sun-induced premature skin ageing and retinoid antagonism. Nature 379, 335-339 (1996).

7. Sporn, M.B., Roberts, A.B., Roche, N.S., Kagechika, H. & Shudo, K. Mechanism of action of retinoids. J Am Acad Dermatol 15, 756-764 (1986).

8. Panabierecastaings, M.H. Retinoic Acid in the Treatment of Keloids. J Dermatol Surg Onc 14, 1275-1276 (1988).

9. Montenegro, L., Panico, A.M., Ventimiglia, A. & Bonina, F.P. In vitro retinoic acid release and skin permeation from different liposome formulations. Int J Pharm 133, 89-96 (1996).

10. Yamaguchi, Y. et al. Successful treatment of photo-damaged skin of nano-scale atRA particles using a novel transderinal delivery. Journal of Controlled Release 104, 29-40 (2005).

11. Shin, S.C., Kim, H.J., Oh, I.J., Cho, C.W. & Yang, K.H. Development of tretinoin gels for enhanced transdermal delivery. European Journal of Pharmaceutics and Biopharmaceutics 60, 67-71 (2005).

12. Pedace, F.J. & Stoughto.R Topical Retinoic Acid in Acne Vulgaris. Brit J Dermatol 84, 465-& (1971).

13. Yavuzer, R.F., Sen, T., Tarimci, N. & Birol, A. Improved efficacy and tolerability of retinoic acid in acne vulgaris. J Am Acad Dermatol 50, P20-P20 (2004).

14. Harris, D.W.S., Buckley, C.C., Ostlere, L.S. & Rustin, M.H.A. Topical Retinoic Acid in the Treatment of Fine Acne Scarring. Brit J Dermatol 125, 81-82 (1991).

15. Das, S., Ng, W.K., Kanaujia, P., Kim, S. & Tan, R.B. Formulation design, preparation and physicochemical characterizations of solid lipid nanoparticles containing a hydrophobic drug: effects of process variables. Colloids Surf B Biointerfaces 88, 483-489 (2011).

16. Liu, J. et al. Isotretinoin-loaded solid lipid nanoparticles with skin targeting for topical delivery. Int J Pharm 328, 191-195 (2007).

17. Jenning, V. & Gohla, S.H. Encapsulation of retinoids in solid lipid nanoparticles (SLN). J Microencapsul 18, 149-158 (2001).

18. Puppi, D., Piras, A.M., Detta, N., Dinucci, D. & Chiellini, F. Poly(lactic-co-glycolic acid) electrospun fibrous meshes for the controlled release of retinoic acid. Acta Biomaterialia 6, 1258-1268 (2010).

19. Brinckerhoff, C.E. & Sporn, M.B. Retinoids and rexinoids for the 21st century: a brave new world for arthritis. J Rheumatol 30, 211-213 (2003).

20. Giordano, G.G., Refojo, M.F. & Arroyo, M.H. Sustained delivery of retinoic acid from microspheres of biodegradable polymer in PVR. Invest Ophthalmol Vis Sci 34, 2743-2751 (1993).

21. Tadros, T., Izquierdo, P., Esquena, J. & Solans, C. Formation and stability of nano-emulsions. Adv Colloid Interface Sci 108-109, 303-318 (2004).

22. Lira, A.A.M. et al. Preparation and characterization of chitosan-treated alginate microparticles incorporating all-trans retinoic acid. J Microencapsul 26, 243-250 (2009).

23. Castro, G.A., Oliveira, C.A., Mahecha, G.A.B. & Ferreira, L.A.M. Comedolytic effect and reduced skin irritation of a new formulation of all-trans retinoic acid-loaded solid lipid nanoparticles for topical treatment of acne. Arch Dermatol Res 303, 513-520 (2011).

24. Belknap, B.S. Treatment of Acne with 5-Percent Benzoyl Peroxide Gel or 0.05-Percent Retinoic Acid Cream. Cutis 23, 856-859 (1979).

25. Shah, K.A., Date, A.A., Joshi, M.D. & Patravale, V.B. Solid lipid nanoparticles (SLN) of tretinoin: potential in topical delivery. Int J Pharm 345, 163-171 (2007).

26. Hou, L., Yao, J., Zhou, J. & Zhang, Q. Pharmacokinetics of a paclitaxel-loaded low molecular weight heparin-all-trans-retinoid acid conjugate ternary nanoparticulate drug delivery system. Biomaterials 33, 5431-5440 (2012).

27. Tran, T.H., Bae, B.C., Lee, Y.K., Na, K. & Huh, K.M. Heparin-folate-retinoic acid bioconjugates for targeted delivery of hydrophobic photosensitizers. Carbohyd Polym 92, 1615-1624 (2013).

28. Varshosaz, J., Sadeghi-aliabadi, H., Ghasemi, S. & Behdadfar, B. Use of magnetic folate-dextran-retinoic acid micelles for dual targeting of doxorubicin in breast cancer. Biomed Res Int 2013, 680712 (2013).

29. Chiellini, E., Corti, A., D'Antone, S. & Solaro, R. Biodegradation of poly (vinyl alcohol) based materials. Prog Polym Sci 28, 963-1014 (2003).

30. Kaneo, Y. et al. Pharmacokinetics and biodisposition of poly(vinyl alcohol) in rats and mice. Drug Metab Pharmacokinet 20, 435-442 (2005).

31. Paradossi, G., Cavalieri, F., Chiessi, E., Spagnoli, C. & Cowman, M.K. Poly(vinyl alcohol) as versatile biomaterial for potential biomedical applications. J Mater Sci-Mater M 14, 687-691 (2003).

32. Peppas, N.A. & Scott, J.E. Controlled Release from Poly(Vinyl Alcohol) Gels Prepared by Freezing-Thawing Processes. Journal of Controlled Release 18, 95-100 (1992).

33. Nair, B. & panel, C.I.R.E. Final report on the safety assessment of polyvinyl alcohol. Int J Toxicol 17, 67-92 (1998).

34. Jiang, Y. et al. In-vivo studies on intraperitoneally administrated poly(vinyl alcohol). J Biomed Mater Res B Appl Biomater 93, 275-284 (2010).

35. Kobayashi, M., Chang, Y.S. & Oka, M. A two year in vivo study of polyvinyl alcohol-hydrogel (PVA-H) artificial meniscus. Biomaterials 26, 3243-3248 (2005).

36. Weis, C. et al. Poly(vinyl alcohol) membranes for adhesion prevention. J Biomed Mater Res B 70B, 191-202 (2004).

37. Rawat, S. et al. Molecular Mechanism of Poly(vinyl alcohol) Mediated Prevention of Aggregation and Stabilization of Insulin in Nanoparticles. Mol Pharm (2015).

38. Orienti, I., Bigucci, F., Gentilomi, G. & Zecchi, V. Self-assembling poly(vinyl alcohol) derivatives, interactions with drugs and control of release. Journal of Pharmaceutical Sciences 90, 1435-1444 (2001).

39. Orienti, I. et al. Modified doxorubicin for improved encapsulation in PVA polymeric micelles. Drug Deliv 12, 15-20 (2005).

40. Yamaoka, T., Tabata, Y. & Ikada, Y. Comparison of body distribution of poly(vinyl alcohol) with other water-soluble polymers after intravenous administration. J Pharm Pharmacol 47, 479-486 (1995).

41. Yang, M. et al. Nanoparticle penetration of human cervicovaginal mucus: The effect of polyvinyl alcohol. Journal of Controlled Release 192, 202-208 (2014).

42. Ensign, L.M., Cone, R. & Hanes, J. Oral drug delivery with polymeric nanoparticles: The gastrointestinal mucus barriers. Advanced Drug Delivery Reviews 64, 557-570 (2012).

43. Mert, O. et al. A poly(ethylene glycol)-based surfactant for formulation of drug-loaded mucus penetrating particles. Journal of Controlled Release 157, 455-460 (2012).

44. Suk, J. et al. Mucus-Penetrating Nanoparticle for Inhaled Gene Therapy for Cystic Fibrosis. Pediatr Pulm 48, 256-256 (2013).

45. Sporn, M.B. Retinoids and suppression of carcinogenesis. Hosp Pract (Off Ed) 18, 83-88, 91-83, 97-88 (1983).

46. Reynolds, C.P., Matthay, K.K., Villablanca, J.G. & Maurer, B.J. Retinoid therapy of high-risk neuroblastoma. Cancer Lett 197, 185-192 (2003).

47. Saiag, P. et al. Treatment of early AIDS-related Kaposi's sarcoma with oral all-trans-retinoic acid: results of a sequential non-randomized phase II trial. Kaposi's Sarcoma ANRS Study Group. Agence Nationale de Recherches sur le SIDA. Aids 12, 2169-2176 (1998).

48. Sporn, M.B. Vitamin A and its analogs (retinoids) in cancer prevention. Curr Concepts Nutr 6, 119-130 (1977).

49. Tallman, M.S. et al. All-trans-retinoic acid in acute promyelocytic leukemia. N Engl J Med 337, 1021-1028 (1997).

50. Manconi, M., Sinico, C., Valenti, D., Loy, G. & Fadda, A.M. Niosomes as carriers for tretinoin. I. Preparation and properties. Int J Pharm 234, 237-248 (2002).

51. Ourique, A.F., Pohlmann, A.R., Guterres, S.S. & Beck, R.C.R. Tretinoin-loaded nanocapsules: Preparation, physicochemical characterization, and photostability study. Int J Pharm 352, 1-4 (2008).

52. Ozpolat, B. & Lopez-Berestein, G. Liposomal-all-trans-retinoic acid in treatment of acute promyelocytic leukemia. Leuk Lymphoma 43, 933-941 (2002).

53. Wilkinson, R.D. Safety of Retinoic Acid in Acne Therapy. Can Med Assoc J 113, 606-& (1975).

54. Vondendriesch, P., Schell, H. & Haneke, E. Acne Fulminans - Treatment with 13-Cis-Retinoic Acid and Indomethacine. Z Hautkrankheiten 61, 1145-& (1986).

55. Dominguez, J., Hojyo, M.T., Celayo, J.L., Dominguez-Soto, L. & Teixeira, F. Topical isotretinoin vs. topical retinoic acid in the treatment of acne vulgaris. Int J Dermatol 37, 54-55 (1998).

56. DeMerlis, C.C. & Schoneker, D.R. Review of the oral toxicity of polyvinyl alcohol (PVA). Food Chem Toxicol 41, 319-326 (2003).

57. Jeong, Y.I. et al. Preparation of poly(DL-lactide-co-glycolide) microspheres encapsulating all-trans retinoic acid. Int J Pharm 259, 79-91 (2003).

58. Wilkinson, R.D. Retinoic Acid in Acne Therapy - Reply. Can Med Assoc J 114, 412-412 (1976).

59. Choi, Y. et al. Long-term delivery of all-trans-retinoic acid using biodegradable PLLA/PEG-PLLA blended microspheres. Int J Pharm 215, 67-81 (2001).

Chapter 10
Summary and Future Work

10.1 Summary

The local controlled delivery of nucleic acids for RNA interference has the potential to directly treat pathologic dysregulated gene expression and dramatically improve patient care.[1] Developing the technology to achieve this goal however has not yet been accomplished. This thesis sought to investigate the potential role of Layer-by-layer (LbL) assembly for the incorporation and controlled local delivery of siRNA. In pursuing this goal we investigated a wide range of potential LbL assemblies, developed a new method for the high-throughput screening of LbL films, and demonstrated the effective delivery of siRNA *in vivo* in three different animal models, targeting four different genes, from three different coated substrates.

In the first chapter of this thesis we described in detail the complexity of wound healing and the prevalence of its related pathologies. The potential role for RNA interference and layer-by-layer technology within the realm of wound care was explored. The context for this work resides largely in the unmet needs to directly treat the complications within wound healing, and how to best develop material systems to achieve this goal. The local delivery of siRNA by LbL was proposed in this chapter and would be explored through the majority of the rest of the thesis.

In chapter two we introduced our earliest studies of LbL film architectures for the incorporation and release of siRNA. We focused on identifying materials that could be used in these assemblies and in what film architectures siRNA incorporation was observed. These preliminary studies investigated both nanoparticle and direct incorporating films, and helped to identify key aspects of film assembly that led to more effective siRNA loading. This work also looked at demonstrating effective release of siRNA from coated surfaces, and helped define our search criteria and refine our investigative methods. We investigated numerous film architectures and demonstrated the flexibility of the LbL platform for delivery of multiple siRNAs, either simultaneously or sequentially with the potential of temporal control of delivery.

In the third chapter of this thesis we focused our investigations on a film architecture containing calcium phosphate nanoparticles. This LbL assembly had been identified from our previous screens as having significant siRNA incorporating and delivery potential, while needing a more focused approach to identify the best possible film architecture for further investigation. Within this work we described four separate film architectures built around the CaP nanoparticle and demonstrated the importance of material choice and assembly for *in vitro* performance. One film architecture $[Prs/CaP/PrS/Lap]_{25}$ was chosen as the best performing due to its significant siRNA-specific gene silencing and good toxicity profile *in vitro*. It was demonstrated to sustain the release of siRNA for up to 10 days in cell conditioned media with maintained bioactive siRNA being released for days from the assembly. This work was our first published LbL assembly that could incorporate and deliver siRNA in vitro for the sustained knockdown of a reporter gene without any added external transfection vectors.[2]

In Chapter 4 we cover the design and development of a microfluidic high-throughput LbL assembly system.[3] The device described in this chapter used capillary force to uniformly fill arrays of microfluidic channels with material solutions for the robust and reproducible assembly of LbL films. We demonstrated the efficacy of these films in recreating classic LbL experiments from literature as well as in pursuing new areas of research in nucleic acid delivery. The device itself could be operated as a bench top device or combined with liquid handling robots for multiplexed assembly of hundreds of films simultaneously. The films assembled required as little as 0.1% of the material per film as compared to conventional LbL assembly techniques, increasing both the material and time efficiency of investigations. The work described in this chapter was instrumental in accelerating research for siRNA delivering LbL films, and we believe has great potential to widen the applicability of LbL films in the future.

In the fifth chapter of this thesis we describe the design and investigation into a tunable LbL film architecture for the sustained delivery of siRNA *in vitro* and *in vivo*. This work was the first to demonstrate the successful delivery of siRNA from an LbL coated nylon bandage substrate *in vivo*. We used the film architecture of $[Poly2/DS]_x[Chi/siRNA]_y$ within this work. The independence with which we could tune the number of layers of each of the constituent films was crucial to the tunability of both siRNA incorporation and release characteristics. This film was able to achieve sustained significant knockdown of a reporter gene in vitro with

minimal impact on cell viability. We chose to use this film architecture to target an upregulated protease expressed in the healing wounds of chronic ulcers in a mouse model of impaired diabetic wound healing, the $Lepr^{db/db}$ mouse. Within this chapter we detailed how the knockdown of MMP-9, a key ECM protease in wound healing that is known to be chronically upregulated in diabetic ulcers, accelerated wound healing by increasing granulation tissue retention within the healing wound.[4] This work followed wound healing in the treated mice for up to two week, with gross digital imaging and histological methods employed to evaluate the wound healing progress. The sustained knockdown of MMP-9 was observed both at the level of mRNA and protein activity, where siMMP-9 treated wounds saw dramatic reduces in both compared to controls. These siMMP-9 treated wounds had significantly increased granulation tissue formation, accelerated re-epithelialization, and increased wound contraction, all indicating superior wound healing. Evaluating the collagen deposition within the wounds also demonstrated the striking differences between the treatment groups, where the siMMP-9 treated wounds had significantly more collagen than controls, with far more of that collagen being mature Type 1 collagen after two weeks of treatment. The knockdown of MMP-9 within this model of chronic wound healing was then demonstrated to be significantly improved due to the siRNA-specific knockdown of MMP-9 after two weeks of treatment.

In Chapter 6 we performed a similar set of experiments using an LbL coated nylon bandage as we had in Chapter 5; however, this work focused on a different LbL film architecture and targeted a different, though connected, chronically upregulated pro-inflammatory cytokine within healing diabetic wounds. Within this work we use the CaP film architecture that was first described in Chapter 3 to locally deliver siRNA to knockdown TNFα within the healing wound. The role of TNFα within the wound drives inflammation, however in chronic ulcers TNFα expression is pathologically upregulated and leads to prolonged inflammation that impairs wound healing.[5] Within this chapter we described the effective knockdown of TNFα within the wounds of diabetic mice, sustained for out to two weeks in vivo. The effects of this knockdown were thoroughly investigated, including its impact on the expression of related genes, inflammation, and wound healing. It was observed that the knockdown of TNFα resulted in significantly altered gene expression within the healing wounds, as well as dramatic differences in the number of inflammatory macrophages within the wounds. These changes resulted in greatly accelerated wound healing, with many of the siTNFα treated wounds fully regenerating a

proliferating epidermis completely closing off the wounds with little contraction. The impact of TNFα knockdown within the healing wounds was striking, accelerating re-epithelialization, improving granulation tissue formation, and reducing the number of inflammatory cells within the healing tissue.

In the seventh chapter of this thesis we turned our previous investigations toward a new target within the arena of wound healing, scar formation. In the previous work we had been concerned with limited collagen production, and the lack of contraction through the healing tissue, now we were on the other side of that coin, wanting to reduce collagen expression and contractile forces within the wound. We performed the *in vivo* experiments in collaboration with Dr. Martin Yarmush's lab at Shriners Burn Hospital in Boston. We chose to investigate scar formation due to burn injury, as this model has been well documented to form highly reproducible contractile scars. CTGF has been reported for almost two decades for its role in mediating much of the cutaneous pro-fibrotic response of TGFβ signaling, and is a well-studied target in reducing scar formation.[6, 7] Here we looked to apply our LbL technology to effectively delivery siCTGF therapy to healing burns to improve wound healing outcomes in rats. We did this by coating silk sutures which were placed through the healing burn wounds after injury. The burn scars were monitored grossly for up to 30 days, and then rats were sacrificed and burns wounds were prepared for histology and RNA isolation. Grossly, the siCTGF treated burns showed significantly reduced contraction compared to controls, which was in close agreement with histological findings. Evaluating the expression of gene that are known to be stimulated by CTGF expression, we observed significant reductions in siCTGF treated wounds of αSMA, TIMP1, and Col1a1, all of which are known to play roles in scar formation. Evaluating the level of tissue remodeling also demonstrated significantly more advanced tissue remodeling in siCTGF treated burns, most likely a result of the reduced TIMP1 expression, allowing for more MMP activity in the healing tissues. Finally, the evaluation of the collagen organization and alignment demonstrated significant improvements in the siCTGF treated burns compared to controls. Importantly, the collagen alignment at the burn margins was greatly reduced in the siCTGF treated wounds, indicating significantly reduced contractile forces within these tissues. Overall, siCTGF therapy was observed to improve scar formation primarily by reducing contraction of the formed scar and improving tissue remodeling.

In Chapter 8 of this work we once again changed both our in vivo target and our coated substrate, focusing on coating microneedle arrays for the transdermal delivery of siRNA to knockdown the reporter gene GFP *in vivo*. This technique used the physical disruption of the skin by microneedles to deliver LbL contained materials into the dermis. We used the same hierarchical LbL film architecture of $[Chi/siRNA]_{25}$, that was previously described in Chapters 5 and 7 of this thesis. Release of the siRNA from these coated microneedles was facilitated by the rapid solvation of a dip-coated layer of the pH-responsive polymer PNMP that was deposited on the microneedles and photoactivated prior to LbL film assembly.[8] Our investigation demonstrated that the microneedles were able to generate a regular pattern of punctures into the dermis, however in many of these insertions sites it was observed that the damage reached all the way to the skeletal muscle and even through the cartilage in the ear. Delivery of the incorporated siRNA was seen to remain highly concentrated in the tissue directly in contact with the microneedle insertion site. After a few days numerous siRNA positive cells were observed in the surrounding tissue. *In vivo* we observed significant GFP reduction in a siRNA-specific manner for up to one week. This knockdown was observed to be largely contained within the site of application without significant changes in the fluorescence of the surrounding tissue. Primarily this work was focused as a proof of concept study, used to demonstrate the flexibility of the LbL film system in this application. However the general approach outlined within this chapter has a number of potential applications ranging from tissue engineering and regenerative medicine to cancer therapy. This sort of approach could have potential in any number of applications where the local delivery of siRNA may be of benefit.

In the final chapter of this thesis we described a new concept for local topical delivery of all-trans retinoic acid (ATRA), which is a common component in many commercial acne creams as well as being a first-line agent in a number of cancer therapies.[9] Use of ATRA however is limited by its serious side-effects such as skin irritation and hair loss as well as its poor chemical stability. Previous investigations have looked to control these undesirable characteristics through controlled release formulations such as creams and emulsions. These strategies however rely on the bolus delivery of active ATRA which is immediately available upon application and contributes to many of these adverse side-effects. To date there has been limited research into polymer-conjugated forms of ATRA, though such a formulation could improve many of these key disadvantages. Within this work we describe the covalent conjugation of ATRA to

poly(vinyl alcohol), an FDA approved excipient, through an ester bond linkage to produce a polymer-drug conjugate (PATRA) that could sustain the release of ATRA for out to ten days *in vitro*. Within this chapter we extensively explored and characterized PATRA for its release and cutaneous delivery. In this research we determined that through the chemical conjugation of ATRA to PVA we formed a nano-fibular micelle which could solubilize significant quantities of the once-insoluble ATRA in water. In in vitro diffusion cell testing, PATRA was observed to be retained within pig skin at an eight-fold higher level than free ATRA after 12 hours. *In vitro* analysis of ATRA activity determined that PATRA conjugated ATRA was as active as free ATRA, indicating no loss in activity for the released ATRA. To add to these *in vitro* studies, i*n vivo* analysis demonstrated that the PATRA conjugated ATRA caused less topical inflammation in mice and was demonstrated to remain present within the skin of treated mice for up to six days.

10.2 Future Work

This thesis looked to develop ultrathin polymer films for the controlled local delivery of siRNA for the treatment of complicated wound healing. Within this work we have detailed a number of successful LbL films that can incorporate and delivery siRNA in vitro as well as in vivo. We also described the design and development of a high-throughput system for the assembly and screening of LbL film libraries. Many of the films described in this work were shown to be capable of tuning siRNA incorporation and release of one or multiple siRNAs in vitro. As a result of the culmination of this work there are still a number of important concepts to be pursued.

10.2.1 Controlled Delivery of Multiple siRNAs

As it was described in detail in Chapter 1 of this thesis, wound healing is a highly orchestrated complex process that evolves with time. Each phase consists of a unique balance of cytokines and cells which operate within the injured tissue to drive the biological processes of wound healing.[10-13] Understanding that dysregulation in one phase of wound healing may involve multiple evolving therapeutic targets, makes apparent the potential impact of temporally controlled siRNA delivery. In this way a single wound treatment could directly address multiple

pathologic dysregulations within the tissue to create the optimal wound healing environment for tissue regeneration.

In an effort to present this concept we did perform some preliminary testing that suggested that controlling the incorporation and release of multiple siRNAs is possible with LbL assemblies. This work is detailed in Chapter 2 of this thesis. In that work we described a hierarchical LbL structure to spatially separate multiple siRNAs within a single film assembly. In conjunction with this work we also demonstrated the ability to control the incorporation of multiple different siRNAs for multiple gene targeting. It was observed that by simply altering the relative concentrations of each siRNA, one could determine the final ratio of siRNA incorporated within the LbL film. Building upon these early findings we believe that it may be possible to build a wound dressing which could fully address the complexity of the wound healing process.

10.2.2 Combination Drug Therapies

As part of the work presented in this thesis we also briefly investigated combination therapy for wound treatment. This work was a collaborative effort with Dr. Ben Almquist, a post-doctoral student in the Hammond lab. The work focused on combining Dr. Almquist's growth factor delivering LbL film system with one of the siRNA delivering films detailed within this thesis. This work was largely unsuccessful due to the complexity of building multiple independently developed films together. Importantly, limiting factors such as pH stability, inter-layer diffusion, and poor film stability led to a number of these complications.

It should be understood however, that combining siRNA therapy with other modes of altering wound healing offers great potential in better treating complicated wounds. Methods have previously been described for combing growth factors and siRNA in hydrogel formulations to improve bone formation, such a combination using LbL assembly could be similarly effective.[14]

10.3 Conclusions

This thesis describes the rational design of ultrathin polymer coatings for the local controlled delivery of RNA interference. The work presented here spans from the first preliminary concepts of LbL-based RNA delivery to its demonstrated effective application in multiple animal models. A central focus for this work was the application of these films for the improved treatment of complicated wounds. To this end we demonstrated the effective delivery of siRNA to dramatically alter wound healing processes, accelerating diabetic chronic wound healing and reducing contraction in burns. The potential for RNA interference in medicine is enormous. The realization of this potential however will rely on the development of better tolerated and more efficient delivery systems. It is hoped that the materials, methods, and tools described within this thesis may contribute in this continuing research to develop RNA-based therapies to improve patient care.

10.4 References

1. Pan, M., Ni, J., He, H., Gao, S. & Duan, X. New Paradigms on siRNA Local Application. BMB Rep (2014).

2. Castleberry, S., Wang, M. & Hammond, P.T. Nanolayered siRNA Dressing for Sustained Localized Knockdown. ACS Nano 7, 5251-5261 (2013).

3. Castleberry, S.A., Li, W., Deng, D., Mayner, S. & Hammond, P.T. Capillary Flow Layer-by-Layer: A Microfluidic Platform for the High-Throughput Assembly and Screening of Nanolayered Film Libraries. ACS Nano (2014).

4. Rayment, E.A., Upton, Z. & Shooter, G.K. Increased matrix metalloproteinase-9 (MMP-9) activity observed in chronic wound fluid is related to the clinical severity of the ulcer. Br J Dermatol 158, 951-961 (2008).

5. Goren, I. et al. Systemic anti-TNFαlpha treatment restores diabetes-impaired skin repair in ob/ob mice by inactivation of macrophages. J Invest Dermatol 127, 2259-2267 (2007).

6. Lipson, K.E., Wong, C., Teng, Y. & Spong, S. CTGF is a central mediator of tissue remodeling and fibrosis and its inhibition can reverse the process of fibrosis. Fibrogenesis Tissue Repair 5, S24 (2012).

7. Penn, J.W., Grobbelaar, A.O. & Rolfe, K.J. The role of the TGF-beta family in wound healing, burns and scarring: a review. Int J Burns Trauma 2, 18-28 (2012).

8. Doh, J. & Irvine, D.J. Photogenerated polyelectrolyte bilayers from an aqueous-processible photoresist for multicomponent protein patterning. J Am Chem Soc 126, 9170-9171 (2004).

9. Sporn, M.B., Roberts, A.B., Roche, N.S., Kagechika, H. & Shudo, K. Mechanism of action of retinoids. J Am Acad Dermatol 15, 756-764 (1986).

10. Park, J.E. & Barbul, A. Understanding the role of immune regulation in wound healing. Am J Surg 187, 11S-16S (2004).

11. Gurtner, G.C., Werner, S., Barrandon, Y. & Longaker, M.T. Wound repair and regeneration. Nature 453, 314-321 (2008).

12. Gurtner, G.C., Rohrich, R.J. & Longaker, M.T. From bedside to bench and back again: technology innovation in plastic surgery. Plast Reconstr Surg 124, 1355-1356 (2009).

13. Sen, C.K. et al. Human skin wounds: a major and snowballing threat to public health and the economy. Wound Repair Regen 17, 763-771 (2009).

14. Manaka, T. et al. Local delivery of siRNA using a biodegradable polymer application to enhance BMP-induced bone formation. Biomaterials 32, 9642-9648 (2011).